INVERSE METHODS IN QUANTUM MANY-BODY PHYSICS

BY

ELI CHERTKOV

DISSERTATION

Submitted in partial fulfillment of the requirements
for the degree of Doctor of Philosophy in Physics
in the Graduate College of the
University of Illinois Urbana-Champaign, 2021

Urbana, Illinois

Doctoral Committee:

Professor Nigel Goldenfeld, Chair
Associate Professor Bryan K. Clark, Director of Research
Professor Jun Song
Associate Professor Bryce Gadway

Abstract

The interactions of many quantum particles can give rise to fascinating emergent behavior and exotic phases of matter with no classical analogues. Examples include phases with topological properties, which can occur at low temperatures in frustrated magnets and certain superconductors, and many-body localized (MBL) phases that do not obey the laws of thermodynamics, which can occur in interacting disordered magnets. Traditionally, such quantum phases of matter have been studied using a "forward" approach, where a model for the phase is solved to understand the phase's properties. In this thesis, we explore an alternative "inverse" approach to the problem, where we find models from properties, and show how inverse methods and related tools can be used to efficiently study topological and MBL physics in a new way.

In Chapter 1, we introduce the theoretical background necessary for understanding this thesis. First, we discuss the typical forward approach used to study quantum physics and some of its limitations. We introduce the alternative inverse approach that we take in this thesis and give some background on how methods for solving inverse problems have been highly successful in areas such as machine learning and classical physics. Next, we describe two types of topological phases of matter, quantum spin liquids with Wilson loops and topological superconductors with Majorana zero modes (MZMs). These phases have exotic properties, such as long-ranged entanglement and anyonic quasiparticles, that make them interesting to study and potentially useful in emerging technologies such as quantum computing. Finally, we provide an overview of the phenomenon of many-body localization, the failure of many quantum particles to thermalize – equilibrate with their surroundings – in the presence of strong interactions and disorder. We introduce the concept of thermalization and discuss how MBL systems defy thermalization. We also explain the various key signatures of MBL physics, such as low-entanglement of eigenstates and the existence of local integrals of motion known as local bits or ℓ-bits.

In Chapter 2, we discuss the main numerical techniques that we used to study quantum many-body systems. First, we discuss the exact but computationally expensive exact diagonalization (ED) method, which can be used to study small systems with few quantum spins. Next, we discuss the variational Monte Carlo (VMC) method, which can be used to compute properties of certain classes of variational wave func-

tions by sampling a Markov chain. Then, we explain techniques for performing calculations with tensor networks, a class of quantum states defined through the contraction of many tensors. Finally, in addition to the state-based methods we just described, we also introduce operator-based methods that we be essential for our inverse approach and our study of MBL.

In Chapter 3, we introduce the eigenstate-to-Hamiltonian construction (EHC) inverse method that finds Hamiltonians with desired eigenstates. We benchmark the method with many different input states in one and two-dimensions. In each case, we find that the EHC method can find many different Hamiltonians with the target state as an eigenstate, and in many cases a ground state. We show how EHC can be used to find new Hamiltonians with interesting ground states, find Hamiltonians with degenerate ground states, and expand the ground state phase diagrams of previously studied Hamiltonians.

In Chapter 4, we introduce the symmetric Hamiltonian construction (SHC) inverse method that finds Hamiltonians with desired symmetries. We use SHC to study quantum spin liquids and topological superconductors. In particular, by providing Wilson loops as input to SHC, we find new types of spin liquid Hamiltonians with properties not seen in previously studied models and, by providing MZMs as input to SHC, we find a large class of superconductor Hamiltonians with tunable MZM physics.

In Chapter 5, we develop a tool that allows us to study MBL physics in higher dimensions than was previously possible. While MBL has been clearly observed in one spatial dimension, it is a key open question whether MBL survives in two or three dimensions. Because of the numerical difficulty of studying two and three dimensional quantum systems, this problem has been largely unexplored. We develop an algorithm for finding approximate ℓ-bits, local integral of motions and a key signature of MBL physics, in arbitrary dimensions. Using this algorithm, we observe a sharp change in the properties of ℓ-bits versus disorder strength for four different models in one, two, and three dimensional spin systems. This provides the first evidence for the existence of a thermal to MBL transition in three dimensions.

In Chapter 6, we present a method for constructing a large family of Hamiltonians with magnetically ordered "spiral colored" ground states. We demonstrate how these Hamiltonian and states can be arranged into many different geometrical patterns. We also show that with slight modification these Hamiltonians can be made to realize quantum many-body scars, a type of anomalous high-energy excited state that does not exhibit thermal properties as is typical for quantum systems that thermalize.

In Chapter 7, we summarize our work and provide an outlook on paths forward.

Acknowledgments

I would like to thank the many people who made my graduate study at the University of Illinois a happy and rewarding experience.

First, I deeply thank my advisor, Professor Bryan Clark, for his excellent mentoring and support. My discussions with him on topics big and small were essential for my success and for my development as a scientist. From our first conversation, he was very willing to discuss with me about my half-formed and out-there ideas. Having these discussions helped me find the ideas that eventually became the topics of this thesis. I am also grateful to Bryan for helping me with countless applications to workshops, summer schools, internships, and jobs and for helping me transition to the field of quantum computing towards the end of my graduate studies.

I thank Michael Foss-Feig and David Hayes from Honeywell Quantum Solutions for their great mentoring during the internship in the last year of my PhD and for helping introduce me to the field of near-term quantum computing. I am excited to join the team and see what the future of quantum computing will bring!

I thank former and current members of Bryan's group, Xiongjie Yu, Dmitrii Kochkov, Benjamin Villalonga Correa, Ryan Levy, Chad Germany, Di Luo, Abid Khan, and James Allen, for our many interesting conversations. I particularly thank Benjamin for a great collaboration on two of the projects that make up this thesis and for his helpful advice on entering the quantum computing industry. I thank Xiongjie, Dima, and Chad for being great office-mates and always willing to chat. I also thank Ryan, Di, Abid, and James for collaborating on two fun quantum computing hackathon projects.

I thank my family for everything they do. I thank my mom, Olga, for her years of constant support and life advice. I thank my dad, Misha, for introducing me to the wonders of science from a young age and helping guide my scientific career. I thank my brothers, George and Danny, for their friendship over the years. I wish them both luck in their work and studies and know they have bright futures ahead of them.

I thank my Illinois friends who were like a second family to me. I thank Minhui for bringing cheer and happiness into my life every day. I thank Paul and Alex for being really fun roommates who were always willing to play complicated board games with me. I thank Brian, Lily, Gloria, Astha, Bikash, Michelle, Alina, Jasso, Kiel, Lazar, Matt, Xueying, and Jahan for all the fun times and adventures we have shared. I thank my friends from Illinois GPS, Devyn, Preetha, Karmela, Gloria, Angela, Brianne, and Will, for years of good conversations, successful matchings, and excellent retreats. I thank my friends from PGSA, Sam and Alex, for all of their hard work making events like Phys Rev run smoothly. I wish you all luck in the next stage of your life!

I thank Lance Cooper for the great advice and support that he has provided to me and many other graduate students in our program.

Funding Agencies: My graduate research has been supported by the University of Illinois Graduate College's Dissertation Completion Fellowship, SciDAC grant DE-FG02-12ER46875, and Department of Energy grant DOE DE-SC0020165. This research is part of the Blue Waters sustained-petascale computing project, which is supported by the National Science Foundation (awards OCI-0725070 and ACI-1238993) and the state of Illinois. Blue Waters is a joint effort of the University of Illinois at Urbana-Champaign and its National Center for Supercomputing Applications.

Academic Disclaimer: The author wrote this dissertation in support of requirements of the degree of Doctor of Philosophy in Physics at the University of Illinois at Urbana-Champaign.

Table of Contents

List of Tables

List of Figures

Chapter 1

Introduction

In this thesis, we investigate a new "inverse" approach to studying quantum many-body systems and use it to study quantum phenomena such as quantum spin liquids and Majorana zero modes. We also explore how related techniques can be used to tackle problems in the field of many-body localization. In Section 1.1, we describe how the inverse approach contrasts with the more traditional methods used to study quantum physics and how it can be used to tackle physics problems in a new way. Section 1.2.1 introduces quantum phases of matter known as quantum spin liquids and Section 1.2.2 discusses the physics of Majorana zero modes, two types of topological systems that we examine in Chapter 4. Finally, Section 1.3 provides background on many-body localization and local integrals of motion, which we explore in Chapter 5.

1.1 A new inverse perspective on quantum physics

A key goal of quantum physics is to understand the relationship between the interactions of many quantum particles and the emergent behavior that results from those interactions. The interactions in a quantum system are specified by a model, or Hamiltonian. The emergent behavior can be described by looking at properties of the model, such as the Hamiltonian's eigenstates or symmetries. Traditionally, the relationship between models and their properties has been studied in a single direction: given a particular model, the model is solved to find its properties. This is what we call the "forward approach" (see Fig. 1.1(a)). In this thesis, we explore an "inverse approach" to this problem in quantum physics, where given a property we look for models with that property (see Fig. 1.1(b)). This inverse approach complements the traditional forward one and allows us to study quantum systems in a new way.

1.1.1 The forward approach

A significant occupation of theoretical physicists is solving models. Since the discovery of the equations of quantum mechanics in the 1920s, many physicists have been focused on solving these equations. This has led to breakthroughs and discoveries that form the foundations of modern quantum physics. For ex-

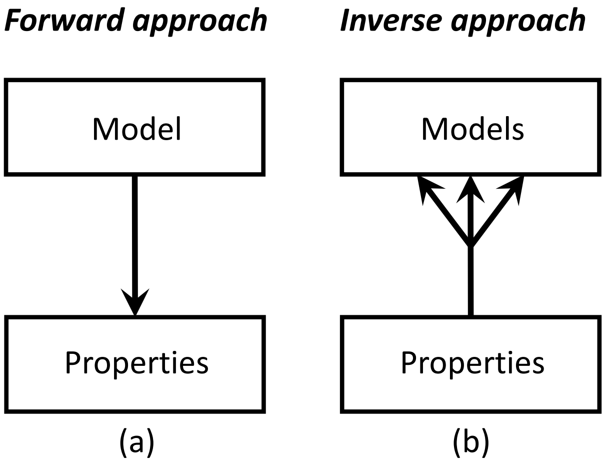

Figure 1.1: (a) Forward and (b) inverse methods in physics.

ample, the solutions to the harmonic oscillator Hamiltonian have led to our understanding of photons and associated technologies such as lasers, and the solutions to the hydrogen atom Hamiltonian have led to our understanding of atomic physics and chemistry.

Unfortunately, beyond a few famous and well-studied models, most Hamiltonians of quantum systems are impractically difficult to solve. This is the case for many Hamiltonians of condensed matter systems, systems which include metals, insulators, magnets, superconductors, and other phases of matter found in real materials. In condensed matter physics, the Hamiltonians of interest are often simplified minimal models that capture the rough features of what in reality is a complicated set of interactions. By studying these minimal models, physicists hope to find properties that are universal to large classes of materials. A famous example of such a model is the Fermi-Hubbard model [1]

$$\hat{H}_{FH} = -t \sum_{\langle ij \rangle, \sigma} (\hat{c}^{\dagger}_{i\sigma}\hat{c}_{j\sigma} + \hat{c}^{\dagger}_{j\sigma}\hat{c}_{i\sigma}) + U \sum_{i} \hat{n}_{i\uparrow}\hat{n}_{i\downarrow} \tag{1.1}$$

where $\hat{c}^{\dagger}_{i\sigma}$ creates an electron at site i in a square lattice with spin σ, $\hat{n}_{i\sigma} = \hat{c}^{\dagger}_{i\sigma}\hat{c}_{i\sigma}$, $\sigma = \uparrow, \downarrow$, t is the hopping amplitude, U is the on-site interaction strength, and the first summation is over nearest neighbor sites on a square lattice. The Fermi-Hubbard model is a simplified model for strongly interacting electrons in a solid and has been used to study Mott insulating physics [2] and high-temperature superconductivity [3] in materials such as the cuprates [4]. Despite being actively studied for over fifty years, its properties are still not entirely understood [5]. This lack of understanding of Hamiltonians such as Eq. (1.1) is due to the fact that these models have no known analytic solutions and must be solved numerically, which requires prohibitive computational cost that is exponential in the number of quantum particles.

The difficulty of solving generic Hamiltonians limits how much we can learn from the forward approach. In this approach, Hamiltonians are studied one at a time and checked to see if they exhibit particular interesting properties. For example, as discussed in Section 1.2.1, a special type of disordered quantum magnet known as a quantum spin liquid is known to exhibit a number of interesting non-local topological properties. Yet, there are very few Hamiltonians known to have spin liquid properties. In practice, to find new spin liquid Hamiltonians, one guesses a particular model, solves it, and checks if it matches expected spin liquid physics. The difficulty in executing this procedure makes the process of finding new spin liquid models (or materials) laborious. For this reason, the forward approach can cause us to overlook models which might contain interesting physics. It would be beneficial to supplement the forward approach with other methods that allow us to overcome this issue.

1.1.2 The inverse approach

In this thesis, we utilize an alternative "inverse" approach, where we look for Hamiltonians with desired properties, to study interesting quantum systems with different types of magnetic and topological order. The hope is that this inverse approach can automate the discovery of new models with desired physics and provide insight into the interplay between interactions and physical properties. Ultimately, this approach could inform the design of new materials or the discovery of new physics.

Inverse problems, problems involving learning a model from data, are important in statistics and machine learning. A well-known inverse problem is the linear regression problem of learning the relation $y = Ax$, i.e., the model specified by the matrix $A \in \mathbb{R}^{m\times n}$, given data points $x_i \in \mathbb{R}^n, y_i \in \mathbb{R}^m$. This problem can be solved, for example, by minimizing the least-squared distance $\sum_i \|y_i - Ax_i\|^2$ using linear algebra techniques. In principle, inverse problems can be ill-posed with either many solutions (many A exactly satisfying $y_i = Ax_i$ for all i) or none (no A that exactly satisfy $y_i = Ax_i$ for all i). Nonetheless, by examining all possible solutions or looking for approximate solutions one can still learn useful models. This is also the case for the task of learning the parameters of high-dimensional models from data sets, an inverse problem common in machine learning. Despite the ill-posed nature of this inverse problem and the potentially high computational cost of solving it, machine learning techniques such as deep learning [6] have proven incredibly successful. They are powerful tools for modeling complicated data and tackling difficult engineering problems, such as classifying images [7, 6] and playing Go [8]. The great success of inverse methods, i.e., methods for solving inverse problems, in statistics and machine learning applications suggests that it is worth developing inverse methods for applications in physics.

Classical inverse problems

In classical many-body physics, inverse methods have been developed to design classical Hamiltonians that produce systems with desired statistical or ground state properties. Consider the classical Ising Hamiltonian

$$H_I = -\sum_{ij} J_{ij} S_i S_j - \sum_i h_i S_i \tag{1.2}$$

where $S_i = \pm 1$ are classical binary spins and the spin-spin interactions J_{ij} and magnetic fields h_i are the parameters of the model. In the classical setting, the Hamiltonian $H_I(\{S_i\})$ is a function that returns the energy for a given spin configuration $\{S_i\}$. In a typical forward problem, we would be given the $\{J_{ij}, h_i\}$ and solve the Ising model to find its properties. These properties could be the model's lowest energy (ground state) spin configuration or statistical expectation values $\langle O \rangle = \sum_{\{S_i\}} p(\{S_i\}) O(\{S_i\})$ of observables $O(\{S_i\})$ such as magnetization at finite temperature T given by the Boltzmann distribution,

$$p(\{S_i\} | \{J_{ij}, h_i\}) = \frac{1}{Z} e^{-H_I(\{S_i\})/T} \tag{1.3}$$

where $Z = \sum_{\{S_i\}} \exp\left(-H_I(\{S_i\})/T\right)$ is the partition function.

In the inverse Ising problem, reviewed in Ref. [9], we are instead interested in determining the Ising model parameters $\{J_{ij}, h_i\}$ from spin configurations sampled from Eq. (1.3). This is a statistical inference problem that can be phrased in terms of maximum likelihood: the goal is to find the $\{J_{ij}, h_i\}$ that maximizes the log-likelihood $\mathcal{L}(\{J_{ij}, h_i\}) = \sum_{\{S_i\}_{data}} \log P(\{S_i\} | \{J_{ij}, h_i\})$ where the sum is over sampled spin configurations. Estimating and optimizing the log-likelihood (or some approximation of it) can be done using Markov chain Monte Carlo [10] and Belief propagation [11–14]. Methods for solving the inverse Ising problem have been used to reconstruct the connections between neurons and the structure of proteins [9].

Similarly, in the inverse statistical mechanics problem introduced in Refs. [15, 16], the goal is to find the Ising model parameters $\{J_{ij}\}$[1] from a desired ground state spin configuration C_0. Refs. [15, 16] tackle this problem numerically by solving the optimization problem

$$\max_{\{J_{ij}\}} \left[\min_{C_k} \Delta\epsilon_k \right], \tag{1.4}$$

where C_k are "competitor" spin configurations and $\Delta\epsilon_k = H_I(C_k) - H_I(C_0)$ is the energy gap between the target spin configuration C_0 and competitor C_k, subject to the constraints $\Delta\epsilon_k \geq 0 \,\forall k$, $-1 \leq J_{ij} \leq 1 \,\forall i, j$. Intuitively, this objective function finds the Ising model with the largest gap between the energies of ground

---

[1] These studies chose to consider Ising models with no magnetic fields, i.e., $h_i = 0$ for all i.

state C_0 and the first excited state spin configuration. The optimization of Eq. (1.4) is performed heuristically and involves iteratively repeating two steps:

1. Given the current competitor list C_k, solve a linear programming [17] problem to find the best J_{ij}.
2. Given the current Ising model with parameters J_{ij}, find the ground state spin configuration C using an optimization algorithm such as simulated annealing [18]. If it is lower in energy than C_0, add it to the competitor list C_k.

Note that the algorithm can fail to find a solution if either optimization step fails. This inverse method has been used to successfully design Ising models with ground states exhibiting stripe and checkerboard patterns [15] as well as more exotic stealthy hyperuniform order [19]. Similar techniques have also been used to find classical interaction potentials that encourage point particles to self-assemble into desired crystalline lattices [20] and potentials that lead to exotic material properties such as negative Poisson ratios [21].

Quantum inverse problems

Inverse problems also arise in quantum many-body quantum physics. The inverse problem that we will focus on is finding *quantum* Hamiltonians, or Hermitian operators acting on a large Hilbert space, with particular properties. Being able to solve this problem in general would be widely useful, as it would allow for the design of quantum systems with targeted physics.

A natural inverse problem of this type is the problem of finding Hamiltonians with a particular desired ground state $|\psi_0\rangle$. Such Hamiltonians are often referred to as *parent Hamiltonians* of $|\psi_0\rangle$. Since quantum phases of matter are determined by ground states, being able to design new Hamiltonians with desired ground states also potentially allows one to design new quantum phases of matter. In general this is a difficult problem, and no efficient general-purpose method exists to solve it. However, tractable methods for finding the parent Hamiltonians of certain classes of quantum states have been developed. In particular, methods exist for finding parent Hamiltonians of matrix product states (MPS) [22–24] and projected entangled pair states (PEPS) [25, 26], two types of tensor network states (see Section 2.3). These methods provide exact analytic expressions for unique, local, frustration-free parent Hamiltonians given MPS or PEPS satisfying certain conditions provided as input. Since each MPS has an associated parent Hamiltonian, one can determine whether two different MPS states are in the same phase by seeing if there is a path between the two states such that the parent Hamiltonians on the interpolating path stay gapped [27, 28]. Parent Hamiltonians of other specific states, such as the resonating valence bond (RVB) state on the Kagome lattice [29–31] (a type of quantum spin liquid state; see Section 1.2.1), have also been found. In many cases, parent

Hamiltonians found using these methods are complicated, involving many-spin interactions that are hard to realize in nature or in synthetic quantum systems.

Another important quantum inverse problem is Hamiltonian learning (sometimes referred to as Hamiltonian tomography), the task of determining the Hamiltonian that generated a system's time evolution [32]. Quantum simulators are special-purpose quantum devices designed to simulate the time-evolution $e^{-it\hat{H}}$ of particular many-body Hamiltonians $\hat{H}$ [33]. As these devices become more sophisticated and capable of simulating longer-time dynamics on larger systems, it becomes harder to classically simulate them. This makes it difficult to classically verify that a quantum simulator is time-evolving the correct Hamiltonian $\hat{H}$. Hamiltonian learning methods [32, 34–40] address this problem by inferring a Hamiltonian from experimental data from the quantum simulator and verifying that it is close to the Hamiltonian the simulator is attempting to implement.

In this thesis, we discuss two methods that we developed for finding local quantum Hamiltonians

$$\hat{H} = \sum_a J_a \hat{h}_a, \tag{1.5}$$

where $\hat{h}_a$ are local Hermitian operators and J_a are real coefficients, with desired properties. The first method, the eigenstate-to-Hamiltonian construction (EHC) (discussed in Chapter 3), finds Hamiltonians with a desired energy eigenstate, a state $|\psi\rangle$ satisfying $\hat{H}|\psi\rangle = E|\psi\rangle$ for constant E [41]. This method does not guarantee that $|\psi\rangle$ will be a ground state, so the Hamiltonians found this way are not necessarily parent Hamiltonians as discussed above. The techniques in this method were developed simultaneously in Refs. [42, 41, 43]. The second method, the symmetric Hamiltonian construction (SHC) (discussed in Chapter 4), finds Hamiltonians with a desired symmetry, a Hermitian operator $\hat{\mathcal{O}}$ that commutes with the Hamiltonian: $[\hat{H}, \hat{\mathcal{O}}] = 0$ [44]. It is based on the so-called slow-operator method developed by Ref. [45]. We apply the EHC and SHC methods to study a variety of condensed matter systems.

The EHC method finds Hamiltonians with a targeted eigenstate $|\psi\rangle$ by looking for local Hamiltonians, Eq. (1.5), that minimize the energy variance, $\langle\psi|\hat{H}^2|\psi\rangle - \langle\psi|\hat{H}|\psi\rangle^2$, with respect to that state. We show that this minimization can be accomplished efficiently, in time polynomial in the system size, by computing and diagonalizing the quantum covariance matrix (or correlation matrix [42]), a quantum generalization of a statistical covariance matrix. We benchmark this method by reconstructing Hamiltonians from their ground states on seven different example systems, which include one-dimensional spin Hamiltonians and a two-dimensional fermionic model, using a variety of numerical tools, including exact diagonalization, variational Monte Carlo, and tensor networks. We also demonstrate how EHC can be used to (1) find new parent

Hamiltonians with previously undiscovered magnetic ground states, (2) find Hamiltonians with multiple degenerate ground states, and (3) expand the ground state phase diagram of known Hamiltonians.

Similarly, the SHC method finds Hamiltonian with a targeted symmetry $\hat{\mathcal{O}}$ by looking for local Hamiltonians that minimize the commutator norm, $\|[\hat{H}, \hat{\mathcal{O}}]\|^2$ where $\|\hat{A}\|^2 = \mathrm{tr}(\hat{A}^\dagger \hat{A})/\mathrm{tr}(I)$. This minimization can be performed efficiently by computing and diagonalizing the commutant matrix [45, 46], which is a generalization of the quantum covariance matrix mentioned above. We compute the commutant matrix efficiently by using the algebraic properties of Pauli matrices, as described in Section 2.4. Our numerical implementation of this method is available as an open-source Python code [47]. Using SHC, we designed large families of Hamiltonians exhibiting the physics of quantum spin liquids and Majorana zero modes, examples of topological phases of matter.

Since the original papers on the eigenstate-to-Hamiltonian method [42, 41, 43], there have been a number of interesting extensions. Ref. [37] developed a method for finding local Hamiltonians from a steady state $\hat{\rho}$, satisfying $i\partial_t \hat{\rho} = [\hat{H}, \hat{\rho}] = 0$, that involves building a constraint matrix similar in form to the quantum covariance matrix and commutant matrix. With a few examples on spin systems, they demonstrated that this method can be used to efficiently reconstruct Hamiltonians from thermal states and time-averaged states. Ref. [39] used this method combined with Bayesian inference to perform efficient Hamiltonian learning. Also, Ref. [48] developed a method for finding Linbladians, a generalization of Hamiltonians for open quantum systems, from steady states.

The EHC method has also been applied in the context of many-body localization (see Section 1.3) and variational optimization (see Section 2.2). Refs. [49, 50] used the EHC method to find large families of 1D many-body localization from the eigenstates of other 1D MBL Hamiltonians, showing that MBL eigenstates are to high accuracy the eigenstates of multiple similar MBL Hamiltonians. A generalization of this idea to 2D MBL Hamiltonians was explored in Ref. [51]. Ref. [52] proposed using EHC as a metric to assess the quality of variational wave functions, which can be used to supplement other more coarse metrics such as energy or variance. In addition, Ref. [53] introduced a new algorithm for variationally lower-bounding the energy of a ground state using the quantum covariance matrix, the central quantity of EHC, and benchmarked it on a variety of spin chains.

1.2 Topological phases of matter

In this thesis, we study two types of topological phases of matter, quantum spin liquids and topological superconductors. In both cases, the systems exhibit a kind of non-local "topological order" which can be characterized by symmetry operators, Wilson loops for the Z_2 spin liquids that we consider and Majorana zero modes for the topological superconductors. These symmetries are what we provide as input to the symmetry-to-Hamiltonian inverse methods in Chapter 4 to design new spin liquid and Majorana zero mode Hamiltonians. In this section, we review the relevant physics of these systems.

1.2.1 Quantum spin liquids

Quantum spin liquids are a type of ground state that can occur in magnetic materials that exhibit strong frustration, the inability of local magnetic moments (or spins) to align due to competing interactions or geometry [54–56]. Candidate spin liquid materials are insulators with strong interactions, so that the electrons are immobile and the electrons' spins strongly fluctuate. The spins in a spin liquid states form a highly correlated "liquid" that prevents order from forming [55]. This is unusual because a ground state, which corresponds to a material's state at zero temperature, is typically ordered according to Landau's theory of phase transitions. While the lack of order in quantum spin liquids is one of its key signatures, this can also occur in other phases of matter, such as in quantum paramagnets. A more distinguishing feature of quantum spin liquids is the presence of long-range entanglement in the ground state, which means that the ground state cannot be transformed into a product state by the application of a finite depth quantum circuit made of local unitary transformations [56].

There are many types of quantum spin liquids, just as there are many types of magnetically ordered states [56]. Generally speaking, quantum spin liquids fall into two broad classes, gapped or gapless spin liquids, which differ by whether the excitation spectrum of the spin liquid Hamiltonian exhibits a finite energy gap between the ground state and first excited state in the thermodynamic limit. Here we will focus on gapped spin liquids, since they are better understood theoretically. Gapped spin liquids have "topological order." Topologically ordered systems exhibit excitations that have topologically non-trivial behavior and possess ground state degeneracy that depends on the topology of the lattice, e.g., whether a 2D lattice is shaped as an open plane or a periodic torus [57, 58]. Fractional quantum Hall systems, two-dimensional electron gases subject to a strong magnetic field, are other examples of systems with topological order. Systems with topological order exhibit quasiparticles with exotic exchange statistics known as anyons, that can be loosely interpreted as generalizations of Fermions and Bosons [59]. In gapped quantum spin liquids, the typical quasiparticles that emerge are called spinons, and carry a spin of 1/2 and a charge of 0 [56]. This "fractionalization" of spin and charge in spin liquids highlights that spinons cannot be interpreted as simple combinations of elementary particles such as electrons, but are rather emergent particles made from the non-trivial collective behavior of many electrons. In contrast, a simple local spin excitation in an insulating

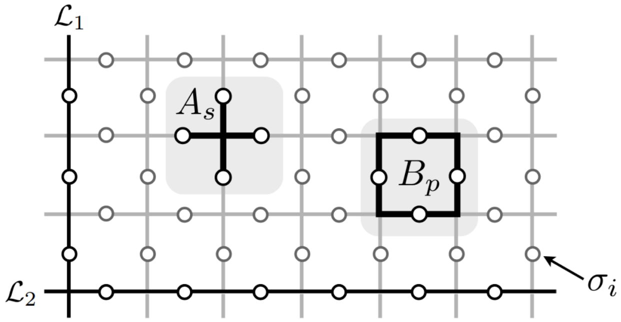

Figure 1.2: (From Ref. [61]) The star and plaquette operators $\hat{A}_s$ and $\hat{B}_p$ of the toric code and two Wilson loop operators $\hat{W}(\mathcal{L}_1), \hat{W}(\mathcal{L}_2)$ that wrap around the torus.

magnet, such as a magnon, would carry integer spin and could be interpreted as a Boson.

The toric code, Z_2 spin liquids, and Wilson loops

Much of our theoretical understanding of gapped quantum spin liquids has come from studying simple exactly solvable models. Here we will describe one of these models, the toric code [60]. The toric code, depicted in Fig. 1.2, is a spin-1/2 Hamiltonian on a square lattice of the form

$$\hat{H}_{TC} = -\sum_s \hat{A}_s - \sum_p \hat{B}_p \tag{1.6}$$

where $\hat{A}_s = \prod_{i\in s} \hat{\sigma}_i^z$ and $\hat{B}_p = \prod_{j\in p} \hat{\sigma}_j^x$ are "star" and "plaquette" operators made of four Pauli-Z and Pauli-X matrices, where the matrices lie on the bonds of the lattice. Since $[\hat{A}_s, \hat{B}_p] = 0$ for all stars s and plaquettes p, $[\hat{H}, \hat{A}_s] = [\hat{H}, \hat{B}_p] = 0$, and the Hamiltonian can be simultaneously diagonalized with the $\hat{A}_s, \hat{B}_p$ operators, making it possible to analytically determine the entire Hamiltonian's spectrum, including the ground states [60]. When the toric code model is on a square lattice with open boundary conditions, the ground state is unique, but when the square lattice is folded into a cylinder or a torus, then the ground state becomes two or four-fold degenerate, respectively.

On the torus, the toric code commutes with Wilson loop operators of the form $\hat{W}^z(\mathcal{L}) = \prod_{j\in\mathcal{L}} \hat{\sigma}_j^z$ that wrap around the two non-contractible loops $\mathcal{L}_1, \mathcal{L}_2$ on the lattice, shown in Fig. 1.2. These operators have eigenvalues ± 1 and the four ground states on the torus correspond to the four possible pairings of eigenvalues $(\pm 1, \pm 1)$ of $\hat{W}^z(\mathcal{L}_1)$ and $\hat{W}^z(\mathcal{L}_2)$. The toric code has three types of Abelian (see Sec. 1.2.2) anyons: e and m particles and a combined em particle[2]. The properties of these anyonic quasiparticles can be described

---

[2] If an e particle is only braided around another e particles, the system wave function is unchanged, suggesting that e is a Boson. Same with the m particle. An em-particle braided around another em-particle results in a minus-sign, suggesting that em is a Fermion. However, when particles of different types are braided around one another, e.g., a e around an m, then the wave function can change non-trivially, which indicates that the set of e, m, and em particles are anyons.

using the modular $\mathcal{S}$ matrix, which can be computed by taking overlaps of minimal entropy states made of the degenerate ground states [62]. In particular, for the toric code with these anyons, the modular $\mathcal{S}$ matrix takes the form [62]:

$$\mathcal{S} = \frac{1}{2}\begin{pmatrix} 1 & 1 & 1 & 1 \\ 1 & 1 & -1 & -1 \\ 1 & -1 & 1 & -1 \\ 1 & -1 & -1 & 1 \end{pmatrix} \tag{1.7}$$

The toric code is an example of a Z_2 quantum spin liquid. Spin liquids of this type all share the same topological properties: they all contain the same anyons and modular matrices.

Experimental studies

While there is a rich theory for topological phases of matter and a few well-understood solvable models for quantum spin liquids, it is difficult to experimentally identify quantum spin liquid phases in real materials [63, 64]. Many different materials have been proposed as candidate quantum spin liquid materials. Many of these materials fall into two types [64]: (1) geometrically frustrated materials where the ground state is expected to be similar to a resonating valence bond state and (2) materials with interactions similar to the quantum spin liquid phase found in the exactly solvable Kitaev honeycomb model [65]. One of the most well-studied candidate quantum spin liquid materials (of type (1)) is Herbertsmithite, a material whose three-dimensional lattice forms sheets of two-dimensional Kagome lattices, a lattice with significant geometric frustration. Inelastic neutron scattering experiments on Herbertsmithite have shown that at low temperatures, below which it would have been expected to order, there are no sharp peaks in the spin excitation spectra but a broad continuum [66]. One interpretation of these results is that the broad continuum corresponds to a band of spinon quasiparticles. However, it is unclear whether these signatures are actually from spin liquid physics or potentially another source such as random defects that can occur in Herbertsmithite, which can lead to similar experimental signals [63].

Recent advances in quantum simulators [33], programmable quantum devices capable of simulating the dynamics of certain quantum systems, and quantum computers [67], quantum devices able to perform arbitrary unitary operations on quantum bits or qubits, have enabled new ways of studying topological phases of matter such as spin liquids. For example, a recent experiment in a superconducting qubit quantum computer simulated the ground state of the toric code Hamiltonian, Eq. (1.6), and was able to experimentally demonstrate the braiding of the e and m quasiparticles [68].

1.2.2 Majorana zero modes

Another example of a quantum system with topological properties and anyonic quasiparticles is a topological superconductor [69]. When topologically non-trivial superconductors have a defect or are in proximity with a topologically trivial material, a quasiparticle can form on the defect or interface [70]. This quasiparticle, which is a zero energy mode of the system, is associated with a Majorana zero-mode (MZM) operator and is a realization of a type of non-Abelian anyon known as an Ising anyon.

Topological quantum computing

While an in-depth discussion of anyons is outside the scope of this thesis, we would like to describe some facts about them to provide context about their importance to topological quantum computation. An excellent review on the subject is Ref. [59]. Anyons are quasiparticles defined by their braiding statistics (braiding two particles can be thought of as moving a particle clockwise in a half-loop around the other). Quantum systems with anyons have degenerate ground states. Generally, anyons come in two types that differ by how they act on this degenerate space: Abelian and non-Abelian. Abelian anyons, such as the quasiparticles of the toric code, cause a state in the ground state space to pick up a complex phase when they are braided. Non-Abelian anyons, such as the Ising anyons in topological superconductors, cause a state in the ground state space to rotate in the space when they are braided. The term non-Abelian refers to the fact that the rotations do not commute, so the order of braiding matters.

Anyons are non-local quasiparticles, which makes them robust to local noise and capable of storing quantum information with low error. This idea underlies using anyons for fault-tolerant quantum computation. The degenerate ground states of anyonic systems defines the Hilbert space used in quantum computation, i.e., the Hilbert space of the qubits. The type of anyon determines the type of quantum computation that can be performed on this Hilbert space. Abelian anyons, for example, can be used to store information in this space so that the information is not destroyed by local perturbations [59], but cannot be used to perform arbitrary manipulations on states in this space that protects against local noise. In other words, Abelian anyons can be used for fault-tolerant quantum memory, but not fault-tolerant quantum computation. Non-Abelian anyons, however, can be used for fault-tolerant quantum computation. By braiding non-Abelian anyons, operations on the topological qubit space can be performed that are insensitive to local noise. To be able to perform an arbitrary quantum computation on qubits, one needs to be able to implement a universal gate set of one and two-qubit gates, such as the Hadamard H gate, the T ($\pi/8$-phase) gate, and the control-Z

gate:

$$H = \frac{1}{\sqrt{2}}\begin{pmatrix} 1 & 1 \\ 1 & -1 \end{pmatrix}, \quad T = \begin{pmatrix} 1 & 0 \\ 0 & e^{i\pi/4} \end{pmatrix}, \quad Z = \begin{pmatrix} 1 & 0 \\ 0 & -1 \end{pmatrix}. \tag{1.8}$$

For certain non-Abelian anyons, such as the so-called Fibonacci anyons, all the gates in this gate set can be realized in a manner that is tolerant to local errors [71, 72]. In this case, all the gates can be realized by braiding anyons that are kept far away from one another, so that local errors have very low probability of spoiling the calculation. For the Ising anyons related to MZMs, many but not all of the necessary gates can be made fault-tolerant in the same way. The T-gate must be realized by bringing the Ising anyons close together, making it an operation unprotected from local errors [70]. Nevertheless, Ising anyons can be combined with quantum error correction techniques to realize error-resilient quantum computers [70].

The Kitaev chain and Majorana zero mode operators

The simplest model of a topological superconductor with MZMs is the Kitaev chain [73]. The Kitaev chain is a model for a chain of non-interacting spin-less fermions with p-wave superconducting pairing:

$$\hat{H}_{KC} = \sum_{j=1}^{L-1}\left(-t\hat{c}_j^\dagger \hat{c}_{j+1} + \Delta \hat{c}_j \hat{c}_{j+1} + \text{H.c.}\right) - \mu \sum_{j=1}^{L} \hat{c}_j^\dagger \hat{c}_j \tag{1.9}$$

where $\hat{c}_j$ is a fermionic annihilation operator at site j ($\{\hat{c}_j, \hat{c}_k\} = 0, \{\hat{c}_j, \hat{c}_k^\dagger\} = \delta_{j,k}$), t is the hopping integral, Δ is the p-wave pairing, and μ is the chemical potential. Consider the case when $\Delta = t$. By diagonalizing this model with open boundary conditions, one finds that its Bogoliubov-de Gennes single particle spectrum changes qualitatively at $\mu = 2t$. For $\mu > 2t$, the system has two bands separated by a gap and is in the topologically trivial phase. For $\mu < 2t$, the system has two zero-energy single particle states in the middle of the gap and is in the topologically non-trivial phase. Note that the Kitaev chain obeys particle-hole symmetry and fermion-parity symmetry ($[\hat{H}_{KC}, (-1)^{\hat{N}}] = 0$ where $\hat{N} = \sum_j \hat{c}_j^\dagger \hat{c}_j$), which make these zero-energy states robust to perturbations that preserve these symmetries.

Note that a "complex" (non-Hermitian) fermionic operator $\hat{c}_j$ can be written as a sum of two Majorana fermions $\hat{a}_j$ and $\hat{b}_j$:

$$\hat{c}_j = (\hat{a}_j + i\hat{b}_j)/2. \tag{1.10}$$

These Majorana fermion operators are "real" (Hermitian) $\hat{a}_j = \hat{a}_j^\dagger, \hat{b}_j = \hat{b}_j^\dagger$ and obey the properties $\hat{a}_j^2 =$

$\hat{b}_j^2 = I$ and $\{\hat{a}_j, \hat{a}_k\} = \{\hat{b}_j, \hat{b}_k\} = 0$ for $j \neq k$ and $\{\hat{a}_j, \hat{b}_k\} = 0$ for all j, k.

In the topologically non-trivial phase of the Kitaev chain, one of the zero-energy states is created by the creation operator $\hat{c}'^{\dagger} = (\hat{\gamma}_1 - i\hat{\gamma}_2)/2$ where (up to small corrections)

$$\hat{\gamma}_1 \propto \sum_{j=1}^{L} (-\mu/2t)^j \hat{a}_j, \quad \hat{\gamma}_2 \propto \sum_{j=1}^{L} (-\mu/2t)^{L+1-j} \hat{b}_{L+1-j} \tag{1.11}$$

are exponentially localized operators on the left and right edges of the chain. The operators $\hat{\gamma}_1$ and $\hat{\gamma}_2$ are examples of MZMs. In general, a MZM [70] is a fermionic operator $\hat{\gamma}$ that squares to identity ($\hat{\gamma}^2 = I$) and commutes with the Hamiltonian ($[\hat{\gamma}, \hat{H}] = 0$). The Kitaev chain MZMs in Eq. (1.11) satisfy these conditions and are also spatially localized on the edges of the chain.

Experimental studies

Much of the experimental effort of realizing Majorana zero modes in the lab has gone into preparing high-quality InAs and InSb semiconductor nanowires that approximately realize the physics of the Kitaev chain [74, 70]. In these systems, a semiconductor nanowire with spin-orbit coupling is put into close proximity with an s-wave superconductor and a Zeeman field in the direction along the nanowire is applied. The resulting system is effectively a spin-less p-wave superconductor of the same type as the Kitaev chain in Eq. (1.9). Ideally, by changing the chemical potential of the nanowire or the applied Zeeman field, the effective model can be put into a topological phase.

Ref. [75] prepared the first example of such a system using an InSb nanowire and measured the differential conductance spectrum, which showed a zero bias peak in the spectrum, consistent with MZMs. While such results are suggestive, such zero bias peaks can also result from Andreev bound states, which are associated with fermionic excitations instead of non-Abelian anyons [75, 70]. To truly verify that these nanowire systems exhibit MZMs at their ends, one would ideally perform a braiding protocol and check that the system evolves as would be expected for Ising anyons.

Recently, the braiding of MZMs has been simulated using three qubits in an IBM superconducting qubit quantum computer [76].

1.3 Many-body localization

Many-body localization (MBL) is a phase of matter where there is a breakdown of thermalization due to strong interactions and disorder. Here we review thermalization in isolated quantum systems and describe how it can fail, leading to MBL and the emergence of quasilocal integrals of motion called ℓ-bits.

1.3.1 Thermalization

In the classical world, we are intimately familiar with thermalization, the process with which a system equilibrates with its surroundings. Whenever we see an ice cube melt or a hot drink cool down, we are observing a system initially far from equilibrium eventually reach a steady state well described by the laws of thermodynamics. In classical statistical mechanics, the behavior of a system in thermal equilibrium can be described by assuming that the classical system is *ergodic*, so that the system uniformly explores the entire space of microstates with the same energy after a long-time [77]. The theory of statistical mechanics, which is based on this ergodic hypothesis, can then be used to derive the laws of thermodynamics.

In the quantum world, we expect thermalization to happen as well. Consider an ideal, isolated quantum system with many degrees of freedom interacting by Hamiltonian $\hat{H}$. The dynamics of the isolated system is described by a unitary time-evolution

$$|\psi(t)\rangle = e^{-it\hat{H}}|\psi(0)\rangle = \sum_n c_n e^{-iE_n t}|n\rangle \tag{1.12}$$

where $|n\rangle$ are the energy eigenstates of $\hat{H}$ with energy E_n, $|\psi(0)\rangle$ is the initial state at time $t = 0$, and c_n are the amplitudes of the initial state in the energy eigenstate basis. Let us consider the case where the initial state is a superposition of eigenstates whose energies lie within a small window of energies $E_n \in [E - \Delta E, E + \Delta E]$. We want there to be many energy eigenstates within this window, so we pick an E in the middle of the spectrum of $\hat{H}$ where the energy density E/V is finite[3].

To observe how thermalization occurs, we need to consider the behavior of a small part of the system. Suppose that we break up the system into two unequal parts A and B, where we chose the size of A to be much smaller than B, but let the combined $A + B$ system approach the thermodynamic limit. We expect that B should act like a thermal reservoir, or bath, to A and cause it to thermalize. The reduced density matrix of subsystem A is given by

$$\rho_A(t) = \mathrm{tr}_B\left(|\psi(t)\rangle\langle\psi(t)|\right) = \sum_{mn} c_m^* c_n e^{-it(E_m - E_n)}\mathrm{tr}_B(|m\rangle\langle n|). \tag{1.13}$$

Since we expect thermalization to occur if we observe our system over a long time, let's consider the long-time average of the density matrix

$$\overline{\rho}_A = \frac{1}{T}\int_0^T \rho_A(t)dt = \sum_{mn} c_m^* c_n \left(\frac{1}{T}\int_0^T e^{-it(E_m - E_n)}dt\right)\mathrm{tr}_B(|m\rangle\langle n|) \approx \sum_n |c_n|^2 \mathrm{tr}_B(|n\rangle\langle n|), \tag{1.14}$$

---

[3] We would not want to pick E near the ground state, for example, since $\hat{H}$ could have a gap which would result in few states in the energy window.

where $T \gg 1/\Delta E$. In time T, the exponential $e^{-it(E_m - E_n)}$ for all $m \neq n$ oscillates many times making the integral vanish for $m \neq n$, giving the approximation in Eq. (1.14).

For the system to thermalize, we expect the time-average density matrix to match a canonical ensemble thermal density matrix of the Boltzmann form

$$\overline{\rho}_A \approx \sum_n |c_n|^2 \mathrm{tr}_A(|n\rangle\langle n|) \approx \rho_{A,thermal} = \frac{1}{Z_A} e^{-\beta \hat{H}_A} \tag{1.15}$$

where $Z_A = \mathrm{tr}_A e^{-\beta \hat{H}_A}$ is the partition function on A, $\hat{H}_A$ is the part of Hamiltonian $\hat{H}$ acting on subsystem A, and β is the inverse temperature determined by matching the average energy of ρ_A to that of $|\psi(0)\rangle$ ($\mathrm{tr}(\rho_{A,thermal}\hat{H}_A) = \langle\psi(0)|\hat{H}_A|\psi(0)\rangle$). Note that the left-hand-side of Eq. (1.15) depends on the initial conditions through c_n, but the right-hand-side does not. For this equation to be consistent, we require that it should hold for all possible initial states, including initial states that are eigenstates, i.e., $|\psi(0)\rangle = |m\rangle$ so that $c_n = \delta_{mn}$. This leads us to the eigenstate thermalization hypothesis.

The eigenstate thermalization hypothesis (ETH) states that the eigenstates $|n\rangle$ of a Hamiltonian with finite energy density are thermal, so that they satisfy $\mathrm{tr}_A(|n\rangle\langle n|) \approx \rho_{A,thermal} = \frac{1}{Z_A}e^{-\beta\hat{H}_A}$. Hamiltonians that satisfy the ETH are called ergodic or thermal. Under ETH, Eq. (1.15) is clearly satisfied. Moreover, ETH implies a number of properties for ergodic systems:

1. The expectation values of local operators vary smoothly with E, since energy eigenstates with nearby energies have nearly identical local reduced density matrices.

2. The eigenstates of an ergodic Hamiltonian have volume-law entanglement, $S_A = -\mathrm{tr}(\rho_A \log \rho_A) \sim Vol(A)$, because $\rho_A \approx \frac{1}{Z_A}e^{-\beta\hat{H}_A}$ according to ETH and $\hat{H}$ is extensive.

1.3.2 Localization

Roughly speaking, ergodic systems spread out information to all parts of the system. Adding disorder to an ergodic system can cause information to spatially localize and fail to spread, which is known as localization. Localized systems fail to satisfy ETH and do not thermalize.

Anderson localization

Anderson localization, originally studied by Philip Anderson in 1958 [78], is localization that occurs in systems of disordered non-interacting fermions with tight-binding Hamiltonians of the form

$$\hat{H}_{Anderson} = t\sum_{\langle ij \rangle}(\hat{c}_i^\dagger \hat{c}_j + \text{H.c.}) + \sum_i \mu_i \hat{c}_i^\dagger \hat{c}_i \tag{1.16}$$

where $\hat{c}_i^\dagger$ are fermionic creation operators, t is the hopping, μ_i are random on-site potentials, and the summation is over nearest-neighbor sites on a d-dimensional cubic lattice. This Hamiltonian can be diagonalized by rotating to a basis of single-particle orbitals $\hat{a}_k^\dagger = \sum_i U_{ki}\hat{c}_i^\dagger$:

$$\hat{H}_{Anderson} = \sum_k \epsilon_k \hat{a}_k^\dagger \hat{a}_k. \tag{1.17}$$

The operator $\hat{a}_k^\dagger$ creates an electron occupying a single-particle orbital wave function of the form $\phi_k(r_i) = U_{ki}$, where r_i is the spatial position of site i in the lattice. Note that the single-particle orbital number operators $\hat{a}_k^\dagger \hat{a}_k$ are conserved quantities that commute with the Hamiltonian.

For $d = 1$ and $d = 2$ dimensions, any amount of disorder in Eq. (1.16) causes the single-particle orbitals to exponentially localize in space [79]. Localized orbitals take the form $\phi_k(r_i) \propto \exp(-|r_i - R_k|/\xi)$ where R_k is the position in space around which the orbital is localized and ξ is a localization length that depends on the disorder strength and is in principle different for each orbital. If we time-evolve a state initially localized in space by the Anderson Hamiltonian, it will with high probability remain near the same location for long times. This implies that Anderson localized systems remember their initial conditions, which implies that they do not thermalize and do not obey ETH. In $d \geq 3$ dimensions, localization only occurs for large enough disorder.

A natural question to ask about Anderson localization is how it is affected by interactions. Does a perturbing interaction destabilize the localized phase so that it always thermalizes? The answer turns out to be *no*. Disorder with interactions can still lead to localization, as we discuss in the next section.

Many-body localization

Many-body localization (MBL) is the interacting generalization of Anderson localization, originally studied by Ref. [80]. The prototypical "standard model" of MBL is the disordered Heisenberg model

$$\hat{H}_{DH} = \sum_{\langle ij \rangle} \hat{\mathbf{S}}_i \cdot \hat{\mathbf{S}}_j + \sum_i h_i S_i^z \tag{1.18}$$

where $S_i^\alpha = \sigma_i^\alpha/2$ for $\alpha = x, y, z$ are spin-1/2 operators on site i, the $h_i \in [-W, W]$ are uniformly distributed random numbers, and W is called the disorder strength. The one-dimensional model in particular has been widely studied, mostly through numerical analysis on small spin chains [81–93]. Through a Jordan-Wigner transformation, the 1D model can be expressed in terms of spinless fermions and takes the same form as Eq. (1.16) but with an additional density-density interaction term $\sum_{\langle ij \rangle} \hat{n}_i \hat{n}_j$. Note also that $\sum_i S_i^z$ commutes with $\hat{H}_{DH}$, so z-magnetization is a quantum number of the system[4].

Since Eq. (1.18) is interacting, it admits no analytic solution and must be studied numerically. If the model fails to thermalize, that is the (finite energy-density) eigenstates of the Hamiltonian do not obey ETH, then we say that the Hamiltonian is MBL. If *all* of the eigenstates of the Hamiltonian do not obey ETH, then the Hamiltonian is called *fully MBL*. Signatures of MBL can be mainly observed in two ways: (1) by studying the properties of individual eigenstates or (2) by studying the dynamics of the system. Both approaches have been taken in theoretical studies, though only (2) is practical to measure in real experiments.

The phase diagram of the 1D disordered Heisenberg model, taken from Ref. [83], is shown in Fig. 1.3. This diagram was obtained by exactly computing the energy eigenstates of the model for many disordered realizations of Eq. (1.18) at different disorder strengths $W = h$ and computing the average of a quantity (participation coefficient, see Ref. [83]) that correlates well with ergodicity. The energy density ϵ of an energy eigenstate with energy E is scaled so that $\epsilon = (E - E_{min})/(E_{max} - E_{min})$ is between 0 and 1. As can be seen in the diagram, the system transitions into a fully MBL regime, where all eigenstates are MBL, above a critical disorder strength of about $W_c \approx 3.7$. The $2 \lesssim W \lesssim W_c$ region, where some eigenstates are ergodic and others are MBL, is known as the mobility edge. It is unclear whether the mobility edge exists in the thermodynamic limit ($N \to \infty$) or whether it is a finite size effect.

While there is significant theoretical and numerical evidence for MBL in one dimension, it is still an open question whether MBL occurs in dimensions greater than one [77]. Some numerical studies have begun to study whether MBL exists in disordered two-dimensional interacting models [94–104], but the results are inconclusive and limited due to the computational difficulty of studying eigenstates or time-evolution of

---

[4] Most numerical studies of this model work in the $S_z = 0$ quantum number sector. In the fermionic model, the S_z symmetry corresponds to particle number conservation and $S_z = 0$ corresponds to half-filling

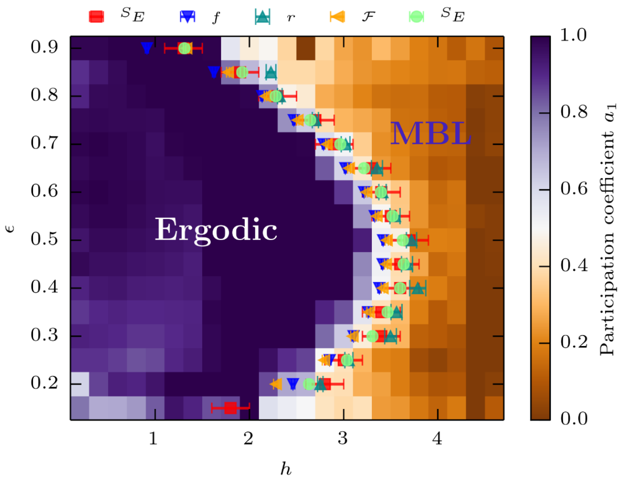

Figure 1.3: (From Ref. [83]) The phase diagram of the one-dimensional disorder Heisenberg model, Eq. (1.18). The energy density of an energy eigenstate (normalized between 0 and 1) is ϵ and $h = W$ is the disorder strength. The shaded regions are determined by analyzing various quantities, such as the average of the level spacing ratio r_n in Eq. (1.19), described in Ref. [83].

two-dimensional systems. This is the problem that we explore in Chapter 5.

Many-body localized systems have a number of key signatures that distinguish them from ergodic ones:

1. Because ETH does not apply, expectation values of local operators under MBL eigenstates with energy E do not vary smoothly with E.

2. The eigenstates of an MBL Hamiltonian have area-law entanglement entropy, while the eigenstates of an ergodic Hamiltonian have volume-law entanglement.

3. MBL systems have an emergent integrability, i.e., they possess an extensive number of local integrals of motion called ℓ-bits (see Section 1.3.3), while ergodic systems do not.

4. When time-evolving a product state by an MBL Hamiltonian, the entanglement entropy of a subsystem grows logarithmically in time, while in ergodic systems it grows linearly with time [105]. This slow-growth can be seen as a consequence of the existence of ℓ-bits. Note also that this is a distinguishing feature between MBL and Anderson localization, as entanglement entropy quickly saturates to a constant value for the Anderson case [79].

5. MBL Hamiltonians have Poisson level-spacing statistics, due to the lack of level repulsion. This means that the average $\langle r \rangle = 1/(2^N - 2) \sum_{n=2}^{2^N-1} r_n$ of the level-spacing ratio

$$r_n = \frac{\min(E_n - E_{n-1}, E_{n+1} - E_n)}{\max(E_n - E_{n-1}, E_{n+1} - E_n)} \tag{1.19}$$

for energy eigenvalues E_n is near the Poisson value $r_{Poisson} \approx 0.39$ predicted by random matrix theory [81–84]. Generic ergodic Hamiltonians have $\langle r \rangle \approx r_{GOE} \approx 0.53$ matching the random matrix theory prediction for the random Gaussian orthogonal ensemble (GOE) of matrices. Poisson statistics can also be seen as coming from ℓ-bits.

Numerical studies of MBL typically look for evidence of some of these properties. In Chapter 5, we look for evidence of ℓ-bits in two and three-dimensional systems.

1.3.3 Local integrals of motion (ℓ-bits)

Many of the properties of fully MBL systems can be understood phenomenologically through the existence of localized integrals of motion known as local bits, or ℓ-bits [105–107]. Like the single-particle orbital density operators $\hat{a}_k^\dagger \hat{a}_k$ in Anderson localized systems, ℓ-bits are conserved quantities that are exponentially localized in space, though they have a more complicated structure.

Suppose that we find a unitary $\hat{U}$ that diagonalizes the spin Hamiltonian of Eq. (1.18). Using this unitary, we can construct operators of the form

$$\hat{\tau}_i^z \equiv \hat{U} \hat{\sigma}_i^z \hat{U}^\dagger \tag{1.20}$$

where $\hat{\sigma}_i^z$ is the Z-Pauli matrix on site i. Since $\hat{\tau}_i^z$ are conjugations of Pauli matrices, they share the same spectral properties. For example, they are traceless and binary

$$\begin{aligned} \mathrm{tr}(\hat{\tau}_i^z) &= \mathrm{tr}(\hat{\sigma}_i^z) = 0 \\ (\hat{\tau}_i^z)^2 &= (\hat{\sigma}_i^z)^2 = I, \end{aligned} \tag{1.21}$$

which imply that exactly half of their eigenvalues are $+1$ and half are -1. Written in terms of the $\hat{\tau}_i^z$ operators, the Hamiltonian takes the form

$$\hat{H}_{DH} = \sum_i \tilde{J}_i \hat{\tau}_i^z + \sum_{ij} \tilde{J}_{ij} \hat{\tau}_i^z \hat{\tau}_j^z + \cdots + \sum_{i_1,\ldots,i_k} \tilde{J}_{i_1,\ldots,i_k} \hat{\tau}_{i_1}^z \cdots \hat{\tau}_{i_k}^z + \cdots . \tag{1.22}$$

The $\hat{\tau}_i^z$ operators are by construction mutually commuting integrals of motion of $\hat{H}_{DH}$:

$$\begin{aligned} [\hat{H}_{DH}, \hat{\tau}_i^z] &= 0 \quad \forall i \\ [\hat{\tau}_i^z, \hat{\tau}_j^z] &= 0 \quad \forall i, j \end{aligned} \tag{1.23}$$

So far this is general and not MBL-specific. Eq. (1.22) is the general form of a diagonalized Hamiltonian and can be quite complicated, involving a linear combination of potentially exponentially many terms with arbitrarily large products of $\hat{\tau}_i^z$ operators. Likewise, the $\hat{\tau}_i^z$ operators can be highly non-trivial and involve linear combinations of exponentially many non-local Pauli strings. While we would expect complicated non-local expressions for $\hat{\tau}_i^z$ and $\hat{H}_{DH}$ for generic ergodic systems, we instead expect these expressions to simplify for MBL Hamiltonian due to their local nature.

Phenomenologically, we hypothesize that for fully MBL Hamiltonians there exists a diagonalizing $\hat{U}$ such that all the $\hat{\tau}_i^z$ operators are quasilocal, i.e., they have support on finitely many sites up to exponentially small corrections. Quasilocal $\hat{\tau}_i^z$ operators are called localized bits or ℓ-bits. In this phenomenological picture of MBL, the Hamiltonian coupling constants in Eq. (1.22) decay exponentially with distance so that

$$\tilde{J}_{i_1,\ldots,i_k} \propto e^{-\max_{i,j\in[1,k]}(\|r_i-r_j\|)/\tilde{\xi}} \tag{1.24}$$

for some localization length $\tilde{\xi}$ where r_i is the spatial position of site i.

While ℓ-bits provide an appealing intuitive picture of MBL, they can be difficult to work with numerically. Importantly, ℓ-bits are not unique. Many unitaries, which differ by permutations, can diagonalize the Hamiltonian. Each one leads to a different set of ℓ-bits which can differ non-trivially and may even fail to be quasilocal. One approach is to use exact diagonalization (see Section 2.1) and numerically search for the permutation that produces the most localized set of ℓ-bits. Many other methods for constructing approximate ℓ-bits have been explored [108–113, 96, 114, 95], with one involving tensor networks (see Section 2.3) being used to study MBL in two-dimensions [98]. In Chapter 5, we present a new numerical method for constructing approximate ℓ-bits that overcomes some of the limitations of these previous methods, which allows us to study ℓ-bits in two and three-dimensional systems.

In the ℓ-bit picture, we assume that MBL systems have an extensive set of quasilocal integrals of motion. This implies a number of properties of MBL Hamiltonians, as described in the previous section. Here we give the intuition for how ℓ-bits give rise to one of those properties: the logarithmic growth of entanglement in MBL systems [105].

Suppose that we initialize our system in a random product state with zero entanglement. At strong disorder, the $\sum_i \tilde{J}_i \hat{\tau}_i^z$ terms dominate the Hamiltonian, causing each spin i to precess around $\hat{\tau}_i^z$ at a rate given by the local magnetic field $\tilde{J}_i$. Two spins at sites i, j separated by distance $r_{ij} = \|r_i - r_j\|$ precess at a much slower rate given by the coupling $\tilde{J}_{ij} \propto e^{-r_{ij}/\tilde{\xi}}$. For the dephasing of these two weakly interacting spins to become significant, we need to time-evolve until $\tilde{J}_{ij} t \sim 1$. This then implies that dephasing is only significant for spins separated up to a distance

$$r_{ij} \sim \tilde{\xi} \log t. \tag{1.25}$$

Using dephasing as a proxy for entanglement, we then expect that at time t only spins up to distance $r_{ij} \propto \log t$ are entangled.

1.3.4 Experimental studies

While the study of MBL has largely been theoretical in nature, there are a number of experiments that have looked for MBL physics with analog cold atom quantum simulators [115–119], superconducting qubit quantum simulators [120–123], and even digital quantum computers [124]. Observing MBL requires preparing and manipulating well-isolated quantum systems. In many of these experiments, coupling with the environment, or noise, can be strong which leads to thermalization, washing out any signatures of MBL. In many of these experiments, the number of qubits simulated is small so that the measurement results can be checked against exact numerics.

In MBL experiments, the typical procedure is to initialize the system into a product state and time-evolve by a Hamiltonian with on-site disorder, such as a Bose-Hubbard or XXZ model. The resulting state can then be measured to compute local observables. For example, in Ref. [118], the imbalance in the number of atoms on the left (N_L) versus right (N_R) side of the system, $I = (N_L - N_R)/(N_L + N_R)$, is measured over time after starting with a product state with $\langle I \rangle \neq 0$. In an ergodic system, the product state quickly thermalizes to the thermal value, $\langle I \rangle_{thermal} = 0$ for the Hamiltonians considered in Ref. [118]. However, in an MBL system, memory of the initial state is retained and $\langle I \rangle \neq 0$ stays non-zero for long times, which is seen experimentally.

As quantum simulators and quantum computers advance, it will be exciting to probe MBL in larger systems than can be simulated classically.

Chapter 2

Methods

In this thesis, we utilize a variety of numerical methods to study quantum systems. In this chapter, we describe the numerical techniques that we used: exact diagonalization (Section 2.1), variational Monte Carlo (Section 2.2), tensor networks (Section 2.3), and operator-based methods (Section 2.4). Exact diagonalization, variational Monte Carlo, and tensor network methods are used to implement the inverse method for constructing Hamiltonians from eigenstates discussed in Chapter 3. The operator-based methods are used in both the inverse method for constructing Hamiltonians from symmetries discussed in Chapter 4, and in the method for constructing ℓ-bits discussed in Chapter 5.

2.1 Exact diagonalization

2.1.1 Background

One of the most direct ways of determining the spectrum of a quantum Hamiltonian is by expressing it as a matrix and diagonalizing it numerically using standard linear algebra techniques. This is known as exact diagonalization (ED). It takes exponential in system size time and memory to perform ED, but the results are exact and unbiased. The exponential cost of performing full ED limits its applications to the simulation of small systems of about 20 spins (or qubits). A review of ED can be found in Ref. [125]

In ED, we use a basis $\{|n\rangle\}$ to represent the Hamiltonian operator $\hat{H}$ as a Hermitian matrix $H_{mn} = \langle m|\hat{H}|n\rangle = H^*_{nm}$. We will restrict our discussion to the case of spin-1/2 Hamiltonians with N spins (or qubits). In this case, the standard computational basis used is the basis of 2^N σ^z-eigenstates, $|\uparrow\ldots\uparrow\rangle$, $|\uparrow\ldots\downarrow\rangle, \ldots,$ $|\downarrow\ldots\downarrow\rangle$ for spins (or $|0\ldots0\rangle$, $|0\ldots1\rangle, \ldots,$ $|1\ldots1\rangle$ for qubits). In this basis, the spectrum of $\hat{H}$ can be determined by solving the eigenvalue problem

$$\sum_{n=1}^{2^N} H_{mn}\psi^k_n = E_k\psi^k_m \tag{2.1}$$

using standard linear algebra techniques, such as the QR algorithm if one is interested in obtaining the full spectrum or the Lanczos algorithm if one is interested in only a few eigenvectors. The complex eigenvector ψ_m^k corresponds to the energy eigenstate $|\psi_k\rangle = \sum_{m=1}^{2^N} \psi_m^k |m\rangle$ with energy eigenvalue E_k.

Once energy eigenvalues and eigenstates are obtained numerically, they can be used to directly compute arbitrary observables, such as correlation functions or entanglement entropies. For example the expectation value of $\hat{O}$ for an eigenstate $|\psi_k\rangle$ would simply be given by matrix vector multiplications

$$\langle\psi_k|\hat{O}|\psi_k\rangle = \sum_{mn} {\psi_m^k}^* O_{mn} \psi_n^k \tag{2.2}$$

where $O_{mn} = \langle m|\hat{O}|n\rangle$ is the operator in basis $\{|n\rangle\}$, which is usually easy to compute.

2.1.2 Sparse local operators

Physical Hamiltonians have additional structure that make them easier to perform calculations with than arbitrary Hermitian matrices. Namely, physical Hamiltonians are usually sparse. As an example, consider the one-dimensional spin-1/2 Heisenberg Hamiltonian, a prototypical spin Hamiltonian:

$$\hat{H} = \sum_{j=1}^{N-1} \mathbf{S}_j \cdot \mathbf{S}_{j+1} = \sum_{j=1}^{N-1} \frac{1}{4}(\sigma_j^x \sigma_{j+1}^x + \sigma_j^y \sigma_{j+1}^y + \sigma_j^z \sigma_{j+1}^z) \tag{2.3}$$

where $\mathbf{S} = (\sigma^x/2, \sigma^y/2, \sigma^z/2)$ and $\sigma^x, \sigma^y, \sigma^z$ are the Pauli matrices. Note that this Hamiltonian is a sum of *Pauli strings*, i.e., tensor products of Pauli matrices and the identity matrix I. For example, $\sigma_j^y \sigma_{j+1}^y$ is short-hand for the Pauli string $I_1 \otimes \cdots \otimes I_{j-1} \otimes \sigma_j^y \otimes \sigma_{j+1}^y \otimes I_{j+2} \otimes \cdots \otimes I_N$. Pauli strings are highly sparse matrices. They are $2^N \times 2^N$ matrices, but only contain 2^N non-zero entries. Therefore, in Eq. (2.3), the Hamiltonian has at most $3(N-1)2^N$ non-zero entries out of all possible 4^N entries. In general, spin Hamiltonians with local interactions are sums of $poly(N)$ Pauli strings, making them sparse as well. This sparsity is practically beneficial for performing ED calculations, as it allows for more memory-efficient storage of Hamiltonians. It is particularly beneficial in calculations of individual eigenstates using iterative methods such as the Lanczos algorithm, since those methods have been well adapted to take advantage of sparse matrix-vector multiplication.

2.1.3 Symmetries

Symmetries reduce the cost of performing ED. A symmetry $\hat{\mathcal{O}}$ is a Hermitian operator that commutes with the Hamiltonian[1], $[\hat{\mathcal{O}}, \hat{H}] = 0$. A fact from linear algebra is that two commuting operators can

---

[1] Sometimes others refer to a symmetry as a unitary operator $\hat{\mathcal{U}}$ that commutes with a Hamiltonian. Such operators also satisfy $\hat{\mathcal{U}}\hat{H}\hat{\mathcal{U}}^\dagger = \hat{H}$.

be simultaneously diagonalized. This means that there exists an orthonormal basis $|E_m, \lambda_n, l\rangle$ such that $\hat{H}|E_m, \lambda_n, l\rangle = E_m|E_m, \lambda_n, l\rangle$ and $\hat{\mathcal{O}}|E_m, \lambda_n, l\rangle = \lambda_n|E_m, \lambda_n, l\rangle$. The l index accounts for the possibility of multiple degenerate states with the same E_m or λ_n eigenvalues. The goal of ED with symmetries is to find this basis.

When working with a symmetry $\hat{\mathcal{O}}$, we usually know the basis $|\lambda_n, l\rangle$ that diagonalizes it. For example, for $\hat{\mathcal{O}} = \sum_i \sigma_i^z$, which commutes with Eq. (2.3), the $|\lambda_n, l\rangle$ eigenstates are spin configurations (product states) with net z-magnetization λ_n. To be explicit, for $N = 2$ spins, the states are

$$\begin{aligned}
&|\lambda_1 = 2, l = 1\rangle = |{\uparrow\uparrow}\rangle\,, \\
&|\lambda_2 = 0, l = 1\rangle = |{\uparrow\downarrow}\rangle\,, \quad |\lambda_2 = 0, l = 2\rangle = |{\downarrow\uparrow}\rangle\,, \\
&|\lambda_3 = -2, l = 1\rangle = |{\downarrow\downarrow}\rangle\,.
\end{aligned} \tag{2.4}$$

Since the states $|\lambda_n, l\rangle$ and $|\lambda_{n'}, l'\rangle$ for $\lambda_n \neq \lambda_{n'}$ are orthogonal and eigenstates of $\hat{H}$, that means that the matrix elements connecting different eigenvalues of $\hat{\mathcal{O}}$ are zero: $\langle\lambda_n, l|\,\hat{H}|\lambda_{n'}, l'\rangle = 0$. In other words, in the $|\lambda_n, l\rangle$ basis, the Hamiltonian is block-diagonal, with different blocks corresponding to different eigenvalues (or quantum numbers) λ_n. If one is able to explicitly construct the Hamiltonian in the $|\lambda_n, l\rangle$ basis, then one can diagonalize the Hamiltonian block by block to find the $|E_m, \lambda_n, l\rangle$ states, which is more efficient than diagonalizing the entire Hamiltonian at once.

More complicated symmetries, for example space group, point group, or continuous symmetries, can also be handled similarly using tools from representation theory [126]. See Ref. [127] for more details on how symmetries can be incorporated into large-scale ED calculations.

2.2 Variational Monte Carlo

2.2.1 Background

Variational Monte Carlo (VMC) is an approach for computing observables of parametrized families of variational wave functions by Markov chain Monte Carlo sampling [128]. Typically, VMC is combined with an optimization procedure, such as stochastic gradient descent, in order to tune the variational wave function until it becomes a good approximate of the ground state of a Hamiltonian. Computing observables with VMC requires polynomial time and memory for many interesting variational wave functions, but only produces approximate results with statistical errors. Performing VMC optimization also requires polynomial time and memory, but can result in a highly biased approximate ground state with properties deviating significantly from the true ground state of the system. VMC can be used to simulate systems of hundreds of spins or qubits. A review of VMC can be found in Ref. [128].

2.2.2 Sampling wave functions using Markov chains

In VMC, our goal is to estimate the expectation value of an observable $\langle\psi_\theta|\hat{O}|\psi_\theta\rangle$ for a variational wave function $|\psi_\theta\rangle$ with parameters θ by sampling a Markov chain. This sampling is done in a computational basis $|R\rangle$[2]. By using the resolution of the identity $I = \sum_R |R\rangle\langle R|$ and assuming $|\psi_\theta\rangle$ is normalized, we see that the expectation value that we are interested in can be written as

$$\begin{aligned}\langle\psi_\theta|\,\hat{O}|\psi_\theta\rangle &= \sum_R \langle\psi_\theta|\,\hat{O}|R\rangle\langle R|\psi_\theta\rangle \\ &= \sum_R \frac{\langle\psi_\theta|\,\hat{O}|R\rangle}{\langle\psi_\theta|R\rangle}|\langle R|\psi_\theta\rangle|^2 \equiv \sum_R O_L(R)P(R) \qquad (2.5)\end{aligned}$$

where $O_L(R) \equiv \langle\psi_\theta|\,\hat{O}|R\rangle/\langle\psi_\theta|R\rangle$ is called the local-energy (when $\hat{O}$ is a Hamiltonian) and $P(R) \equiv |\langle R|\psi_\theta\rangle|^2$ is a probability distribution. Note that we are usually interested in estimating local observables $\hat{O}$ that are a sum of $poly(N)$ Pauli strings, where N is the system size. For such observables, the local-energy for a fixed $|R\rangle$ can be written as

$$O_L(R) = \sum_{R'} \frac{\langle\psi_\theta|R'\rangle}{\langle\psi_\theta|R\rangle}\langle R'|\hat{O}|R\rangle \qquad (2.6)$$

where $\langle R'|\hat{O}|R\rangle \neq 0$ for only $poly(N)$ possible $|R'\rangle$. Therefore, for local observables, it is efficient to compute the local-energy provided that $\langle\psi_\theta|R'\rangle/\langle\psi_\theta|R\rangle$ is efficient to evaluate.

The expectation value of Eq. (2.5) can be estimated as

$$\langle\psi_\theta|\,\hat{O}|\psi_\theta\rangle \approx \frac{1}{N_S}\sum_{s=1}^{N_S} O_L(R_s) \qquad (2.7)$$

where $R_1, \ldots, R_{N_S}$ are samples drawn from $P(R)$. In VMC, this sampling can be done efficiently (for certain variational wave functions $|\psi_\theta\rangle$) by using the Metropolis Markov chain Monte Carlo algorithm [129, 130].

The Metropolis algorithm generates samples from a desired probability distribution $P(R)$ by constructing a Markov chain, a memoryless random process, with that probability distribution as its steady state distribution and sampling from it. Markov chains generate samples over time, with each new sample depending only on the sample from the previous time-step. In the Metropolis algorithm, each new Markov chain sample

---

[2] This basis is usually the same σ^z-basis used in ED described in Section 2.1 but it can be arbitrary.

is produced in two steps: (1) a move from a configuration R to R' is proposed with transition probability $T(R \to R')$ and (2) the move is accepted with acceptance probability

$$A(R \to R') = \min\left(1, \frac{P(R')}{P(R)} \frac{T(R' \to R)}{T(R \to R')}\right). \tag{2.8}$$

There is great freedom in choosing the transition probability $T(R \to R')$ and different choices can affect how often moves are accepted and how quickly the Markov chain reaches its steady state. In the context of VMC on spin systems, the proposed move is often chosen to be a random spin flip (where spin configuration R' differs from configuration R by flipping the spin at a random site i) or a random spin exchange (where R' differs from R by exchanging the spins at random sites i, j), in which case $T(R \to R') = T(R' \to R)$ is constant.

It is important to note that both the calculation of the acceptance probability in Eq. (2.8)[3] and the evaluation of the local-energy in Eq. (2.7) require computing the wave function ratio $\langle\psi_\theta|R'\rangle/\langle\psi_\theta|R\rangle$. Therefore, VMC is only efficient if it is possible to efficiently compute this ratio[4].

2.2.3 The variational principle and optimization

The variational principle states that the energy of any state is an upper bound on the ground state energy. By optimizing a variational wave function $|\psi_\theta\rangle$ so that its energy is minimized, we can find an approximation to the true ground state.

Consider the basis of energy eigenstates $|n\rangle$ of $\hat{H}$ with energies E_n, where $|0\rangle$ is the ground state with energy E_0. Any normalized state $|\psi\rangle$ can be expanded in this basis

$$|\psi\rangle = \sum_n c_n |n\rangle \tag{2.9}$$

where $\sum_n |c_n|^2 = 1$. The average energy of this state is then

$$\langle\psi|\hat{H}|\psi\rangle = \sum_n |c_n|^2 E_n \geq \sum_n |c_n|^2 E_0 = E_0, \tag{2.10}$$

proving the result.

In VMC optimization, one performs gradient descent to minimize the average energy of the wave function $|\psi_\theta\rangle$ and lower this upper bound. Gradient descent works by iteratively updating the parameters in the

---

[3] Since $P(R')/P(R) = |\langle\psi_\theta|R'\rangle/\langle\psi_\theta|R\rangle|^2$.

[4] Interestingly, since only the ratio is ever required in VMC, one can perform VMC calculations using unnormalized wave functions.

direction that minimizes the objective function (the energy)

$$\theta' = \theta - \eta\partial_\theta\langle\psi_\theta|\hat{H}|\psi_\theta\rangle \tag{2.11}$$

where η is the step size or learning rate. The energy gradients can be computed using Markov chain Monte Carlo as described in the previous section. In particular, the expression for a gradient is

$$\begin{aligned}\partial_\theta\langle\psi_\theta|\hat{H}|\psi_\theta\rangle &= \sum_{R,R'}\partial_\theta\Big(\langle\psi_\theta|R\rangle\langle R|\hat{H}|R'\rangle\langle R'|\psi_\theta\rangle\Big) \\ &= \sum_{R,R'}\langle R|\hat{H}|R'\rangle\left[(\partial_\theta\langle\psi_\theta|R\rangle)\langle R'|\psi_\theta\rangle + \langle\psi_\theta|R\rangle(\partial_\theta\langle R'|\psi_\theta\rangle)\right] \\ &= \sum_{R,R'}\langle R|\hat{H}|R'\rangle\left[\frac{\partial_\theta\langle\psi_\theta|R\rangle}{\langle\psi_\theta|R'\rangle}|\langle R'|\psi_\theta\rangle|^2 + \frac{\partial_\theta\langle R'|\psi_\theta\rangle}{\langle R|\psi_\theta\rangle}|\langle\psi_\theta|R\rangle|^2\right] \\ &= \sum_{R,R'} 2\mathrm{Re}\left[\langle R'|\hat{H}|R\rangle\frac{\partial_\theta\langle\psi_\theta|R'\rangle}{\langle\psi_\theta|R\rangle}\right]|\langle R|\psi_\theta\rangle|^2 \equiv \sum_R \tilde{O}_L(R)P(R)\end{aligned} \tag{2.12}$$

where $P(R) \equiv |\langle R|\psi_\theta\rangle|^2$ is the probability distribution of $|\psi_\theta\rangle$ and $\tilde{O}_L(R) \equiv 2\mathrm{Re}\left[\sum_{R'}\langle R'|\hat{H}|R\rangle\frac{\partial_\theta\langle\psi_\theta|R'\rangle}{\langle\psi_\theta|R\rangle}\right]$ is a modified local energy that involves computing ratios of the gradient of the wave function over the wave function. By sampling configurations $R_s \sim P(R)$ from a Markov chain, the gradient can be estimated as before by computing

$$\partial_\theta\langle\psi_\theta|\hat{H}|\psi_\theta\rangle \approx \frac{1}{N_S}\sum_{s=1}^{N_S}\tilde{O}_L(R_s), \tag{2.13}$$

which can be done efficiently as long as the gradient ratios $(\partial_\theta\langle\psi_\theta|R'\rangle)/\langle\psi_\theta|R\rangle$ can be efficiently computed.

Another optimization procedure often used in VMC optimization is stochastic reconfiguration [128]. This procedure can be interpreted as performing imaginary time evolution $e^{-\beta\hat{H}}|\psi_\theta\rangle$ in many small steps and after each step projecting into the space of variational states of the form $|\psi_\theta\rangle$. After many steps, this evolution will reach the ground state, assuming the projection is accurate enough, since $e^{-\beta\hat{H}}|\psi_\theta\rangle = \sum_n e^{-\beta E_n}\langle n|\psi_\theta\rangle|n\rangle \xrightarrow{\beta\to\infty} |0\rangle$.

2.2.4 Types of variational wave functions

Many types of variational wave functions that can be implemented efficiently in VMC have been examined over the years. Examples include Slater Determinants, Fermionic resonating valence bond states, projected BCS states [128], and neural networks [131]. An example of a variational wave function that cannot be implemented efficiently in VMC is a generic Bosonic resonating valence bond state [132], a state whose wave function ratio evaluation involves the computation of a permanent – a task that is known to be computationally difficult.

2.3 Tensor network methods

2.3.1 Background

Tensor networks states are a class of quantum states whose state amplitudes are described by the contraction of a network of tensors. They provide a useful theoretical framework for understanding entanglement in quantum systems. Particular types of tensor networks, such as matrix product states or tree tensor networks, are computationally efficient to work with and can be used to approximate the ground states of local Hamiltonians. For one-dimensional gapped local Hamiltonians, it is possible to find highly accurate matrix product state representations of the ground state for systems with hundreds of spins. One can view tensor networks as a class of variational wave functions, like those used in VMC, whose properties can be computed directly by contracting tensors rather than by sampling Markov chains. Excellent reviews of tensor networks can be found in Refs. [133–138].

A simple example of a tensor network state is

$$|\psi\rangle = \sum_{ijkl\sigma_1\sigma_2} A_{ijk\sigma_1} B_{jkl\sigma_2} C_{il} |\sigma_1\sigma_2\rangle \tag{2.14}$$

where A and B are rank-4 tensors and C is a rank-2 tensor. Tensor networks have convenient diagrammatic representations, using the Penrose graphical notation. In this notation, a rank-k tensor is represented as a shape with k lines coming out of it, one for each index. When two shapes share a line, that corresponds to a contraction, or summation, over the shared index. For example, the tensor network in Eq. (2.14) is depicted diagrammatically in Fig. 2.1. Contracted indices (indices i, j, k, l in the example) are called *virtual* indices and non-contracted indices (indices σ_1, σ_2) are called *physical* indices, since they correspond to the degrees of freedom of the quantum systems, such as spin configurations.

2.3.2 Matrix product states

Matrix product states (MPS) are a widely used type of tensor network with a one-dimensional structure. An MPS on an open chain of L sites takes the form

$$|\psi\rangle = \sum_{\sigma_1,\ldots,\sigma_L} A_1^{(\sigma_1)} \cdots A_L^{(\sigma_L)} |\sigma_1 \cdots \sigma_L\rangle \tag{2.15}$$

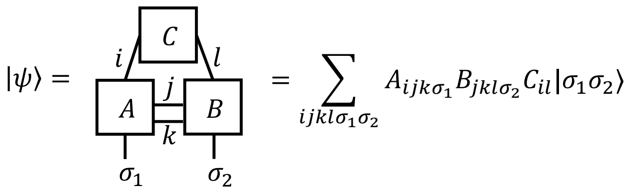

Figure 2.1: The tensor network of Eq. (2.14) represented diagrammatically. Here for clarity we explicitly label all the indices in the tensor network, but in many situations they are drawn without labels.

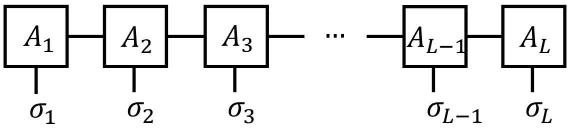

Figure 2.2: A matrix product state.

where $A_i^{(\sigma)}$ is a $\chi \times \chi$ matrix (except for $i = 1, L$, when it is a row or column vector) where χ is the bond-dimension and $\sigma_i = 0, \ldots, d-1$ where d is the local Hilbert space dimension ($d = 2$ for spins or qubits). Fig. 2.2 shows the diagrammatic representation of Eq. (2.15). In general, MPS with periodic boundaries can also be considered.

Matrix product states have a gauge freedom that can be exploited to simplify calculations. In particular, MPS can be put into a "canonical form" that allows for more efficient MPS contractions. The process of putting an MPS into canonical form involves iterating the following procedure:

1. Between neighboring sites i and j, construct the tensor $B_{\alpha\sigma_i;\beta\sigma_j} = \sum_\gamma (A_i^{\sigma_i})_{\alpha\gamma}(A_j^{\sigma_j})_{\gamma\beta}$.
2. Perform a singular value decomposition[5] on the matrix B_{ab} where $a = (\alpha, \sigma_i)$ and $b = (\beta, \sigma_j)$ are grouped indices. This will return $B = U\Lambda V^\dagger$, where U and V are unitary matrices and $\Lambda_{ii} = \lambda_i \geq 0$ is a diagonal matrix of singular values.
3. Update the MPS tensors on sites i and j: $(A_i^{(\sigma_i)})_{\alpha\beta} \leftarrow U_{(\alpha\sigma_i);\beta}$ and $(A_j^{(\sigma_j)})_{\alpha\beta} \leftarrow \sum_\gamma \lambda_\gamma V^\dagger_{\gamma;(\beta\sigma_j)}$.

After this procedure, the A_i tensor on site i is an isometry, satisfying either $\sum_{\sigma_i} A_i^{\sigma_i\dagger} A_i^{\sigma_i} = I$ when $i < j$ or $\sum_{\sigma_i} A_i^{\sigma_i} A_i^{\sigma_i\dagger} = I$ when $j > i$, but the A_j tensor on site j is not. By repeating this procedure from $i = 1$ to $i = L-1$ (from $i = L$ to $i = 2$), we can make the $A_1, \ldots, A_{L-1}$ ($A_2, \ldots, A_L$) MPS tensors into isometries, which is known as the left-canonical form (right-canonical form). One can also push the non-isometric tensor, called the orthogonality center of the MPS, into any site in the middle of the MPS, which is known as the

---

[5] This same procedure can also be done using a QR decomposition. In that case, we would essentially replace U with Q and $\Lambda V^\dagger$ with R.

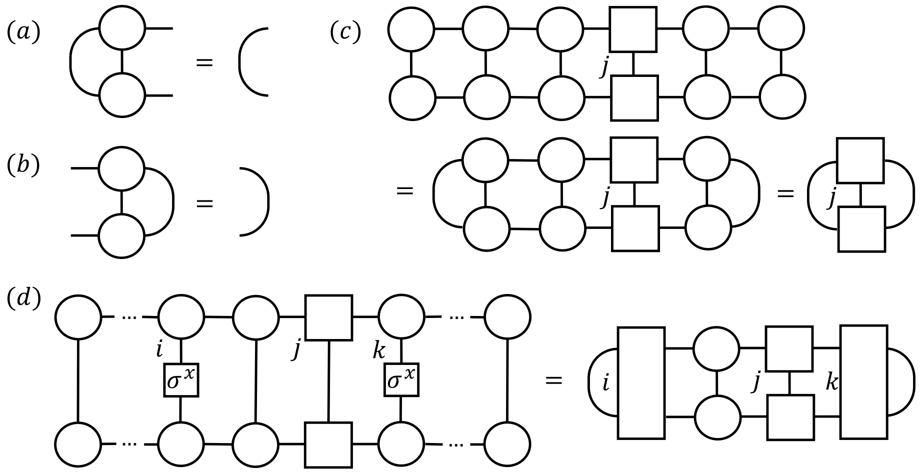

Figure 2.3: The isometry condition for an MPS tensor in (a) left-canonical and (b) right-canonical form. (c) The contraction $\langle\psi|\psi\rangle$ of an MPS $|\psi\rangle$ in mixed-canonical form with orthogonality center at site j. (d) The contraction of a correlation function $\langle\psi|\sigma_i^x\sigma_k^x|\psi\rangle$ for an MPS with orthogonality center $j \in (i,k)$.

mixed-canonical form[6]. Fig. 2.3(a)-(b) show what the isometry conditions of canonized MPS tensors looks like diagrammatically. In this figure, circles represent isometries and squares represent generic tensors.

Numerous quantities can be efficiently computed for an MPS in canonical form by using the properties of the isometric tensors. For example, the norm of a canonized MPS with orthogonality center at site j simplifies to a summation involving only a single tensor $\langle\psi|\psi\rangle = \sum_{\sigma_j\alpha\beta}(A_j^{(\sigma_j)})_{\alpha\beta}(A_j^{(\sigma_j)^*})_{\alpha\beta}$, as shown in Fig. 2.3(c). Similarly, the computation of expectation values of Pauli strings also drastically simplifies compared to the general tensor contraction of an MPS not in canonical form. For a Pauli string $\prod_{l=i}^{k}\sigma_l^{s_l}$ between sites i and k, the expectation value $\langle\psi|\prod_{l=i}^{k}\sigma_l^{s_l}|\psi\rangle$ for an MPS with orthogonality center j between i and k involves the contraction of $2|i-k|$ tensors rather than $2L$ tensors as would be required for a non-canonized MPS. An example of this simplification for a 2-local Pauli string is shown in Fig. 2.3(d).

Matrix product states with constant bond dimensions are good approximations for the ground states of one-dimensional gapped local Hamiltonians [139]. Moreover, there exists an efficient classical algorithm, the density matrix renormalization group (DMRG), for constructing these ground state MPS [140]. An open-source implementation of DMRG and other MPS algorithms is available in Ref. [141].

2.3.3 Parent Hamiltonians

For generic matrix product states, local frustration-free *parent Hamiltonians* can be explicitly constructed with those MPS as exact ground states [24]. These parent Hamiltonians are explicit solutions to the inverse

---

[6] Note that in some MPS algorithms, such as the density matrix renormalization group, the orthogonality center of the MPS is repeatedly moved, or sweeped, from one edge of the chain to the other.

problem of finding Hamiltonians with desired ground states for a limited class of states. Our description of MPS parent Hamiltonians closely follows Ref. [142].

Consider a length L translationally-invariant MPS $|\psi\rangle$ with periodic boundary conditions in canonical form, with MPS tensor $A^{(\sigma)}$. For this MPS, we define the map

$$\Gamma_L : X \to \sum_{\sigma_1,\ldots,\sigma_L=0}^{d-1} \operatorname{tr}\left(XA^{(\sigma_1)}\cdots A^{(\sigma_L)}\right)|\sigma_1\ldots\sigma_L\rangle \tag{2.16}$$

which maps $\chi \times \chi$ matrices in the virtual bond space to vectors in the d^L-dimensional Hilbert space of states. An MPS for which the map Γ_L is injective for $L \geq L_0$ but not $L < L_0$ is called a L_0-injective MPS or *injective* MPS for short. Generic MPS are injective, with the set of non-injective MPS forming a set of measure zero.

For an L_0-injective MPS, the reduced density matrix on L consecutive sites ρ_L has rank χ^2 for $L \geq L_0$, i.e., the rank of the MPS density matrix is limited by the bond-dimension χ. The Hilbert space of states on L_0 has dimension d^{L_0}, which is generally larger than χ^2. When this is the case, there is a $d^{L_0} - \chi^2$ dimensional subspace of the Hilbert space that ρ_{L_0} does not act on. Call P_n the projector onto this space for sites $j = n$ to $j = n + L_0 - 1$. For these projectors, $P_n\rho_{L_0} = 0$ (and therefore $P_n|\psi\rangle = 0$).

We can construct a parent Hamiltonian using a sum of these projectors on neighboring blocks

$$\hat{H}_{PH} = \sum_{n=1}^{L} P_n. \tag{2.17}$$

The MPS $|\psi\rangle$ is the unique ground state of $\hat{H}_{PH}$ [24]. This Hamiltonian is local since each P_n acts on up to a constant L_0 sites (assuming constant bond-dimension χ). It is also frustration-free, which means that its ground state $|\psi\rangle$ is also the ground state of each local term P_n of the Hamiltonian.

2.3.4 Other tensor networks

There are many types of tensor networks that have been explored in the literature, with various network topologies (See Fig. 2.4 for some examples). Unfortunately, many of these tensor networks are much more difficult to contract than matrix product states, such as the projected entangled pair states (PEPS) [25], the two-dimensional generalization of MPS. However, tree-tensor networks (TTN) [144] and the multi-scale entanglement-renormalization ansatz (MERA) [145] are examples of tensor networks that can be efficiently contracted due to their special structure. In fact, an efficient DMRG-like algorithm exists for optimizing TTNs [146].

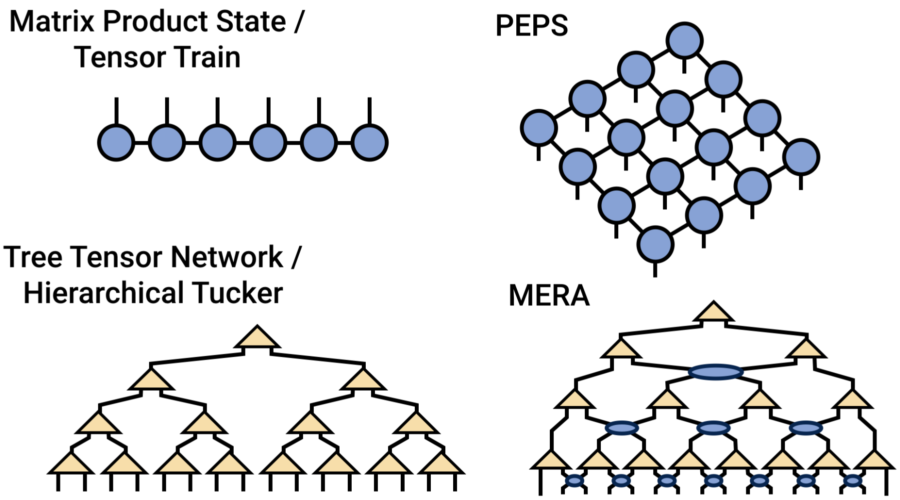

Figure 2.4: (From Ref. [143]) Examples of commonly studied tensor networks.

Note that parent Hamiltonians can also be constructed for PEPS in a similar manner as for MPS [26, 142].

2.4 Operator-based methods

Many numerical methods for studying quantum many-body systems, such as the other methods described in this chapter, work by performing calculations using quantum states. However, it can be fruitful to instead perform calculations using operators that act on those states. This is particularly helpful when analyzing the symmetries of a quantum system. In general, working with operators is more computationally expensive than working with quantum states, since the space of operators is much larger than the space of states. However, when operators are expected to be local, then a small basis of local operators can be used to perform efficient calculations.

A quantum state $|\psi\rangle$ is a vector in a complex Hilbert space. For example, for N-qubit systems, $|\psi\rangle \in (\mathbb{C}^2)^{\otimes N}$, which is a 2^N-dimensional space. The operators $\hat{A} : (\mathbb{C}^2)^{\otimes N} \to (\mathbb{C}^2)^{\otimes N}$ that act on vectors in this space also form their own $(2^N)^2 = 4^N$ dimensional complex vector space. A basis for this operator space is $|j\rangle \langle k|$ for $j, k = 1, \dots, 2^N$, where $\{|j\rangle\}_{j=1}^{2^N}$ is an orthonormal basis for the state space $(\mathbb{C}^2)^{\otimes N}$. Moreover, like for the state space, the operator space has an inner product: the Hilbert-Schmidt inner product

$$\langle \hat{A}, \hat{B} \rangle \equiv \mathrm{tr}\left(\hat{A}^\dagger \hat{B}\right)/\mathrm{tr}(I) \tag{2.18}$$

where I is the identity operator, so that $\mathrm{tr}(I) = 2^N$ for N qubits[7]. One can check that, since $\{|j\rangle\}_{j=1}^{2^N}$ is an orthonormal basis, the $|j\rangle\langle k|$ operators are also orthogonal (though not normalized in our convention).

Hermitian operators, which satisfy $\hat{A}^\dagger = \hat{A}$, are of particular interest since they represent physical observables such as correlation functions and Hamiltonians. These operators form a real vector space, which can be spanned by a basis of Hermitian operators, such as the basis with operators $|j\rangle\langle j|, |j\rangle\langle k| + |k\rangle\langle j|, i|j\rangle\langle k| - i|k\rangle\langle j|$ where $j < k, j, k \in \{1, \dots, 2^N\}$. Another important basis is the basis of Pauli strings $\hat{\mathcal{S}}_a = \prod_{j=1}^N \sigma_j^{s_j}$, where $s_j \in \{0, 1, 2, 3\}$, $\sigma^0 = I$, and σ^s for $s = 1, 2, 3$ are Pauli matrices (see also Section 2.1). Pauli strings are orthonormal with respect to the inner product in Eq. (2.18) and span the entire 4^N-dimensional space of N-qubit operators. Note that, through the Jordan-Wigner transformation (see Sections B.2, B.4, and B.3), a Pauli string can be converted into a fermionic operator, so they can be used to represent operators acting on fermions in addition to spins and qubits.

In this thesis, we will mainly be interested in *local* Hermitian operators. For qubit or spin systems, a k-local operator $\hat{H}$ is an operator that is a linear combinations of k-local Pauli strings

$$\hat{H} = \sum_a J_a \hat{\mathcal{S}}_a \tag{2.19}$$

where a k-local Pauli string is a product of at most k non-identity Pauli matrices. Many well-studied Hamiltonians, such as the Heisenberg spin chain in Eq. (2.3), are 2-local, though some Hamiltonians, such as the 4-local toric code Hamiltonian in Eq. (1.6) [60], have more non-local interactions. Essentially, most Hamiltonians of interest are k-local for a small constant k. The space of such k-local operators has dimension[8] $\sum_{k'=1}^{k} \binom{N}{k'} 3^{k'}$, which for a fixed k is polynomial in N. By only considering strictly local operators, we are able to work in a polynomially-sized basis of operators and avoid the exponential cost of working with the full exponentially-sized operator space. This is what makes the inverse method for constructing Hamiltonians with desired eigenstates, described in Chapter 3, efficient. If one is instead interested in quasi-local operators, which have exponentially decaying support $J_a \sim e^{-k/\xi}$ for k-local Pauli strings $\hat{\mathcal{S}}_a$, then one can approximate the quasi-local operator using a strictly local basis of operators. This is what we do in Chapter 5 to find approximate quasi-local integrals of motion (ℓ-bits) in many-body localized systems.

When performing computations with operators, we will need to be able to compute the product AB, commutator $[A, B] = AB - BA$, or anticommutator $\{A, B\} = AB + BA$ between two operators $A = \sum_a J_a \hat{\mathcal{S}}_a$ and $B = \sum_b K_b \hat{\mathcal{S}}_b$, as well as traces of operators. These can all be done efficiently by using the algebraic

---

[7] Since we are working with finite-dimensional vector spaces, the Hilbert-Schmidt inner product is equivalent to the Frobenius inner product.

[8] This is assuming arbitrary long-range k-local interactions. If spatial locality is also required, the dimensionality is reduced further.

properties of Pauli strings. In particular, for Pauli matrices,

$$\sigma^a \sigma^b = \delta_{ab} I + i\epsilon_{abc}\sigma^c \tag{2.20}$$

where ϵ_{abc} is the fully anti-symmetric tensor or Levi-Civita symbol, $(\sigma^a)^2 = I$, and $\mathrm{tr}(\sigma^a) = 0$. These properties imply that all Pauli strings except for the identity operator are traceless and that any product (or commutator or anticommutator) of two Pauli strings is another Pauli string. These properties make algebraic manipulation of operators that are linear combinations of Pauli strings simple. For more details on how we perform these manipulations, see Appendices B.2 and B.6, or our open-source Python code [47].

Chapter 3

From eigenstates to Hamiltonians

This chapter is based on the work presented in Ref. [41], ©2021 American Physical Society, done in collaboration with my advisor Prof. Bryan Clark.

3.1 Introduction

Our understanding of quantum many-body physics comes primarily from the use of "forward methods." In the forward method approach, shown in Fig. 3.1(a), a quantum model describing a material, e.g., a model Hamiltonian, is solved. Often solving each Hamiltonian is difficult requiring expensive numerics or complex analytic approaches. This restricts our attention to a few representative Hamiltonians or materials which support particular properties or interesting physics. However, the space of quantum models is vast and high-dimensional. The forward approach provides a limited perspective by restricting our focus to a small fraction of this space. The entire space, though, almost certainly contains a myriad of interesting physical Hamiltonians corresponding to undiscovered phases, unknown exactly solvable points, and Hamiltonians with desirable properties.

While determining the ground state properties from a Hamiltonian is difficult, understanding interesting physics from simple prototypical wave functions is more straightforward. For this reason, wave functions such as resonating valence bond (RVB) states [147, 148], projected BCS states [148–150], and Laughlin wave functions [151, 152] have been widely used to understand spin liquids, high temperature superconductivity, and fractional quantum Hall physics in situations where Hamiltonian methods have not been feasible. Since these prototypical wave functions are easier to work with, one can consider using them as inputs for an "inverse method" approach for constructing parent Hamiltonians that have these wave functions as ground states. In fact, parent Hamiltonians have already been constructed in a variety of contexts and include, among others [153, 154, 26, 155–160, 107], RVB parent Hamiltonians on a Kagome lattice [29–31], matrix product state parent Hamiltonians for one-dimensional systems [22–24], and Haldane pseudopotentials for a 2D electron gas [161, 162]. However, the methods for constructing parent Hamiltonians are wave function-specific, normally produce one or a small number of parent Hamiltonians, and often result in unphysical models. To overcome these limitations, we developed a novel inverse method that automates the construction of parent Hamiltonians from wave functions by searching for models in a large space of "physically reasonable" Hamiltonians. More broadly, inverse methods have been successful in applications such as solving machine learning problems [6], targeting many-particle ordering in classical materials [15, 16, 19, 20, 163–173, 21], and promoting certain properties in quantum many-body systems [174–179].

Our new inverse method, Eigenstate-to-Hamiltonian Construction (EHC), takes as input a target wave function and a target space of Hamiltonians and produces as output the Hamiltonians within the target space for which the wave function is an eigenstate (see Fig. 3.1(b)). EHC can be readily implemented with existing numerical tools. The key step of the method is the evaluation and analysis of the quantum covariance matrix (QCM) (see Eq. (3.1)). The wave functions provided as input to EHC need only to be represented in a way in which the QCM can be determined, such as numerically through the density matrix renormalization group (DMRG) [140] or variational Monte Carlo (VMC) [180]. We show that EHC can be implemented in an efficient manner, with the procedure scaling quadratically in the number of variational parameters in the target space of Hamiltonians being considered.

EHC helps solve an important general problem that has been actively pursued for decades, finding Hamiltonians with interesting ground state physics, by using the inverse approach of constructing parent Hamiltonians from wave functions. As described above, parent Hamiltonians have been constructed, with significant effort, in many specific contexts to better understand physical systems ranging from spin liquids to fractional quantum Hall systems. EHC replaces the insight required to find parent Hamiltonians with an efficient and general approach that can automate their discovery.

While this work focuses on describing the method and demonstrating its approach through a number of simple illustrative examples, it is important to note that there are many known interesting wave functions that this method could be fruitfully applied to in the future. Examples range from the projective symmetry group (PSG) wave functions [57, 181–183], which span a large number of spin liquid phases, to Gutzwiller-projected wave functions, which are heavily used in variational studies of unconventional superconductivity [149, 184, 150], to wave functions for fractional Chern insulators [185]. Finding physically realistic parent Hamiltonians for these wave functions could lead to important breakthroughs in spin liquid physics, high temperature superconductivity, and topological phases of matter. There are also a myriad of other potential uses for the EHC framework in fields such as quantum material design, cold-atom quantum simulation, and quantum computing. For example, the EHC framework could help cold-atom experimentalists find Hamiltonians for specific quantum ground states which are constructible within the hardware constraints of their experiment.

After explaining the method, we discuss three broad applications of EHC. In each application, we discover some unexpected relations between wave functions and the space of Hamiltonians.

(I) *Hamiltonian Discovery:* The most straightforward application of EHC is to discover new, simpler, or more experimentally accessible parent Hamiltonians for wave functions without known parent Hamiltonians. To illustrate this procedure, we provide as input to EHC a uniform superposition of frustrated spin configurations and automatically find Hamiltonians with this state as an exact ground state.

(II) *State Collision:* A second application of EHC is to the study of degenerate ground states. Here we introduce a generalized form of EHC, called Degenerate Eigenstate-to-Hamiltonian Construction (DEHC), that receives as input many wave functions and find spaces of Hamiltonians for which those wave functions are degenerate eigenstates. DEHC can be used to identify level crossings where two potential phases collide or to identify Hamiltonians with topological degeneracy. We illustrate this approach by colliding the ground states of the Majumdar-Ghosh model [186, 187] and the XXZ0 two-leg ladder [188], which are singlet dimer states and projected 3-coloring states, respectively.

(III) *Phase Expansion:* As a final application, we show how to use EHC to take a known ground state wave function and expand the region of Hamiltonian space over which this wave function is a ground state. Surprisingly, we discover that many previously known models are in fact special points in large spaces of non-trivial Hamiltonians with identical ground states. We show examples of this procedure by expanding the ground state phase diagram of the XX chain, the Heisenberg chain, the Kitaev chain, and a 2D BdG model.

Altogether, in applications (I)-(III), we use seven different types of wave functions as input to EHC and in each case are able to successfully construct new non-trivial parent Hamiltonians.

3.2 Method

In this section, we introduce our new method, the Eigenstate-to-Hamiltonian Construction (EHC). EHC takes as input both a target state $|\psi_T\rangle$ and a target space of Hamiltonians $\hat{H}_T$ and produces as output the space of Hamiltonians that contains $|\psi_T\rangle$ as an energy eigenstate, which we call the *eigenstate space* of Hamiltonians. Within the eigenstate space, it is possible for the state $|\psi_T\rangle$ to be a ground state in a particular region, which we call the *ground state manifold.* This hierarchy of Hamiltonian spaces is depicted in Fig. 3.2.

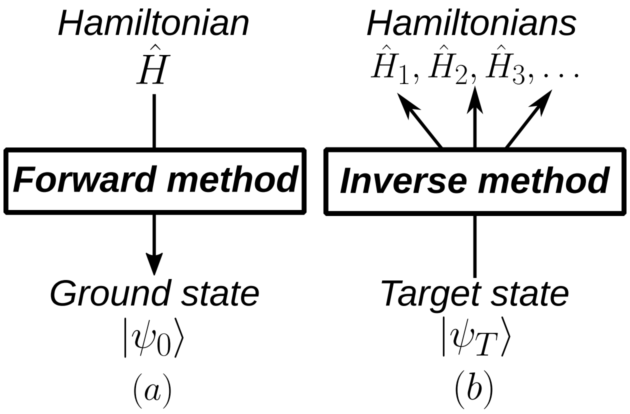

Figure 3.1: (a) A typical *forward method* used in quantum mechanics finds the ground state $|\psi_0\rangle$ of a single Hamiltonian $\hat{H}$. (b) We introduce a new *inverse method*, EHC, that finds Hamiltonian(s) $\hat{H}_1, \hat{H}_2, \ldots$ from a target state $|\psi_T\rangle$, with the property that $|\psi_T\rangle$ is an energy eigenstate of these Hamiltonian(s).

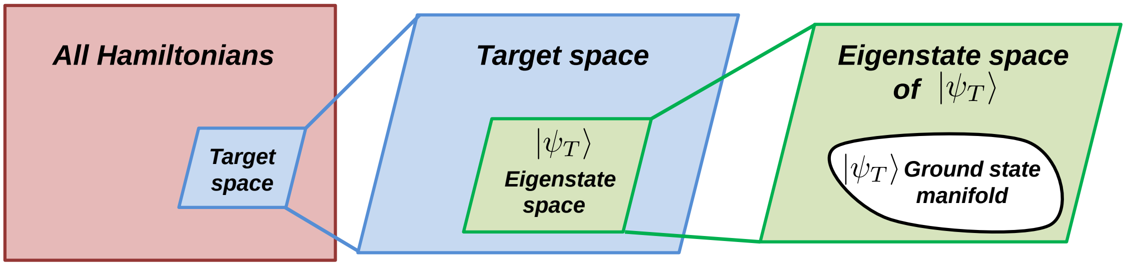

Figure 3.2: All Hamiltonians of a finite-dimensional quantum system form a real vector space of Hermitian operators (shown in red). Eigenstate-to-Hamiltonian Construction (EHC) is performed in a *target space* of Hamiltonians, a physically meaningful subspace of the entire vector space chosen by the user (shown in blue). The output of EHC is the *eigenstate space*, a subspace of the target space consisting of Hamiltonians that contain a target wave function $|\psi_T\rangle$ as an energy eigenstate (shown in green). Using ground state methods, one can further map out the *ground state manifold*, the region in eigenstate space where the target state $|\psi_T\rangle$ is a ground state (shown in white).

The target space of Hamiltonians $\hat{H}_T$ is a subspace of the vector space of all possible Hamiltonians. The possible states of a finite system of N quantum degrees of freedom with local dimension d, e.g., $d = 2$ for $s = 1/2$ spins, form a complex vector space of dimension d^N. The possible Hamiltonians that can act on this system are all $d^N \times d^N$ Hermitian operators, which form a real vector space of dimension $\left(d^N\right)^2 = d^{2N}$. The target space is a small d_T-dimensional *physically meaningful* subspace of Hamiltonian space that we choose when using the EHC method. In particular, we define our target space by choosing a basis of $d_T \ll d^{2N}$ Hermitian operators $\{\hat{h}_a\}_{a=1}^{d_T}$. Defined this way, the target space contains Hamiltonians of the form $\hat{H}_T = \sum_{a=1}^{d_T} J_a \hat{h}_a$ with real J_a. While any set of linearly independent Hermitian operators can be used to define the target space, some natural choices for operators include local one and two-site operators.

The central tool used in EHC is the *quantum covariance matrix* (QCM), a $d_T \times d_T$ matrix whose matrix elements are given by

$$(C_T)_{ab} = \langle \hat{h}_a \hat{h}_b \rangle_T - \langle \hat{h}_a \rangle_T \langle \hat{h}_b \rangle_T \tag{3.1}$$

where $\langle \hat{\mathcal{O}} \rangle_T \equiv \langle \psi_T | \, \hat{\mathcal{O}} | \psi_T \rangle / \, \langle \psi_T | \psi_T \rangle$ and $a, b = 1, \ldots, d_T$. The QCM is a quantum-mechanical generalization of a classical covariance matrix, where statistical expectation values of random variables under a probability distribution are replaced by quantum expectation values of Hermitian operators under a wave function. It can be easily shown that C_T is Hermitian and positive semi-definite. Most importantly, C_T can be used to compute the energy variance of the target state for Hamiltonians in the target space:

$$\sigma_T^2 = \langle \hat{H}_T^2 \rangle_T - \langle \hat{H}_T \rangle_T^2 = \sum_{a=1}^{d_T} \sum_{b=1}^{d_T} J_a (C_T)_{ab} J_b \geq 0. \tag{3.2}$$

From Eq. (3.2), one can see that an eigenvector of C_T with zero eigenvalue corresponds to a vector of coupling constants $\tilde{J}_a$ and therefore a Hamiltonian $\tilde{H} = \sum_a \tilde{J}_a \hat{h}_a$ with zero energy variance under the target state $|\psi_T\rangle$. Simply by computing the null space of the QCM, we are able to find the eigenstate space of Hamiltonians for $|\psi_T\rangle$.

There are three general cases for the dimensionality of the null space of the QCM. (1) In the case of a one-dimensional null space, there is a single null vector, and therefore a uniquely specified Hamiltonian [189–191] in the target space, for which the target state $|\psi_T\rangle$ is an eigenstate. (2) In the case of a many-dimensional null space, there is a multi-dimensional space of Hamiltonians, which includes any Hamiltonian which can be constructed from a linear combination of the null vectors, which have $|\psi_T\rangle$ as an eigenstate. The null vectors obtained from numerical decompositions are often in poor representations that are difficult to interpret. To overcome this issue we use an algorithm, described in Ref. [192], which heuristically generates the sparsest basis for the null space. This ensures that each Hamiltonian generated from a basis state in our eigenstate space is constructed from only a small number of distinct Hermitian operators $\hat{h}_a$. While we find this decomposition fruitful in understanding the resulting Hamiltonians, it is still an important open problem to determine other useful ways of representing the vectors in the null space. (3) Finally, in the case when the QCM has no null space, the target state $|\psi_T\rangle$ is not an eigenstate of any Hamiltonian within the chosen target space of Hamiltonians. Nonetheless, the smallest eigenvalues of the QCM still potentially contain useful information. Eigenvectors of the QCM with small eigenvalues correspond to Hamiltonians with small variance under the target state $|\psi_T\rangle$. This means that the lowest eigenvectors of the QCM represent Hamiltonians under which the target wave function $|\psi_T\rangle$ is "close" to an eigenstate. It will be important future work to better understand the implications of this.

EHC is a simple, non-iterative, and remarkably efficient procedure that only requires the computation of $d_T^2 + d_T$ expectation values of correlation functions $\langle \hat{h}_a \hat{h}_b \rangle_T$ and observables $\langle \hat{h}_a \rangle_T$. Standard numerical methods for computing such expectation values, such as VMC, DMRG, or exact diagonalization (ED), can be used to evaluate the entries of the QCM. For our specific calculations, we used DMRG, i.e., matrix product state (MPS) methods, and VMC.

When using DMRG, we represent the target state $|\psi_T\rangle$ as a MPS, and the Hermitian operators $\hat{h}_a$ as low bond dimension matrix product operators (MPOs). This allows us to efficiently evaluate $\langle \hat{h}_a \hat{h}_b \rangle_T$ and $\langle \hat{h}_a \rangle_T$ with standard methods, by contracting the MPS $|\psi_T\rangle$ with the $\hat{h}_a \hat{h}_b$ and $\hat{h}_a$ MPOs. We performed our MPS calculations on finite size systems of up to $N = 32$ sites and were able to compute all of the entries of the QCM to machine precision.

With VMC, we estimated the expectation values of observables $\hat{\mathcal{O}} \in \{\hat{h}_a \hat{h}_b, \hat{h}_a\}$ under the variational target wave function $|\psi_T\rangle$:

$$\langle \hat{\mathcal{O}} \rangle_T = \frac{\langle \psi_T | \hat{\mathcal{O}} | \psi_T \rangle}{\langle \psi_T | \psi_T \rangle} = \sum_R \frac{|\langle \psi_T | R \rangle|^2}{\sum_{R'} |\langle \psi_T | R' \rangle|^2} \frac{\langle R | \hat{\mathcal{O}} | \psi_T \rangle}{\langle R | \psi_T \rangle}$$

by sampling configurations $|R\rangle$ from the probability distribution $\propto |\langle \psi_T | R \rangle|^2$ with Metropolis Markov chain Monte Carlo and computing $O(R) \equiv \langle R | \hat{\mathcal{O}} | \psi_T \rangle / \langle R | \psi_T \rangle$ [193]. The $O(R)$ can be concurrently evaluated during the Markov chain sampling, which means the entries of the QCM have reduced relative statistical noise. Alternatively, with VMC, one can also generate the QCM from a $N_s \times d_T$ sample matrix $M_{sa} = \langle R_s | \hat{h}_a | \psi_T \rangle / \langle R_s | \psi_T \rangle$ for $\{|R_s\rangle\}_{s=1}^{N_s}$ sampled from $\propto |\langle \psi_T | R \rangle|^2$. The sample matrix can be computed more efficiently than the QCM directly, requiring calculating d_T observables per sample instead of d_T^2. Moreover, similar to principle component analysis (PCA), one can perform SVD on an appropriately-shifted sample matrix to learn about the eigenvectors of the QCM [1].

We empirically found that even though VMC produces a noisy statistical estimate of the QCM, we can still robustly identify properties of the QCM. Interestingly, the dimensionality of the null space has significantly lower statistical noise than the numerical entries of the null vectors.

Finally, in addition to EHC, we developed a generalized form of the method for finding a space of Hamiltonians with multiple target wave functions $|\psi_{T,1}\rangle, |\psi_{T,2}\rangle, \ldots$ as *degenerate* energy eigenstates, called Degenerate Eigenstate-to-Hamiltonian Construction (DEHC), that we discuss in the appendix.

---

[1] In fact, to learn about the null space of the QCM, one can choose the configurations in the sample matrix arbitrarily.

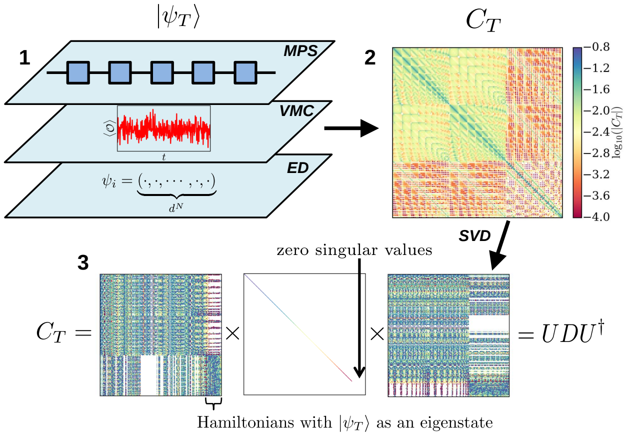

Figure 3.3: The steps of Eigenstate-to-Hamiltonian Construction (EHC). **1** Represent the target state $|\psi_T\rangle$ numerically using, for example, MPS, VMC, or ED techniques. **2** Compute the quantum covariance matrix (QCM) C_T given by Eq. (3.1). **3** Perform a singular value decomposition (SVD) to decompose C_T into $C_T = UDU^\dagger$, with the columns of U representing the singular vectors and the diagonal entries of D representing their corresponding singular values. Identify the null vectors, i.e., the singular vectors with zero singular values. The null vectors correspond to the coupling constants of Hamiltonians with $|\psi_T\rangle$ as an energy eigenstate. The C_T matrix depicted is the QCM for the XX chain ground state used in our phase expansion example.

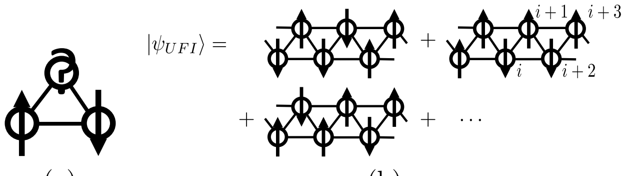

(a) (b)

Figure 3.4: (a) For a classical Ising antiferromagnetic triangle, all three bond energies cannot be simultaneously minimized, leading to a six-fold ground state degeneracy. (b) The uniform frustrated Ising (UFI) state is a uniform superposition of the ground states of an antiferromagnetic Ising model on a lattice of triangles. In this case, we consider the UFI state on a triangular two-leg ladder.

3.3 Results and discussion

With a few illustrative examples, we demonstrate three applications of the EHC method – Hamiltonian discovery, state collision, and phase expansion. Additional examples of phase expansion on the Heisenberg chain and the Kitaev chain are discussed in the appendix. A brief summary of our results using the EHC method are shown in Table 3.1.

3.3.1 Hamiltonian discovery

In this section, we investigate a new type of wave function and use the EHC method to construct a parent Hamiltonian for which it is a ground state.

Target state(s)	d_T	Dim. e.s. space	Dim. g.s. manifold
$\lvert\psi_{UFI}\rangle$	111	21	≥ 3
$\lvert\psi^{\pm}_{SD}\rangle$	8	4	4
$\lvert\psi^{m,l}_{P3C}\rangle$	8	3	3
$\lvert\psi^{\pm}_{SD}\rangle$ & $\lvert\psi^{m,l}_{P3C}\rangle$	8	2	2
$\lvert\psi_{XX}\rangle$	198	22	≥ 3
$\lvert\psi_{BCS}\rangle$	408	16	≥ 2
$\lvert\psi^{\pm}_{KC}\rangle$	210	77	≥ 22
$\lvert\psi_{H}\rangle$	198	39	≥ 3
$\lvert\psi^{\pm}_{SD}\rangle$	198	108	≥ 36

Table 3.1: A summary of the results of Eigenstate-to-Hamiltonian Construction (EHC) calculations performed in this work. Target states and a target space of Hamiltonians of dimension d_T are provided as input to EHC. The output of EHC is an eigenstate space of Hamiltonians. Ground state methods were used to map out the ground state manifold, but often could only provide a lower bound on the dimensionality of the manifold. The first row is our Hamiltonian discovery result, the next three rows are our state collision results, and the last rows are our phase expansion results. The phase expansion results for the ground states of the Kitaev chain, Heisenberg chain, and Majumdar-Ghosh model, $|\psi^{\pm}_{KC}\rangle, |\psi_H\rangle, |\psi^{\pm}_{SD}\rangle$, respectively, were obtained for length $N = 12$ chains and are discussed in the appendix.

We choose a quantum state that is derived from classical magnetically frustrated spin configurations. As shown in Fig. 3.4(a), an Ising antiferromagnet on a triangle-tiled lattice exhibits geometric frustration, which results in a large ground state degeneracy. The simplest such model is the antiferromagnetic Ising model on the triangular two-leg ladder: $\hat{H}_I = \sum_{i=1}^{N} \left(\sigma^z_i \sigma^z_{i+1} + \frac{1}{2}\sigma^z_i \sigma^z_{i+2}\right)$. This model contains combinatorially many ground state spin configurations chosen so that each triangle has exactly two up or two down spins. We analyze a new type of wave function, called the uniform frustrated Ising (UFI) state $|\psi_{UFI}\rangle$, shown in Fig. 3.4(b), which is an equal superposition of the $\hat{H}_I$ ground state spin configurations. We use the UFI state as the target state in EHC and discover Hamiltonians for which it is the ground state. While we do not study the properties of this state, our consideration of it is inspired by other wave functions that are uniform superpositions of ordered states, such as the uniform RVB state [147, 148] and uniform dimer states [194–196], which have played important roles in spin liquid physics. We represented our target wave function $|\psi_T\rangle = |\psi_{UFI}\rangle$ numerically as a matrix product state (MPS) for finite periodic ladders of size $N = 8, 12, 16$.

In addition to the target wave function $|\psi_T\rangle$, EHC needs a target space of physically meaningful Hamiltonians $\hat{H}_T = \sum_{a=1}^{d_T} J_a \hat{h}_a$ in which to search for parent Hamiltonians. For our target space of Hamiltonians, we considered a large $d_T = 111$ dimensional space of Hamiltonians spanned by periodic, local operators made from products of Pauli matrices on up to 3 sites separated spatially up to a distance of 3 sites away on the ladder. Some operators in this target space include:

$$\begin{aligned} \hat{h}_1 &\equiv \sum_{i=1}^{N} \sigma_i^x & \hat{h}_5 &\equiv \sum_{i=1}^{N} \sigma_i^x \sigma_{i+1}^y \\ \hat{h}_{28} &\equiv \sum_{i=1}^{N} \sigma_i^z \sigma_{i+3}^x & \hat{h}_{66} &\equiv \sum_{i=1}^{N} \sigma_i^x \sigma_{i+1}^z \sigma_{i+3}^z. \end{aligned} \tag{3.3}$$

Using the finite MPS representation of $|\psi_{UFI}\rangle$, we computed the 111×111 quantum covariance matrix (QCM) for the target space defined by the operators $\hat{h}_1, \ldots, \hat{h}_{111}$. We identified 21 null vectors of the QCM. These correspond to a space of 21 Hamiltonians with $|\psi_{UFI}\rangle$ as an eigenstate, which includes the Ising model $\hat{H}_I$. Here, we focus on two non-trivial operators in this space

$$\begin{aligned} \hat{H}_{UFI}^{(1)} &= \sum_{i=1}^{N} \frac{1}{2} \sigma_i^z \sigma_{i+2}^z + \sigma_i^z \sigma_{i+3}^z + \sigma_i^x \sigma_{i+1}^z \sigma_{i+2}^z - \sigma_{i-2}^z \sigma_i^x \sigma_{i+1}^z \\ \hat{H}_{UFI}^{(2)} &= \sum_{i=1}^{N} \frac{1}{2} \sigma_i^z \sigma_{i+2}^z + \sigma_i^z \sigma_{i+3}^z + \sigma_{i-2}^z \sigma_{i-1}^z \sigma_i^x - \sigma_{i-1}^z \sigma_i^x \sigma_{i+2}^z. \end{aligned}$$

which contain Ising interactions within and between triangles on the ladder as well as off-diagonal three site interactions of the form $\sigma^x \sigma^z \sigma^z$ between triangles. These operators exist in four-site unit cells. We found that the UFI state is an $E = -N/2$ energy eigenstate of these operators. Other operators in the eigenstate space are discussed in the appendix.

Using DMRG and ED for ladders of $N = 8, 12, 16, 20$ sites, we studied the ground state manifold of the Hamiltonian

$$J\hat{H}_I + J_1 \hat{H}_{UFI}^{(1)} + J_2 \hat{H}_{UFI}^{(2)}. \tag{3.4}$$

Interestingly, for $J > 0$ and $0 < J_1/J = J_2/J < J_c/J$, we found that the UFI state is a ground state of Eq. (3.4), where J_c/J depends on system size ($J_c/J \approx 0.25, 0.20, 0.175$ for $N = 8, 12, 16$, respectively). Moreover, for the system sizes studied, we determined empirically that for this range of parameters $|\psi_{UFI}\rangle$ exists in a degenerate ground state manifold containing $5 + N/4$ states. Ultimately, our results show that there is a family of quantum models adiabatically connected to the antiferromagnetic Ising two-leg ladder with the UFI state as a ground state.

3.3.2 State collision

In this section, we consider many wave functions at the same time and use our inverse method to construct parent Hamiltonians that have all of them as degenerate ground states.

Naively, one might attempt to solve this problem by applying the EHC method repeatedly, once for each wave function, and combining the results. However, this approach would only reveal where in Hamiltonian space the wave functions are simultaneous eigenstates, but not where they are *degenerate* eigenstates. To properly solve this problem, one needs to use the generalization of EHC for degenerate wave functions, DEHC, to find the appropriate eigenstate space. In the following example, we apply DEHC to a triangular two-leg ladder system and search for the eigenstate space where two singlet dimer states and all "projected 3-coloring states" are degenerate.

The singlet dimer states are $|\psi^{\pm}_{SD}\rangle = (|\psi_{1,2}\psi_{3,4}\cdots\psi_{N-1,N}\rangle \pm |\psi_{2,3}\psi_{4,5}\cdots\psi_{N,1}\rangle)/\sqrt{2}$ where $|\psi_{i,j}\rangle \equiv (|{\uparrow_i}{\downarrow_j}\rangle - |{\downarrow_i}{\uparrow_j}\rangle)/\sqrt{2}$ is a singlet dimer between sites i and j. The states $|\psi^{\pm}_{SD}\rangle$ are the two degenerate ground states of the periodic Majumdar-Ghosh model [186, 187].

The projected 3-coloring states [188] are projected product states of the form $|\psi^{m,l}_{P3C}\rangle \equiv P_{S_z=m}\Big(\bigotimes_{i=1}^{N}|n_i\rangle\Big)$ where $|n_i\rangle \equiv (|{\uparrow_i}\rangle + \omega^{n_i}|{\downarrow_i}\rangle)/\sqrt{2}$ with $n_i \in \{0,1,2\}$, $P_{S_z=m}$ is a projection onto the S_z-sector with magnetization m, $\omega \equiv e^{i2\pi/3}$, and each triangle of the two-leg ladder is 3-colored so that n_i, n_{i+1}, n_{i+2} are different for every i. The parameter l labels the two possible 3-colorings of the two-leg ladder. There are $2N$ linearly independent projected 3-coloring states $|\psi^{m,l}_{P3C}\rangle$.

As input to DEHC, we provide a $d_T = 8$ dimensional target space of Hamiltonians spanned by local two-site exchange and Ising interactions on even and odd sites. The first four operators, which act on even sites, are

$$\begin{aligned} \hat{h}_1 &\equiv \sum_{i=1}^{N/2}\sum_{\rho=x,y} S^{\rho}_{2i}S^{\rho}_{2i+1} \qquad & \hat{h}_2 &\equiv \sum_{i=1}^{N/2} S^{z}_{2i}S^{z}_{2i+1} \\ \hat{h}_3 &\equiv \sum_{i=1}^{N/2}\sum_{\rho=x,y} S^{\rho}_{2i}S^{\rho}_{2i+2} \qquad & \hat{h}_4 &\equiv \sum_{i=1}^{N/2} S^{z}_{2i}S^{z}_{2i+2} \end{aligned} \tag{3.5}$$

where $S^{\rho}_i = \sigma^{\rho}_i/2$ are spin-1/2 operators. The other four act on odd sites. Also provided as input to DEHC, are all $2N+2$ projected 3-coloring and singlet dimer states.

From a single DEHC calculation, we found the following two-dimensional space of Hamiltonians for which the singlet dimer states and projected 3-coloring states are degenerate eigenstates

$$K_1 \left(\sum_{i=1}^{N} \hat{H}^{(i,1)}_{XXZ0} + \frac{1}{2} \sum_{i=1}^{N} \hat{H}^{(i,2)}_{XXZ0} \right) + K_2 \sum_{i=1}^{N} (-1)^i \hat{H}^{(i,2)}_{XXZ0} \tag{3.6}$$

with parameters K_1 and K_2 defining the space, where $\hat{H}^{(i,r)}_{XXZ0} \equiv S^x_i S^x_{i+r} + S^y_i S^y_{i+r} - \frac{1}{2} S^z_i S^z_{i+r}$ [2]. This space of Hamiltonians is where the two sets of states "collide" and become degenerate with one another.

To better understand the Hamiltonians surrounding this "collision region," we performed two more DEHC calculations, one with only the singlet dimer states as input and one with only the projected 3-coloring states as input. In both cases, we considered the same 8-dimensional target space of Hamiltonians described above.

From one calculation, we found that the singlet dimer states $|\psi^{\pm}_{SD}\rangle$ are degenerate energy eigenstates of a four-dimensional space of Hamiltonians

$$\begin{aligned} &\sum_{i=1}^{N} \sum_{\rho=x,y} \left[J_{xy} \left(S^{\rho}_i S^{\rho}_{i+1} + \frac{1}{2} S^{\rho}_i S^{\rho}_{i+2} \right) + (-1)^i \delta_{xy} S^{\rho}_i S^{\rho}_{i+2} \right] \\ &+ \sum_{i=1}^{N} \left[J_z \left(S^z_i S^z_{i+1} + \frac{1}{2} S^z_i S^z_{i+2} \right) + (-1)^i \delta_z S^z_i S^z_{i+2} \right] \end{aligned} \tag{3.7}$$

with parameters $J_{xy}, J_z, \delta_{xy}, \delta_z$ defining the space.

From the other calculation, we found that the projected 3-coloring states $|\psi^{m,l}_{P3C}\rangle$ are degenerate eigenstates of a three-dimensional space of Hamiltonians

$$J_{XXZ0} \sum_{i=1}^{N} \hat{H}^{(i,1)}_{XXZ0} + \epsilon_e \sum_{i=1}^{N/2} \hat{H}^{(2i,2)}_{XXZ0} + \epsilon_o \sum_{i=1}^{N/2} \hat{H}^{(2i+1,2)}_{XXZ0} \tag{3.8}$$

where $J_{XXZ0}, \epsilon_e, \epsilon_o$ are the three parameters defining the space.

Informed by our inverse method calculations, we could effectively map out the ground state manifolds of the singlet dimer states and the projected 3-coloring states by performing DMRG on the models defined by Eqs. (3.6), (3.7), (3.8) on finite size ladders of size $N = 12, 16, 32$. Due to the low dimensionality of the Hamiltonian spaces considered in this example, we are able to visualize how the singlet dimer and projected 3-coloring parent Hamiltonians "collide" in Hamiltonian space. A visualization of this collision, shown in two different ways, is depicted in Fig. 3.5.

Fig. 3.5(a) shows the ground state manifold of the singlet dimer states $|\psi^{\pm}_{SD}\rangle$ contained in a three-dimensional projection of their four-dimensional eigenstate space. Fig. 3.5(b) shows the ground state man-

---

[2] In terms of Eq. (3.7), this corresponds to $K_1 \equiv J_{xy}, K_2 \equiv \delta_{xy}$ subject to the constraints $J_z = -J_{xy}/2, \delta_z = -\delta_{xy}/2$. In terms of Eq. (3.8), this corresponds to $K_1 \equiv J_{XXZ0}, K_2 \equiv \epsilon_e - J_{XXZ0}/2 = -\epsilon_o + J_{XXZ0}/2$ or $\epsilon_e = K_1/2 + K_2$ and $\epsilon_o = K_1/2 - K_2$.

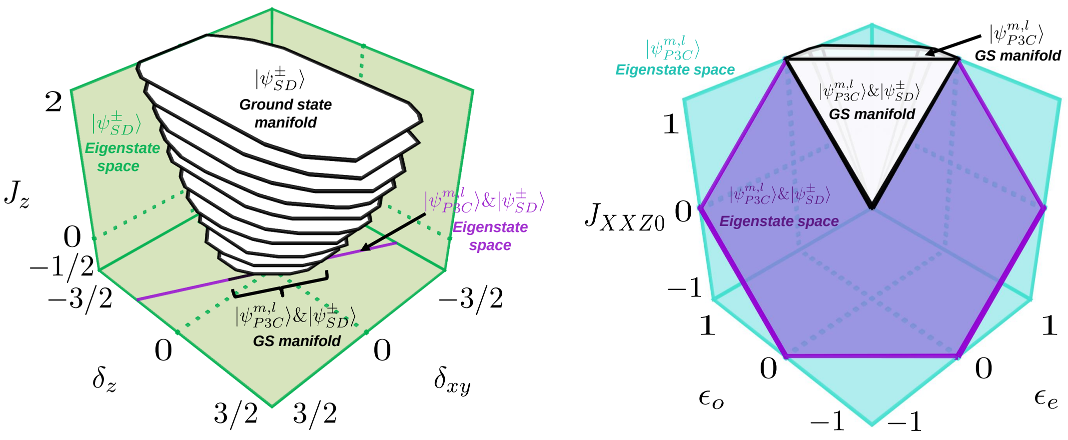

(a) (b)

Figure 3.5: **State collision example.** Collision of the singlet dimer states $|\psi^{\pm}_{SD}\rangle$ and the projected 3-coloring states $|\psi^{m,l}_{P3C}\rangle$ from (a) the perspective of the singlet dimer eigenstate space, which is given by Eq. (3.7) with $J_{xy} = 1$ and is shown in green and (b) the perspective of the projected 3-coloring eigenstate space, which is given by Eq. (3.8) and is shown in teal. The space where all of the states are degenerate eigenstates is given by Eq. (3.6) and is shown in purple; it appears as a line in (a) and a plane in (b). The collision region, where all states are degenerate ground states, occurs on the indicated line segment in (a) and in the indicated triangular region in (b).

ifold of the projected 3-coloring states $|\psi^{m,l}_{P3C}\rangle$ contained in their three-dimensional eigenstate space. The combined eigenstate space where $|\psi^{\pm}_{SD}\rangle$ and $|\psi^{m,l}_{P3C}\rangle$ are degenerate energy eigenstates, is depicted in purple in both Fig. 3.5(a) and Fig. 3.5(b). From DMRG and ED, we found that the collision region occurs for the set of parameters $K_1 > 0$ and $-1/2 \leq K_2/K_1 \leq 1/2$ [3]. The collision region appears as a line segment in Fig. 3.5(a) and as a triangular region in Fig. 3.5(b).

Note that the singlet dimer eigenstate space can be constructed from an anisotropic generalization of a known space of "block operators" described by Ref. [197], which we discuss in the appendix. Similarly, the projected 3-coloring eigenstate space is largely made up of a known space of triangle-tiled Hamiltonians described by Ref. [188].

3.3.3 Phase expansion

In this section, we show with two examples, the XX chain and a 2D BDG model, how EHC can be used to expand the zero-temperature phase diagram about a known Hamiltonian $\hat{H}_0$ to find a non-trivial many-dimensional manifold of Hamiltonians with the same ground state wave function as $\hat{H}_0$.

When phase expanding from $\hat{H}_0$, there are generically two classes of new Hamiltonians one might find:

---

[3] In terms of Eq. (3.7), this corresponds to $J_{xy} > 0, J_z = -J_{xy}/2, \delta_z = -\delta_{xy}/2$, and $-1/2 \leq \delta_{xy}/J_{xy} \leq 1/2$. In terms of Eq. (3.8), this corresponds to $J_{XXZ0} > 0, \epsilon_e/J_{XXZ0} = 1 - \epsilon_o/J_{XXZ0}$ and $0 \leq \epsilon_e/J_{XXZ0} \leq 1$.

Hamiltonians that commute with $\hat{H}_0$ and those that do not. Adding $\hat{H}_0$-commuting Hamiltonians to $\hat{H}_0$ not only preserves the target state $|\psi_T\rangle$ as an eigenstate, but actually preserve all eigenstates and only acts to shift the eigenvalues. These Hamiltonians can be the result of conserved quantities, such as total S_z^2. In our phase expansion results, we, unsurprisingly, find such Hamiltonians. However, surprisingly, we also find non-$\hat{H}_0$-commuting Hamiltonians with $|\psi_T\rangle$ as an eigenstate. Adding such Hamiltonians to $\hat{H}_0$ preserves the target state $|\psi_T\rangle$ as an energy eigenstate while modifying other eigenstates. For example, in the XX chain and Heisenberg chain (see appendix) we find new Hamiltonians that do not commute with their respective $\hat{H}_0$.

The periodic XX chain, $\hat{H}_{XX} = \sum_{n=1}^{N} \left(S_n^x S_{n+1}^x + S_n^y S_{n+1}^y \right)$, has an antiferromagnetic ground state $|\psi_{XX}\rangle$. We represent $|\psi_{XX}\rangle$ as a MPS, which we obtain by performing DMRG on periodic XX chains of length $N = 12$. Because *a priori* we do not know what a possible expanded phase diagram of $|\psi_{XX}\rangle$ might look like, we considered a large target space of Hamiltonians spanned by $d_T = 3\binom{N}{2} = 3N(N-1)/2 = 198$ two-site spin operators of the form

$$S_i^x S_j^x \qquad S_i^y S_j^y \qquad S_i^z S_j^z \tag{3.9}$$

where $1 \leq i < j \leq N$. Note that these operators are simple and physically reasonable in that they only involve two-site spin interactions, though they are non-local for spins arranged on a chain. One can easily see that the original Hamiltonian $\hat{H}_{XX}$ is contained in this target space.

Using a MPS representation of $|\psi_{XX}\rangle$, we computed the QCM for the target space given by Eq. (3.9), which is depicted in Fig. 3.3, and found that its null space was spanned by 22 null vectors for $N = 12$, where 12 were related to total S_z conservation (see supplement for details) and 4 appeared to be from finite-size effects. The remaining 6 null vectors corresponded to a space of Hamiltonians

$$\hat{H}_{XX}^{(c,\epsilon)} \equiv \sum_{n=1}^{N} \epsilon^n f^{(c)}(n) \left(S_n^x S_{n+1}^x + \epsilon S_n^y S_{n+1}^y \right) \tag{3.10}$$

where $\epsilon = \pm 1$ and $f^{(c)}(n) = 1, \sin(2\pi n/N), \cos(2\pi n/N)$ for $c = 0, 1, 2$, respectively. These operators correspond to particular types of sinusoidally modulated and anisotropic XX chain interactions. Note that $|\psi_{XX}\rangle$ is a zero energy eigenstate of all of these operators, except for $\hat{H}_{XX}^{(0,+)} = \hat{H}_{XX}$. Also, the four operators $\hat{H}_{XX}^{(c,\epsilon)}$ for $c = 1, 2$ and $\epsilon = \pm 1$ do not commute with $\hat{H}_{XX}$. In fact, the six operators in Eq. (3.10) do not commute with one another except in $\epsilon = \pm 1$ pairs, so that $\left[\hat{H}_{XX}^{(c,+)}, \hat{H}_{XX}^{(c,-)} \right] = 0$ for all c.

Next, informed by the results of EHC, we mapped out the ground state manifold of $|\psi_{XX}\rangle$ by performing ground state calculations on Hamiltonians in the space described by Eq. (3.10) [4]. We find a highly non-trivial ground state manifold for the Hamiltonian

$$\sum_{c=0,1,2} \sum_{\epsilon=\pm 1} J_{c,\epsilon} \hat{H}_{XX}^{(c,\epsilon)} \tag{3.11}$$

defined by the six parameters $J_{0,\pm}, J_{1,\pm}, J_{2,\pm}$. We analyzed the ground state manifold empirically by considering two and three-dimensional projections of this space subject to the constraint $J_{0,+} = 1$. For example, for finite size systems we found the following (approximate) two-dimensional regions where $|\psi_{XX}\rangle$ was the ground state: $|J_{0,-}| + |J_{c,\epsilon}| \lesssim 1$ for $c = 1, 2$ and $\epsilon = \pm 1$; $|J_{c,-}| + |J_{c,+}| \lesssim 1$ for $c = 1, 2$; and $(J_{1,\epsilon_1})^2 + (J_{2,\epsilon_2})^2 \lesssim 1$ for $\epsilon_1, \epsilon_2 = \pm 1$. We also observed an example of a three-dimensional ground state manifold for $|\psi_{XX}\rangle$ with the approximate shape of a tetrahedron, depicted in Fig. 3.6(b). The tetrahedron-like manifold has endpoints at approximately $(J_{0,-}, J_{1,+}, J_{1,-}) = (-1, -1, -1), (1, 1, -1), (1, -1, 1), (-1, 1, 1)$ in coupling constant space. One implication of our results is that the ground state of the XX chain is robust to specific sinusoidally modulated XX-like perturbations. Note that the Hamiltonians found in Eq. (3.11) are related to a mapping discussed in Ref. [198].

Finally, we discuss an application of the EHC method to a two-dimensional system using variational Monte Carlo (VMC) to calculate the QCM. In this example, we performed phase expansion on the ground state of the following BdG Hamiltonian on an $L \times L$ square lattice

$$\begin{aligned}\hat{H}_{BdG} = &- \sum_{(x,y),\sigma} (c^\dagger_{(x,y),\sigma} c_{(x+1,y),\sigma} + c^\dagger_{(x,y),\sigma} c_{(x,y+1),\sigma} + h.c.) \\ &+ \sum_{(x,y)} (c_{(x,y),\uparrow} c_{(x,y),\downarrow} + h.c.)\end{aligned}$$

where (x, y) indicates the coordinates of a site in the lattice. This model is the parent Hamiltonian of the s-wave BCS wave function $|\psi_{BCS}\rangle = \prod_k (u_k + v_k c^\dagger_{k\uparrow} c^\dagger_{-k\downarrow})|0\rangle$ with BCS parameters u_k, v_k defined in the standard way and $\Delta_k = \Delta = t = 1, \mu = 0$.

The target space provided as input to EHC was spanned by all possible one and two-site operators of

---

[4] In this case, the spin-1/2 Hamiltonian can be converted into a non-interacting Hamiltonian of spinless fermions with the Jordan-Wigner transformation. The many-body ground state energy can then be efficiently computed by diagonalizing a one-body Hamiltonian.

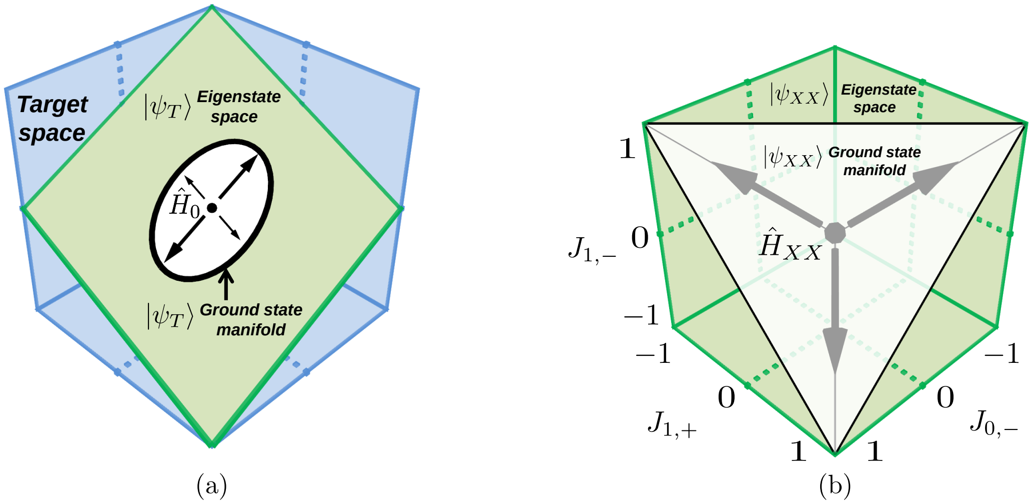

Figure 3.6: **Phase expansion schematic and example.** (a) Schematic representing the expansion of a phase diagram about a known Hamiltonian $\hat{H}_0$, which has a known ground state $|\psi_T\rangle$. Shown is the target space (blue) provided as input to the EHC method, the eigenstate space (green) of $|\psi_T\rangle$ produced as the output of EHC and the expanded ground state manifold (white) of $|\psi_T\rangle$. (b) Numerical results for the phase expansion about the Hamiltonian $\hat{H}_{XX}$ with ground state $|\psi_{XX}\rangle$. Shown is a three-dimensional projection (green) of the six-dimensional eigenstate space of $|\psi_{XX}\rangle$, given by Eq. (3.11) with $J_{0,+} = 1$ and $J_{2,\pm} = 0$ and the ground state manifold of $|\psi_{XX}\rangle$ (white), which almost has the shape of a tetrahedron. For simplicity of visualization, here we plot a tetrahedron, which contains most of the ground state manifold, though ignores a small curved region which extends slightly beyond the tetrahedron.

the form

$$\sum_{\sigma} n_{(x,y)\sigma}, \quad n_{(x,y)\uparrow}n_{(x,y)\downarrow}, \quad \sum_{\sigma}(c^{\dagger}_{(x,y)\sigma}c_{(x',y')\sigma} + h.c.),$$
$$(c_{(x,y)\uparrow}c_{(x',y')\downarrow} + h.c.), \quad \sum_{\sigma,\sigma'} n_{(x,y)\sigma}n_{(x',y')\sigma'}.$$

In our calculations, we considered an $N = 4 \times 4 = 16$ site system, which made the dimension of this target space $d_T = 408$.

Using VMC, we numerically estimated the QCM for the $N = 16$ site BCS state in this target space. The eigenstate space produced by the EHC method contained 16 operators. One interesting Hamiltonian in this space is the staggered s-wave pairing operator

$$\hat{H}_s = \sum_{(x,y)} (-1)^{x+y}(c_{(x,y),\uparrow}c_{(x,y),\downarrow} + h.c.). \tag{3.12}$$

The s-wave BCS state $|\psi_{BCS}\rangle$ is a zero energy eigenstate of this operator. Numerically, we determined that $|\psi_{BCS}\rangle$ is actually the ground state of the phase expanded model $t\hat{H}_{BdG}+\Delta_s\hat{H}_s$ for $t > 0$ and $-1 \leq \Delta_s/t \leq 1$, even for large system sizes. An alternative approach for constructing parent Hamiltonians from BCS ground states is given in Ref. [153].

Other examples of phase expansion for the Kitaev chain, Heisenberg chain, and Majumdar-Ghosh model are discussed in the appendix. A visualization of the QCMs computed in our phase expansion results and their spectra are shown in Fig. 3.7. Note that for each QCM considered, there are many eigenvalues that are zero to numerical precision, which are separated by many orders of magnitude from the non-zero eigenvalues. We note that for frustration-free models, such as the Kitaev chain and Majumdar-Ghosh model, we found eigenstate spaces that were much higher-dimensional than for the other models we considered.

3.4 Summary

We have developed the Eigenstate-to-Hamiltonian Construction (EHC) which is an efficient inverse method that can be used to produce spaces of physically meaningful parent Hamiltonians from a wave function. Analogous to variational wave function approaches to the forward problem, EHC is a variational Hamiltonian approach that finds parent Hamiltonians from a class of models. We anticipate that it will play a similarly important role in strongly-correlated physics.

The key to the EHC method is computing the quantum covariance matrix (QCM) (see Eq. (3.1)),

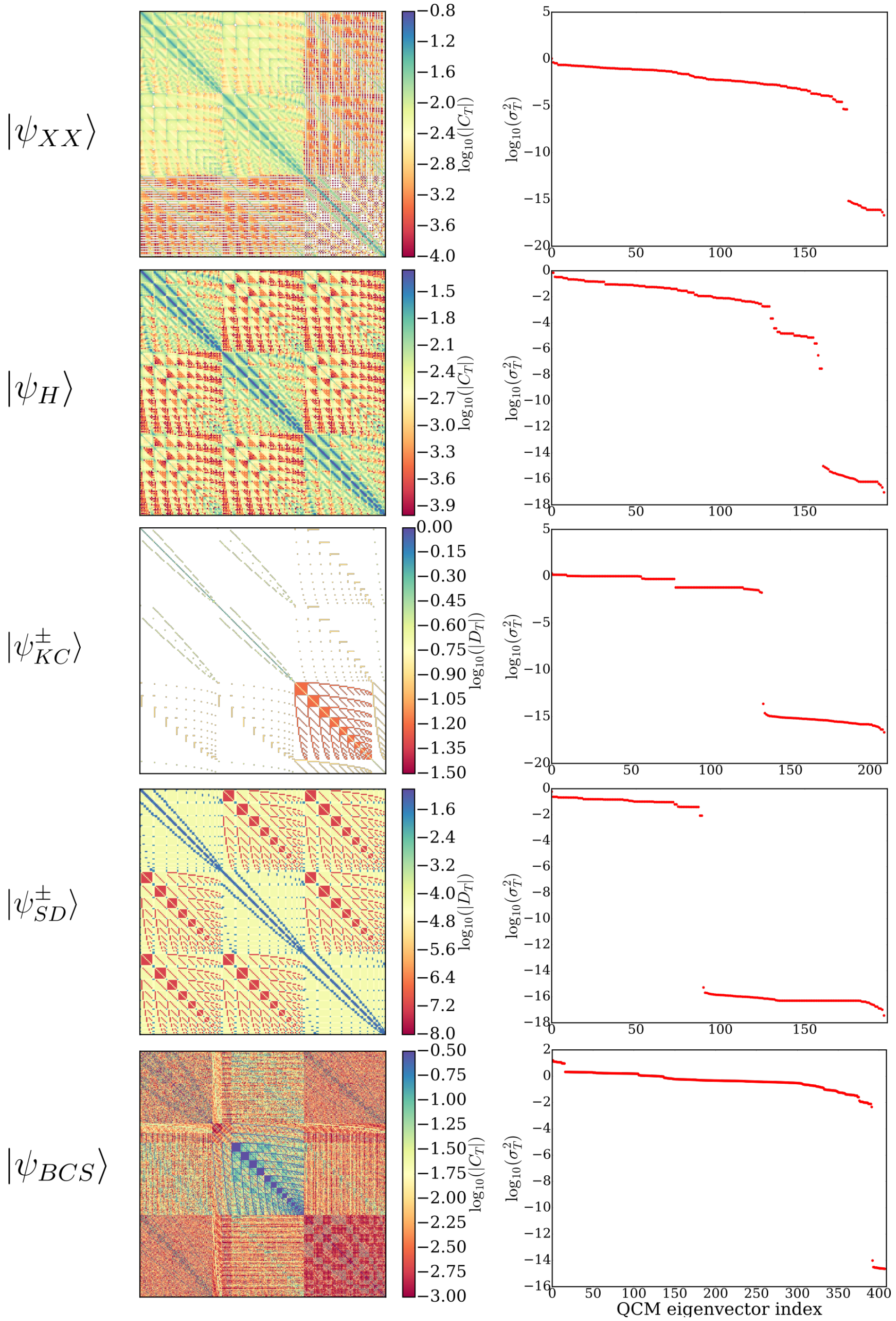

Figure 3.7: A summary of phase expansion results obtained in this work. In each row, we show the target state(s) provided as input to EHC (and DEHC), the QCMs C_T (and DQCMs D_T, see supplement) we calculated, and their spectra on a log scale. The eigenvectors of a QCM (or DQCM) are vectors of coupling constants that correspond to Hamiltonians with variance σ_T^2 under the target state $|\psi_T\rangle$. The QCM for $|\psi_{BCS}\rangle$ in the bottom row was statistically estimated using variational Monte Carlo, while the others were computed with matrix product states.

from which parent Hamiltonians can be found. Even though for the examples presented in this work we computed the QCM using VMC and DMRG, one can certainly compute the QCM using various other analytical, numerical, and experimental approaches. For example, one can compute the QCM in the context of sign-problem free Hamiltonians using quantum Monte Carlo.

We have described some sample applications of EHC in which we revealed some interesting and unforeseen structure of Hamiltonian space. We demonstrated how to find new types of Hamiltonians with EHC by automatically constructing parent Hamiltonians for a uniform superposition of frustrated Ising spin configurations. The discovered parent Hamiltonians are non-trivial quantum models that are adiabatically connected to the degenerate ground state manifold of the classical Ising antiferromagnet. This example clearly illustrates how the EHC method can quickly and with minimal theoretical ingenuity produce parent Hamiltonians that might otherwise take significant effort or insight to discover.

We also showed how the degenerate version of EHC, DEHC, can find regions of Hamiltonian space where many wave functions are degenerate, which allows one to automatically identify level-crossings or topological degeneracies between different states. We demonstrated this by finding the space where singlet dimer states and 3-coloring states "collide," resulting in a highly degenerate ground state manifold corresponding to a first-order quantum phase transition.

Finally we showed how to use EHC to expand the phase diagram of known model Hamiltonians, such as the XX chain, the Kitaev chain, the Heisenberg chain, and a 2D s-wave BdG model. In doing so, we showed that these specific models are actually special points in Hamiltonian space and that their ground states are shared with surrounding Hamiltonians in large, non-trivial regions in this space.

3.5 Conclusions

The EHC approach fits into a broader class of techniques, such as machine learning approaches, for automating physical understanding that previously required significant insight. Moreover, given the relation between the QCM and covariance matrices used in statistics, data science, and machine learning, one might expect methods developed in those contexts, such as principal component analysis, to be applicable to EHC and quantum systems.

The standard approach to condensed matter physics is to take a Hamiltonian and determine emergent properties represented by it ground state(s). Historically this has been difficult because of the exponential computational complexity in determining the exact ground state wave function. In this work, we invert this approach, demonstrating a new approach to condensed matter physics. Starting with wave functions with desired properties, we find Hamiltonians with these ground states in time quadratic in the dimension of the local Hamiltonian space explored by EHC. This new perspective asks us to consider more broadly the structure of the larger phase space of physically meaningful Hamiltonians.

EHC is a general tool that allows both theorists and experimentalist to construct Hamiltonians that have interesting physics or targeted properties in their ground states. Example uses might include targeting ground states in cold-atom systems as well as applications to spin liquids, fractional quantum Hall physics, unconventional superconductivity, many-body localization, frustrated magnetism, and continuum ab-initio approaches. EHC is a key step toward the long-term goal of material design of strongly correlated materials.

Chapter 4

From symmetries to Hamiltonians

This chapter is based on the work presented in Ref. [44], ©2021 American Physical Society, done in collaboration with Dr. Benjamin Villalonga Correa and my advisor Prof. Bryan Clark.

4.1 Introduction

Symmetry is central to our understanding of the phases of matter seen in nature. Many phase transitions, such as those of liquids, magnets, or superconductors, can be described by the spontaneous breaking of symmetry according to Landau's theory [199]. Moreover, the existence of space group and point group symmetries in crystalline phases of matter highly influences the formation of order in these systems. Even topological phases of matter, exotic quantum phases that are notable for their lack of order, have non-trivial topological symmetries that give rise to their exotic properties.

We propose a new approach for studying quantum phases of matter based on symmetries. Our new approach, the symmetric Hamiltonian construction (SHC), is an algorithm that takes as input symmetries and produces as output Hamiltonians that obey those symmetries. The SHC is an example of an inverse method, a method for generating models from data. Inverse methods are widely used throughout machine learning, such as in deep learning [6]. In physics, they have been used in classical systems to design interaction potentials that stabilize crystalline and magnetic order [20, 15, 16, 19] and in quantum systems to design or reconstruct Hamiltonians from eigenstates or density matrices [41–43, 37, 48] as well as to build single-body Hamiltonians compatible with a given symmetry group [200]. The SHC algorithm extends ideas developed in the slow operator method [45] and is quite general. The symmetries provided as input can be either integrals of motion, which can generate continuous symmetries, or discrete symmetry transformations. Example symmetries include particle number conservation, $SU(2)$ symmetry, and point group symmetries, as well as more exotic topological symmetries such as those that we consider in this work. The Hamiltonians produced as output can be interacting as well as non-interacting; and can be made to commute or anticommute with the input symmetry operators. Our numerical implementation of the SHC is publicly available as the QOSY:

Quantum Operators from Symmetry `Python` package [47].

In this work, we use the SHC to construct new Hamiltonians for two topological systems: superconductors with Majorana zero modes and Z_2 quantum spin liquids. We engineer superconducting Hamiltonians that commute with Majorana zero mode operators whose spatial distributions are specified as input. Separately, we construct multiple new interacting Z_2 quantum spin liquid Hamiltonians on different lattice geometries that commute with topologically non-trivial Wilson loop operators.

Majorana zero modes are integrals of motion that occur in certain superconductors that exhibit the statistics of Majorana fermions [70], an exotic class of fermions that are their own antiparticles [201]. In addition to their importance to fundamental physics, Majorana fermions, which are non-Abelian anyons, have potential applications as the building blocks for qubits in fault-tolerant quantum computers [59, 70]. Many experiments have attempted to observe Majorana fermions by engineering particular superconducting Hamiltonians, such as the Kitaev chain [202], that are theoretically known to host Majorana zero modes [203]. To expedite the experimental search for Majorana fermions, it is desirable to expand the small list of superconducting Hamiltonians known to possess Majorana zero modes. For this reason, we apply the SHC to design new examples of such Hamiltonians. We successfully construct a large family of local, highly tunable superconducting Hamiltonians that commute with Majorana zero modes that can be distributed arbitrarily in space. Many of these Hamiltonians have the potential to be realized in experiment.

Quantum spin liquids are exotic magnets in which spins do not order even at zero temperature due to quantum fluctuations [55]. Gapped quantum spin liquids are topologically ordered, meaning that they exhibit anyonic quasiparticles, ground state degeneracy that depends on the topology of the underlying lattice, and non-local symmetries. In particular, gapped Z_2 spin liquids host Abelian anyons and a particular set of symmetries known as Wilson loops, non-local loop operators with non-trivial topological properties. Despite significant study, there are few known model Hamiltonians that exhibit the physics of Z_2 quantum spin liquids. Some exactly solvable Hamiltonians, such as the toric code [73] and related models [155, 204, 205, 73, 206, 207], are often sums of commuting operators while other candidate Z_2 spin liquid Hamiltonians [208, 209] are difficult to solve numerically.

Using the SHC, we find new families of Z_2 spin liquid Hamiltonians for spins on the square and kagome lattices. The Hamiltonians that we discover are not sums of commuting operators, are not frustration-free, and can possess local and non-local integrals of motion. We find that these Hamiltonians, perturbed in an appropriate way, exhibit GOE level-spacing statistics in particular quantum number sectors, suggesting that they could be non-integrable. These models provide new, interesting examples of Z_2 topological order in spin systems.

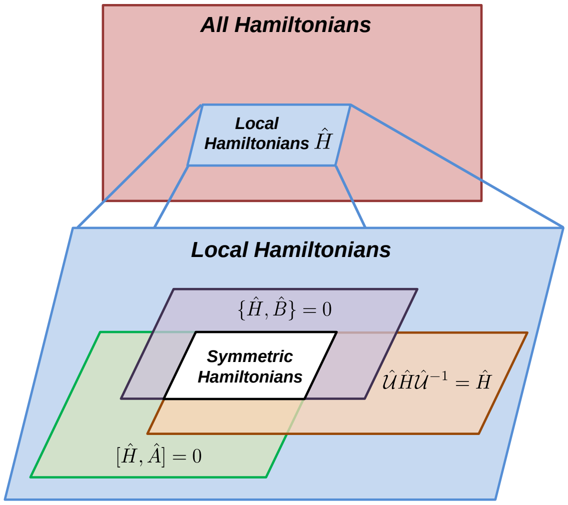

Figure 4.1: The set of all possible Hamiltonians is a large vector space (shown in red). We are interested in a small subspace of this space that consists of local Hamiltonians (shown in blue). Local Hamiltonians with particular symmetries, such as Hamiltonians that commute with the integral of motion $\hat{A}$ or anti-commute with the antisymmetry $\hat{B}$ or are invariant under the symmetry transformation $\hat{\mathcal{U}}$, are also vector spaces (shown in green, purple, and orange, respectively). The symmetric Hamiltonian construction takes as input a list of symmetries, such as $\hat{A}$, $\hat{B}$, and $\hat{\mathcal{U}}$, and produces as output the space of local symmetric Hamiltonians that obey all of these symmetries (shown in white).

The remainder of this chapter is organized as follows. Section 4.2 describes the SHC method. Section 4.3 details our construction of superconducting Hamiltonians that commute with Majorana zero modes. Section 4.4 describes the new Z_2 spin liquids that we found by searching for Hamiltonians that commute with Wilson loops. We conclude in Section 4.5.

4.2 The symmetric Hamiltonian construction method

In this section, we describe the symmetric Hamiltonian construction (SHC) procedure for generating Hamiltonians with desired symmetries (see Fig. 4.1), which includes integrals of motion (Sec. 4.2.1) and symmetry transformations (Sec. 4.2.2). In Sec. 4.2.3, we describe how these calculations can be interpreted as finding the "ground states" of super-operator "Hamiltonians."

Our numerical implementation of these methods is publicly available as the QOSY: Quantum Operators from Symmetry `Python` package [47], whose features are briefly discussed in Appendix B.6.

4.2.1 Constructing Hamiltonians with desired integrals of motion

Here we present our method for constructing Hamiltonians with a desired integral of motion, i.e., a Hermitian operator $\hat{\mathcal{O}}$ that commutes with the Hamiltonian $[\hat{H},\hat{\mathcal{O}}]=0$. This method takes in as input an integral of motion $\hat{\mathcal{O}}$ and produces as output Hamiltonians $\hat{H}$ that commute with $\hat{\mathcal{O}}$. Our *inverse* method for finding these symmetric Hamiltonians is based on the slow operator method [45], a forward method for finding integrals of motion from Hamiltonians.

In the inverse method, our goal is to find a Hamiltonian that minimizes the norm of the commutator

$$\varepsilon \equiv \|[\hat{H}, \hat{\mathcal{O}}]\|^2 \tag{4.1}$$

subject to the constraint that $\|\hat{H}\| = 1$ (which can always be achieved with a trivial normalization), where $\|\hat{\mathcal{O}}\|^2 \equiv \mathrm{tr}\left(\hat{\mathcal{O}}^\dagger \hat{\mathcal{O}}\right)/\mathrm{tr}\left(\hat{I}\right)$ is the Frobenius norm and $\hat{I}$ is the identity operator.

In the slow operator forward method, the goal is to find *integrals of motion* that minimize Eq. (4.1) for a given Hamiltonian. Numerically, this has been done using exact diagonalization [45, 46, 210, 211], matrix product operators [211, 212], and other tensor networks [98]. In these contexts, the Hamiltonians studied were non-integrable models and the minimal commutator norms ε discovered were often small, but not exactly zero, making the optimized operators approximate integrals of motion. Generically, we expect the inverse problem to be easier than the forward one. This is because integrals of motion can be highly non-local while physical Hamiltonians should be local. Since local operators make up a much smaller space of operators, it is much easier to search for local Hamiltonians than non-local integrals of motion. In Section 4.4, for particular $\hat{\mathcal{O}}$, we are able to efficiently find Hamiltonians for which $\varepsilon \approx 10^{-16}$ in finite-size systems.

Instead of representing the operators $\hat{H}$ and $\hat{\mathcal{O}}$ in Eq. (4.1) as matrices or tensor networks, we find it useful to expand *both* of these operators in a basis of *operator strings* $\hat{\mathcal{S}}_1, \ldots, \hat{\mathcal{S}}_d$ that span a d-dimensional space of Hermitian operators. In particular, we consider three different types of operator strings, Pauli strings, Fermion strings, and Majorana strings, to represent all possible spin-1/2 and fermionic operators.

For a system of n spin-1/2 qubits, we define a 4^n-dimensional basis of *Pauli strings*:

$$\hat{\mathcal{S}}_a = \hat{\sigma}_1^{t_1} \otimes \cdots \otimes \hat{\sigma}_n^{t_n} \tag{4.2}$$

where $a = 1, \ldots, 4^n$ is a unique index for the operator, $t_i \in \{0, 1, 2, 3\}$, $\hat{\sigma}^0 = \hat{I}$, and $\hat{\sigma}^1, \hat{\sigma}^2, \hat{\sigma}^3$ are Pauli matrices.

For a system of n fermions, we likewise define a 4^n-dimensional basis of *Fermion strings*, which come in three types:

$$\hat{\mathcal{S}}_a = \begin{cases} \hat{c}^\dagger_{i_1} \cdots \hat{c}^\dagger_{i_m} \hat{c}_{i_m} \cdots \hat{c}_{i_1}, \\ \hat{c}^\dagger_{i_1} \cdots \hat{c}^\dagger_{i_m} \hat{c}_{j_l} \cdots \hat{c}_{j_1} + \text{H.c.}, \\ i\hat{c}^\dagger_{i_1} \cdots \hat{c}^\dagger_{i_m} \hat{c}_{j_l} \cdots \hat{c}_{j_1} + \text{H.c.}, \end{cases} \tag{4.3}$$

where $\hat{c}^\dagger_j$ and $\hat{c}_j$ are fermionic creation and anhillation operators, $1 \leq i_1 < \ldots < i_m \leq n, 1 \leq j_1 < \ldots \leq j_l \leq n$, $0 \leq l \leq m \leq n$, and the indices are lexicographically ordered so that $(j_1, \ldots, j_l) < (i_1, \ldots, i_m)$.

Finally, for fermions, we also define a 4^n-dimensional basis of *Majorana strings*:

$$\hat{\mathcal{S}}_a = i^{\sigma_a} \hat{\tau}_1^{t_1} \cdots \hat{\tau}_n^{t_n} \tag{4.4}$$

where $t_i \in \{0, 1, 2, 3\}$, $(\hat{\tau}_i^0, \hat{\tau}_i^1, \hat{\tau}_i^2, \hat{\tau}_i^3) = (\hat{I}, \hat{a}_i, \hat{b}_i, \hat{d}_i)$, and $\sigma_a \in \{0, 1\}$ is chosen to make $\hat{\mathcal{S}}_a$ Hermitian. The operators $\hat{a}_i \equiv \hat{c}_i + \hat{c}^\dagger_i, \hat{b}_i \equiv -i(\hat{c}_i - \hat{c}^\dagger_i)$ are Majorana fermions and $\hat{d}_i \equiv -i\hat{a}_i\hat{b}_i = \hat{I} - 2\hat{c}^\dagger_i\hat{c}_i$ is a fermion parity operator. A discussion of the properties of these three operator string bases is provided in Appendices B.2, B.3, and B.4.

We perform our SHC calculations directly in a basis of operator strings. The Hamiltonian (unknown) and integral of motion (known) can be written in terms of operator strings as $\hat{H} = \sum_a J_a \hat{\mathcal{S}}_a$ and $\hat{\mathcal{O}} = \sum_b g_b \hat{\mathcal{S}}_b$, respectively, where J_a (unknown) and g_b (known) are real coupling constants. Our goal is to find J_a such that the commutator norm is zero: $\varepsilon = 0$. The commutator between two operator strings can be expanded in terms of other operator strings

$$[\hat{\mathcal{S}}_a, \hat{\mathcal{S}}_b] = \sum_c f^c_{ab} \hat{\mathcal{S}}_c \tag{4.5}$$

where $f^c_{ab} = -f^c_{ba}$ are (basis-dependent) structure constants. Importantly, for bases of Pauli strings and Majorana strings, the structure constants f^c_{ab} are highly sparse and easy to compute algebraically without representing the operator strings as matrices or tensor networks (see Appendices B.2 and B.4 for details). Computing the structure constants for Fermion strings, however, is not efficient, so we instead perform computations in the Majorana string basis and convert back and forth to the Fermion string basis as needed.

Using the structure constants, we define the Liouvillian matrix $(L_{\hat{\mathcal{O}}})_{ca} \equiv \sum_b g_b f^c_{ab}$, which describes how operator strings commute with the known integral of motion: $[\hat{\mathcal{S}}_a, \hat{\mathcal{O}}] = \sum_c (L_{\hat{\mathcal{O}}})_{ca} \hat{\mathcal{S}}_c$.

Finally, using the Liouvillian matrix, we can define the *commutant matrix* $C_{\hat{\mathcal{O}}}$ [46], the central quantity that we will work with in the inverse method [1]:

$$C_{\hat{\mathcal{O}}} \equiv L^{\dagger}_{\hat{\mathcal{O}}} L_{\hat{\mathcal{O}}}. \tag{4.6}$$

The commutator norm can then be written as a quadratic form involving the commutant matrix

$$\varepsilon = J^T C_{\hat{\mathcal{O}}} J \tag{4.7}$$

where J is the vector of coupling constants of the Hamiltonian. The commutant matrix $C_{\hat{\mathcal{O}}}$ is Hermitian and positive semi-definite, making its eigenvalues real and non-negative.

A normalized eigenvector J of $C_{\hat{\mathcal{O}}}$ with eigenvalue ε corresponds to a Hamiltonian $\hat{H} = \sum_a J_a \hat{\mathcal{S}}_a$ whose commutator norm with $\hat{\mathcal{O}}$ is $\left\| [\hat{H}, \hat{\mathcal{O}}] \right\|^2 = \varepsilon$. This indicates that the operators $\hat{H}$ and $\hat{\mathcal{O}}$ exactly commute when J is a null vector, i.e., an eigenvector with zero eigenvalue ($\varepsilon = 0$), of the commutant matrix. Therefore, a null vector J corresponds to a Hamiltonian $\hat{H}$ with $\hat{\mathcal{O}}$ as an integral of motion. Moreover, since any linear combination of null vectors is also a null vector, we see that the null space of $C_{\hat{\mathcal{O}}}$ corresponds to an entire vector space of Hamiltonians with the desired integral of motion $\hat{\mathcal{O}}$.

We now can see that the inverse method for finding Hamiltonians with a desired integral of motion amounts to finding the null space, or zero modes, of the commutant matrix. As we will discuss in Sec. 4.2.3, computing the null space of the commutant matrix can be done in a number of ways. The simplest way to do this is to explicitly construct the commutant matrix and diagonalize it numerically for a finite-dimensional basis of operator strings. This is feasible when searching for Hamiltonians since they can be represented as local operators, which can be spanned by relatively low-dimensional spaces of local operator strings.

For a fixed d-dimensional space of operators, it is interesting to consider the possible dimensionality of the commutant matrix's null space. If the null space of $C_{\hat{\mathcal{O}}}$ is one-dimensional, then there is a unique Hamiltonian $\hat{H}$ in the chosen space that commutes with $\hat{\mathcal{O}}$. If the null space dimension is greater than one, then there are many Hamiltonians $\hat{H}_1, \hat{H}_2, \ldots$ in that space that, in any linear combination, commute with $\hat{\mathcal{O}}$. If the null space dimension is zero, then there is no Hamiltonian that exactly commutes with $\hat{\mathcal{O}}$ in the chosen space. Nonetheless, since the eigenvalues of $C_{\hat{\mathcal{O}}}$ correspond to commutator norms, the smallest eigenvalue eigenvector of $C_{\hat{\mathcal{O}}}$ corresponds to the Hamiltonian in the space that is "closest" to commuting with $\hat{\mathcal{O}}$ [2].

We also generalize this inverse method to construct Hamiltonians with desired *antisymmetries*, i.e.,

---

[1] As discussed in the Appendix, this is the form of the commutant matrix for an orthonormal basis of operator strings, such as the Pauli string or Majorana string bases.

[2] This is related to the original motivation to name the forward method the *slow operator method*, since energy eigenstates exhibit *slowly* varying expectation values over these quasi-integrals of motion.

Hamiltonians $\hat{H}$ that *anti-commute* with a desired operator $\hat{\mathcal{O}}$. To find Hamiltonians that anti-commute with $\hat{\mathcal{O}}$, we look for Hamiltonians that minimize the anti-commutator norm

$$\bar{\varepsilon} = ||\{\hat{H}, \hat{\mathcal{O}}\}||^2 = J^T \bar{C}_{\hat{\mathcal{O}}} J \tag{4.8}$$

where $\bar{C}_{\hat{\mathcal{O}}} = \bar{L}^{\dagger}_{\hat{\mathcal{O}}} \bar{L}_{\hat{\mathcal{O}}}$ is the *anti-commutant matrix*, $(\bar{L}_{\hat{\mathcal{O}}})_{ca} \equiv \sum_b g_b \bar{f}^c_{ab}$, and $\{\hat{\mathcal{S}}_a, \hat{\mathcal{S}}_b\} \equiv \sum_c \bar{f}^c_{ab} \hat{\mathcal{S}}_c$. Similar to the method described above, finding Hamiltonians that anti-commute with $\hat{\mathcal{O}}$ amounts to finding the null space of the anti-commutant matrix $\bar{C}_{\hat{\mathcal{O}}}$.

Finally, we note that the inverse method described in this section is directly related to the recently developed eigenstate-to-Hamiltonian construction (EHC) algorithm [41–43] for constructing Hamiltonians from eigenstates. In fact, as pointed out in Ref. [42], if the integral of motion corresponds to a pure state density matrix, $\hat{\mathcal{O}} = |\psi\rangle \langle\psi|$, then the commutant matrix of Eq. (4.6) is proportional to the quantum covariance matrix $\langle\psi| \hat{\mathcal{S}}_a \hat{\mathcal{S}}_b |\psi\rangle - \langle\psi| \hat{\mathcal{S}}_a |\psi\rangle \langle\psi| \hat{\mathcal{S}}_b |\psi\rangle$, which is the central quantity computed in the EHC algorithm. Moreover, if the integral of motion is a mixed state density matrix, then the SHC method is closely related to the method described in Ref. [37] for learning Hamiltonians from local measurements.

4.2.2 Constructing Hamiltonians that are invariant under desired symmetry transformations

Next, we detail how to construct Hamiltonians that are invariant under desired discrete symmetry transformations, i.e., unitary operators $\hat{\mathcal{U}}_g$ associated with a finite group $g \in G$ that leave the Hamiltonian invariant $\hat{\mathcal{U}}_g \hat{H} \hat{\mathcal{U}}_g^{-1} = \hat{H}$. Since $[\hat{H}, \hat{\mathcal{U}}_g] = 0$, in principle the method from Sec. 4.2.1 could be applied. However, generically, $\hat{\mathcal{U}}_g$ will be a sum of many operator strings, making such calculations intractable in the basis of operator strings. Instead, in this section, we describe two alternative efficient approaches that take as input a finite symmetry group G made of symmetry transformations, such as space group, time-reversal, and charge-conjugation symmetries, and produce as output Hamiltonians invariant under the action of these transformations.

In the first approach, we directly symmetrize our basis of operator strings to produce a new basis of symmetric operators [200]

$$\hat{\mathcal{S}}'_a \equiv \sum_{g \in G} g \cdot \hat{\mathcal{S}}_a \tag{4.9}$$

where $g \cdot \hat{\mathcal{S}}_a$ is the group action of the element g on the operator string $\hat{\mathcal{S}}_a$, which maps that operator string to a linear combination of other operator strings. This is similar to a symmetrization procedure performed by Ref. [200]. For finite groups of order $|G|$ and bases of operator strings of dimension d, we can enumerate over all operator strings and perform this calculation in time $d|G|$. When performing such calculations, one needs to take care to ignore non-symmetrizable operator strings [3] and not include linearly dependent symmetrized operators. In this new symmetrized basis, any linear combination $\hat{H} = \sum_a J_a \hat{\mathcal{S}}'_a$ of the symmetrized operators is a Hamiltonian that is invariant under the transformations in the symmetry group G.

In the second approach, we analyze the spectrum of the representations of the generators of the symmetry group G in the space of operator strings. In particular, consider an element $g \in G$ that can be represented by a unitary (or anti-unitary) operator $\hat{\mathcal{U}}_g$ acting on the usual Hilbert space of states. The action of the symmetry transformation g on an operator string is given by conjugation with $\hat{\mathcal{U}}_g$ and can be expanded in terms of other operator strings:

$$g \cdot \hat{\mathcal{S}}_a \equiv \hat{\mathcal{U}}_g \hat{\mathcal{S}}_a \hat{\mathcal{U}}_g^{-1} = \sum_b (D_g)_{ba} \hat{\mathcal{S}}_b. \tag{4.10}$$

The matrix D_g is the representation of the symmetry transformation g on the space of operator strings and for common symmetry operators, such as space group symmetries, particle-hole symmetry, and time-reversal symmetry, can be straight-forwardly computed as we discuss in Appendix B.5. From Eq. (4.10), we see that a Hamiltonian $\hat{H} = \sum_a J_a \hat{\mathcal{S}}_a$ transforms under the symmetry as [4]

$$g \cdot \hat{H} = \hat{\mathcal{U}}_g \hat{H} \hat{\mathcal{U}}_g^{-1} = \sum_a J_a \hat{\mathcal{U}}_g \hat{\mathcal{S}}_a \hat{\mathcal{U}}_g^{-1} = \sum_{a,b} (D_g)_{ba} J_a \hat{\mathcal{S}}_b. \tag{4.11}$$

From Eq. (4.11), we see that $g \cdot \hat{H} = \pm \hat{H}$ when J is an eigenvector of D_g with eigenvalue ± 1. The $(+1)$-eigenvalue eigenvectors correspond to the coupling constants of Hamiltonians with g as a symmetry so that $[\hat{H}, \hat{\mathcal{U}}_g] = 0$. Likewise, the (-1)-eigenvalue eigenvectors correspond to Hamiltonians with g as an *antisymmetry* so that $\{\hat{H}, \hat{\mathcal{U}}_g\} = 0$. Therefore, we see that we can find Hamiltonians that are invariant under a desired symmetry transformation g by finding the $(+1)$-eigenvectors of the representation D_g, and likewise for antisymmetries the (-1)-eigenvectors of D_g. To find Hamiltonians that are invariant under all of the symmetry transformations in the symmetry group G, one can compute the intersection of the $(+1)$-eigenspaces of the representations of the group's generators.

---

[3] Consider the Majorana string $\hat{\mathcal{S}}_1 \equiv i\hat{a}_1\hat{a}_2$ and the symmetry group of permutations $G = \{(12), (21)\}$. Upon symmetrization, this string is $\hat{\mathcal{S}}'_1 \equiv (12) \cdot i\hat{a}_1\hat{a}_2 + (21) \cdot i\hat{a}_1\hat{a}_2 = i\hat{a}_1\hat{a}_2 + i\hat{a}_2\hat{a}_1 = i\hat{a}_1\hat{a}_2 - i\hat{a}_1\hat{a}_2 = 0$, making it unsymmetrizable.

[4] Antiunitary operators, such as time-reversal, are antilinear transformations. Since we require $\hat{H}$ to be Hermitian, the J_a are real and are unaffected by the antilinearity of $\hat{\mathcal{U}}_g$.

4.2.3 Constructing Hamiltonians with desired symmetries by finding the ground states of superoperators

In the methods described above in Secs. 4.2.1 and 4.2.2, we perform calculations in a Hilbert space of Hermitian operators. The commutant matrix $C_{\hat{\mathcal{O}}}$ and representation D_g can be interpreted as *superoperators* acting on operators in this space. From this perspective, we can frame the inverse problem of constructing Hamiltonians with a set of desired symmetries and antisymmetries as finding the ground state of a particular Hermitian, positive semi-definite "superoperator Hamiltonian."

In particular, if we desire to construct Hamiltonians that commute with integrals of motion $\hat{\mathcal{O}}_1, \dots, \hat{\mathcal{O}}_{N_1}$, anti-commute with $\hat{\mathcal{O}}'_1, \dots, \hat{\mathcal{O}}'_{N_2}$, are invariant under symmetry transformations $g_1, \dots, g_{M_1}$ and anti-invariant under $g'_1, \dots, g'_{M_2}$, then we can do so by finding the "ground states" of the superoperator Hamiltonian

$$\begin{aligned}\mathcal{H} \equiv \sum_{i=1}^{N_1} C_{\hat{\mathcal{O}}_i} + \sum_{j=1}^{N_2} \bar{C}_{\hat{\mathcal{O}}'_j} + \sum_{k=1}^{M_1} \left[I - \frac{1}{2}(D_{g_k} + D^\dagger_{g_k}) \right] \\ + \sum_{l=1}^{M_2} \left[I + \frac{1}{2}(D_{g'_l} + D^\dagger_{g'_l}) \right] \end{aligned} \tag{4.12}$$

which is Hermitian and positive semi-definite by construction, where I is the identity superoperator. If we find ground states of $\mathcal{H}$ that have zero "energy," then we have found Hamiltonians that obey all of the desired symmetries at once. If the ground state energy is non-zero, then the energy indicates how much the discovered Hamiltonian fails to commute (or anti-commute) with the given symmetries.

The simplest way to find the ground states of the superoperator Hamiltonian $\mathcal{H}$ is to write it as a matrix in a basis of operators and perform exact diagonalization on the matrix, e.g., using the Lanczos algorithm. Consider performing such a calculation in the Pauli string basis. Rather than working in the full 4^n-dimensional space of operators for a system of n spins, it is convenient to consider a much smaller basis of range-R k-local Pauli strings. Range-R k-local Pauli strings are Pauli strings made from a product of k (non-Identity) Pauli matrices on sites separated spatially by at most the maximum distance R. For example, the space of range-2 3-local Pauli strings on a 1D chain includes all possible spin Hamiltonians with three-site interactions between nearest and next nearest neighbor sites. In Sections 4.3 and 4.4, we obtain our results by exactly diagonalizing $\mathcal{H}$ in range-R k-local bases of Majorana strings and Pauli strings.

Finally, we note that many other well-developed methods can be used to find the ground states of $\mathcal{H}$. For example, one can represent the superoperator $\mathcal{H}$ as a matrix product operator [213, 212] and perform DMRG to find its ground state(s) or use methods such as variational Monte Carlo or other forms of quantum Monte Carlo to do so. In attempting this, one should keep in mind that, even though the notion of locality might be kept in $\mathcal{H}$, there is no known guarantee for its gapped/gapless nature, which might hinder the applicability of these methods.

4.3 Hamiltonians with zero modes

In this section, we use the SHC to analytically design non-interacting and interacting Hamiltonians that commute with a desired pair of zero modes that can be distributed arbitrarily in space. First, we present some theoretical background on zero modes and Majorana zero modes (MZMs). Then, we describe our general framework for constructing these Hamiltonians out of "bond operator" building blocks, which are two-site operators that involve fermionic hopping, pairing, and chemical potentials. Finally, we provide examples of how this procedure can produce various Hamiltonians that commute with zero modes. We start by finding p-wave superconducting Hamiltonians that exactly commute with either exponentially-decaying MZMs, Gaussian-distributed MZMs, or zero modes with complicated spatial distributions. Then we give examples of s-wave superconducting Hamiltonians and interacting Hamiltonians that commute with MZMs.

Background. A zero mode $\hat{\gamma}$ is a Hermitian operator that [214–216]:

1. commutes with the Hamiltonian: $[\hat{\gamma}, \hat{H}] = 0$
2. squares to identity: $\hat{\gamma}^2 = \hat{I}$
3. anticommutes with fermion parity: $\{\hat{\gamma}, (-1)^{\hat{N}}\} = 0$

where $\hat{H}$ is a Hamiltonian that conserves fermion parity $[\hat{H}, (-1)^{\hat{N}}] = 0$, where $(-1)^{\hat{N}} \equiv \prod_j (\hat{I} - 2\hat{n}_j)$. Property 1 indicates that a zero mode is a symmetry of the system; property 2 indicates that its eigenvalues are ± 1; and property 3 indicates that each state $|\psi_+\rangle$ with definite fermion parity $\eta = \pm 1$ comes paired with an orthogonal state $|\psi_-\rangle \equiv \hat{\gamma}|\psi_+\rangle$ with opposite parity $-\eta$. For fermion-parity-conserving Hamiltonians, the opposite parity states $|\psi_+\rangle$ and $|\psi_-\rangle$ are degenerate energy eigenstates.

Generically, zero modes come in pairs. For M pairs of zero modes, the operators $\hat{\gamma}^{(1)}, \ldots, \hat{\gamma}^{(2M)}$ all commute with the Hamiltonian and satisfy the anticommutation relations

$$\{\hat{\gamma}^{(m)}, \hat{\gamma}^{(n)}\} = 2\delta_{mn}. \tag{4.13}$$

These $2M$ zero modes lead to a 2^M-fold degeneracy in each of the eigenstates of the Hamiltonian. By pairing zero modes into complex fermions $\hat{f}_m \equiv (\hat{\gamma}^{(2m-1)} + i\hat{\gamma}^{(2m)})/2$ for $m = 1, \ldots, M$, we can see that the number operators $\hat{f}_m^\dagger \hat{f}_m$ commute with the Hamiltonian and each other. Therefore, these operators are simultaneously diagonalizable and the Hamiltonian eigenstates can be labeled by the occupation numbers

$0, 1$ for each of the M number operators [59]. From properties 1-3, we can deduce that these 2^M many-body states are degenerate in energy and that the $\hat{f}_m^\dagger$ operators create single-quasiparticle modes of zero energy. Finally, we mention that *Majorana* zero modes (MZMs) are zero modes that are spatially localized and well-separated from one another [70]. These properties allow such zero modes to exhibit the non-Abelian statistics of Ising anyons [59].

In this work, we will consider zero modes of the form

$$\begin{aligned}\hat{\gamma}^{(1)} &= \sum_j \alpha_j^{(1)} \hat{a}_j + \beta_j^{(1)} \hat{b}_j, \\ \hat{\gamma}^{(2)} &= \sum_j \alpha_j^{(2)} \hat{a}_j + \beta_j^{(2)} \hat{b}_j, \end{aligned} \tag{4.14}$$

where $\alpha_j^{(1)}, \beta_j^{(1)}$ and $\alpha_j^{(2)}, \beta_j^{(2)}$ are real parameters that specify the "amplitudes" of the zero modes on site j (or, more generically, orbital j). To ensure that $\hat{\gamma}^{(1)}$ and $\hat{\gamma}^{(2)}$ are zero modes with the properties mentioned above, the parameters are constrained such that $(\hat{\gamma}^{(1)})^2 = (\hat{\gamma}^{(2)})^2 = \hat{I}$ and $\{\hat{\gamma}^{(1)}, \hat{\gamma}^{(2)}\} = 0$. This implies that the zero modes are orthonormal,

$$\begin{aligned}||\hat{\gamma}^{(1)}||^2 &= \sum_j (\alpha_j^{(1)})^2 + (\beta_j^{(1)})^2 = 1, \\ ||\hat{\gamma}^{(2)}||^2 &= \sum_j (\alpha_j^{(2)})^2 + (\beta_j^{(2)})^2 = 1, \\ \langle \hat{\gamma}^{(1)}, \hat{\gamma}^{(2)} \rangle &= \sum_j \alpha_j^{(1)} \alpha_j^{(2)} + \beta_j^{(1)} \beta_j^{(2)} = 0. \end{aligned} \tag{4.15}$$

Framework for designing zero mode Hamiltonians. We present a novel framework, illustrated in Fig. 4.2, for designing Hamiltonians that commute with a desired pair of zero modes $\hat{\gamma}^{(1)}$ and $\hat{\gamma}^{(2)}$ that can be distributed arbitrarily in space. Here we focus on the case of two zero modes, though it is straightforward to generalize to an arbitrary number. Given a spatial distribution of the two zero modes specified by the values of $\alpha_j^{(1)}, \beta_j^{(1)}$ and $\alpha_j^{(2)}, \beta_j^{(2)}$ in Eq. (4.14), we output a family of Hamiltonians

$$\hat{H}_{ZM} = \sum_{ij} J_{ij} \hat{h}_{ij}, \tag{4.16}$$

that commute with the two zero modes and are built from Hermitian bond operators

$$\begin{aligned}\hat{h}_{ij} = &\Big[(\tilde{t}^R_{ij} + i\tilde{t}^I_{ij})\hat{c}^\dagger_i \hat{c}_j + (\tilde{\Delta}^R_{ij} + i\tilde{\Delta}^I_{ij})\hat{c}^\dagger_i \hat{c}^\dagger_j + \text{H.c.}\Big] \\ &+ \tilde{\mu}^{(ij)}_i \hat{n}_i + \tilde{\mu}^{(ij)}_j \hat{n}_j,\end{aligned} \tag{4.17}$$

which act only on sites i and j. The J_{ij} are real parameters that independently scale each bond operator and are arbitrary up to the constraint that they must be non-zero on a connected graph of bonds $\{(i, j)\}$. This constraint guarantees that the Hamiltonians *do not commute with any other zero modes that are linear combinations of the Majorana fermions* $\hat{a}_j$ *and* $\hat{b}_j$ *other than* $\hat{\gamma}^{(1)}$ *and* $\hat{\gamma}^{(2)}$ [5]. The family of Hamiltonians in Eq. (4.16) includes Hamiltonians on various lattices and graphs such as square lattices, kagome lattices, tetrahedral lattices, trees, and aperiodic tilings.

We were able to determine the analytic form of the bond operators $\hat{h}_{ij}$ and their properties by computing the commutant matrices $C_{\hat{\gamma}^{(1)}}, C_{\hat{\gamma}^{(2)}}$, and $C_{\hat{h}_{ij}}$, as described in Appendix B.7. The parameters of the bond operators $\hat{h}_{ij}$ depend on the zero mode amplitudes $\alpha^{(1)}_j, \beta^{(1)}_j$ and $\alpha^{(2)}_j, \beta^{(2)}_j$ on orbitals i and j and take the form

$$\begin{aligned}\tilde{t}^R_{ij} &\equiv -\alpha^{(1)}_i \beta^{(2)}_j + \beta^{(1)}_i \alpha^{(2)}_j - \alpha^{(1)}_j \beta^{(2)}_i + \beta^{(1)}_j \alpha^{(2)}_i, \\ \tilde{t}^I_{ij} &\equiv -\alpha^{(1)}_i \alpha^{(2)}_j - \beta^{(1)}_i \beta^{(2)}_j + \alpha^{(1)}_j \alpha^{(2)}_i + \beta^{(1)}_j \beta^{(2)}_i, \\ \tilde{\Delta}^R_{ij} &\equiv -\alpha^{(1)}_i \beta^{(2)}_j - \beta^{(1)}_i \alpha^{(2)}_j + \alpha^{(1)}_j \beta^{(2)}_i + \beta^{(1)}_j \alpha^{(2)}_i, \\ \tilde{\Delta}^I_{ij} &\equiv +\alpha^{(1)}_i \alpha^{(2)}_j - \beta^{(1)}_i \beta^{(2)}_j - \alpha^{(1)}_j \alpha^{(2)}_i + \beta^{(1)}_j \beta^{(2)}_i, \\ \tilde{\mu}^{(ij)}_i &\equiv 2(\alpha^{(1)}_j \beta^{(2)}_j - \beta^{(1)}_j \alpha^{(2)}_j), \\ \tilde{\mu}^{(ij)}_j &\equiv 2(\alpha^{(1)}_i \beta^{(2)}_i - \beta^{(1)}_i \alpha^{(2)}_i).\end{aligned} \tag{4.18}$$

For the chemical potential parameters $\tilde{\mu}^{(ij)}_i$ and $\tilde{\mu}^{(ij)}_j$, we add an (ij) superscript to make clear that these chemical potentials on sites i and j are associated with the bond operator $\hat{h}_{ij}$ and not another bond operator, such as $\hat{h}_{ik}$ or $\hat{h}_{kj}$. Also, importantly, we choose an ordering convention for our fermionic operators and require that $i < j$ for each bond operator $\hat{h}_{ij}$ to be consistent with our convention.

Each bond operator $\hat{h}_{ij}$ individually commutes with $\hat{\gamma}^{(1)}$ and $\hat{\gamma}^{(2)}$, though overlapping bond operators do not commute with one another: $[\hat{h}_{ij}, \hat{h}_{jk}] \neq 0$. This makes the $\hat{H}_{ZM}$ Hamiltonians analogous to frustration-

---

[5] There is an additional subtlety, discussed in Appendix B.7, that arises when $(\alpha^{(1)}_i, \beta^{(1)}_i, \alpha^{(1)}_j, \beta^{(1)}_j) \propto (\alpha^{(2)}_i, \beta^{(2)}_i, \alpha^{(2)}_j, \beta^{(2)}_j)$. In this case, the $\hat{h}_{ij}$ bond operator does not uniquely isolate the $\hat{\gamma}^{(1)}, \hat{\gamma}^{(2)}$ zero modes as the only zero modes that commute with $\hat{H}_{ZM}$. Such bond operators can be added to the Hamiltonian $\hat{H}_{ZM}$, but they do not count towards the connected graph constraint.

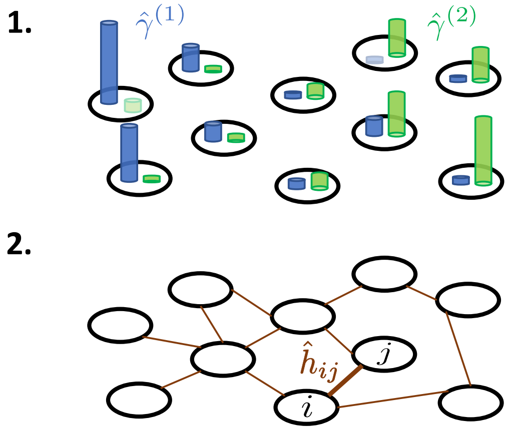

Figure 4.2: Steps for constructing zero mode Hamiltonians on an arbitrary graph. **1.** Specify the spatial distributions of the zero modes $\hat{\gamma}^{(1)}$ and $\hat{\gamma}^{(2)}$ by choosing their amplitudes $\alpha_j^{(1)}, \beta_j^{(1)}$ and $\alpha_j^{(2)}, \beta_j^{(2)}$, respectively, on the vertices j of the graph. **2.** Draw a set of edges between the vertices until the vertices and edges form a connected graph. The resulting graph represents a family of Hamiltonians of the form $\hat{H}_{ZM} = \sum_{ij} J_{ij}\hat{h}_{ij}$, where $J_{ij} \neq 0$ on the (i, j) edges and $\hat{h}_{ij}$ are bond operators specified by Eq. (4.17). These Hamiltonians exactly commute with $\hat{\gamma}^{(1)}$ and $\hat{\gamma}^{(2)}$ and no other zero modes of the form of Eq. (4.14).

free Hamiltonians, which by definition have ground states that are simultaneously the ground states of each local term in the Hamiltonian [217, 218].

We can rewrite Eq. (4.16) as

$$\hat{H}_{ZM} = \sum_{ij} \left[(t_{ij}^R + it_{ij}^I)\hat{c}_i^\dagger \hat{c}_j + (\Delta_{ij}^R + i\Delta_{ij}^I)\hat{c}_i^\dagger \hat{c}_j^\dagger + \text{H.c.} \right] \\ + \sum_j \mu_j \hat{n}_j \tag{4.19}$$

whose parameters take on the values

$$t_{ij}^R = J_{ij}\tilde{t}_{ij}^R, \quad t_{ij}^I = J_{ij}\tilde{t}_{ij}^I, \quad \Delta_{ij}^R = J_{ij}\tilde{\Delta}_{ij}^R, \quad \Delta_{ij}^I = J_{ij}\tilde{\Delta}_{ij}^I, \tag{4.20}$$

and

$$\mu_j = \sum_{i<j} J_{ij}\tilde{\mu}_j^{(ij)} + \sum_{i>j} J_{ji}\tilde{\mu}_j^{(ji)}. \tag{4.21}$$

The chemical potential on a site j is the sum of the chemical potentials contributed by each bond operator. The need for two sums is due to our choice of convention that $i < j$ for each bond operator $\hat{h}_{ij}$.

To simplify the remaining discussion in our examples, we consider the restricted class of zero modes with

$\beta_j^{(1)} = \alpha_j^{(2)} = 0$ for all j:

$$\hat{\gamma}^{(1)} = \sum_j \alpha_j \hat{a}_j, \qquad \hat{\gamma}^{(2)} = \sum_j \beta_j \hat{b}_j, \tag{4.22}$$

where we relabeled $\alpha_j^{(1)} \to \alpha_j$ and $\beta_j^{(2)} \to \beta_j$. One reason to consider this class of zero modes is that it contains the zero modes of the Kitaev chain [202]. Another reason is that, upon normalization, these zero modes automatically satisfy Eq. (4.15).

For the zero modes of Eq. (4.22), the bond operator can be simplified to

$$\begin{aligned}\hat{h}_{ij} \equiv \tilde{t}_{ij} \left(\hat{c}_i^\dagger \hat{c}_j + \text{H.c.} \right) + \tilde{\Delta}_{ij} \left(\hat{c}_i^\dagger \hat{c}_j^\dagger + \text{H.c.} \right) \\ + \tilde{\mu}_i^{(ij)} \hat{n}_i + \tilde{\mu}_j^{(ij)} \hat{n}_j \end{aligned} \tag{4.23}$$

where

$$\begin{aligned} \tilde{t}_{ij} &\equiv 1 + \frac{\alpha_j/\alpha_i}{\beta_j/\beta_i}, \quad \tilde{\Delta}_{ij} \equiv 1 - \frac{\alpha_j/\alpha_i}{\beta_j/\beta_i} \\ \tilde{\mu}_i^{(ij)} &\equiv -2\alpha_j/\alpha_i, \quad \tilde{\mu}_j^{(ij)} \equiv -2\beta_i/\beta_j. \end{aligned} \tag{4.24}$$

Example: Exponentially decaying Majorana zero modes. As a first example, we discuss how to use our framework to construct p-wave 1D chain Hamiltonians with exponentially decaying Majorana zero modes. We will see that the models we construct this way are closely related to the Kitaev chain, which has nearly exponentially decaying MZMs [202].

As input, we choose two MZMs exponentially localized at each edge of a 1D chain of L spinless fermions:

$$\hat{\gamma}^{(1)} \propto \sum_{j=1}^{L} e^{-j/\xi} \hat{a}_j, \quad \hat{\gamma}^{(2)} \propto \sum_{j=1}^{L} e^{-(L-j)/\xi} \hat{b}_j, \tag{4.25}$$

where $\xi > 0$ is a correlation length in units of the lattice spacing.

For a bond between the sites i and j separated by a distance $d = |i-j|$, the parameters of the bond operator Eq. (4.24) become

$$\tilde{t}_{ij} = 1 + e^{-2d/\xi},\ \tilde{\Delta}_{ij} = 1 - e^{-2d/\xi},\ \tilde{\mu}_i^{(ij)} = \tilde{\mu}_j^{(ij)} = -2e^{-d/\xi}.$$

The bond operators with these specific parameters define a large family of Hamiltonians $\hat{H}_{ZM} = \sum_{ij} J_{ij} \hat{h}_{ij}$ that exactly commute with the zero modes of Eq. (4.25).

First, we will focus on a simple, interesting subspace of these zero mode Hamiltonians. In particular, we consider those Hamiltonians constrained to have constant nearest neighbor ($d = 1$) hopping $-t$ on a 1D chain. We implement this constraint by choosing $J_{ij} = -t\delta_{i,j-1}/\tilde{t}_{ij}$ for each bond (i,j). Given this constraint and our input zero modes, we find a unique Hamiltonian that commutes with the desired zero modes

$$\begin{aligned}\hat{H}^{(1)}_{\text{exp}} &= \sum_{ij} J_{ij}\hat{h}_{ij} = \sum_{j=1}^{L-1} -(t/\tilde{t}_{j,j+1})\hat{h}_{j,j+1} \\ &= \sum_{j=1}^{L-1}(-t\hat{c}^\dagger_j\hat{c}_{j+1} - \Delta^{(1)}\hat{c}^\dagger_j\hat{c}^\dagger_{j+1} + \text{H.c.}) - \sum_{j=1}^{L}\mu^{(1)}_j\hat{n}_j,\end{aligned} \tag{4.26}$$

where

$$\begin{aligned}\Delta^{(1)}/t &\equiv \tanh(1/\xi), \\ \mu^{(1)}_j/t &\equiv \begin{cases} -1/\cosh(1/\xi) & j = 1, L \\ -2/\cosh(1/\xi) & \text{otherwise.}\end{cases}\end{aligned} \tag{4.27}$$

Note that this Hamiltonian almost matches the Kitaev chain [202] with pairing $\Delta/t = \tanh(1/\xi)$ and chemical potential $\mu/t = -2/\cosh(1/\xi)$, though slightly differs at the edges $j = 1, L$ of the chain: $\hat{H}^{(1)}_{\text{exp}} = \hat{H}_{KC} + \frac{\mu}{2}\hat{n}_1 + \frac{\mu}{2}\hat{n}_L$.

Another interesting subspace of this large family of Hamiltonians is the space of Hamiltonians with d-th neighbor bonds for $1 < d < L/2$. For this subspace, we choose the constraint that $J_{ij} = -t\delta_{i,j-d}/\tilde{t}_{ij}$. Under this constraint, we can use the bond operators to construct the following Hamiltonians

$$\hat{H}^{(d)}_{\text{exp}} = \sum_{j=1}^{L-d}(-t\hat{c}^\dagger_j\hat{c}_{j+d} - \Delta^{(d)}\hat{c}^\dagger_j\hat{c}^\dagger_{j+d} + \text{H.c.}) - \sum_{j=1}^{L}\mu^{(d)}_j\hat{n}_j, \tag{4.28}$$

where

$$\begin{aligned}\Delta^{(d)}/t &\equiv \tanh(d/\xi), \\ \mu^{(d)}_j/t &\equiv \begin{cases} -1/\cosh(d/\xi) & \min(j-1, L-j) < d \\ -2/\cosh(d/\xi) & \text{otherwise.}\end{cases}\end{aligned} \tag{4.29}$$

Interestingly, all Hamiltonians of Eq. (4.28), in any linear combination, exactly commute with the exponentially decaying MZMs of Eq. (4.25). However, note that only the nearest-neighbor $d = 1$ Hamiltonian connects together all of the sites in the 1D chain, while the $d > 1$ Hamiltonians form disconnected graphs. Therefore, Hamiltonians of the form $\sum_{d=1}^{L/2-1} J_d \hat{H}_{\text{exp}}^{(d)}$ with $J_1 \neq 0$ commute with exactly two zero modes, while those with $J_1 = 0$ potentially commute with more than two.

Example: Gaussian-distributed Majorana zero modes. Next, we construct Hamiltonians that commute with MZMs that are spatially localized as Gaussians of width σ centered at positions $\mathbf{x}_1$ and $\mathbf{x}_2$. We provide as input zero modes with the amplitudes

$$\alpha_{\mathbf{x}} \propto \exp\left(-(\mathbf{x}-\mathbf{x}_1)^2/2\sigma^2\right), \, \beta_{\mathbf{x}} \propto \exp\left(-(\mathbf{x}-\mathbf{x}_2)^2/2\sigma^2\right)$$

where we replaced the site label j with its spatial coordinate $\mathbf{x}$ in a lattice so that $\alpha_j, \beta_j \to \alpha_{\mathbf{x}}, \beta_{\mathbf{x}}$. For concreteness, we will consider a 1D chain lattice and 2D square lattice, but the same construction applies to arbitrary lattices in any dimension.

The $\alpha_{\mathbf{x}}, \beta_{\mathbf{x}}$ parameters determine the coefficients of the bond operator $\hat{h}_{ij} \to \hat{h}_{\mathbf{x},\mathbf{x}+\delta}$ that connects the site i at position $\mathbf{x}$ to site j at position $\mathbf{x}+\delta$. For Gaussian-distributed zero modes, the parameters of the bond operator $\hat{h}_{\mathbf{x},\mathbf{x}+\delta}$ of Eq. (4.23) satisfy

$$\begin{aligned}
\frac{\tilde{\Delta}_{\mathbf{x},\mathbf{x}+\delta}}{\tilde{t}_{\mathbf{x},\mathbf{x}+\delta}} &\equiv \tanh\left((\mathbf{x}_2-\mathbf{x}_1)\cdot\delta/2\sigma^2\right) \\
\frac{\tilde{\mu}_{\mathbf{x}}^{(\mathbf{x},\mathbf{x}+\delta)}}{\tilde{t}_{\mathbf{x},\mathbf{x}+\delta}} &\equiv -\frac{2e^{-[(\mathbf{x}-\mathbf{x}_1)\cdot\delta+\delta^2]/2\sigma^2}}{1+e^{-(\mathbf{x}_2-\mathbf{x}_1)\cdot\delta/\sigma^2}} \\
\frac{\tilde{\mu}_{\mathbf{x}+\delta}^{(\mathbf{x},\mathbf{x}+\delta)}}{\tilde{t}_{\mathbf{x},\mathbf{x}+\delta}} &\equiv -\frac{2e^{[(\mathbf{x}-\mathbf{x}_2)\cdot\delta+\delta^2]/2\sigma^2}}{1+e^{-(\mathbf{x}_2-\mathbf{x}_1)\cdot\delta/\sigma^2}}.
\end{aligned} \tag{4.30}$$

An interesting property to note is that $\tilde{\Delta}_{\mathbf{x},\mathbf{x}+\delta}/\tilde{t}_{\mathbf{x},\mathbf{x}+\delta}$ is actually independent of position $\mathbf{x}$ and only depends on the displacement of the MZMs $\mathbf{x}_2 - \mathbf{x}_1$ and the direction of the bond δ.

By arranging these bond operators uniformly onto the nearest neighbor bonds of a 1D chain or 2D square lattice, i.e., choosing $J_{\mathbf{x},\mathbf{y}} = -t\delta_{\mathbf{x},\mathbf{y}-\delta}/\tilde{t}_{\mathbf{x},\mathbf{y}}$, we construct the following two Hamiltonians that commute with the two Gaussian-distributed zero modes

$$\hat{H}_{1D} = \sum_{x=1}^{L-1}\left[-t\hat{c}_x^\dagger \hat{c}_{x+1} - \Delta_{x,x+1}\hat{c}_x^\dagger \hat{c}_{x+1}^\dagger + \text{H.c.}\right] - \sum_{x=1}^{L} \mu_x \hat{n}_x, \tag{4.31}$$

$$\begin{aligned}
\hat{H}_{2D} = &\sum_{\mathbf{x}}\sum_{\delta=\hat{\mathbf{x}},\hat{\mathbf{y}}}\left[-t\hat{c}_{\mathbf{x}}^\dagger \hat{c}_{\mathbf{x}+\delta} - \Delta_{\mathbf{x},\mathbf{x}+\delta}\hat{c}_{\mathbf{x}}^\dagger \hat{c}_{\mathbf{x}+\delta}^\dagger + \text{H.c.}\right] \\
&- \sum_{\mathbf{x}} \mu_{\mathbf{x}} \hat{n}_{\mathbf{x}},
\end{aligned} \tag{4.32}$$

where the pairings and chemical potentials can be generated from Eq. (4.30) by applying Eqs. (4.20)-(4.21).

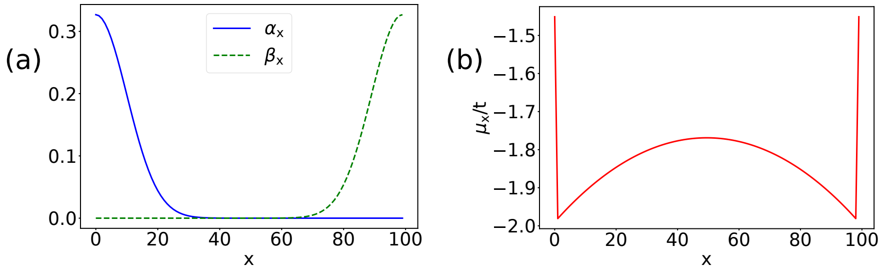

Figure 4.3: (a) Two 1D Majorana zero modes $\hat{\gamma}^{(1)} = \sum_x \alpha_x \hat{a}_x$ and $\hat{\gamma}^{(2)} = \sum_x \beta_x \hat{b}_x$ of the form of Eq. (4.22) with Gaussian profiles of width $\sigma = 10$, on a 100-site chain. (b) The spatial distribution of the chemical potential μ_x for the Hamiltonian Eq. (4.31) with a constant pairing $\Delta_{x,x+1}/t \approx 0.4582$ that commutes with the two Majorana zero modes.

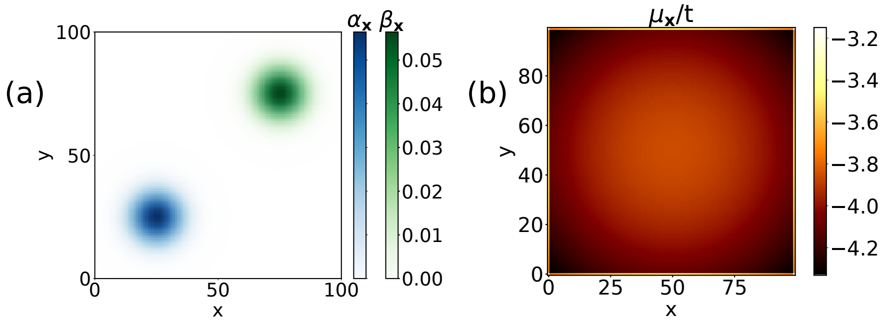

Figure 4.4: (a) Two 2D Majorana zero modes $\hat{\gamma}^{(1)} = \sum_{\mathbf{x}} \alpha_{\mathbf{x}} \hat{a}_{\mathbf{x}}$ and $\hat{\gamma}^{(2)} = \sum_{\mathbf{x}} \beta_{\mathbf{x}} \hat{b}_{\mathbf{x}}$ with Gaussian profiles of width $\sigma = 10$ localized at two corners of a 100×100 square lattice. (b) The spatial distribution of the chemical potential $\mu_{\mathbf{x}}$ for the Hamiltonian Eq. (4.32) with constant pairing $\Delta_{\mathbf{x},\mathbf{x}+\hat{\mathbf{x}}}/t = \Delta_{\mathbf{x},\mathbf{x}+\hat{\mathbf{y}}}/t \approx 0.2449$ that commutes with the two Majorana zero modes. Note that while the chemical potential $\mu_{\mathbf{x}}$ shown in (b) is highly symmetric, e.g., has four-fold rotation symmetry, the pairing term $\Delta_{\mathbf{x},\mathbf{x}+\hat{\mathbf{x}}}$ of Hamiltonian Eq. (4.32) (not shown) is, like the zero modes shown in (a), not as symmetric.

To illustrate, we show the chemical potential distributions for a 100-site 1D chain and a 100×100 2D square lattice with Gaussian Majorana zero modes in Figs. 4.3 and 4.4, respectively. Again, there is nothing special about chains, square lattices, 1D, or 2D. The same Hamiltonian as Eq. (4.32), but in different dimensions and with different lattice vectors δ, would also commute exactly with two Gaussian-distributed MZMs. Even more generally, a similar construction for any arbitrarily connected graph is straightforward, as discussed above.

Example: Zero modes with complicated spatial distributions. Using the $\hat{h}_{ij}$ bond operators, we can also design Hamiltonians with zero modes that have highly non-trivial spatial distributions.

To illustrate, we provide as input to our framework a pair of two spatially separated "Majorana" MZMs shaped according to a portrait of Ettore Majorana, shown in Fig. 4.5(a). As we did above, we also lay down bond operators uniformly onto a 2D square lattice so that the nearest-neighbor hopping between sites is $-t$. The Hamiltonian that we find, whose parameters are shown in Fig. 4.5(b)-(d), is both complicated and simple. It is complicated because of the non-trivial spatial distributions of the pairing and chemical potential terms, but it is also simple because of its locality and non-interacting nature.

We also construct Hamiltonians that commute with exotic zero modes with non-trivial spatial distributions that possess some but not all of the properties of MZMs. Recall that a MZM is (1) spatially localized into a single location and (2) well separated from other MZMs. Here we consider two examples of zero modes that break the first of these two properties. As we did above, we consider a 2D square lattice geometry for our Hamiltonians and require constant hopping between sites. In our first example, shown in Fig. 4.6(a), we provide as input a pair of zero modes that are spatially localized into *two* locations but still well-separated from one another. The parameters of the resulting Hamiltonian are shown in Fig. 4.6(b)-(c). In our second example, shown in Fig. 4.6(d), we provide as input a pair of well-separated zero modes in which one of the modes is spatially delocalized into a ring surrounding the other zero mode. The parameters of the Hamiltonian that commutes with the pair of zero modes are shown in Fig. 4.6(e)-(f). In both cases, the chemical potential distributions and pairing distributions required to produce these zero modes are quite non-trivial.

Note that for the Hamiltonians depicted in Figs. 4.5 and 4.6, we use the same notation (replacing the labels $i, j \to \mathbf{x}, \mathbf{x}+\delta$) as we did for the Gaussian zero modes, but the $\mu_{\mathbf{x}}, \Delta_{\mathbf{x},\mathbf{x}+\delta}$ parameters are from the more general Eq. (4.24) instead of the special-case Eq. (4.30).

Example: s-wave superconducting Hamiltonians with Majorana zero modes. While we have restricted our attention to spinless fermions with p-wave superconductivity, it is also possible to use our framework to construct spinful Majorana zero mode Hamiltonians with different superconducting order parameters. However, building these models can come at the expense of breaking symmetries, such as spinful time-reversal symmetry and spin conservation in the z-direction; or the complication of employing spin-orbit coupling or applying a local magnetic field. To add spins to our models, we substitute our labels with $i, j \to i\sigma, j\sigma'$ where i, j now correspond to sites and $\sigma, \sigma' \in \{\uparrow, \downarrow\}$ to spins.

Using our framework, we construct a 1D s-wave superconducting Hamiltonian with exponentially localized MZMs on the edges in two steps. (1) First, we construct two disconnected number-conserving Hamiltonians, one for the spin-up fermions and one for the spin-down fermions, that commute with four zero modes (two at each edge). (2) Second, we add a coupling between the up and down spins that does not commute with two of the four zero modes, leaving only one zero mode on each edge. Below we describe the two steps in detail.

(1) Consider the spin-up fermions. We first want to construct a Hamiltonian that commutes with a pair of spin-up exponentially decaying edges modes, both of which decay at rate $0 < r < 1$ from the left

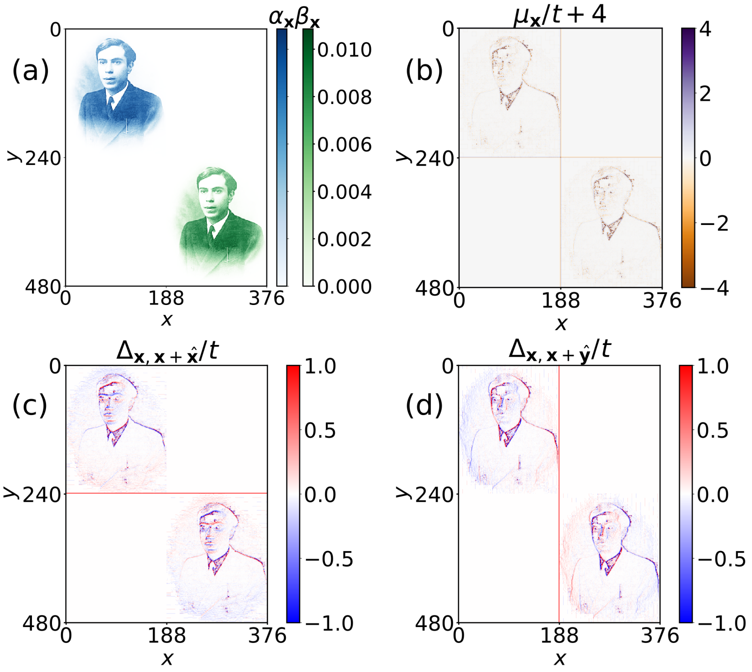

Figure 4.5: (a) Two Majorana zero modes shaped like Ettore Majorana. The (b) chemical potential $\mu_{\mathbf{x}}/t$, (c) x-direction pairing, and (d) y-direction pairing of the Hamiltonian Eq. (4.16) (with bond operator parameters Eq. (4.24)) that commutes with the Majorana zero modes.

edge: $\hat{\gamma}_{\uparrow}^{(1)} \propto \sum_{j=1}^{L} r^j \hat{a}_{j\uparrow}, \hat{\gamma}_{\uparrow}^{(2)} \propto \sum_{j=1}^{L} r^j \hat{b}_{j\uparrow}$. For these two zero modes, the corresponding bond operator between neighboring sites in the chain is $\hat{h}_{j\uparrow,j+1\uparrow} = (\hat{c}_{j\uparrow}^{\dagger}\hat{c}_{j+1,\uparrow} + \text{H.c.}) - r\hat{n}_{j\uparrow} - r^{-1}\hat{n}_{j+1\uparrow}$. Note that because the two zero modes are decaying in the same direction this operator has no superconducting pairing, only hopping and chemical potential. Now, consider the spin-down fermions. We would like to construct another Hamiltonian that commutes with two spin-down zero modes decaying exponentially at the same rate from the right edge: $\hat{\gamma}_{\downarrow}^{(1)} \propto \sum_{j=1}^{L} r^{-j} \hat{a}_{j\downarrow}, \hat{\gamma}_{\downarrow}^{(2)} \propto \sum_{j=1}^{L} r^{-j} \hat{b}_{j\downarrow}$. For these zero modes, the bond operator between neighboring sites is $\hat{h}_{j\downarrow,j+1\downarrow} = (\hat{c}_{j\downarrow}^{\dagger}\hat{c}_{j+1,\downarrow} + \text{H.c.}) - r^{-1}\hat{n}_{j\downarrow} - r\hat{n}_{j+1\downarrow}$. We can add the spin-up and spin-down bond operators together to construct a 1D chain Hamiltonian $-t\sum_{j=1}^{L-1}\sum_{\sigma}\hat{h}_{j\sigma,j+1\sigma}$ that commutes with the four zero modes $\hat{\gamma}_{\uparrow}^{(1)}, \hat{\gamma}_{\uparrow}^{(2)}, \hat{\gamma}_{\downarrow}^{(1)}, \hat{\gamma}_{\downarrow}^{(2)}$.

(2) To ensure that only one zero mode persists at each edge, we add a perturbing bond operator $\hat{h}_{j\uparrow,j\downarrow} = i\hat{b}_{j\uparrow}\hat{a}_{j\downarrow} = -\hat{c}_{j\uparrow}^{\dagger}\hat{c}_{j\downarrow} - \hat{c}_{j\uparrow}^{\dagger}\hat{c}_{j\downarrow}^{\dagger} + \text{H.c.}$ that commutes with $\hat{\gamma}_{\uparrow}^{(1)}$ and $\hat{\gamma}_{\downarrow}^{(2)}$ but not with $\hat{\gamma}_{\downarrow}^{(1)}$ and $\hat{\gamma}_{\uparrow}^{(2)}$.

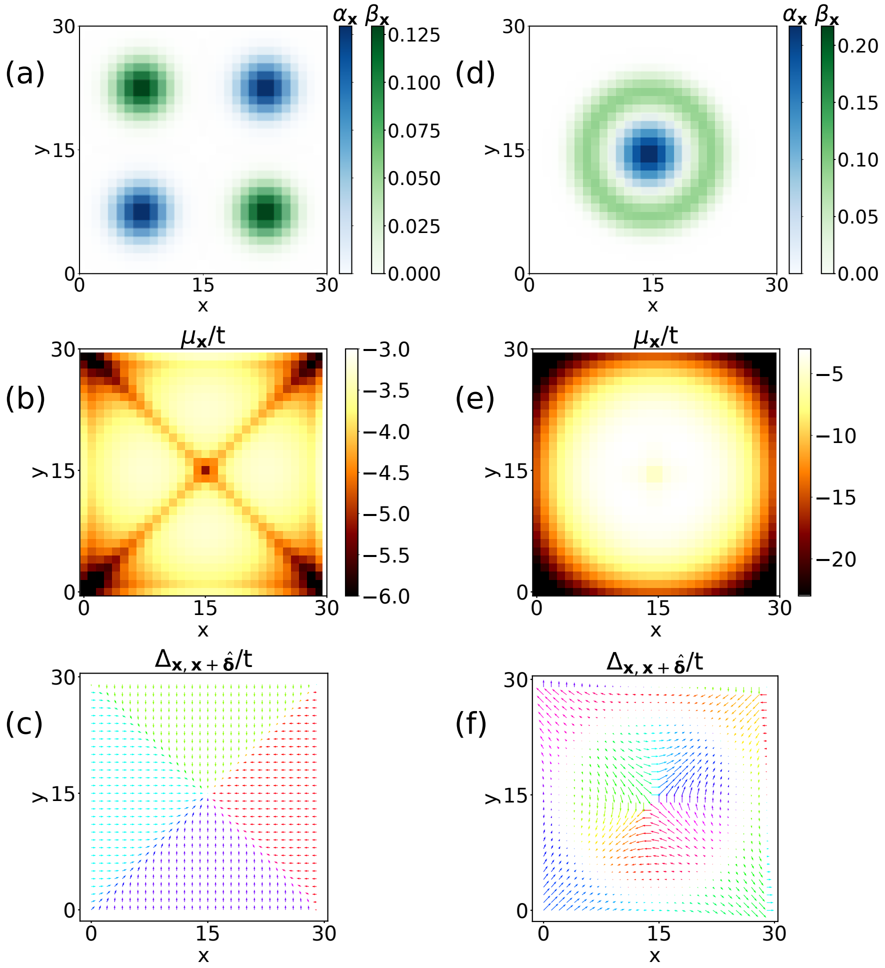

Figure 4.6: Examples of Hamiltonians on a 30×30 square lattice that commute with exotic zero modes. (a) Two zero modes, each of which is split into two well-separated Gaussians. The (b) chemical potential $\mu_{\mathbf{x}}/t$ and (c) pairing, represented as a vector $(\Delta_{\mathbf{x},\mathbf{x}+\hat{\mathbf{x}}}/t, \Delta_{\mathbf{x},\mathbf{x}+\hat{\mathbf{y}}}/t)$, of the Hamiltonian Eq. (4.16) (with bond operator parameters Eq. (4.24)) that commutes with the two split zero modes. (d) A Gaussian-shaped zero mode surrounded by a ring-shaped zero mode. The (e) chemical potential and (f) pairing of the Hamiltonian that commutes with the Gaussian and ring zero modes. The colors of the vectors in (c) and (f) correspond to their angles.

Altogether, the Hamiltonian that we construct is

$$\begin{aligned}\hat{H}_{s\text{-wave}} &= -t\sum_{j=1}^{L-1}\sum_{\sigma=\uparrow,\downarrow}\hat{h}_{j\sigma,j+1\sigma} + \Delta_s\sum_{j=1}^{L}\hat{h}_{j\uparrow,j\downarrow} \\ &= -t\sum_{j=1}^{L-1}\sum_{\sigma=\uparrow,\downarrow}(\hat{c}^\dagger_{j\sigma}\hat{c}_{j+1\sigma} + \text{H.c.}) - \mu\sum_{j=2}^{L-1}\hat{n}_j \\ &\quad - \Delta_s\sum_{j=1}^{L}(\hat{c}^\dagger_{j\uparrow}\hat{c}_{j\downarrow} + \hat{c}^\dagger_{j\uparrow}\hat{c}^\dagger_{j\downarrow} + \text{H.c.}) + \hat{H}_{\text{edge}}, \end{aligned} \tag{4.33}$$

where t and Δ_s are real free parameters, $\hat{n}_j \equiv \hat{n}_{j\uparrow} + \hat{n}_{j\downarrow}$, $\mu = -t(r + r^{-1})$, and the edge term is

$$\hat{H}_{\text{edge}} = t(r\hat{n}_{1\uparrow} + r^{-1}\hat{n}_{1\downarrow} + r^{-1}\hat{n}_{L\uparrow} + r\hat{n}_{L\downarrow}), \tag{4.34}$$

which involves a chemical potential and magnetic field. This Hamiltonian is an s-wave superconductor that commutes with only the two desired Majorana zero modes $\hat{\gamma}^{(1)}_{\uparrow}$ and $\hat{\gamma}^{(2)}_{\downarrow}$. In this case, this Hamiltonian breaks time-reversal symmetry, does not conserve z-magnetization, involves spin-orbit coupling of the same strength as the pairing, and requires a finely tuned magnetic field at the edge. This edge magnetic field, however, we do not expect to be essential and could possibly be removed by slightly modifying the spatial distributions of the input zero modes.

Interacting Hamiltonians with zero modes. Finally, we mention how to construct *interacting* Hamiltonians that commute with particular zero modes. The main fact to note is that if Hermitian operators $\hat{A}$ and $\hat{B}$ commute with a zero mode $\hat{\gamma}^{(1)}$, then so do the Hermitian operators $i[\hat{A},\hat{B}]$ and $\{\hat{A},\hat{B}\}$ if they are non-zero. For example, for bond operators $\hat{h}_{ij}$ and $\hat{h}_{jk}$ that commute with $\hat{\gamma}^{(1)}$ and $\hat{\gamma}^{(2)}$, the operator $\{\hat{h}_{ij},\hat{h}_{jk}\} \neq 0$ also commutes with $\hat{\gamma}^{(1)}$ and $\hat{\gamma}^{(2)}$. Using this observation, we can construct the class of fermion-parity-conserving interacting Hamiltonians

$$\begin{aligned}\hat{H}_{IZM} = &\sum_{ij} c_{ij}\hat{h}_{ij} + \sum_{ijkl} d_{ijkl}\{\hat{h}_{ij},\hat{h}_{kl}\} + \sum_{ijkl} e_{ijkl} i[\hat{h}_{ij},\hat{h}_{kl}] \\ &+ \sum_{ijklmn} f_{ijklmn}\{\hat{h}_{ij},\{\hat{h}_{kl},\hat{h}_{mn}\}\} + \cdots\end{aligned}$$

where the coefficients $c_{ij}, d_{ijkl}, \ldots$ form a connected graph. These Hamiltonians often contain complicated interacting terms such as $\hat{n}_i\hat{n}_j$, $\hat{n}_i\hat{c}^\dagger_j\hat{c}_k + \text{H.c.}$, $\hat{n}_i\hat{c}^\dagger_j\hat{c}^\dagger_k + \text{H.c.}$, etc.

As an example, consider the s-wave Hamiltonian Eq. (4.33) that we constructed above. To this Hamiltonian we can add an interacting term between neighboring sites of the form $\sum_j\{\hat{h}_{j\uparrow,j\downarrow},\hat{h}_{j+1\uparrow,j+1\downarrow}\}/2 = -\sum_j \hat{b}_{j\uparrow}\hat{a}_{j\downarrow}\hat{b}_{j+1\uparrow}\hat{a}_{j+1\downarrow}$ and still have the resulting Hamiltonian commute with exactly the same two zero modes. When written in terms of complex fermions $\hat{c}_j$ and $\hat{c}_j^\dagger$, this term is a sum of eight quartic fermionic operators, many of which do not conserve particle number.

4.4 Z_2 quantum spin liquid Hamiltonians

In this section, we use the SHC to numerically construct large classes of new Z_2 quantum spin liquid Hamiltonians on the square and kagome lattices. We discover many Hamiltonians that commute with the Wilson loops shown in Fig. 4.7. All of these Hamiltonians have at least four-fold degenerate ground states. We perform exact diagonalization on these Hamiltonians and determine that many have *exactly* four-fold ground state degeneracy. For many of these Hamiltonians with four-fold ground states, we compute the modular S-matrix and find that it exactly matches the modular S-matrix of Z_2 spin liquids. Generically, the Z_2 spin liquid Hamiltonians that we find are not sums of commuting projectors, nor frustration-free. For some of these Hamiltonians, the Wilson loops are "rigid", i.e., they are only of a fixed length. In other Hamiltonians we find that some Wilson loops can be deformed, or extended to arbitrary length, like Wilson loops in the toric code.

The Hamiltonians with deformable Wilson loops possess many local integrals of motion, while those with rigid loops do not. For none of these Hamiltonians do the integrals of motion that we identify form a complete mutually commuting set that fully specifies all of the eigenstates. While it is possible that there are integrals of motion we do not know about, we are able to explicitly rule out some types of integrals of motion. An exhaustive numerical search rules out the existence of any additional truly local integrals of motion up to some range. A novel eigenstate clustering approach, discussed in Appendix B.8, rules out the existence of a complete set of integrals of motion that commutes with a class of (Wilson-loop-preserving) perturbations of the Hamiltonian. Finally, we consider the level-spacing statistics of the Z_2 spin liquid Hamiltonians under these perturbations. For the energy levels of these perturbed Hamiltonians in individual quantum number sectors, we find GOE level-spacing statistics suggesting non-integrable behavior.

Background. Wilson loops arise as integrals of motion in Z_2 quantum spin liquids. Consider a square lattice of spins wrapped into a torus so that there are periodic boundaries in both directions. On the torus, we can form two topologically inequivalent non-contractible loops $\mathcal{L}_{\hat{\mathbf{x}}}$ and $\mathcal{L}_{\hat{\mathbf{y}}}$ that span the entire system. Consider four non-local Wilson loop operators $\hat{X}_{\mathcal{L}_{\hat{\mathbf{x}}}}, \hat{X}_{\mathcal{L}_{\hat{\mathbf{y}}}}, \hat{Z}_{\mathcal{L}_{\hat{\mathbf{x}}}}$ and $\hat{Z}_{\mathcal{L}_{\hat{\mathbf{y}}}}$ with non-trivial support along these two loops. Suppose that these Wilson loop operators are integrals of motion of a Hamiltonian $\hat{H}$, that they square to identity (so that their eigenvalues are ± 1), and that they obey the following set of commutation and anti-commutation relations

$$
\begin{aligned}
[\hat{X}_{\mathcal{L}_{\hat{\mathbf{x}}}}, \hat{X}_{\mathcal{L}_{\hat{\mathbf{y}}}}] &= [\hat{Z}_{\mathcal{L}_{\hat{\mathbf{x}}}}, \hat{Z}_{\mathcal{L}_{\hat{\mathbf{y}}}}] = 0 \\
[\hat{X}_{\mathcal{L}_{\hat{\mathbf{x}}}}, \hat{Z}_{\mathcal{L}_{\hat{\mathbf{x}}}}] &= [\hat{X}_{\mathcal{L}_{\hat{\mathbf{y}}}}, \hat{Z}_{\mathcal{L}_{\hat{\mathbf{y}}}}] = 0 \\
\{\hat{X}_{\mathcal{L}_{\hat{\mathbf{x}}}}, \hat{Z}_{\mathcal{L}_{\hat{\mathbf{y}}}}\} &= \{\hat{Z}_{\mathcal{L}_{\hat{\mathbf{x}}}}, \hat{X}_{\mathcal{L}_{\hat{\mathbf{y}}}}\} = 0.
\end{aligned} \tag{4.35}
$$

The existence of Wilson loops satisfying these properties implies at least a four-fold degeneracy in each of the energy eigenstates of the Hamiltonian $\hat{H}$.

In this work, we will focus on a particularly simple set of Wilson loops of the form

$$
\begin{aligned}
\hat{X}_{\mathcal{L}_{\hat{\mathbf{x}}}} &= \prod_{j\in\mathcal{L}_{\hat{\mathbf{x}}}} \hat{\sigma}^x_j, \quad \hat{Z}_{\mathcal{L}_{\hat{\mathbf{x}}}} = \prod_{j\in\mathcal{L}_{\hat{\mathbf{x}}}} \hat{\sigma}^z_j, \\
\hat{X}_{\mathcal{L}_{\hat{\mathbf{y}}}} &= \prod_{j\in\mathcal{L}_{\hat{\mathbf{y}}}} \hat{\sigma}^x_j, \quad \hat{Z}_{\mathcal{L}_{\hat{\mathbf{y}}}} = \prod_{j\in\mathcal{L}_{\hat{\mathbf{y}}}} \hat{\sigma}^z_j,
\end{aligned} \tag{4.36}
$$

where $\mathcal{L}_{\hat{\mathbf{x}}}$ and $\mathcal{L}_{\hat{\mathbf{y}}}$ are two *straight-line* topologically distinct non-contractible loops across the torus that wind in the horizontal and vertical directions, respectively (see Fig. 4.7(a)). It can be verified that the Wilson loops of Eq. (4.36) square to identity and satisfy the properties of Eq. (4.35). These particular Wilson loops are integrals of motion of the toric code, a well known solvable Z_2 spin liquid Hamiltonian that is a sum of commuting terms [204]. Note that there are also $\hat{Y}_{\mathcal{L}} \propto \hat{X}_{\mathcal{L}}\hat{Z}_{\mathcal{L}}$ Wilson loops, though they are not independent from the ones in Eq. (4.36). Also, there are actually many straight-line Wilson loop operators whose loops are parallel to $\mathcal{L}_{\hat{\mathbf{x}}}$ and $\mathcal{L}_{\hat{\mathbf{y}}}$, though shifted by $j\hat{\mathbf{y}}$ or $k\hat{\mathbf{x}}$. We will refer to these shifted loops as $\mathcal{L}^{(j)}_{\hat{\mathbf{x}}}$ and $\mathcal{L}^{(k)}_{\hat{\mathbf{y}}}$ for $j, k = 1, \ldots, L$. In addition to these Wilson loops on the square lattice, we also consider straight-line Wilson loops of the same form as Eq. (4.36) on the periodic kagome lattice. We refer to the kagome Wilson loops as $\hat{Z}_{\mathcal{L}_{\mathbf{a}_1}}, \hat{X}_{\mathcal{L}_{\mathbf{a}_1}}, \hat{Z}_{\mathcal{L}_{\mathbf{a}_2}}, \hat{X}_{\mathcal{L}_{\mathbf{a}_2}}$, where $\mathbf{a}_1 = (1, 0)$ and $\mathbf{a}_2 = (1/2, \sqrt{3}/2)$ are the kagome lattice vectors (see Fig. 4.7(c)).

Finally, we would like to mention the form of the toric code on the kagome lattice, as it will be relevant to our later discussion. The toric code model can be defined on many lattices, such as the honeycomb lattice. While it is customary for the spins of the toric code to be on the links of the lattice, in this work we always consider spins to be on the sites. When the spins are defined on sites instead of links, the honeycomb toric code gets mapped to the kagome lattice. This model, which we will refer to as the kagome toric code model,

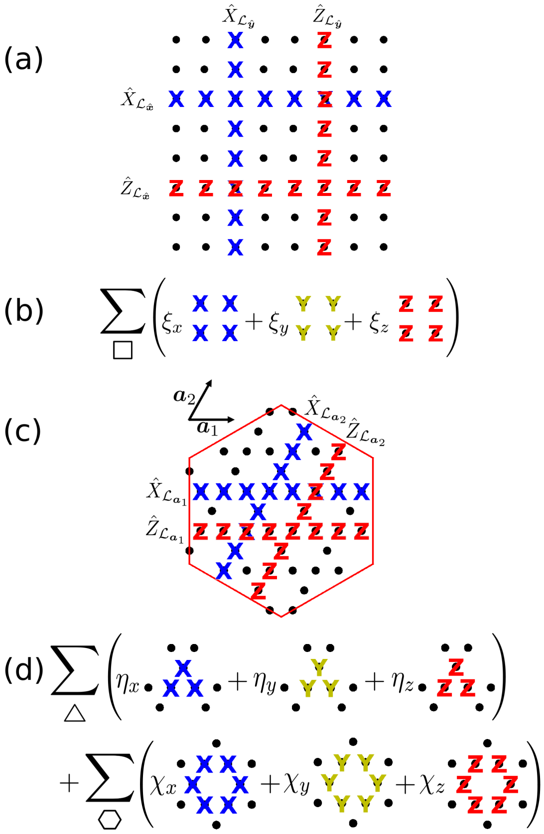

Figure 4.7: (a) The Wilson loops on the square lattice provided as input to the SHC method. (b) The Hamiltonians produced as output by SHC, which commute with the Wilson loops in (a) and obey the square lattice symmetries. (c) The Wilson loops on the kagome lattice provided as input to the SHC method. (d) The Hamiltonians produced as output by SHC, which commute with the Wilson loops in (c) and obey the kagome lattice symmetries. Note that the triangle summation includes all upward and downward facing triangles.

is

$$\hat{H}_{TC,\text{kagome}} = -\sum_{\triangle} \hat{X}_{\triangle} - \sum_{\hexagon} \hat{Z}_{\hexagon} \tag{4.37}$$

where the $\hat{X}_{\triangle} = \prod_{j\in\triangle} \hat{\sigma}_j^x$ and $\hat{Z}_{\hexagon} = \prod_{j\in\hexagon} \hat{\sigma}_j^z$ operators are three-spin and six-spin interactions defined on the triangles and hexagons, respectively, of the lattice. The model has the same essential features as the square lattice toric code: it is a sum of commuting terms, the $\hat{X}_{\triangle}, \hat{Z}_{\hexagon}$ are local integrals of motion, and the model commutes with the straight-line Wilson loops $\hat{Z}_{\mathcal{L}_{\mathbf{a}_1}}, \hat{X}_{\mathcal{L}_{\mathbf{a}_1}}, \hat{Z}_{\mathcal{L}_{\mathbf{a}_2}}, \hat{X}_{\mathcal{L}_{\mathbf{a}_2}}$.

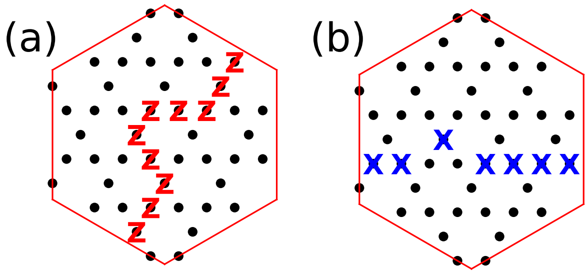

Figure 4.8: (a) A Z-Wilson loop deformed around a hexagon. (b) An X-Wilson loop deformed around a triangle.

4.4.1 Z_2 spin liquid Hamiltonians on the square lattice

SHC numerics. To generate new Z_2 spin liquid Hamiltonians on the square lattice, we provided a list of desired symmetries as input to SHC: (1) the four straight-line Wilson loop operators $\hat{X}_{\mathcal{L}_{\hat{\mathbf{x}}}}, \hat{Z}_{\mathcal{L}_{\hat{\mathbf{x}}}}, \hat{X}_{\mathcal{L}_{\hat{\mathbf{y}}}}, \hat{Z}_{\mathcal{L}_{\hat{\mathbf{y}}}}$ (see Fig. 4.7(a)); and (2) the symmetry group of the square lattice, generated by translations of lattice vectors $\hat{\mathbf{x}}, \hat{\mathbf{y}}$, 90°-rotation, and reflection about the side of a square. Note that using the $\hat{X}, \hat{Z}$ pair of Wilson loops is an arbitrary choice and we could have instead used the $\hat{X}, \hat{Y}$ or $\hat{Y}, \hat{Z}$ pair. Given this input, one might expect that the SHC would produce the toric code as output, since it is an example of a square lattice Hamiltonian that commutes with Wilson loops of this form. However, it does *not* because the toric code's translational symmetry is generated by translations of $2\hat{\mathbf{x}}$ and $2\hat{\mathbf{y}}$ instead of $\hat{\mathbf{x}}$ and $\hat{\mathbf{y}}$.

We performed the SHC calculations on a finite-size $N = 8 \times 8 = 64$ site lattice. We used a basis of range-R k-local Pauli strings, where $R = 2$ and $k \in \{1, 2, 3, 4, 5\}$; this includes up to five-spin interactions on nearest, next-nearest, and next-next nearest neighbor sites on the square lattice. Before symmetrization by spatial symmetries, this basis was $67,584$-dimensional. After symmetrization, the basis was reduced to a 234-dimensional basis of spatially-symmetric Hamiltonians. In this 234-dimensional basis, we numerically constructed the commutant matrices $C_{\hat{X}_{\mathcal{L}_{\hat{\mathbf{x}}}}}, C_{\hat{Z}_{\mathcal{L}_{\hat{\mathbf{x}}}}}, \ldots$ for the four Wilson loops and found three vectors that were null vectors of all of these matrices. These three vectors correspond to the coupling constants of three Hamiltonians with all of the desired symmetries. This three-dimensional space of symmetric Hamiltonians takes the form

$$\hat{H}_{\text{square}} = \sum_{\square} \left(\xi_x \hat{X}_{\square} + \xi_y \hat{Y}_{\square} + \xi_z \hat{Z}_{\square} \right), \tag{4.38}$$

where $\hat{X}_{\square} = \prod_{j \in \square} \hat{\sigma}^x_j, \hat{Y}_{\square} = \prod_{j \in \square} \hat{\sigma}^y_j$, and $\hat{Z}_{\square} = \prod_{j \in \square} \hat{\sigma}^z_j$ are four-spin interactions on the nearest neighbor squares of the lattice and ξ_x, ξ_y, ξ_z are arbitrary real constants. These Hamiltonians are depicted in Fig. 4.7(b).

Numerical checks of Z_2 order. While the Hamiltonians of Eq. (4.38) commute with the Wilson loop operators, it is not guaranteed that they are Z_2 spin liquids. In this section, we numerically tested particular Hamiltonians in this space to check if they have Z_2 topological order. By construction, these Hamiltonians commute with Wilson loops satisfying Eq. (4.35) and so are guaranteed to have eigenstates with degeneracies that are multiples of four. However, it is possible that they have *greater* than four-fold degeneracy, either due to the existence of accidental degeneracy or additional symmetries that we did not require.

For each $\hat{H}_{\text{square}}$ that we tested, we used exact diagonalization (ED) to determine if the ground state was *exactly* four-fold degenerate. If it was, we then calculated the modular S-matrix, a quantity that encodes the properties of anyons in a topologically ordered system [59, 62]. The modular S-matrix is an overlap matrix $S_{ij} \equiv \langle \Xi_i^{\hat{\mathbf{x}}} | \Xi_j^{\hat{\mathbf{y}}} \rangle$ between minimally-entangled-states (MES) $|\Xi_i^{\hat{\mathbf{x}}}\rangle$ and $|\Xi_i^{\hat{\mathbf{y}}}\rangle$ for $i = 1, \ldots, 4$ across loops $\mathcal{L}_{\hat{\mathbf{x}}}$ and $\mathcal{L}_{\hat{\mathbf{y}}}$ of the torus. The MES are particular linear combinations of the four degenerate ground states in the system that minimizes the Renyi entanglement entropy along the cuts defined by loops $\mathcal{L}_{\hat{\mathbf{x}}}$ and $\mathcal{L}_{\hat{\mathbf{y}}}$. For the toric code, the MES are e and m flux eigenstates along the two loops, i.e., they are eigenstates of the Wilson loop operators $\hat{Z}_{\mathcal{L}}, \hat{X}_{\mathcal{L}}$ [62]. Assuming this holds for the $\hat{H}_{\text{square}}$ Hamiltonians as well, we computed the MES for our Hamiltonians by finding the flux eigenstates of $\hat{Z}_{\mathcal{L}_\delta}, \hat{X}_{\mathcal{L}_\delta}$ for $\delta = \hat{\mathbf{x}}, \hat{\mathbf{y}}$ from the four-fold degenerate ground states. In particular, for $\delta = \hat{\mathbf{x}}$ and $\hat{\mathbf{y}}$, we built the set of four MES $|\Xi_1^\delta\rangle, \ldots, |\Xi_4^\delta\rangle$ by computing the (unique) ground state of $\hat{H}_{\text{square}} - \kappa_e \hat{Z}_{\mathcal{L}_\delta} - \kappa_m \hat{X}_{\mathcal{L}_\delta}$ for $(\kappa_e, \kappa_m) = (+1, +1), (+1, -1), (-1, +1), (-1, -1)$, respectively. We numerically verified for the $\xi_x = \xi_y = \xi_z = -1$ Hamiltonian on the 4×4 lattice that the MES that we used did in fact minimize the Renyi entanglement entropy across the $\mathcal{L}_{\hat{\mathbf{x}}}$ and $\mathcal{L}_{\hat{\mathbf{y}}}$ cuts of the torus, as is expected [62].

Using ED, we checked 27 particular $\hat{H}_{\text{square}}$ Hamiltonians on a 4×4 square lattice to determine if they were Z_2 spin liquids. We considered the $3^3 = 27$ possible Hamiltonians with ξ_α set to $-1, 0, +1$ for each $\alpha = x, y, z$. Six of these Hamiltonians (up to cyclic permutations of ξ_x, ξ_y, ξ_z), listed in Table 4.1, had exactly four degenerate ground states. For these six Hamiltonians, we computed the modular S-matrix and found it to be [6]

$$S = \frac{1}{2} \begin{pmatrix} 1 & 1 & 1 & 1 \\ 1 & 1 & -1 & -1 \\ 1 & -1 & 1 & -1 \\ 1 & -1 & -1 & 1 \end{pmatrix} \tag{4.39}$$

---

[6] Each MES is determined up to a phase. We chose those phases so that the first row and column of the modular S-matrix are real and positive.

ξ_x	0	0	0	0	$+1$	-1
ξ_y	$+1$	$+1$	-1	-1	$+1$	-1
ξ_z	$+1$	-1	$+1$	-1	-1	-1

Table 4.1: Six square lattice Hamiltonians $\hat{H}_{\text{square}}$ of the form of Eq. (4.38) that have Z_2 topological order on the 4×4 lattice. This table excludes cyclic permutations of (ξ_x, ξ_y, ξ_z) that also have Z_2 topological order.

up to numerical precision. This S-matrix corresponds to Z_2 topological order [62].

Symmetries of the discovered Hamiltonians. Here we consider the symmetries of the Hamiltonians that we found. By construction, these models possess straight-line Wilson loops as integrals of motion and obey the spatial symmetries of the square lattice. However, it is possible that these Hamiltonians possess additional symmetries that we did not require.

We numerically determined that the $\hat{H}_{\text{square}}$ Hamiltonians listed in Table 4.1 do not possess highly local integrals of motions. We verified this numerically by using the slow operator forward method, i.e., by computing the commutant matrices $C_{\hat{H}_{\text{square}}}$ for each of the Hamiltonians in Table 4.1 with a local basis of operators. For the Hamiltonians tested, we found no integrals of motion with up to 9-site terms on a local 3×3 square cluster of sites in the lattice. The fact that these Hamiltonians do not possess such local integrals of motion suggests that the Wilson loops of these models are "rigid," i.e., cannot be locally deformed.

Even without any apparent local integrals of motion, we are able to identify a set of mutually commuting integrals of motion built from the straight-line Wilson loops. Consider an $L_x \times L_y$ square lattice. Without local integrals of motion, the $\hat{Z}_{\mathcal{L}_{\hat{\mathbf{x}}}^{(j)}}, \hat{Z}_{\mathcal{L}_{\hat{\mathbf{y}}}^{(k)}}$ Wilson loops for $j = 1, \dots, L_y; k = 1, \dots, L_x - 1$ are all *independent* conserved quantities [7]. The same is true for the X Wilson loops, but the X Wilson loops do not commute with all of the Z Wilson loops (see Eq. (4.35)). Nonetheless, products of *two* X loops do commute with all of the Z loops. Therefore, the set of operators

$$
\begin{aligned}
&\{\hat{Z}_{\mathcal{L}_{\hat{\mathbf{x}}}^{(j)}}\}_{j=1}^{L_y}, \quad \{\hat{Z}_{\mathcal{L}_{\hat{\mathbf{y}}}^{(k)}}\}_{k=1}^{L_x-1}, \\
&\{\hat{X}_{\mathcal{L}_{\hat{\mathbf{x}}}^{(j)}} \hat{X}_{\mathcal{L}_{\hat{\mathbf{x}}}^{(j+1)}}\}_{j=1}^{L_y-1}, \quad \{\hat{X}_{\mathcal{L}_{\hat{\mathbf{y}}}^{(k)}} \hat{X}_{\mathcal{L}_{\hat{\mathbf{y}}}^{(k+1)}}\}_{k=1}^{L_x-2}
\end{aligned} \tag{4.40}
$$

form a set of $2L_x + 2L_y - 4$ mutually commuting operators.

Generically, the square lattice $\hat{H}_{\text{square}}$ Hamiltonians of Eq. (4.38) also possess a global integral of motion that is a sum of Pauli strings. These Hamiltonians can be written as a sum of two commuting operators

---

[7] The $\hat{Z}_{\mathcal{L}_{\hat{\mathbf{x}}}^{(j)}}, \hat{Z}_{\mathcal{L}_{\hat{\mathbf{y}}}^{(k)}}$ operators satisfy $\prod_{j=1}^{L_y} \hat{Z}_{\mathcal{L}_{\hat{\mathbf{x}}}^{(j)}} = \prod_{k=1}^{L_x} \hat{Z}_{\mathcal{L}_{\hat{\mathbf{y}}}^{(k)}}$, so one of the operators is dependent on the rest.

$\hat{H}_{\text{square}} = \hat{A} + \hat{B}$, where

$$\hat{A} \equiv \sum_{\square_A} (\xi_x \hat{X}_{\square_A} + \xi_y \hat{Y}_{\square_A} + \xi_z \hat{Z}_{\square_A}) \tag{4.41}$$

$$\hat{B} \equiv \sum_{\square_B} (\xi_x \hat{X}_{\square_B} + \xi_y \hat{Y}_{\square_B} + \xi_z \hat{Z}_{\square_B}), \tag{4.42}$$

and $\square_A$ are the "black squares" and $\square_B$ are the "white squares" of a black-white checkboard pattern laid down on the square lattice. Since $[\hat{A}, \hat{B}] = 0$, we can consider one of these operators, say $\hat{B}$, as a global integral of motion, so that $[\hat{H}_{\text{square}}, \hat{B}] = 0$. The $\hat{B}$ operator also commutes with the integrals of motion listed in Eq. (4.40).

Note that the $\hat{H}_{\text{square}}$ Hamiltonians of Eq. (4.38) are not sums of commuting terms nor frustration-free, making them difficult to solve analytically. The set of mutually commuting integrals of motion of Eqs. (4.40) and (4.42) is not enough to fully diagonalize the $\hat{H}_{\text{square}}$ Hamiltonians, but can be used to block diagonalize them into quantum number sectors, allowing us to more effectively study these models numerically.

Level-spacing statistics. Typically, the level-spacing statistics of a quantum Hamiltonian are either distributed according to the Gaussian orthogonal ensemble (GOE) distribution or the Poisson distribution. If the level-spacing statistics are GOE distributed, then that is good evidence that the system is non-integrable. For Hamiltonians with many integrals of motion, such as the ones we found, the level-spacing statistics will generally appear Poisson when considering energies spread out over multiple quantum number sectors of the integrals of motion. However, it is possible for the statistics to be GOE in particular quantum number sectors.

Using ED, we numerically examined the level-spacing statistics of particular $\hat{H}_{\text{square}}$ Hamiltonians, i.e., the statistics of the level-spacing ratio $r_n = \min(\delta_n, \delta_{n-1})/\max(\delta_n, \delta_{n-1})$ where $\delta_n \equiv E_n - E_{n-1}$ and E_n are the sorted energy eigenvalues of the Hamiltonian. For the Poisson distribution the average level-spacing ratio is expected to be $\langle r_{\text{Poisson}} \rangle = 0.3863$, while for the GOE distribution it should be $\langle r_{\text{GOE}} \rangle = 0.5307$. After accounting for the quantum number sectors we know about – i.e., the ones listed in Eqs. (4.40) and (4.42) – we observed significant degeneracy in the spectrum, leaving only a small number of unique energy levels on the 8×4 square lattice that we considered. To break this degeneracy, we perturbed the sixth Hamiltonian of Table 4.1 by a random perturbation, resulting in the Hamiltonian

$$-\sum_{\square} (\hat{X}_{\square} + \hat{Y}_{\square} + \hat{Z}_{\square}) + \epsilon \delta \hat{H} \tag{4.43}$$

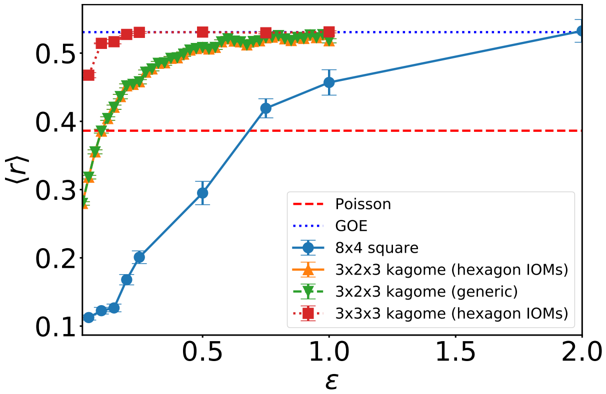

Figure 4.9: The average level-spacing ratios versus disorder strength ϵ for the Hamiltonian Eq. (4.43) on an 32-site square lattice (8x4 square), the Hamiltonian Eq. (4.52) on an 18-site kagome lattice (3x2x3 kagome (hexagon IOMs)), the Hamiltonian Eq. (4.53) on an 18-site kagome lattice (3x2x3 kagome (generic)), and the Hamiltonian Eq. (4.52) on a 27-site kagome lattice (3x3x3 kagome (hexagon IOMs)). The 18-site kagome lattice calculations were averaged over 100 random Hamiltonians, while the others were averaged over 10 random Hamiltonians. The energy levels considered were obtained in particular quantum number sectors, as described in Appendix B.8.

where $\delta\hat{H} = \sum_{\square} h_{\square}\hat{Z}_{\square}$ and $h_{\square}$ are random numbers drawn from the uniform distribution between -1 and 1 for each square and ϵ is the disorder strength. This particular perturbation breaks the spatial symmetries of the square lattice, but preserves the Wilson loop integrals of motion in Eq. (4.40) (and a modified global integral of motion Eq. (4.42)) and generically destroys the eigenstate degeneracy within the known quantum number sectors. After this perturbation, there are still eigenstates in a given quantum number sector that do not couple with each other. We cluster these eigenstates by grouping together the connected set of states that couple through the perturbation to the Hamiltonian (see Appendix B.8). This coupling still leaves multiple eigenstates per cluster and suggests the existence of some "hidden" integrals of motion we have not explicitly identified. For 10 random realizations of Eq. (4.43) for ϵ from 0 to 6, we computed the average level-spacing ratio within these clusters. As shown in Fig. 4.9, as ϵ increases to 2 the average level-spacing ratio $\langle r \rangle$ approaches the GOE value. However, it does decrease slightly below that value for larger ϵ, as shown in Fig. B.1. For the 8×4 square lattice, the eigenstate clusters we found were quite small, typically containing either 28 or 35 states. We also tested 10 random realizations of these perturbed Hamiltonians with disorder strengths $\epsilon = 0.25, 0.5, 0.75, 1$ on a 4×4 square lattice and observed that they always possessed exactly four-fold degenerate ground states, suggesting that the perturbed models are also Z_2 spin liquids.

4.4.2 Z_2 spin liquid Hamiltonians on the kagome lattice

SHC numerics. To construct new Z_2 quantum spin liquid Hamiltonians on the kagome lattice, we provided as input to SHC: (1) the four straight-line Wilson loop operators $\hat{X}_{\mathcal{L}_{\mathbf{a}_1}}, \hat{Z}_{\mathcal{L}_{\mathbf{a}_1}}, \hat{X}_{\mathcal{L}_{\mathbf{a}_2}}, \hat{Z}_{\mathcal{L}_{\mathbf{a}_2}}$ (see Fig. 4.7(c)); and (2) the symmetry group of the kagome lattice generated by translations of lattice vectors $\mathbf{a}_1$ and $\mathbf{a}_2$, 60°-rotation, and reflection.

We performed our SHC calculations on the finite-size $N = 48$ site symmetric cluster shown in Fig. 4.7(c). To construct Hamiltonians, we used a basis of range-R 3-local and 6-local Pauli strings, where $R = 2/\sqrt{3}$. Before symmetrization by spatial symmetries, this basis was $31,536$-dimensional. After symmetrization, the basis was reduced to a 220-dimensional space. In this large space of local Hamiltonians, we found the following six-dimensional space of symmetric Hamiltonians that exactly obey all of the desired symmetries

$$\begin{aligned}\hat{H}_{\text{kagome}} = \sum_{\triangle} \left(\eta_x \hat{X}_{\triangle} + \eta_y \hat{Y}_{\triangle} + \eta_z \hat{Z}_{\triangle} \right) \\ + \sum_{\hexagon} \left(\chi_x \hat{X}_{\hexagon} + \chi_y \hat{Y}_{\hexagon} + \chi_z \hat{Z}_{\hexagon} \right),\end{aligned} \tag{4.44}$$

where η_α, χ_α for $\alpha = x, y, z$ are arbitrary real constants, $\hat{X}_{\triangle} = \prod_{j \in \triangle} \hat{\sigma}^x_j, \hat{Y}_{\hexagon} = \prod_{j \in \hexagon} \hat{\sigma}^y_j, \ldots$, and the summations are over all of the triangles (both upward and downward facing) and hexagons in the kagome lattice. These Hamiltonians are depicted in Fig. 4.7(d).

We also note that we performed the same SHC calculations with a basis of range-R k-local Pauli strings with $R = 2/\sqrt{3}$ and $k \in \{1, 2, 3, 4, 5, 6\}$ and found six additional symmetric Hamiltonians, which involve four and five-site interactions. These Hamiltonians can be written in terms of products of triangle operators:

$$\begin{aligned}\sum_{\langle \triangle, \triangle' \rangle} \hat{X}_{\triangle} \hat{X}_{\triangle'}, \sum_{\langle \triangle, \triangle' \rangle} \hat{Y}_{\triangle} \hat{Y}_{\triangle'}, \sum_{\langle \triangle, \triangle' \rangle} \hat{Z}_{\triangle} \hat{Z}_{\triangle'}, \\ \sum_{\langle \triangle, \triangle' \rangle} i(\hat{X}_{\triangle} \hat{Y}_{\triangle'} + \hat{X}_{\triangle'} \hat{Y}_{\triangle}), \sum_{\langle \triangle, \triangle' \rangle} i(\hat{X}_{\triangle} \hat{Z}_{\triangle'} + \hat{X}_{\triangle'} \hat{Z}_{\triangle}), \\ \sum_{\langle \triangle, \triangle' \rangle} i(\hat{Y}_{\triangle} \hat{Z}_{\triangle'} + \hat{Y}_{\triangle'} \hat{Z}_{\triangle}),\end{aligned}$$

where the summations are over nearest-neighbor triangles $\triangle$ and $\triangle'$ that overlap at a single site. While we include these Hamiltonians for completeness, we will not examine their properties in the discussion below. We instead will focus on the Hamiltonians of Eq. (4.44).

Numerical checks of Z_2 order. Using ED on finite-size kagome lattices, we found Hamiltonians of the form of Eq. (4.44) that exhibit Z_2 topological order. On a $3 \times 2 \times 3 = 18$ site kagome lattice, we considered $\hat{H}_{\text{kagome}}$ Hamiltonians with all possible $3^3 = 27$ combinations of $\eta_\alpha = -1, 0, +1$ for $\alpha = x, y, z$ with $(\chi_x, \chi_y, \chi_z) = (0, 0, -1)$. We found that 24 of these 27 Hamiltonians had four-fold degenerate ground states and exactly the Z_2 modular S-matrix of Eq. (4.39), which we computed in the same way as described in the previous section. The three Hamiltonians that did not have these properties were the effectively classical $(\eta_x, \eta_y, \eta_z) = (0, 0, -1), (0, 0, 0), (0, 0, +1)$ Hamiltonians.

Symmetries of discovered Hamiltonians. By construction, all of the $\hat{H}_{\text{kagome}}$ Hamiltonians of Eq. (4.44) obey the symmetries of the kagome lattice and commute with the straight-line Wilson loops. Yet, generic $\hat{H}_{\text{kagome}}$ Hamiltonians do not possess any highly local integrals of motion. We checked this numerically using the slow operator forward method. In particular, we computed the commutant matrix $C_{\hat{H}_{\text{kagome}}}$ for 100 random $\hat{H}_{\text{kagome}}$ Hamiltonians, with η_α, χ_α sampled uniformly from $[-1, 1]$, and found that they had no null vectors for local bases of Pauli strings on the triangles, bowties, and hexagons of a 48-site kagome lattice. For generic $\hat{H}_{\text{kagome}}$ Hamiltonians, these calculations suggest that there are no local integrals of motion and that the Wilson loops are rigid like they were for the square lattice Hamiltonians. For these generic Hamiltonians, we can identify the following set of mutually commuting integrals of motion

$$\{\hat{Z}_{\mathcal{L}^{(j)}_{\mathbf{a}_1}}, \hat{Z}_{\mathcal{L}^{(k)}_{\mathbf{a}_2}}, \hat{X}_{\mathcal{L}^{(j)}_{\hat{\mathbf{a}_1}}} \hat{X}_{\mathcal{L}^{(j+1)}_{\hat{\mathbf{a}_1}}}, \hat{X}_{\mathcal{L}^{(k)}_{\hat{\mathbf{a}_2}}} \hat{X}_{\mathcal{L}^{(k+1)}_{\hat{\mathbf{a}_2}}}\}. \tag{4.45}$$

However, as we discuss below, particular subspaces of these Hamiltonians possess different sets of mutually commuting integrals of motion, which do include local integrals of motion and deformable Wilson loops.

For example, the Hamiltonians in the four-dimensional subspace of Hamiltonians

$$\sum_{\triangle} \left(\eta_x \hat{X}_\triangle + \eta_y \hat{Y}_\triangle + \eta_z \hat{Z}_\triangle\right) + \sum_{\hexagon} \chi_z \hat{Z}_{\hexagon}, \tag{4.46}$$

where $\chi_z \neq 0$, commute with $\hat{Z}_{\hexagon}$ for all hexagons. For these models, we can therefore build a large set of mutually commuting operators

$$\{\hat{Z}_{\hexagon}, \hat{Z}_{\mathcal{L}_{\mathbf{a}_1}}, \hat{Z}_{\mathcal{L}_{\mathbf{a}_2}}, \hat{X}_{\mathcal{L}^{(j)}_{\hat{\mathbf{a}_1}}} \hat{X}_{\mathcal{L}^{(j+1)}_{\hat{\mathbf{a}_1}}}, \hat{X}_{\mathcal{L}^{(k)}_{\hat{\mathbf{a}_2}}} \hat{X}_{\mathcal{L}^{(k+1)}_{\hat{\mathbf{a}_2}}}\}. \tag{4.47}$$

Moreover, for these models, the Wilson loops are partially deformable: no Wilson loops can be deformed around triangles, but the Z Wilson loops can be deformed around hexagons. Similar subspaces with different hexagon operators, e.g., with $\chi_x \neq 0, \chi_y = \chi_z = 0$, also exist and have the same properties.

Likewise, Hamiltonians of the form

$$\sum_{\triangle} \eta_z \hat{Z}_{\triangle} + \sum_{\hexagon} \left(\chi_x \hat{X}_{\hexagon} + \chi_y \hat{Y}_{\hexagon} + \chi_z \hat{Z}_{\hexagon} \right), \tag{4.48}$$

where $\eta_z \neq 0$, commute with $\hat{Z}_{\triangle}$ for all triangles. For these models, we can build an even larger set of mutually commuting operators

$$\{\hat{Z}_{\triangle},\, \hat{Z}_{\mathcal{L}_{\mathbf{a}_1}},\, \hat{Z}_{\mathcal{L}_{\mathbf{a}_2}},\, \hat{X}_{\mathcal{L}^{(j)}_{\hat{\mathbf{a}_1}}} \hat{X}_{\mathcal{L}^{(j+1)}_{\hat{\mathbf{a}_1}}},\, \hat{X}_{\mathcal{L}^{(k)}_{\hat{\mathbf{a}_2}}} \hat{X}_{\mathcal{L}^{(k+1)}_{\hat{\mathbf{a}_2}}}\}, \tag{4.49}$$

since there are more triangles than hexagons in the kagome lattice. For these models, the Z Wilson loops can be deformed around triangles, but no Wilson loops can be deformed around hexagons.

Interestingly, the kagome lattice toric code of Eq. (4.37) is a particularly special point, $(\eta_x, \eta_y, \eta_x, \chi_x, \chi_y, \chi_z) = (-1, 0, 0, 0, 0, -1)$, in the space of Hamiltonians. It is special in that *both* X triangles and Z hexagons are local integrals of motion, making X Wilson loops deformable about triangles and Z Wilson loops deformable around hexagons (see Fig. 4.8). Since the toric code is an exactly solvable model, it is interesting to consider perturbing it to better understand the other models in this space of Hamiltonians, which have different symmetry properties. Fig. 4.10 shows the full spectra of three families of Hamiltonians that all include the toric code as a special point. The Hamiltonians of Fig. 4.10(a) are of the type described in Eq. (4.46), the Hamiltonians of Fig. 4.10(b) are of the type described in Eq. (4.48), and the Hamiltonians of Fig. 4.10(c) are generic $\hat{H}_{\text{kagome}}$ Hamiltonians of the type described in Eq. (4.44). Notably, the ground state for each of the Hamiltonians shown stayed exactly four-fold degenerate, though the gap to the first-excited states did decrease with large enough perturbations.

Generically, the kagome lattice $\hat{H}_{\text{kagome}}$ Hamiltonians of Eq. (4.44), like the square lattice models, also possess a global integral of motion that is a sum of Pauli strings. A generic $\hat{H}_{\text{kagome}}$ Hamiltonian is a sum of two commuting terms, $\hat{H}_{\text{kagome}} = \hat{C} + \hat{D}$, where

$$\hat{C} = \sum_{\triangle} (\eta_x \hat{X}_{\triangle} + \eta_y \hat{Y}_{\triangle} + \eta_z \hat{Z}_{\triangle}) \tag{4.50}$$

$$\hat{D} = \sum_{\hexagon} (\chi_x \hat{X}_{\hexagon} + \chi_y \hat{Y}_{\hexagon} + \chi_z \hat{Z}_{\hexagon}) \tag{4.51}$$

are the terms only on the triangles or hexagons of the kagome lattice, respectively. We can take one of these operators, say $\hat{D}$, as a global integral of motion, since $[\hat{H}_{\text{kagome}}, \hat{D}] = 0$.

The $\hat{H}_{\text{kagome}}$ Hamiltonians of Eq. (4.44) are not sums of commuting terms nor frustration-free. Gener-

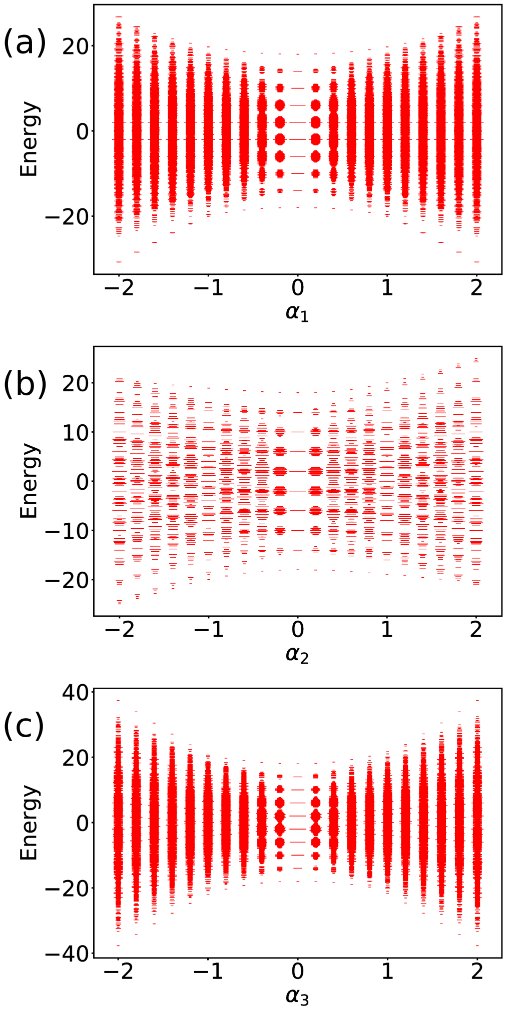

Figure 4.10: The full spectra of the Hamiltonians (a) $\hat{H}_{TC,\text{kagome}} + \alpha_1 \sum_{\triangle} \hat{Z}_{\triangle}$, (b) $\hat{H}_{TC,\text{kagome}} + \alpha_2 \sum_{\hexagon} \hat{X}_{\hexagon}$, and (c) $\hat{H}_{TC,\text{kagome}} + \alpha_3 (\sum_{\triangle} \hat{Z}_{\triangle} + \sum_{\hexagon} \hat{X}_{\hexagon})$ on a $3 \times 2 \times 3$ kagome lattice. The width of each horizontal line corresponds to the degeneracy of the energy eigenstates, plotted on a log scale. The smallest degeneracy is four-fold, which occurs for all of the ground states of these models, and the largest degeneracy is about $80,000$-fold, which occurs for the eigenstates in the center of the toric code's spectrum ($\alpha_1 = \alpha_2 = \alpha_3 = 0$).

ically, the set of mutually commuting integrals of motion that we found do not fully specify the degrees of freedom of the model and cannot be used to fully diagonalize the $\hat{H}_{\text{kagome}}$ Hamiltonians, except at the special points corresponding to the toric code model. However, the set of mutually commuting integrals of motion Eq. (4.45) (or Eq. (4.47) or (4.49)) and Eq. (4.51) can be used to block diagonalize the Hamiltonians into quantum number sectors, which allows us to more effectively study these models numerically.

Level-spacing statistics. We examined the level-spacing statistics of the Hamiltonians we discovered with the SHC to see if they obeyed GOE or Poisson statistics in their quantum number sectors. Initially, we computed the level-spacing statistics of the Hamiltonians in Fig. 4.10 for $3 \times 2 \times 3 = 18$ and $3 \times 3 \times 3 = 27$ site kagome lattices in the quantum number sectors of Eq. (4.45) (or Eq. (4.47) or (4.49)) and Eq. (4.51). Like we observed for the square lattice Hamiltonians, the kagome lattice Hamiltonians possess large eigenstate degeneracy. We again remove these degeneracies by considering perturbed Hamiltonians of the form

$$-\sum_{\triangle}(\hat{X}_{\triangle} + \hat{Z}_{\triangle}) - \sum_{\hexagon} \hat{Z}_{\hexagon} + \epsilon\delta\hat{H}' \tag{4.52}$$

$$-\sum_{\triangle}(\hat{X}_{\triangle} + \hat{Z}_{\triangle}) - \sum_{\hexagon} (\hat{X}_{\hexagon} + \hat{Z}_{\hexagon}) + \epsilon\delta\hat{H}' \tag{4.53}$$

where $\delta\hat{H}' = \sum_{\triangle} h_{\triangle}\hat{Z}_{\triangle}$ and $h_{\triangle}$ are random numbers drawn from the uniform distribution between -1 and 1 for each triangle and ϵ is the disorder strength. These particular perturbations break the spatial symmetries of the kagome lattice, but still preserve the integrals of motion described in the previous section.

On 18-site lattices, for both Hamiltonians Eqs. (4.52) and (4.53), the $\delta\hat{H}'$ perturbation was sufficient to produce GOE statistics at intermediate ϵ for the 256 energy levels in the considered quantum number sectors, as shown in Fig. 4.9. On the 27-site lattice (for which we only considered Hamiltonian Eq. (4.52)), this perturbation was not sufficient to produce GOE statistics; instead we found that there were additional unidentified "hidden" quantum number sectors that were affecting the level-spacing results. Using the eigenstate clustering approach described in Appendix B.8, we identified (within one sector) the set of eigenstates that correspond to a hidden quantum number sector without identifying their corresponding integrals of motion. This procedure involved looking at the set of energy eigenstates coupled through the perturbation $\delta\hat{H}'$. After accounting for the hidden quantum numbers, our originally 8192-dimensional sector was reduced to four 2048-dimensional hidden sectors, suggesting that for the 27-site lattice there are likely two missing binary integrals of motion that we were unable to directly identify. Using the energy levels in the hidden sectors, we computed the average level-spacing ratio and observed that it indeed approached the GOE value as ϵ increased, in fact doing so much more rapidly than for the 18-site lattice (see Fig. 4.9). This seems to suggest that the non-GOE behavior for low ϵ could be a finite-size effect. We also numerically determined the ground state degeneracy of 10 random realizations of the Hamiltonians of Eqs. (4.52) and (4.53) with disorder strengths $\epsilon = 0.25, 0.5, 0.75, 1$ on an 18-site kagome lattice. For all random Hamiltonians considered, the ground states were exactly four-fold degenerate, suggesting that these perturbed models are still Z_2 spin liquids.

4.5 Discussion and conclusions

We have introduced a new approach, the symmetric Hamiltonian construction (SHC), for constructing Hamiltonians with desired symmetries. This method is general and can be used to construct families of Hamiltonians that commute (or anti-commute) with desired integrals of motion, such as zero mode and Wilson loop operators, and are invariant (or anti-invariant) under discrete symmetry transformations, such as point-group symmetries. In this work, we applied the SHC approach to design new topologically ordered Hamiltonians by providing as input to the method integrals of motion with topological properties and spatial symmetries. We analytically determined large families of superconducting Hamiltonians with Majorana zero modes (MZMs) and numerically found new Z_2 spin liquid Hamiltonians on the square and kagome lattices.

Using the SHC, we developed a general framework for designing Hamiltonians that commute with a pair of zero mode operators. In this framework, we provide as input the spatial distribution of two zero modes and as output produce Hamiltonians that commute exactly with those two zero modes and no others. These Hamiltonians can be put onto arbitrary lattice geometries, e.g., square, kagome, tetrahedral, or quasicrystal lattices, or even arbitrary graphs. Some examples of Hamiltonians that we designed with this framework are: a one-dimensional s-wave superconducting Hamiltonian that commutes with two exponentially-localized MZMs, a two-dimensional p-wave superconducting Hamiltonian that commutes with Gaussian-localized MZMs, and two-dimensional Hamiltonians that commute with exotic semi-localized zero modes.

Using the SHC numerically, we discovered new classes of Z_2 spin liquid Hamiltonians on the square and kagome lattices whose properties differ from known solvable models. The Hamiltonians are not sums of commuting projectors nor are they frustration-free. Generically, these Hamiltonians possess many integrals of motion, though not enough to fully diagonalize the Hamiltonian. We observed that particular perturbations of these Hamiltonians, which break spatial symmetries but preserve the integrals of motion, exhibit GOE level-spacing statistics in their quantum number sectors. Many of the Hamiltonians that we found, even with these perturbations, possess numerically exact four-fold ground state degeneracy in finite-size systems.

There are many future directions for using the SHC to study topological order. Our general framework for designing zero mode Hamiltonians opens the door to the design of new experiments to search for MZMs.

Using our framework, it is now possible for experimentalists to design a Hamiltonian with MZMs that best fits their experimental constraints, rather than focusing on a particular idealized model such as the Kitaev chain. To realize these MZM Hamiltonians in the lab, these experiments need some degree of control over the spatial distribution of some combination of chemical potentials, magnetic fields, superconducting pairings, or hoppings, in fermionic superconducting systems. Such control can potentially be realized in existing experiments, such as in Josephson junction arrays [219], superconductor-semiconductor heterostructures [74], twisted bilayer graphene [220], and strain-modulated superconductors [221, 222]. Our framework also potentially allow theorists to design new model Hamiltonians with new exotic zero mode physics, such as zero modes that realize non-Ising non-Abelian anyons or zero modes displaying the physics of higher-order topological insulators and superconductors [223, 224]. One can also use similar techniques as we used to discover Z_2 spin liquids in order to find other topologically ordered Hamiltonians. For example, by providing as input different topological symmetry operators, such as different types of Wilson loops, one can attempt to discover new model Hamiltonians with double semion or Fibonacci anyons.

Broadly speaking, the SHC is a tool that can be used to systematically study Hamiltonians with symmetries of interest. For example, it can be used to find all local Hamiltonians consistent with particular crystallographic symmetries. Once identified, these models can then be studied numerically or analytically to better understand their behavior. The SHC method can also be used to generate (potentially interacting) realizations of Hamiltonians from well-known symmetry classifications, such as the "ten-fold way" classification of non-interacting topological insulators and superconductors [225]. It could also be used to engineer Hamiltonians with properties that make them easier to study. Certain classes of interacting fermionic Hamiltonians with specific symmetries are known to be sign-problem-free, a property that allows for their efficient numerical simulation using methods such as quantum Monte Carlo [226–228]. The SHC method could be used to generate particular realizations of Hamiltonians with such symmetries, and thereby provide many new sign-problem-free Hamiltonians for numerical study. The availability of new numerically solvable models could provide valuable insights into strongly correlated systems.

Chapter 5

Numerical evidence for many-body localization in two and three dimensions

This chapter is based on the work presented in Ref. [229], ©2021 American Physical Society, done in collaboration with Dr. Benjamin Villalonga Correa and my advisor Prof. Bryan Clark.

5.1 Introduction

It is natural to expect quantum systems to obey statistical mechanics. However, there is increasing evidence that there exist disordered strongly interacting quantum systems that do not obey the laws of statistical mechanics and never reach thermal equilibrium – a phenomenon known as many-body localization (MBL) [78, 230, 231, 80, 79, 232, 77]. A key feature of MBL systems is they exhibit robust emergent integrability, i.e., they possess many quasilocal conserved quantities (known as ℓ-bits) [105, 106, 233]. The existence of these robust conserved quantities is strongly related to other well-known properties of MBL, such as area-law entanglement of excited states and logarithmic growth of entanglement entropy under time-evolution [79, 232, 77]. Numerical methods have been key to studying MBL [83, 234, 83, 84, 235, 236, 85, 90, 237, 91, 238], but have mostly been limited to small finite-size systems and one spatial dimension.

A key open question that remains is the role of dimensionality in MBL [77]. In one-dimension, there is significant numerical and analytic evidence for MBL phenomena (although even this is still controversial [239]). In higher dimensions, the situation is less clear. Cold-atom experiments show some signatures of slow thermalization in two and three dimensions [118, 119, 115]. Some have argued that MBL phases are unstable to rare ergodic regions that trigger thermalizing avalanches [240, 241]. Others have suggested that an MBL phase might survive but only in nonstandard thermodynamic limits [242–244]. In this work we take a pragmatic approach and numerically search for ℓ-bits in higher dimensions, which we take as a practical signature of MBL. Being able to predict properties of MBL in higher dimensions is also key to making the connection to two and three dimensional cold-atom experiments. While some numerical approaches exist in two-dimensions [94–104], simulating MBL in higher dimensions is still largely intractable and it is important to develop new numerical techniques, particularly in three-dimensions, where to our knowledge no numerical studies have been done.

In this work, we present a new algorithm for finding approximate ℓ-bits (or ℓ-bit-like operators [242]) in interacting disordered systems of arbitrary dimensions. In MBL systems, an exact ℓ-bit is an operator that (1) is quasilocal, (2) commutes with the Hamiltonian, and (3) has a binary spectrum, i.e., a spectrum of half $+1$ and half -1 eigenvalues. Our algorithm constructs an *approximate* ℓ-bit by finding an operator that satisfies these three properties as closely as possible. Property (1) is approximated by representing the approximate ℓ-bit as a linear combination of finitely many local Pauli strings, while properties (2) and (3) are approximated by minimizing an objective function using gradient descent. Some previously developed numerical methods for finding ℓ-bits in MBL systems have attempted to enforce these properties exactly [108–113]. Other methods have attempted to numerically construct operators that approximately satisfy properties (1) and (2) and either exactly enforce the binary property (3) [96, 114] or do not enforce that property at all [45, 245, 46, 95, 210, 246, 211]. Many of these methods have required numerically expensive calculations, e.g., exact diagonalization or large bond-dimension tensor networks, and, except for the methods of Refs. [95, 96, 98], have been limited to the study of one-dimensional chains. Our algorithm can efficiently produce operators that are reasonable approximations of binary, quasilocal ℓ-bits in arbitrary dimensions.

Using our algorithm, we study four model Hamiltonians: the disordered Heisenberg model in one, two, and three-dimensions, and the disordered hard-core Bose-Hubbard model in two-dimensions (also examined in Refs. [98, 99]). In all models studied, we find high quality ℓ-bits at high disorder strengths suggesting MBL behavior and see statistical signatures of a potential transition from localized to delocalized integrals of motions. Our results provide new evidence for the existence of MBL phenomenology in two and three-dimensions.

5.2 Background

In this work, we investigate two different types of Hamiltonians. First, we consider the disordered spin-1/2 Heisenberg model

$$H = \sum_{\langle ij \rangle} \mathbf{S}_i \cdot \mathbf{S}_j + \sum_i h_i S_i^z \tag{5.1}$$

where the first summation is over nearest neighbor sites of a 1D, 2D, or 3D lattice, $h_i \in [-W, W]$ are random numbers drawn from a uniform distribution, and W is the disorder strength. The 1D model has been extensively investigated numerically, mostly using exact diagonalization [81–85] and tensor networks [86–93]. However, the model in higher dimensions has, up to this point, been largely unexplored [95, 102].

Second, we consider the disordered Bose-Hubbard model

$$H = -\sum_{\langle ij \rangle} \left(a_i^\dagger a_j + \text{H.c.} \right) + \frac{U'}{2} \sum_i n_i (n_i - 1) + \sum_i \delta_i n_i \tag{5.2}$$

where the first summation is over nearest neighbor sites of a two-dimensional square lattice, $a_i^\dagger$ and a_i are bosonic creation and annihilation operators, $n_i \equiv a_i^\dagger a_i$, and δ_i are random on-site potentials drawn from a Gaussian distribution with full-width half-maximum Δ. This model approximately describes the interactions between bosonic ^{87}Rb atoms in a two-dimensional disordered optical lattice experiment [118], where a potential MBL-ergodic transition was observed at $\Delta_c^{exp} \approx 5.5(4)$ with $U' = 24.4$. Refs. [98] numerically studied this model in the hard-core limit using tensor networks, where they found a transition at $\Delta_c^{tn} \approx 19$; we too work in this limit.

Generically, a Hamiltonian such as Eq. (5.1) or (5.2) can be represented as

$$H = \sum_i \tilde{h}_i \tau_i^z + \sum_{i,j} \tilde{J}_{ij} \tau_i^z \tau_j^z + \sum_{i,j,k} \tilde{J}_{ijk} \tau_i^z \tau_j^z \tau_k^z + \cdots \tag{5.3}$$

where $\tilde{h}_i, \tilde{J}_{ij}, \ldots$ are coupling constants and $\tau_i^z = U^\dagger \sigma_i^z U$ where U is a unitary that diagonalizes the Hamiltonian. The τ_i^z operators are integrals of motion ($[H, \tau_i^z] = 0$) that mutually commute ($[\tau_i^z, \tau_j^z] = 0$) and have a binary spectrum ($(\tau_i^z)^2 = I$ and $\operatorname{tr}(\tau_i^z) = 0$). Note that these operators are not unique since there exist many unitaries that diagonalize H. In MBL systems, the τ_i^z operators can be made quasilocal, so that the support of the operators decays rapidly away from a single site on which they are localized, and are known as ℓ-bits. A τ_i^z operator can be written as

$$\tau_i^z = \sum_{a=1}^{|B|} c_a \mathcal{O}_a, \tag{5.4}$$

where c_a is a real coefficient, $\mathcal{O}_a$ is a Pauli string (a product of Pauli matrices, such as $\sigma_1^x \sigma_3^x \sigma_5^z$), and $B = \{\mathcal{O}_a\}_{a=1}^{|B|}$ is a basis of Pauli strings of size $|B|$. The quasilocality of ℓ-bits make it possible to accurately represent them using a small, finite basis B of local Pauli strings.

To quantify quasilocality, we can define the weight $w_{\mathbf{r}}$ of a τ_i^z operator [211, 109] as

$$w_{\mathbf{r}} = \frac{\sum_{a \in B_{\mathbf{r}}} |c_a|^2}{\sum_{\mathbf{r}'} \sum_{b \in B_{\mathbf{r}'}} |c_b|^2} \tag{5.5}$$

where $\mathbf{r}$ is the spatial coordinate of a site in the lattice and $B_{\mathbf{r}}$ is the set of (labels of) Pauli strings in the basis B with (non-identity) support on lattice coordinate $\mathbf{r}$. The weight $w_{\mathbf{r}}$ decays rapidly in MBL phases,

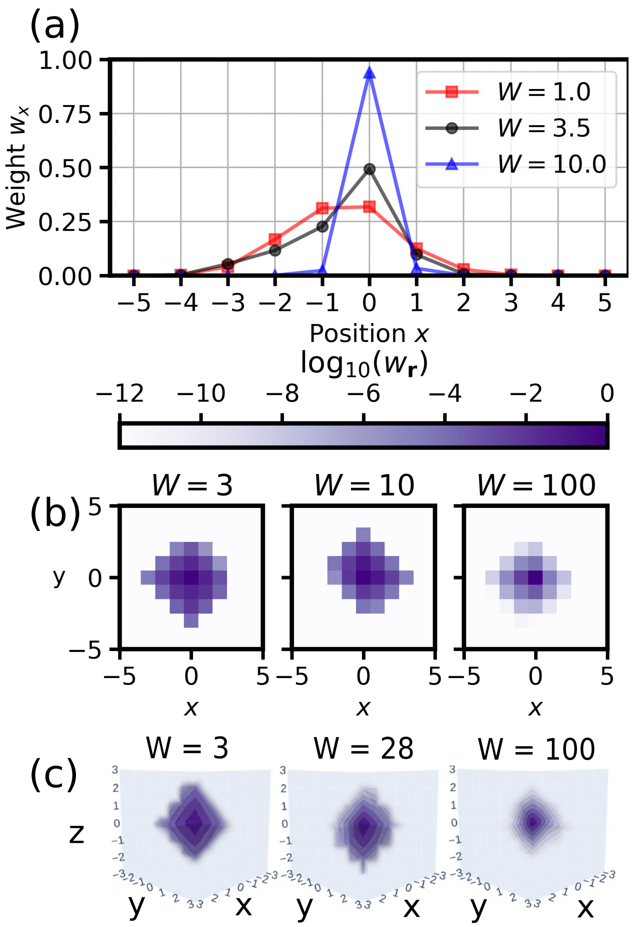

Figure 5.1: Typical weights $w_\mathbf{r}$ of random τ_i^z for the (a) 1D, (b) 2D, and (c) 3D disordered Heisenberg models at different disorder strengths.

as shown in Fig. 5.1.

5.3 Method

Our algorithm constructs quasilocal operators τ_i^z that approximately commute with the Hamiltonian and are approximately binary. In particular, the algorithm optimizes the c_a parameters in Eq. (5.4) to minimize the objective function

$$Z[\{c_a\}] = \alpha \|[H, \tau_i^z]\|^2 + \beta \|(\tau_i^z)^2 - I\|^2, \tag{5.6}$$

where $\alpha, \beta > 0$, $\|O\|^2 \equiv \mathrm{tr}\left(O^\dagger O\right)/\mathrm{tr}\,(I)$ is the Frobenius norm, and I is the identity operator. As described in the appendix, this minimization is done using gradient descent and Newton's method. Note that if the second term of Eq. (5.6) is zero, then the eigenvalues of τ_i^z have exactly equal sectors of ± 1 eigenvalues because τ_i^z is traceless. Also note that while we do not constrain τ_i^z to be normalized ($\|\tau_i^z\|^2 = \sum_a c_a^2 = 1$), it stays approximately normalized during the optimization because of the second term of Eq. (5.6). We set $\alpha = \beta = 1$.

Rather than perform a single minimization of Eq. (5.6) in a fixed basis B, we iteratively and adaptively build the basis during the minimization (similar in spirit to selected configuration interaction, an adaptive basis technique in quantum chemistry [247–250]). The steps of the algorithm are:

1. Initialize $B = \{\sigma_i^z\}$.

2. Expand B by adding new Pauli strings.

3. Minimize Eq. (5.6) in basis B.

4. Repeat steps 2–3 while $|B| \leq |B|_{max}$.

In step 1, we initialize the basis with a single Pauli matrix at site i. In step 2, we expand the basis by including new Pauli strings that are important for minimizing the objective in Eq. (5.6). In particular, our heuristic expansion procedure is two-step: (a) first, we compute $[H, [H, \tau_i^z]] = \sum_a c'_a \mathcal{O}_a$ and add M_1 new Pauli strings $\mathcal{O}_a$ to B with the largest amplitudes $|c'_a|$ [1]; (b) then, we compute $(\tau_i^z)^2 - I = \sum_a c''_a \mathcal{O}_a$ and add M_2 new Pauli strings to B with the largest amplitudes $|c''_a|$. The logic behind step (a) is that, to cancel the remainder of $[H, \tau_i^z]$, we need to add Pauli strings that, when commuted through the Hamiltonian, coincide with the remainder. These are the terms in $[H, [H, \tau_i^z]]$. The logic is similar for step (b). In our calculations, we set $M_1 = M_2 = 100$ and perform 11 basis expansions, so that we expand by up to 200 Pauli strings per iteration to a maximum basis size of $|B|_{max} = 2201$. In step 3, we perform gradient descent with the c_a parameters in Eq. (5.4) initialized to the optimized values obtained in the previous basis size, but rescaled so they are normalized to one.

We execute our algorithm on 1D, 2D, and 3D periodic lattices of size 101, 21 × 21 and 11 × 11 × 11, respectively. It is important to note that, because of the basis sizes $|B|$ considered, the optimized τ_i^z never reach the lattice boundaries, indicating that our calculations do not exhibit any finite system-size effects or boundary effects, but do exhibit finite *basis-size* effects.

Our code is available online [251] and is based on the Qosy package [47].

---

[1] In order to save memory and time in our calculations, we modified step (a) so that only the largest 2000 terms of $[H, \tau_i^z]$ were kept before computing $[H, [H, \tau_i^z]]$.

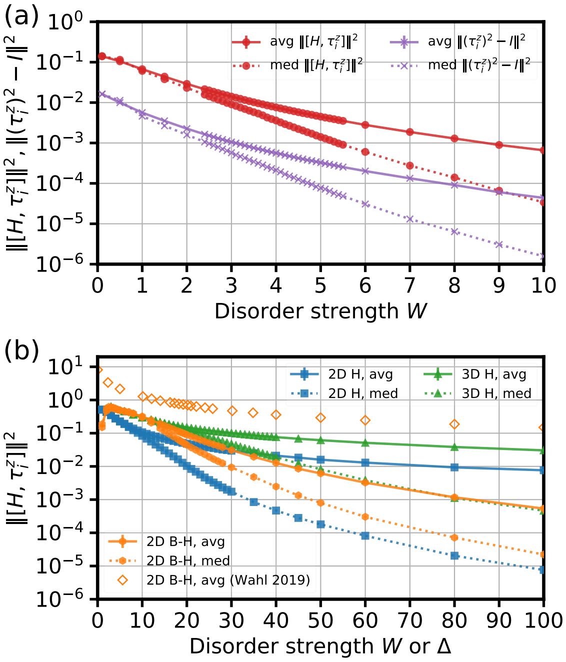

Figure 5.2: The average and median commutator norms $\|[H,\tau_i^z]\|^2$ and binarities $\|(\tau_i^z)^2 - I\|^2$ (only for (a)) of our optimized τ_i^z operators for the disordered (a) 1D Heisenberg model and (b) 2D and 3D Heisenberg models and 2D hard-core Bose-Hubbard model. The average commutator norms obtained by Ref. [98] (Wahl 2019) using shallow 2D tensor networks for the 2D Bose-Hubbard model are also shown. Note that the method of Ref. [98] finds all τ_i^z in a 10×10 lattice, while our method finds only a single τ_i^z.

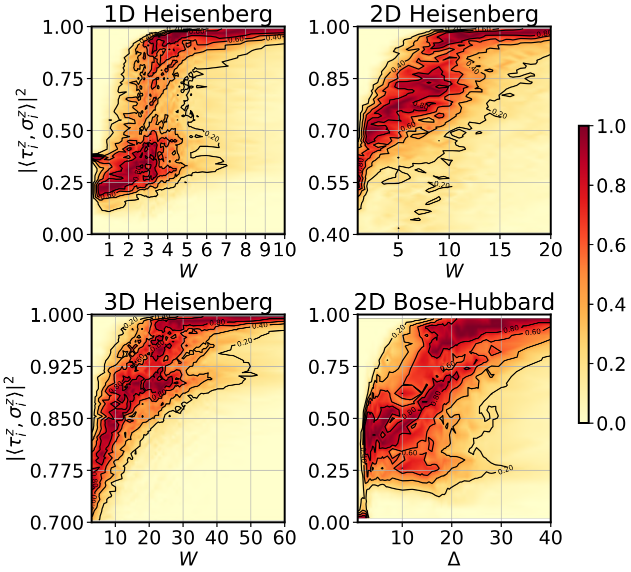

Figure 5.3: Interpolated histograms of $|\langle\tau_i^z,\sigma_i^z\rangle|^2$ at different disorder strengths. The histograms are made of 50 evenly spaced bins (25 for 2D Bose-Hubbard) and are normalized so that at a fixed disorder strength the maximum of the histogram is at a value of 1. The black lines are contour lines corresponding to normalized histogram values of 0.2, 0.4, 0.6, and 0.8.

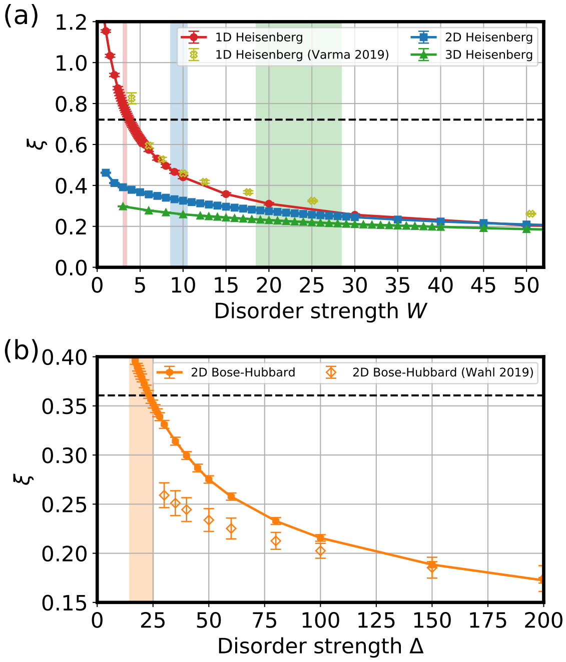

Figure 5.4: The average correlation lengths of our τ_i^z operators versus disorder strength. For comparison, we show average correlation lengths of ℓ-bits obtained by Ref. [112] (Varma 2019) for the 1D model and by Ref. [98] (Wahl 2019) for the 2D Bose-Hubbard model. Horizontal dashed lines are drawn at (a) $\xi = 1/\ln(4)$ and (b) $\xi = 1/\ln(4^2)$; shading indicates our estimates of the transition regions (see Fig. 5.3 and appendix).

5.4 Results and discussion

Using our algorithm, we obtain τ_i^z operators for 1600 random realizations of the disordered Heisenberg models of Eq. (5.1) and for 800 realizations of the disordered hard-core Bose-Hubbard model of Eq. (5.2) [2]. In this section, we present some statistical properties of the (normalized) τ_i^z operators that our algorithm finds after the final iteration of basis expansions (see appendix for earlier iterations).

At high disorder, we find τ_i^z operators that are largely binary and nearly commute with the Hamiltonian for all four models studied (see Fig. 5.2). This is anticipated in an MBL phase where quasilocal operators should be well represented by a small local basis of operators. However, the algorithm's ability to find good ℓ-bits becomes 1–2 orders of magnitude worse with respect to both the commutator norm $\|[H,\tau_i^z]\|^2$ and binarity $\|(\tau_i^z)^2 - I\|^2$ with decreasing disorder strength.

An important statistical quantity that we consider is the overlap $|\langle \tau_i^z, \sigma_i^z \rangle|^2$ [3] (see Fig. 5.3 for their distributions). At high disorder, most τ_i^z operators are localized so that $|\langle \tau_i^z, \sigma_i^z \rangle|^2 \approx 1$, with the distribution

---

[2] We use the same set of (scaled) disorder patterns for all W for a fixed model but different disorder patterns for different models.

[3] Note that when we compute this quantity we use the σ_i^z on the site i with the largest weight (see Eq. (5.5)) rather than the σ_i^z used to initialize the basis B. In general, the τ_i^z operators discovered with our method can "drift" away from their initial site, though this tends to only become significant at low disorder strength (see appendix).

exhibiting a quickly decaying tail away from this value. At low disorder, there are almost no operators with $|\langle \tau_i^z, \sigma_i^z \rangle|^2 \approx 1$; instead most operators have an overlap with a non-zero value significantly below one. For all the models studied, we find a rapid change in the probability distribution of these operator overlaps over a narrow region of disorder; within this region we see hints of bimodality [236, 85, 234] of the probability distribution. We would anticipate that this rapid change signals a "transition."

We find in 1D that the location of this transition region is in good agreement with the accepted location of the MBL-ergodic transition in the range $3 \lesssim W \lesssim 3.5$ [82, 88, 83–85, 93, 245, 46, 246, 211, 110, 109]. Moreover, the transition region of $14.5 \lesssim \Delta \lesssim 25.5$ in the 2D hard-core Bose-Hubbard model is consistent with the critical disorder strength of $\Delta_c^{tn} \approx 19$ estimated by Ref. [98]. The rapid changes in the probability distributions of $|\langle \tau_i^z, \sigma_i^z \rangle|^2$ in the 2D and 3D Heisenberg models and their high overlap at large disorder then suggests that similar MBL transitions exist in these models as well. These transitions happen around $8.5 \lesssim W \lesssim 10.5$ and $18.5 \lesssim W \lesssim 28.5$, respectively. See appendix for details on the estimation of the approximate location of the transition regions.

We note that in 1D, the two peaks of $|\langle \tau_i^z, \sigma_i^z \rangle|^2$ in the transition region are more separated than in higher dimensions. We believe this is due to limitations of the basis size; in 1D, as the basis size $|B|$ grows the separation between the peaks also grows (see appendix) and we expect the same to hold for other models.

Another quantity we use to characterize τ_i^z is the correlation length, shown in Fig. 5.4. We obtain correlation lengths by fitting the function $\tilde{w}_{\mathbf{r}} = e^{-\|\mathbf{r}-\mathbf{r}_i\|/\xi} / (\sum_{\mathbf{r}'} e^{-\|\mathbf{r}'-\mathbf{r}_i\|/\xi})$ to the weight $w_{\mathbf{r}}$ of Eq. (5.5) for the τ_i^z centered at site $\mathbf{r}_i$ using a non-linear least-squares fit [4]. We should note that while this fitting procedure gave sensible results for all models, other reasonable ways of fitting these approximate ℓ-bits were less robust. For a wide range of disorder strengths, our 1D Heisenberg model correlation lengths agree with those obtained by Ref. [112] (see appendix for additional correlation length comparisons). For large disorder strengths, our 2D Bose-Hubbard correlation lengths agree with those obtained by Ref. [98] using shallow 2D tensor networks, but take on larger values at low disorder strength. As shown in Fig. 5.2(b), our ℓ-bits have significantly lower commutator norms, so might be able to more accurately capture the τ_i^z operators near the transition. As expected theoretically, none of the correlation lengths diverge at the "transition." Interestingly, we empirically find that $\xi \approx 1/\ln(4^d)$, where d is the spatial dimension, near the transition region. While the $d = 1$ value agrees with some theoretical predictions [112], we are not aware of expected values of correlation lengths at the transition region in higher d and these values in larger dimensions might be coincidental.

Finally, we note that for the 2D Bose-Hubbard model we see a sharp change in the histogram of $|\langle \tau_i^z, \sigma_i^z \rangle|^2$

---

[4] Note that the summation in the denominator of $\tilde{w}_{\mathbf{r}}$ is only over the positions $\mathbf{r}'$ where $w_{\mathbf{r}'} \neq 0$ and $\mathbf{r}_i \equiv \mathrm{argmax}_{\mathbf{r}} w_{\mathbf{r}}$.

at $\Delta \approx 3$ (see Fig. 5.3) somewhat close to the $\Delta_c^{exp} \approx 5.5(4)$ value obtained experimentally by Ref. [118]. Near this disorder strength the binarity of our ℓ-bits increases sharply and so this behavior could simply be attributed to a breakdown of our algorithm (see appendix); nonetheless, we cannot rule out that the algorithm breaking down near this low Δ is somehow related to the results seen in the experimental systems.

5.5 Outlook

We present an algorithm for constructing high-quality approximations of quasilocal binary integrals of motion and use it to study MBL in four different models. This algorithm works by adaptively building a basis of operators in which to construct the quasilocal integrals of motion (ℓ-bits). Using this algorithm, we find the first theoretical evidence for MBL in three dimensions.

Our algorithm is well suited for studying ℓ-bits in more general settings than has previously been possible. For example, it can be used to construct approximate ℓ-bits for models on complicated lattice geometries, for fermionic models (in which Majorana strings can be used instead of Pauli strings; see Ref. [44]), or for models with potential MBL-MBL transitions [252]. Moreover, using the strategy of Ref. [95], the ℓ-bits constructed with this algorithm could be used to push highly excited states into the ground state. Our algorithm can also be applied beyond MBL to construct localized zero modes in interacting topological systems [217, 44] or (with slight adjustment) to construct unitary operators that commute with given Hamiltonians or symmetries.

Chapter 6

Motif magnetism and quantum many-body scars

This chapter is based on the work presented in Ref. [253], done in collaboration with my advisor Prof. Bryan Clark.

6.1 Introduction

A subsystem of an isolated quantum system tends to equilibrate with the rest of the system, a process known as thermalization. Thermalization generally occurs in quantum systems obeying the eigenstate thermalization hypothesis (ETH) [254–258], which states that energy eigenstates with finite energy density appear thermal and so exhibit thermal properties such as volume-law entanglement entropy. While ETH holds for many quantum systems, known as ergodic systems, it can sometimes be violated. For example, in many-body localized (MBL) systems [259, 81, 82, 79, 232, 77], systems with strong disorder and interactions, all or a significant fraction of eigenstates appear athermal, e.g., exhibit area-law entanglement entropy. In certain non-disordered systems with local constraints, such as the one-dimensional chain of Rydberg atoms recently studied in the experiment in Ref. [260], most eigenstates are thermal and yet a set of measure zero eigenstates in the middle of the spectrum, known as quantum many-body scars, exhibit athermal behavior.

Following the experimental observation in Ref. [260], there has been an extensive search for systems with quantum many-body scars[260–286]. Some scar states have a high overlap with particular product states and have constant energy spacings. These properties imply that the time-evolution of these product states exhibits periodic revivals, a clearly athermal behavior which can be observed experimentally. In contrast, the time-evolution of a generic product state will lead to thermalization, since it has vanishing overlap with scar states. It is useful to find examples of simple Hamiltonians with such scar states so that they can be realized in experiments.

In a series of recent works [188, 287, 278, 288], a large family of spin Hamiltonians with exactly known "projected 3-colored" eigenstates has been found with a number of interesting properties, such as large eigenstate degeneracy and quantum many-body scars [278]. This family of Hamiltonians, which have finetuned XXZ interactions, is built out of a triangle motif. By tiling together triangles, we can build these Hamiltonian on geometries such as the triangular, kagome, hyperkagome, and pyrochlore lattices [188]. The 3-colored Hamiltonian on the kagome lattice appears to be at the intersection of many different phases, which include ordered phases and potential quantum spin liquid phases [188], suggesting that this family of Hamiltonians includes special points in phase diagrams that connect different phases of matter. When the triangle motifs are added together with positive coefficients, the resulting Hamiltonians are frustration-free and the projected 3-colored states are exact ground states, but when the triangle motifs are added together with positive and negative coefficients, the resulting Hamiltonians are frustrated and the projected 3-colored states are exact eigenstates in the middle of the spectrum. These states have log-law entanglement, large overlap with certain product states, and constant energy spacing, making them quantum many-body scars that exhibit periodic revivals [278].

In this work, we generalize the 3-colored Hamiltonians into a larger class of n-colored Hamiltonians. We show that the n-colored Hamiltonians have degenerate "projected spiral colored" eigenstates, which can be made into ground states or quantum many-body scars that exhibit periodic revivals. These Hamiltonians, which involve nearest and next-nearest neighbor XXZ interactions [289, 188], are built out of n-spin motifs, which can be shaped as polygons or polyhedra. We give examples of many types of n-colored lattices that can be built out of such motifs, such as Archmidean tilings and quasicrystal lattices. We provide numerical evidence for the existence of quantum many-body scars with simple periodic revivals in these systems.

6.2 Motif Construction

In this work, we construct Hamiltonians built out of motifs. A motif is a spatial pattern of spins that will be repeated to construct larger structures. In our case, we consider motifs that are polygons and polyhedra with spins at the vertices. For each polygon or polyhedron motif, we associate a motif Hamiltonian. First, we explain how we construct the motif Hamiltonians from a previously studied spin chain Hamiltonian. Then, we describe the nature of the ground states in these motif Hamiltonians, which exhibit "spiral colored" magnetic order.

6.2.1 Motif Hamiltonians

Consider a small, periodic chain of L_p spins. When the spins in the chain are evenly arranged on a circle, we see that they form a regular polygon. For example, a periodic chain of $L_p = 6$ spins forms a regular hexagon. Therefore, a finite length spin chain defines a polygon motif and a spin chain Hamiltonian can be interpreted as a motif Hamiltonian on a polygon motif. Similarly, polyhedron motif Hamiltonians can also be built out of spin chain Hamiltonians by arranging the spins appropriately.

The spin chain Hamiltonians that we use to define our motif Hamiltonians were originally studied by Refs. [289, 290]. These Hamiltonians take the form

$$\hat{H}_p[Q_p] = \sum_{r=1,2} \sum_{i=1}^{L_p} J_r^{XY} (\hat{\sigma}_i^x \hat{\sigma}_{i+r}^x + \hat{\sigma}_i^y \hat{\sigma}_{i+r}^y) + J_r^Z \hat{\sigma}_i^z \hat{\sigma}_{i+r}^z \tag{6.1}$$

where $\hat{\sigma}_i^x, \hat{\sigma}_i^y, \hat{\sigma}_i^z$ are Pauli matrices on site i, the boundary conditions are periodic, L_p is the length of the chain, $Q_p = 2\pi m/L_p$ for $m = 0, \ldots, L_p - 1$ is a free parameter, and the coupling constants satisfy

$$\begin{aligned} \frac{J_1^Z}{J_1^{XY}} &= \cos(Q_p) = -\frac{J_1^{XY}}{4J_2^{XY}} \\ \frac{J_2^Z}{J_2^{XY}} &= \cos(2Q_p) = -1 + \frac{1}{8}\left(\frac{J_1^{XY}}{J_2^{XY}}\right)^2 \end{aligned} \tag{6.2}$$

and $J_2^{XY} > 0$. Note that these Hamiltonians have nearest and next-nearest neighbor exchange and Ising interactions of a particular form. For later convenience, following Ref. [188], we will refer to a two-site

$$J^{XY} (\hat{\sigma}_i^x \hat{\sigma}_j^x + \hat{\sigma}_i^y \hat{\sigma}_j^y) + J^Z \hat{\sigma}_i^z \hat{\sigma}_j^z \tag{6.3}$$

interaction with coupling constants $J^Z/J^{XY} = \alpha$ and $J^{XY} > 0$ ($J^{XY} < 0$) as an antiferromagnetic (ferromagnetic) $XXZ[\alpha]$ bond.

We call the Hamiltonians of Eq. (6.1) with fixed finite L_p *motif Hamiltonians* because of their role in our construction of Hamiltonians built out of motifs. For each polygon or polyhedron motif p, we will associate a potentially different motif Hamiltonian $\hat{H}_p[Q_p]$.

Note that the Hamiltonians in Eq. (6.1) commute with the global z-magnetization operator $\hat{S}_z = \sum_i \hat{\sigma}_i^z$.

6.2.2 Motif Hamiltonian ground states: spiral colored states and projected spiral colored states

The Hamiltonians in Eq. (6.1) have many degenerate ground states[289]. In this degenerate ground state space, there are product states of the form

$$
\begin{aligned}
|\psi_p[Q_p, \phi_p]\rangle &\equiv \bigotimes_{j=0}^{Lp-1} \frac{1}{\sqrt{2}} \left(|\uparrow\rangle_{j+1} + e^{i(Q_p j + \phi_p)} |\downarrow\rangle_{j+1} \right) \\
&= \bigotimes_{j=1}^{L_p} |\gamma_j\rangle_j
\end{aligned} \tag{6.4}
$$

where ϕ_p is an arbitrary angle [289]. These states, which Ref. [289] referred to as "canted spiral" states, are spin waves with the spin at site j pointing in the xy-plane of the Bloch sphere at an angle of $Q_p j + \phi_p$ with the x-axis. Note that the phases $Q_p j = 2\pi m j / L_p$ are N_c-th primitive roots of unity, where $N_c = L_p / \gcd(m, L_p)$. Therefore, each spin state can be labeled with a "color" $\gamma_j = m j N_c / L_p \bmod N_c \in [0, N_c - 1]$ that corresponds to one of the N_c roots of unity. For example, for $L_p = 3, Q_p = 2\pi/3, \phi_p = 0$, the local $|\gamma\rangle$ states are

$$
|0\rangle = (|\uparrow\rangle + |\downarrow\rangle)/\sqrt{2}, \quad |1\rangle = (|\uparrow\rangle + \omega |\downarrow\rangle)/\sqrt{2},
$$
$$
|2\rangle = (|\uparrow\rangle + \omega^2 |\downarrow\rangle)/\sqrt{2},
$$

where $\omega = e^{i2\pi/3}$, and have been called "red", "green", and "blue" states in previous studies[188, 287, 278, 288]. Therefore, we refer to Eq. (6.4) as "spiral colored" states. These states are ground states of Eq. (6.1) with energy

$$
E_p \equiv L_p(J_1^Z + J_2^Z) = -L_p(2 + \cos(2Q_p))J_2^{XY}. \tag{6.5}
$$

Due to the global z-magnetization symmetry of the Hamiltonian, we can construct other states in the ground state space by taking projections of the product state in Eq. (6.4). In particular, the projected spiral colored states

$$
\hat{P}_{S_z} |\psi_p[Q_p, \phi_p]\rangle, \tag{6.6}
$$

where $\hat{P}_{S_z}$ projects onto the S_z quantum number sector of $\hat{S}_z$, are also exact ground states of the motif Hamiltonian in Eq. (6.1). Other degenerate ground states of Eq. (6.1) with anyonic properties are described in Ref. [290].

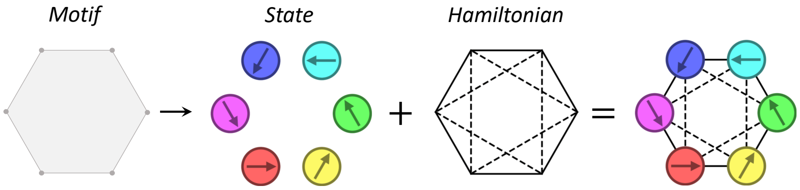

Figure 6.1: An example of a motif state (Eq. (6.4)) and motif Hamiltonian (Eq. (6.1)) for a hexagon motif. The solid (dashed) lines indicate nearest (next-nearest) neighbor spin-spin interactions in the motif Hamiltonian. The colored arrows indicate the orientation of the spins in the spiral colored states on the motifs.

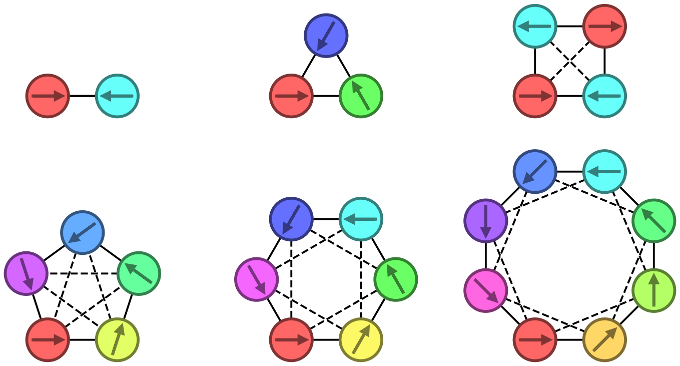

Figure 6.2: Examples of motif states and motif Hamiltonians for motifs of $L_p = 2, 3, 4, 5, 6, 8$ spin regular polygons. The motif states $|\psi_p[Q_p, \phi_p]\rangle$ have $Q_p = 2\pi/L_p, \phi_p = 0$ and so are spiral colored states with $N_c = L_p$ colors, except for the square motif which has $Q_p = \pi$ and is 2-colored.

	Q_p	N_c	J_1^{XY}	J_1^Z	J_2^{XY}	J_2^Z
$L_p = 2$	0	1	-1	-1	—	—
	π	2	1	-1	—	—
$L_p = 3$	0	1	-1	-1	—	—
	$\pm 2\pi/3$	3	1	$-1/2$	—	—
$L_p = 4$	0	1	-1	-1	$1/2$	$1/2$
	$\pm\pi/2$	4	0	0	1	-1
	π	2	1	-1	$1/2$	$1/2$
$L_p = 5$	0	1	-1	-1	$1/4$	$1/4$
	$\pm 2\pi/5$	5	-1	$-1/2\varphi$	$\varphi/2$	$-\varphi^2/4$
	$\pm 4\pi/5$	5	1	$-\varphi/2$	$1/2\varphi$	$1/4\varphi^2$
$L_p = 6$	0	1	-1	-1	$1/4$	$1/4$
	$\pm\pi/3$	6	-1	$-1/2$	$1/2$	$-1/4$
	$\pm 2\pi/3$	3	1	$-1/2$	$1/2$	$-1/4$
	π	2	1	-1	$1/4$	$1/4$
$L_p = 8$	0	1	-1	-1	$1/4$	$1/4$
	$\pm\pi/4$	8	-1	$-1/\sqrt{2}$	$1/\sqrt{8}$	0
	$\pm\pi/2$	4	0	0	1	-1
	$\pm 3\pi/4$	8	1	$-1/\sqrt{2}$	$1/\sqrt{8}$	0
	π	2	1	-1	$1/4$	$1/4$
$L_p \geq 5$	$2\pi m/L_p$	$L_p/\gcd(m, L_p)$	$-\mathrm{sign}(\cos(Q_p))$	$-\lvert\cos(Q_p)\rvert$	$1/(4\lvert\cos(Q_p)\rvert)$	$-\lvert\cos(Q_p)\rvert(\tan(Q_p)^2 - 1)/4$

Table 6.1: The coupling constants $J_1^{XY}, J_1^Z, J_2^{XY}, J_2^Z$ of motif Hamiltonians (Eq. (6.1)) that have spiral colored state ground states (Eq. (6.4)), scaled so that $|J_1^{XY}| = 1$ and $J_2^{XY} > 0$. The spiral colored state wave vector is $Q_p = \pm 2\pi m/L_p$ where $m = 0, 1, \ldots, \lfloor L_p/2 \rfloor$ and N_c is the number of distinct colors in the spiral colored state. The constant $\varphi = (1 + \sqrt{5})/2$ is the golden ratio.

For our purposes, we will only consider motifs with a small number of spins L_p. Fig. 6.1 shows an example of an $L_p = 6$ motif shaped as a hexagon, depicting both the (unprojected) spiral colored state of Eq. (6.4) and the motif Hamiltonian of Eq. (6.1). Fig. 6.2 shows $L_p = 2, 3, 4, 5, 6, 8$ spin motifs shaped as regular polygons. Table 6.1 lists the coupling constants of the motif Hamiltonians[1] and the number of colors for different L_p and Q_p. We point out that the Hamiltonians with 3-colored ground states made from triangular motifs, referred to as the $XXZ0 = XXZ[-1/2]$ model in previous works [291, 188, 41, 287, 278, 288], is a special case ($L_p = 3, Q_p = \pm 2\pi/3$) of the more general family of polygonal motif Hamiltonians with spiral colored ground states considered in this work.

Finally, it is important to note that $|\psi_p[Q_p, \phi_p]\rangle$ and $|\psi_p[-Q_p, \phi_p']\rangle$ for generic[2] Q_p, ϕ_p, and ϕ_p' are linearly independent, but non-orthogonal, ground states of $\hat{H}_p$.

---

[1] Note that for $L_p = 2, 3$ the next-nearest neighbor bonds are actually nearest neighbor bonds and for $L_p = 4$ the next-nearest neighbor bonds are doubled.

[2] If $Q_p = 0$ or π and $\phi_p = \phi_p'$, then $|\psi_p[Q_p, \phi_p]\rangle \propto |\psi_p[-Q_p, \phi_p']\rangle$ are proportional so they are not linearly independent.

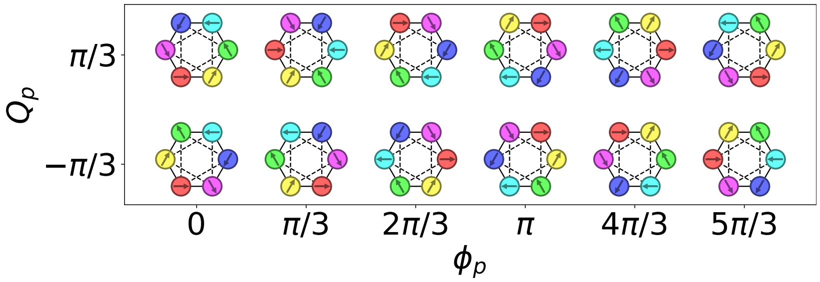

Figure 6.3: Spiral colored states with $Q_p = \pm\pi/3$ and $\phi_p = 2\pi m/L_p$ for $m = 0, \ldots, L_p - 1$ on a hexagonal motif. All of the depicted states are ground states of the same motif Hamiltonian $\hat{H}_p[Q_p] = \hat{H}_p[-Q_p]$ in Eq. (6.1).

6.3 Hamiltonians made from motifs

Here we describe how to construct Hamiltonians on structures built from motifs with projected spiral colored eigenstates. These Hamiltonians can be frustration-free, in which case the projected spiral colored states are ground states on each motif, or frustrated, in which case the states are excited states.

Consider a geometric structure composed of motifs, such as a triangular lattice tiled by triangles. By taking a linear combination of Hamiltonians on those motifs, we can build a Hamiltonian on the entire system. We focus on Hamiltonians of this form with an additional Zeeman term

$$\hat{H} = \sum_p J_p \hat{H}_p[Q_p] - h \sum_i \hat{\sigma}_i^z. \tag{6.7}$$

In order for Eq. (6.7) to have projected spiral colored eigenstates, the $\hat{H}_p[Q_p]$ need to be added together in such a way so that the spiral colored product states $|\psi_p[Q_p, \phi_p]\rangle$ (Eq. (6.4)) on overlapping motifs p agree. In practice, the rules for adding together motif Hamiltonians can be understood through visual inspection: spiral-colored motifs can only be added together if the colors on spins shared between neighboring motifs match (see Fig. 6.4).

First, suppose that $h = 0$. Then the spiral colored states

$$|C\rangle = \bigotimes_j |\gamma_j\rangle_j, \tag{6.8}$$

where $|\gamma_j\rangle_j$ in state $|\psi_p[Q_p, \phi_p]\rangle$ must be the same on each motif p containing site j, are eigenstates of Eq. (6.7). There can be many $|C\rangle$ because of the degeneracy between $|\psi_p[Q_p, \phi_p]\rangle$ and $|\psi_p[-Q_p, \phi'_p]\rangle$ on each motif. For example, in Ref. [188], the authors found that certain lattices built from triangle motifs, such as the kagome lattice, have exponentially many different 3-colorings, i.e., exponentially many linearly

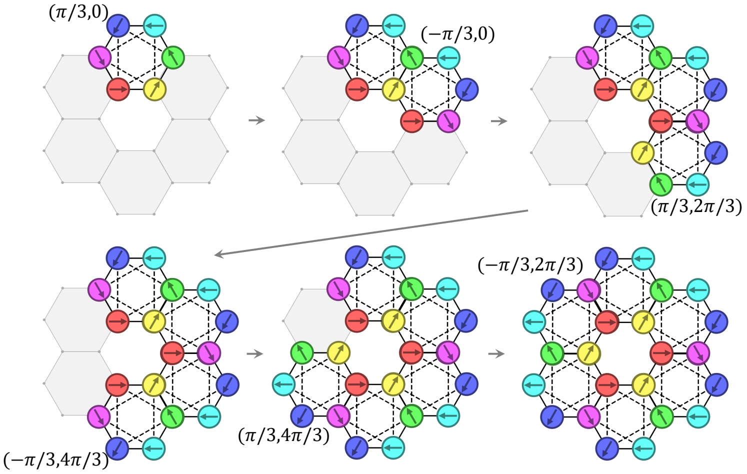

Figure 6.4: An example of how to construct a 6-colored Hamiltonian (Eq. (6.7)) with a spiral colored eigenstate (Eq. (6.8)) using a hexagonal motif. Each newly added hexagon motif p is labelled by the (Q_p, ϕ_p) for the motif spiral colored state $|\psi_p[Q_p, \phi_p]\rangle$ (Eq. (6.4)) on that hexagon (See also Fig. 6.3). Note that no motif Hamiltonian is added to the center hexagon since that hexagon cannot be 6-colored in the appropriate way.

independent $|C\rangle$. When $J_p \geq 0$ for all motifs p, then the spiral colored states $|C\rangle$ are ground states of $J_p \hat{H}_p$ and $\hat{H}$, making Eq. (6.7) a frustration-free Hamiltonian. If however, the J_p alternate in sign, then $|C\rangle$ are excited states of $J_p \hat{H}_p$ and $\hat{H}$ and Eq. (6.7) is frustrated.

Next, suppose that $h > 0$. This breaks the degeneracies in different S_z sectors and makes the product states $|C\rangle$ no longer eigenstates. Instead, the *projected* product states

$$|C_{S_z}\rangle \equiv \frac{\hat{P}_{S_z}|C\rangle}{\|\hat{P}_{S_z}|C\rangle\|} = \frac{1}{\mathcal{N}_{S_z}}\hat{P}_{S_z}|C\rangle, \tag{6.9}$$

where $\mathcal{N}_{S_z}$ is a S_z-sector normalization constant, are eigenstates of Eq. (6.7) with energies $\sum_p J_p E_p - hS_z$. Note, however, that many of the projected spiral colored states are *not* linearly independent. For example, $\hat{P}_{S_z=N}|C\rangle = |\uparrow \cdots \uparrow\rangle$ for all $|C\rangle$ where N is the number of spins in the system. If the Hamiltonian is frustration-free so that $J_p \geq 0$ for all motifs p, then $|\uparrow \cdots \uparrow\rangle$ is the ground state and the $|C_{S_z}\rangle$ are the lowest energy states in each S_z sector. If the Hamiltonian is frustrated so that the J_p alternate in sign, then the $|C_{S_z}\rangle$ are excited states. Ref. [278] showed that projected product states of this form have log-law entanglement entropy, which indicates that the $|C_{S_z}\rangle$ are athermal and for frustrated Hamiltonians in Eq. (6.7) can be quantum many-body scars.

6.4 Results

6.4.1 Examples of spiral colored systems

The Hamiltonian in Eq. (6.7) and its associated spiral colored eigenstates can be realized in many different lattice geometries built out of motifs. In this section we describe how this can be done. First, we begin by analyzing in more detail the properties of the n-spin motifs listed in Table 6.1. Then, we provide examples of different geometries that can be constructed from these motifs.

Bonds. The simplest motif is the 2-spin motif, or bond. In this case, the 2-spin motif Hamiltonian is simply $\hat{H}_p[Q_p] = \mp(\hat{\sigma}_1^x\hat{\sigma}_2^x + \hat{\sigma}_1^y\hat{\sigma}_2^y) - \hat{\sigma}_1^z\hat{\sigma}_2^z$ for $Q_p = 0, \pi$.

When $Q_p = 0$, this is a ferromagnetic Heisenberg bond and the (1-colored) spiral colored state $(|{\uparrow}\rangle_1 + e^{i\phi_p}|{\downarrow}\rangle_1)(|{\uparrow}\rangle_2 + e^{i\phi_p}|{\downarrow}\rangle_2)$, which corresponds to two aligned spins in the xy-plane, is a ground state. Note that this implies that $|+\rangle_i \otimes |+\rangle_j$ is an eigenstate of any Heisenberg bond $\mathbf{S}_i \cdot \mathbf{S}_j$ with energy[3] $+1/4$. This also implies that $|+\cdots+\rangle$ is an exact eigenstate of any Hamiltonian made of only Heisenberg bonds. If all the Heisenberg bonds are ferromagnetic (antiferromagnetic), then $|+\cdots+\rangle$ is the ground state (highest excited state). However, if some bonds are ferromagnetic and some are antiferromagnetic, then $|+\cdots+\rangle$ (and by symmetry $|\chi\cdots\chi\rangle$ for any single-spin state $|\chi\rangle$) would be an eigenstate in the middle of the spectrum and would likely be a quantum many-body scar state.

When $Q_p = \pi$, the 2-spin motif Hamiltonian is an antiferromagnetic XXZ$[-1]$ bond and the (2-colored) state $(|{\uparrow}\rangle_1 + e^{i\phi_p}|{\downarrow}\rangle_1)(|{\uparrow}\rangle_2 + e^{i(\phi_p+\pi)}|{\downarrow}\rangle_2)$, which corresponds to two anti-aligned spins in the xy-plane, is a ground state. The 2-colored XXZ$[-1]$ model is also discussed in Ref. [288].

The $Q_p = 0$ and $Q_p = \pi$ bonds are quantum analogs of ferromagnetic and antiferromagnetic Ising bonds and promote order analogous to ferromagnetic and Néel order, though in the xy-plane. When "spiral coloring" a lattice, the $Q_p = 0$ bond can be added between any two aligned spins and the $Q_p = \pi$ bond can be added between any two anti-aligned spins. By itself, the $Q_p = 0$ bond can 1-color any lattice. Similarly, by itself, the $Q_p = \pi$ bond can 2-color any bipartite graph, such as square, honeycomb lattices (see Fig. 6.5(a)), and pyrochlore lattices.

Regular polygons. The next simplest motifs are regular polygons, shown in Fig. 6.2. The smallest example is the equilateral triangle, made of $L_p = 3$ sites. When $Q_p = \pm 2\pi/3$, the triangle motif Hamiltonian is made of three $XXZ[-1/2]$-bonds and is known as the XXZ0 model [291, 188]. It has 3-colored ground states $(|{\uparrow}\rangle_1 + e^{i\phi_p}|{\downarrow}\rangle_1)(|{\uparrow}\rangle_2 + e^{i(\phi_p \pm 2\pi/3)}|{\downarrow}\rangle_2)(|{\uparrow}\rangle_3 + e^{i(\phi_p \mp 2\pi/3)}|{\downarrow}\rangle_3)$, that correspond to spins at 120° angles from one another in the xy-plane. The 3-colored state has a unique property among the spiral colored states

---

[3] The Heisenberg bond has energy eigenvalues $-3/4, 1/4, 1/4, 1/4$, so $|{+}{+}\rangle$ is in the degenerate $+1/4$ eigenspace of the operator.

on polygons: all permutations of the three colors ($|012\rangle, |021\rangle, |102\rangle, \ldots$) produce valid spiral colored states. This property does not hold for example for a spiral colored state on a hexagon, where for instance $|021345\rangle$ would not be a valid spiral colored state. Note also that there is a constraint that occurs when building lattices out of edge-sharing polygon motifs: $Q_p = -Q_{p'}$ if polygons p and p' share an edge. In some lattices, this constraint cannot be satisfied unless some motifs in the lattice are missing, as can be seen in Fig. 6.4. Finally, note that 4-colored square motifs have vanishing nearest neighbor interactions (see Table 6.1), so cannot be used to construct Hamiltonians with 4-colored spiral colored eigenstates.

Polyhedra. Motifs involving four or more spins can be reshaped in three-dimensions into polyhedra. A natural type of polyhedron motif to consider is an antiprism, a polyhedron that is composed of two parallel copies of a regular polygon connected by an alternating band of triangles. The nearest and next-nearest neighbor interactions in the motif Hamiltonian of Eq. (6.1) act between and within the two parallel polygons, respectively. Fig. 6.6(a) shows an example of an antiprism motif (an octahedron motif). Other types of polyhedra motifs are those that can be built out of polygon motifs. For example, a truncated octahedron motif can be made out of eight hexagon motifs, as shown in Fig. 6.6(b).

Polygon and polyhedron motifs can be combined into many different geometries. Here we list some examples of different geometries of spin systems that can be spiral colored using the motifs that we have described above:

1. *Archimedean tilings.* Archimedean tilings are tilings of the Euclidean plane by regular polygons [292]. Examples of spiral colored Archimedean tilings are shown in Fig. 6.5.

2. *Honeycombs.* Space-filling tesselations of three-dimensional space, or honeycombs, can be constructed out of certain polyhedra [292]. For example, a bitruncated cubic honeycomb can be made up of truncated octahedra.

3. *Lattices with polygons and polyhedra in the unit cell.* The lattices of crystalline materials can have unit cells with polygons or polyhedra in them. For example, in frustrated magnets, the spins can be arranged into a two-dimensional kagome lattice, which has two triangles in a unit cell, or a three-dimensional pyrochlore lattice, which has tetrahedra in its unit cell.

4. *Aperiodic tilings.* Aperiodic patterns, such as those seen in quasicrystals [293, 294], can be built out of simple motifs. Fig. 6.7 shows an example of an aperiodic spiral colored Penrose tiling [295] made from pentagon motifs.

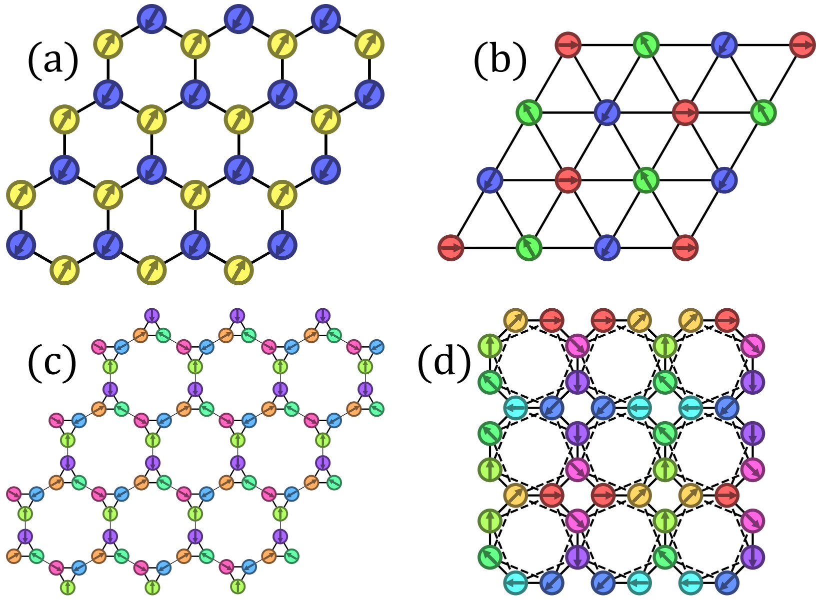

Figure 6.5: Spiral colored Archimedean tilings. (a) A 2-colored Honeycomb lattice made from bond motifs. (b) A 3-colored triangular lattice made from triangle motifs. (c) A 2- and 3-colored truncated Hexagonal tiling lattice made from bond and triangle motifs. (d) An 8-colored square-octagon lattice made from octagon motifs.

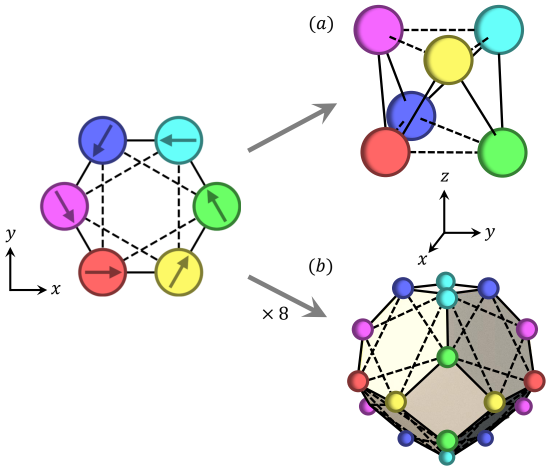

Figure 6.6: Spiral colored states and Hamiltonians on a three-dimensional (a) anti-prism (octahedron) motif and (b) a truncated octahedron motif made from a two-dimensional polygon (hexagon) motif.

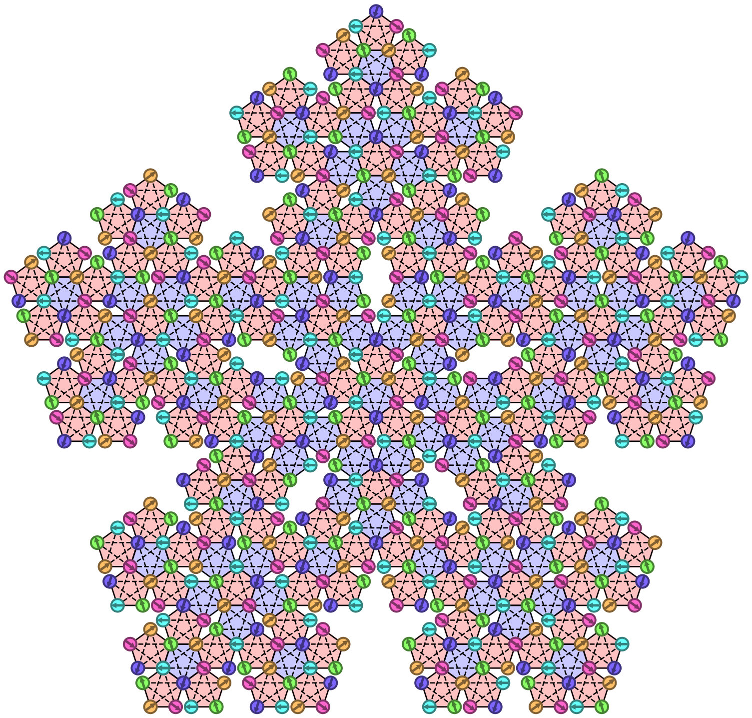

Figure 6.7: A spiral colored state on an aperiodic Penrose diagram made of pentagon motifs. The shaded pentagons have nearest neighbor ferromagnetic $XXZ[1/2\varphi]$ and next-nearest neighbor antiferromagnetic $XXZ[-\varphi/2]$ interactions, where $\varphi = (1+\sqrt{5})/2$ is the golden ratio. Purple (red) pentagons have $Q_p = +2\pi/5$ ($Q_p = -2\pi/5$).

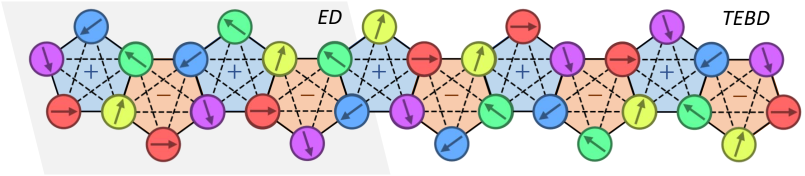

Figure 6.8: A spiral colored state $|C\rangle$ on a chain of pentagons. Projected spiral colored state $|C_{S_z}\rangle \propto \hat{P}_{S_z}|C\rangle$ are quantum many-body scars of the Hamiltonian in Eq. (6.10). Positive (negative) terms in the Hamiltonian are indicated by blue and a "+" (red and a "−"). Our exact diagonalization (ED) calculations were done on the 14 spins in the first 4 pentagons, highlighted in gray. Our time-evolved block decimation (TEBD) calculations were done on the 32 spins in the 10 pentagons shown.

6.4.2 Numerical signatures of quantum many-body scars

In this section, we provide numerical evidence that the projected spiral colored states $|C_{S_z}\rangle$ are quantum many-body scars of frustrated Hamiltonians in Eq. (6.7) and that the scars give rise to periodic revivals when time-evolving from the unprojected $|C\rangle$ state. (See Ref. [278] for a similar analysis for 3-colored states.) We use exact diagonalization (ED) and the time-evolved block decimation (TEBD) algorithm [296] to analyze the eigenstates and study the dynamics of these scar Hamiltonians.

Consider the pentagon chain Hamiltonian in a magnetic field

$$\hat{H} = \sum_{j=1}^{M} (-1)^{j-1} \hat{H}_{p_j}[2\pi/5] - h \sum_{i=1}^{N} \hat{\sigma}_i^z \tag{6.10}$$

where $p_1, \ldots, p_M$ are edge-sharing pentagons arranged into a line as shown in Fig. 6.8. This chain has open boundary conditions and $N = 3M + 2$ spins. The motif Hamiltonians $\hat{H}_{p_j}[2\pi/5]$ are normalized according to the $L_p = 5$ row in Table 6.1. Note that the nearest neighbor bonds shared between pentagons exactly cancel. Also, note that $\hat{H}$ anticommutes with the 180° spatial rotation operator $\hat{R}$, which can be seen by rotating the pentagon chain about its center and noting that the "+" and "−" signs swap so that $\hat{H} \to -\hat{H}$. Since $\{\hat{H}, \hat{R}\} = 0$, each energy E eigenstate $|E\rangle$ has an associated energy $-E$ eigenstate $\hat{R}|E\rangle$.

In our analysis of this model, we will focus on a particular spiral colored state $|C\rangle$ shown in Fig. 6.8. Because of the magnetic field, $|C\rangle$ is not an energy eigenstate of the Hamiltonian, but the projected $|C_{S_z}\rangle$ states are, with energies $-hS_z$. The $|C_{S_z}\rangle$ states are in the middle of the spectrum of their own S_z sectors, suggesting that they are scar states. Since $|C\rangle$ is a linear combination of these states, it inherits their athermal properties. To verify the nature of the scar states in this system, we will check that: (1) generic energy eigenstates of Eq. (6.10) are thermal, (2) the $|C_{S_z}\rangle$ states are athermal, and (3) that the time evolution of the product state $|C\rangle$, which only has non-zero weight on scar states, exhibits periodic revivals unlike the time evolution of a random product state, which rapidly thermalizes.

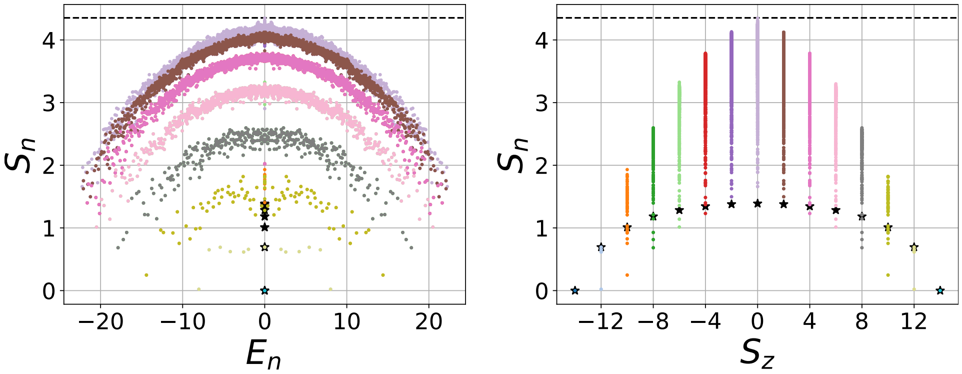

Figure 6.9: **Left:** The half-cut entanglement entropy S_n of the energy eigenstates of $|\psi_n\rangle$ of the pentagon chain Hamiltonian in Eq. (6.10) with $h = 0$ versus energy E_n, computed using ED on 14 spins. Different colors correspond to different S_z sectors. **Right:** Entropy S_n versus S_z quantum number. The black stars correspond to the entropies of the projected spiral colored states $|C_{S_z}\rangle$. The black dashed line corresponds to the average half-cut entropy of a Haar-random pure state.

First, we use full ED on the 14-spin pentagon chain shown in Fig. 6.8 to compute the properties of the energy eigenstates. Fig. 6.9 shows the von-Neumann half-chain entanglement entropy $S_n = -\text{tr}(\rho_n \log \rho_n)$ for each eigenstate $|\psi_n\rangle$ $[\rho_n = \text{tr}_{\{j=N/2+1,\ldots,N\}}(|\psi_n\rangle\langle\psi_n|)]$ in each S_z sector. The half-cut entropies of the $|C_{S_z}\rangle$ states are marked with black stars and the average half-cut Page entropy for a Haar-random pure state[297] $S_{avg} = N/2 \log 2 - 1/2$ is marked with a black dashed line for reference. The entropies of the $|\psi_n\rangle$ eigenstates with E and S_z near zero are close to the Page entropy. We also compute the average level-spacing ratio $r_n = \frac{\min(E_n - E_{n-1}, E_{n+1} - E_n)}{\max(E_n - E_{n-1}, E_{n+1} - E_n)}$, where E_n are the ordered energy eigenvalues, for the energy eigenstates in each S_z sector. For an ergodic Hamiltonian, $\langle r\rangle$ is expected to be near the Gaussian orthogonal ensemble (GOE) value of $r_{GOE} = 0.5307$, while for an integrable model, it is expected to be near the Poisson value of $r_{Poisson} = 0.3863$. We find that $\langle r\rangle_{S_z}$ are within a few error bars of r_{GOE} for $S_z = \pm 8, 6, 4, 2$, but not $S_z = 0$ (see Fig. 6.10). We believe that this is due to a hidden symmetry in the $S_z = 0$ sector that we did not take into account in our analysis, which can make $\langle r\rangle$ approach the $r_{Poisson}$ value. The large entanglement of generic finite energy density eigenstates and the GOE level-spacing statistics in most S_z sectors provide strong evidence that Eq. (6.10) is an ergodic Hamiltonian with mostly thermal eigenstates.

Next, we compute the half-cut entanglement entropies of the energy eigenstates and the $|C_{S_z}\rangle$ states, shown in Fig. 6.9. Through ED, we find that the 14-spin Hamiltonian has a degeneracy of 1, 2, 9, 2, 23, 2, 37, 128, 37, 2, 23, 2, 9, 2, 1 at zero energy for $S_z = -14, \ldots, 14$. Due to this degeneracy, the zero energy eigenstates obtained through numerical diagonalization can be arbitrary linear combinations of the degenerate states and have ill-defined entropies, which is why there is not perfect agreement between the numerical and exact $|C_{S_z}\rangle$ eigenstates in Fig. 6.9. Nonetheless, we numerically verify that the $|C_{S_z}\rangle$ states

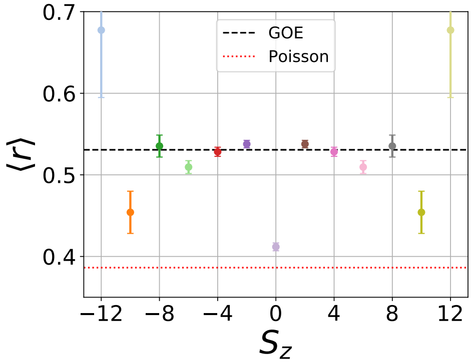

Figure 6.10: The average level-spacing ratio $\langle r \rangle$ in each S_z quantum number sector of the pentagon chain Hamiltonian depicted in Fig. 6.8, computed using ED on 14 spins. The error bars are standard errors of the mean.

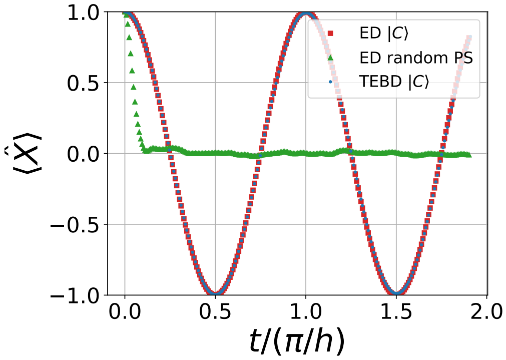

Figure 6.11: The expectation value of $\hat{X} = \hat{\sigma}_6^x$ under the pentagon chain Hamiltonian with $h = 0.5$ using $|C\rangle$ and a random product state whose 6th spin is set to $|+\rangle$ as initial conditions. The $|C\rangle$ evolution was computed using ED for 14 spins and TEBD for 32 spins.

are exact eigenstates of Eq. (6.10) with energies in the middle of the spectra and with low entanglement entropy far from the Page value. This indicates that the $|C_{S_z}\rangle$ are athermal eigenstates.

Finally, we examine the time-evolution of our system with different initial product states to see how the athermal nature of the scar states manifests itself in dynamics that can be observed experimentally. First, we consider the initial state $|C\rangle$. Since it is a superposition of scar states $|C_{S_z}\rangle$ at different S_z with energies $-hS_z$, the time-evolved state will be

$$|\psi(t)\rangle = e^{-it\hat{H}}|\psi(0)\rangle = \sum_{S_z} \mathcal{N}_{S_z} e^{ithS_z} |C_{S_z}\rangle. \tag{6.11}$$

This state exhibits periodic revivals, which can be detected by measuring local observables. For example, the x-magnetization of a single spin will oscillate

$$\langle\psi(t)|\,\hat{\sigma}_i^x\,|\psi(t)\rangle = \sum_{S_z,S_z'} \mathcal{N}_{S_z'}^*\mathcal{N}_{S_z}e^{ith(S_z-S_z')}\left\langle C_{S_z'}\right|\hat{\sigma}_i^x\left|C_{S_z}\right\rangle \tag{6.12}$$

with a period $T=\frac{2\pi}{h\Delta S_z}=\frac{\pi}{h}$ since $\left\langle C_{S_z'}\right|\hat{\sigma}_i^x\left|C_{S_z}\right\rangle \neq 0$ only when $S_z'=S_z\pm 2$. As discussed in the appendix, during the time-evolution, the spins in $|C\rangle$ precess around the z-axis at frequency $2\pi/T$ so $|C(t)\rangle = e^{-it\hat{H}}|C\rangle$ remains as a product state.

Using ED on the 14-spin pentagon chain and TEBD on the 32-spin chain (using the ITensor library [141]), we compute Eq. (6.12) for the $i=6$ spin, which is initially in the $|+\rangle$ state (see Fig. 6.11). We clearly see the characteristic revival with period $T=\pi/h$. Next, we consider using a random product state whose $i=6$ spin is set to $|+\rangle$ as the initial state. As shown in Fig. 6.11, the same observable for the random product state quickly decays to zero, signaling thermalization.

6.5 Conclusions and outlook

We introduced a large family of Hamiltonians with exact projected spiral colored eigenstates built out of n-spin motifs. We showed that these Hamiltonians can be frustration-free so that these states are ground states or frustrated so that they are quantum many-body scars.

The spiral colored Hamiltonians have simple two-local interactions, can be realized in many different geometries, and generate periodic revival dynamics for simple initial product states. These features make these models promising candidates for experimental observation of quantum many-body scars. One option would be to find a magnetic material with spiral colored physics and observe its dynamics from an initially polarized state in an applied magnetic field [278]. Another option would be to simulate the periodic revival dynamics of these spiral colored Hamiltonians using a cold atom quantum simulator [33] or a digital quantum computer [67]. In these dynamics experiments, one could also examine how robust the periodic revivals are to different perturbations to the Hamiltonian.

It would also be interesting to explore the connections of these spiral colored Hamiltonians with frustrated magnetism and spin liquid physics. It is possible that previously studied two and three-dimensional magnetic Hamiltonians are close enough to the spiral colored models so that they inherit some of their low-temperature properties from the spiral colored states. It is also possible that there exist models on lattices with exponentially many spiral colored ground states, like the 3-colored kagome model with exponentially degenerate 3-colorings, which could potentially be close to a quantum spin liquid phase.

Finally, the techniques developed here could be used to find new families of Hamiltonians with exact scar states. For example, by using motif Hamiltonians with valence bond ordered ground states, such as the Majumdar-Ghosh model [186, 187], families of Hamiltonians with valence bond solid scar states could be built. More generally, motif Hamiltonians with specific desired eigenstates could be built using eigenstate-to-Hamiltonian algorithms [42, 41, 43] or parent Hamiltonian techniques [24, 26] and could be used to design many new families of scar models built from motifs.

Chapter 7

Conclusions, outlook, and future work

In this thesis, we discussed inverse methods for designing Hamiltonians with desired eigenstates and symmetries. We used these methods to study the physics of topological phases of matter, such as spin liquids and Majorana zero modes. We also developed new methods to probe the physics of many-body localization in greater than one dimension. Here we will summarize our main results and discuss our outlook on future work in these areas.

7.1 Eigenstate-to-Hamiltonian construction

We and others [41–43, 37] developed the eigenstate-to-Hamiltonian construction (EHC) algorithm that is able to find local Hamiltonians in polynomial time with a desired quantum state as an eigenstate. In Chapter 3, we benchmarked the EHC algorithm on seven one and two-dimensional quantum systems and showed how it could be used to find non-trivial new parent Hamiltonians, to find Hamiltonians with degenerate ground state, or to expand ground state phase diagrams.

Since our work in this area, others have used the EHC algorithm for applications in Hamiltonian learning [39], variational optimization [53, 52], and many-body localization [49–51]. In addition, extensions of the EHC algorithm for finding Hamiltonians [37] and Liouvillians [48] from steady states were developed.

It will be exciting to see how the EHC algorithm will be used to find new physics. A potential application of EHC is to find new quantum spin liquid Hamiltonians from known spin liquid wave functions, such as the resonating valence bond state [147, 148] or projective symmetry group wave functions [57]. While we attempted such EHC calculations, we had difficulties in interpreting the results of our calculations, discussed in Appendix E. These difficulties will be important to overcome for finding spin liquid Hamiltonians and in other future applications of EHC. A potential path forward for using EHC to find parent Hamiltonians is discussed in Appendix F. We also believe that it will be important future work to build a deeper understanding of the spectral properties of the quantum covariance matrix, since it plays a key part of the EHC method.

7.2 Symmetric Hamiltonian construction

We developed the symmetric Hamiltonian constuction (SHC) algorithm [41], based on the slow operator method [45], that is able to find local Hamiltonians in polynomial time with a desired symmetry operator. In Chapter 4, we show how the method can be used to design Z_2 quantum spin liquid Hamiltonians from Wilson loop operators and large families of superconducting Hamiltonians with desired Majorana zero modes.

The quantum spin liquid Hamiltonians that we found with SHC have unusual properties not seen in previously studied models, such as non-integrability and no local integrals of motion. This demonstrates that the method can be used to discover new topological ordered systems. It will be exciting future work to provide as input other symmetry operators to SHC to look for topological Hamiltonians with different types of anyons, such as the anyons in the double-semion model or Fibonnaci anyons [59].

The zero mode Hamiltonians that we found form a large class of fermionic Hamiltonians that have the potential to be realized experimentally. It would be interesting to see if these Hamiltonians could be implemented in superconducting devices or if they could be used to inform the design of new MZM systems. It would also be exciting to see how time-dependent versions of these Hamiltonians could be used to realize and study protocols for braiding Majorana [298].

There is also work that can be done to improve or extend the SHC method. Similar complications as stated in Appendix E for EHC also arise in SHC, which will need to be addressed to make future progress. In addition, the SHC method is only efficient if the symmetries and Hamiltonians considered are local, so that they can be represented in a small basis of operators. While this is true in the examples we consider, it will be important to find other interesting problems with this locality restriction or to see if the restriction can be relaxed without excessive computational overhead. We have explored this idea in our work on ℓ-bits, where we found an SHC-like algorithm for finding local binary integrals of motion.

7.3 Many-body localization in higher dimensions

By adapting techniques from the SHC method, we developed an algorithm for constructing local binary integrals of motion, which we used to find approximate ℓ-bits – the key phenomenological quantity in many-body localized (MBL) systems. In Chapter 5, we demonstrate that this algorithm can successfully find good ℓ-bits for four different models in one, two, and three-dimensions. By looking at the properties of these ℓ-bits, we observe a transition from an MBL phase to an ergodic phase as a function of disorder strength, signaled by an abrupt change in the nature of the ℓ-bits. The results in one and two dimensions agree with previous work, which validates our approach. The results in three dimensions provide the first theoretical evidence for MBL physics in three-dimensions.

There are paths forward for using these techniques to study MBL and other phenomena. It would be interesting to apply our algorithm to study MBL in two-dimensional systems that have not been previously studied, such as disordered Heisenberg models on lattices with geometric frustration such as the kagome lattice. In addition, the algorithm that we developed, which is heuristic, can likely be significantly improved. An improved algorithm could gather more accurate results, particularly near the MBL-ergodic transition where the ℓ-bits change most dramatically. This method could also be used to study local integrals of motion in other systems, such as interacting generalizations of Majorana zero modes in interacting topological superconductors.

There is still much to learn about many-body localization in higher dimensions. We need more numerical methods able to probe ℓ-bits or simulate dynamics in two and three-dimensional systems in order to perform finite-size scaling studies. In addition, the field of MBL will benefit greatly from the continued improvement in quantum simulators and quantum computers. Using this technology, it will soon be possible to perform accurate dynamics simulations with more qubits than can be simulated classically. Such simulations could provide clear experimental evidence for the existence (or lack there-of) of MBL in higher dimensions.

Appendix A

From eigenstates to Hamiltonians

A.1 Degenerate Eigenstate-to-Hamiltonian Construction

Here we present Degenerate Eigenstate-to-Hamiltonian Construction (DEHC), a generalization of the EHC method for constructing Hamiltonians with multiple target states as degenerate energy eigenstates.

In this formulation, the input is a set of Hermitian operators $\{\hat{h}_a\}_{a=1}^{d_T}$ and M target states $|\psi_{T,1}\rangle, \ldots, |\psi_{T,M}\rangle$. However, first, we describe the method by considering using a target density matrix $\hat{\rho}_T$ as input rather than the set of target states. Then, we discuss how the density matrix can be defined in terms of our target states to achieve the desired result. Using the density matrix $\hat{\rho}_T$, we can define the density matrix quantum covariance matrix (DQCM), a generalization of the QCM, whose matrix elements are

$$(D_T)_{ab} = \langle \hat{h}_a \hat{h}_b \rangle_T - \langle \hat{h}_a \rangle_T \langle \hat{h}_b \rangle_T \tag{A.1}$$

where the expectation values are defined by a trace over the target density matrix: $\langle \hat{\mathcal{O}} \rangle_T \equiv \operatorname{tr}\left(\hat{\rho}_T \hat{\mathcal{O}}\right)$. The D_T matrix, like the QCM C_T discussed in the main text, is Hermitian and positive semi-definite.

Despite the apparent similarity of the DQCM to the QCM, the null space of the DQCM has a different interpretation than that of the QCM. To see this, consider a vector of coupling constants J_a in the null space of D_T. This vector corresponds to a Hamiltonian $\hat{H} = \sum_{a=1}^{d_T} J_a \hat{h}_a$ with energy eigenstates $|n\rangle$. Let us express the target density matrix in terms of the eigenstates of $\hat{H}$ so that $\hat{\rho}_T = \sum_{m,n} \rho_{mn} |m\rangle \langle n|$, where the normalization is such that $\operatorname{tr}(\hat{\rho}_T) = \sum_n p_n = 1$ where $p_n \equiv \rho_{nn} \geq 0$. Since J_a is in the null space of D_T, the Hamiltonian $\hat{H}$ has zero energy variance, which can be expressed as

$$\begin{aligned}
\sigma_T^2 &= \operatorname{tr}\left(\hat{\rho}_T \hat{H}^2\right) - \operatorname{tr}\left(\hat{\rho}_T \hat{H}\right)^2 \\
&= \sum_n p_n E_n^2 - \left(\sum_n p_n E_n\right)^2 \\
&= \sum_n p_n E_n \left(E_n - \sum_m p_m E_m\right) = 0
\end{aligned} \tag{A.2}$$

where the E_n are the energy eigenvalues of $|n\rangle$. For Eq. (A.2) to be satisfied, each term in the summation needs to be zero, which occurs when $E_n = \langle \hat{H} \rangle_T = \sum_m p_m E_m =$ constant for all n for which $p_n > 0$. This means that the states $|n\rangle$ with $p_n > 0$ in the density matrix are degenerate eigenstates of the Hamiltonian $\hat{H}$. Therefore, it becomes apparent that the null space of the DQCM corresponds to a space of Hamiltonians that contain multiple target wave functions as degenerate energy eigenstates. Finally, we can invert this perspective, and use a set of target states $|\psi_{T,1}\rangle, \ldots, |\psi_{T,M}\rangle$ to define our target density matrix $\hat{\rho}_T = \sum_{m=1}^{M} p_m |\psi_{T,m}\rangle \langle \psi_{T,m}|$ with $p_m > 0$ and $\sum_{m=1}^{M} p_m = 1$. Note that in DEHC the target states need not be orthogonal to one another, only linearly independent, and that the choice of p_m does not affect the null space of the DQCM. We always used $p_1 = \cdots = p_M = 1/M$ in our calculations.

When we compute the DQCM, we find it useful to break up the calculation into individual calculations for each target state. From Eq. (A.1) and our definition for the target density matrix, the DQCM can be expressed in terms of the target states $|\psi_{T,m}\rangle$ as follows

$$(D_T)_{a,b} = \sum_{m=1}^{M} p_m \langle \hat{h}_a \hat{h}_b \rangle_{T,m} - \left(\sum_{m=1}^{M} p_m \langle \hat{h}_a \rangle_{T,m} \right) \left(\sum_{m'=1}^{M} p_{m'} \langle \hat{h}_b \rangle_{T,m'} \right) \tag{A.3}$$

where $\langle \hat{\mathcal{O}} \rangle_{T,m} \equiv \langle \psi_{T,m} | \hat{\mathcal{O}} | \psi_{T,m} \rangle / \langle \psi_{T,m} | \psi_{T,m} \rangle$ is an expectation value for a single target state $|\psi_{T,m}\rangle$. We emphasize that calculating the DQCM with Eq. (A.3) is different than calculating many QCMs $C_{T,1}, \ldots, C_{T,M}$. Moreover, the intersection of the null spaces of $C_{T,1}, \ldots, C_{T,M}$ correspond to Hamiltonians with the target states as simultaneous eigenstates, but not necessarily degenerate eigenstates. Numerically, one can compute the DQCM with matrix product states and variational Monte Carlo, just as described in the main text.

A.2 Uniform frustrated Ising state eigenstate space

For the uniform frustrated Ising (UFI) state $|\psi_{UFI}\rangle$, which is a uniform superposition of the ground states of a frustrated antiferromagnetic Ising model on a two-leg triangular ladder, we found a 21 dimensional space of Hamiltonians with $|\psi_{UFI}\rangle$ as an eigenstate using EHC. In the main text, we discussed three of these Hamiltonians, $\hat{H}_I, \hat{H}_{UFI}^{(1)}$ and $\hat{H}_{UFI}^{(2)}$. Here we present additional operators that we found.

We were able to identify the following operators in the target space we considered:

$$\sum_{i=1}^{N} \sigma_i^z + \frac{1}{3}\sigma_i^z \sigma_{i+1}^z \sigma_{i+2}^z$$
$$\sum_{i=1}^{N} \sigma_i^z - \frac{1}{2}\sigma_i^z \sigma_{i+1}^z \sigma_{i+3}^z - \frac{1}{2}\sigma_i^z \sigma_{i+2}^z \sigma_{i+3}^z$$
$$\sum_{i=1}^{N} \sigma_i^z - \sigma_i^x \sigma_{i+2}^z + \sigma_i^z \sigma_{i+2}^x - \sigma_i^z \sigma_{i+2}^z \sigma_{i+3}^z$$
$$\sum_{i=1}^{N} \sigma_i^x + \sigma_i^x \sigma_{i+1}^z \sigma_{i+2}^z + \sigma_i^x \sigma_{i+1}^z \sigma_{i+3}^z + \sigma_i^x \sigma_{i+2}^z \sigma_{i+3}^z$$
$$\sum_{i=1}^{N} \sigma_i^x + \sigma_i^z \sigma_{i+1}^z \sigma_{i+2}^x + \sigma_i^z \sigma_{i+1}^z \sigma_{i+3}^x + \sigma_i^z \sigma_{i+2}^z \sigma_{i+3}^x$$
$$\sum_{i=1}^{N} \sigma_i^x \sigma_{i+1}^z \sigma_{i+3}^x + \sigma_i^y \sigma_{i+1}^z \sigma_{i+3}^y + \sigma_i^x \sigma_{i+2}^z \sigma_{i+3}^x + \sigma_i^y \sigma_{i+2}^z \sigma_{i+3}^y$$
$$\sum_{i=1}^{N} \sigma_i^x \sigma_{i+1}^x \sigma_{i+2}^x - \sigma_i^x \sigma_{i+1}^y \sigma_{i+2}^y - \sigma_i^y \sigma_{i+1}^x \sigma_{i+2}^y - \sigma_i^y \sigma_{i+1}^y \sigma_{i+2}^x$$
$$\sum_{i=1}^{N} \sigma_i^x \sigma_{i+1}^x \sigma_{i+3}^z - \sigma_i^y \sigma_{i+1}^y \sigma_{i+3}^z - \sigma_i^z \sigma_{i+2}^x \sigma_{i+3}^x + \sigma_i^z \sigma_{i+2}^y \sigma_{i+3}^y$$
$$\sum_{i=1}^{N} \sigma_i^x \sigma_{i+1}^x \sigma_{i+2}^z - \sigma_i^y \sigma_{i+1}^y \sigma_{i+2}^z - \sigma_i^z \sigma_{i+1}^x \sigma_{i+2}^x - \sigma_i^z \sigma_{i+1}^y \sigma_{i+2}^y.$$

The UFI state is a zero energy eigenstate of each of these operators and any linear combination of them. These operators, as well as $\hat{H}_{UFI}^{(1)}$ and $\hat{H}_{UFI}^{(2)}$, seem to enforce constraints on the spin configurations making up the UFI state. This might be related to the up-up-down constraint used to construct the state. We note that at least some of the Hamiltonians of the form $H_I + J_1\hat{H}_{UFI}^{(1)} + J_2\hat{H}_{UFI}^{(2)}$ for non-zero J_1 and J_2 have $|\psi_{UFI}\rangle$ as a ground states, but we did not exhaustively determine the ground state manifold.

A.3 Additional examples of phase expansion

Here we present additional results obtained by using EHC and DEHC to construct new parent Hamiltonians with the same ground states as known model Hamiltonians. A summary of these results are shown in Table A.1.

Target state(s)	d_T	Dim. e.s. space	Dim. g.s. manifold
$\lvert\psi_{KC}^{\pm}\rangle$	210	77	≥ 22
$\lvert\psi_H\rangle$	198	39	≥ 3
$\lvert\psi_{SD}^{\pm}\rangle$	198	108	≥ 36

Table A.1: A summary of phase expansion results obtained in this work that are not presented in detail in the main text. Target states and the dimensions of the input target space, the output eigenstate space, and the ground state manifold are listed. Each of these examples were for length $N = 12$ chains. For each of the ground state manifolds, we could only identify a lower bound for its dimensionality.

A.3.1 Kitaev chain ground states

In this section, we discuss our results of using the DEHC method to construct parent Hamiltonians for the ground state of the Kitaev chain model of superconducting spinless fermions: $\hat{H}_{KC} = \sum_{i=1}^{N-1}\left(-c_i^\dagger c_{i+1} + c_i c_{i+1} + h.c.\right)$. This Hamiltonian is known to have two zero energy single-particle edge modes and, correspondingly, two degenerate many-body ground states [202]. We specify the two degenerate ground states $|\psi_{KC}^{\pm}\rangle$ of $\hat{H}_{KC}$ as the target states $|\psi_{T,1}\rangle$ and $|\psi_{T,2}\rangle$ provided as input to DEHC. We obtain matrix product state representations of these states by performing DMRG on a finite size chain of $N = 12$ sites.

The target space of Hamiltonians that we provide as input to DEHC is the d_T-dimensional space spanned by all possible one and two-site operators of the form

$$n_i, \quad (c_i^\dagger c_j + h.c.), \quad (c_i c_j + h.c.), \quad n_i n_j \tag{A.4}$$

where $d_T = N + 3\binom{N}{2} = N + 3N(N-1)/2 = 210$ for the $N = 12$ site chain. By examining the null space of the DQCM matrix, we found that the eigenstate space of Hamiltonians was spanned by 77 operators of four types. Three types of operators we found were

$$\begin{aligned}
\hat{H}_{KC}^{(0,i)} &= \left(-c_i^\dagger c_{i+1} + c_i c_{i+1} + h.c.\right) \\
\hat{H}_{KC}^{(1,i)} &= \frac{1}{2}\left(c_i c_{i+1} + h.c.\right) + n_i n_{i+1} - \frac{1}{2}\left(n_i + n_{i+1}\right) \\
\hat{H}_{KC}^{(2,j)} &= \frac{1}{2}\left(-c_j^\dagger c_{j+2} + c_j c_{j+2} + h.c.\right) - n_{j+1}
\end{aligned} \tag{A.5}$$

for $1 \leq i \leq N-1$ and $1 \leq j \leq N-2$. There are $N - 1 = 11$ operators of type $\hat{H}_{KC}^{(0,i)}$ and $\hat{H}_{KC}^{(1,i)}$ and $N - 2 = 10$ operators of type $\hat{H}_{KC}^{(2,i)}$. The energy eigenvalues of $|\psi_{KC}^{\pm}\rangle$ for $\hat{H}_{KC}^{(0,i)}, \hat{H}_{KC}^{(1,i)}$, and $\hat{H}_{KC}^{(2,j)}$ are $-1, -1/2$, and $-1/2$, respectively. Moreover, we numerically verified that the target states are exact ground states of each of the $\hat{H}_{KC}^{(0,i)}, \hat{H}_{KC}^{(1,i)}$ operators and that $[\hat{H}_{KC}^{(0,i)}, \hat{H}_{KC}^{(1,i)}] = 0$. The structure of these operators, i.e., that they involve only local one and two-site operators, is consistent with the fact that the Kitaev chain is frustration-free and that the two degenerate ground states of $\hat{H}_{KC}$ can be expressed as product states over the sites [217].

In addition to the operators presented in Eq. (A.5), we find non-local operators also contained in the eigenstate space:

$$\hat{H}_{KC}^{(3,k,l)} = \sum_{\delta=0,1} \left(-c_{k+\delta}^{\dagger} c_{l-\delta} + (-1)^{\delta} c_{k+\delta} c_{l-\delta} + h.c. \right) \tag{A.6}$$

where $1 \leq k \leq N-3$ and $k+3 \leq l \leq N$. There are $(N-2)(N-3)/2 = 45$ of the $\hat{H}_{KC}^{(3,k,l)}$ operators for the $N = 12$ chain. Note that these operators, unlike the ones from Eq. (A.5), are not nearest-neighbor, but can connect sites separated by distances of up to $N/2$. The $|\psi_{KC}^{\pm}\rangle$ states are zero energy eigenstates of these operators.

To demonstrate a non-trivial ground state manifold that exists in the eigenstate space spanned by the above operators, we considered an interacting chain with next-nearest neighbors of the form

$$\sum_{i=1}^{N-1} \left(t\hat{H}_{KC}^{(0,i)} + U\hat{H}_{KC}^{(1,i)} \right) + t' \sum_{j=1}^{N-2} \hat{H}_{KC}^{(2,j)}. \tag{A.7}$$

Using DMRG on a length $N = 12$ chain, we empirically determined that the Kitaev chain ground states $|\psi_{KC}^{\pm}\rangle$ are also degenerate ground states of Eq. (A.7) for $t > 0$ and $U/t \gtrsim 2[(t'/t)^2 - 1]$. At $t' = 0$, this model corresponds to a previously discovered interacting Kitaev chain model described by Ref. [217].

Many physically reasonable Hamiltonians on various lattice geometries, such as open square lattices, ladders, and cylinders, with interactions and anisotropy can be constructed from the operators in this space, all with the one-dimensional $|\psi_{KC}^{\pm}\rangle$ states as degenerate eigenstates and possibly many with them as ground states. For example, the Hamiltonian

$$\sum_{i=1}^{N/2-1} \left(t_{\parallel}\hat{H}_{KC}^{(0,2i)} + U_{\parallel}\hat{H}_{KC}^{(1,2i)} \right) + t_{=} \sum_{i=1}^{N/2-2} \hat{H}_{KC}^{(3,2i,2i+3)} + t_{\times} \sum_{j=1}^{N-2} \hat{H}_{KC}^{(2,j)}, \tag{A.8}$$

which is constructed from the above operators, forms a particular interacting two-leg ladder model that has the $|\psi_{KC}^{\pm}\rangle$ states as degenerate eigenstates.

A.3.2 Heisenberg chain ground state

In this section, we discuss our results of using EHC to find new parent Hamiltonians for the ground state $|\psi_H\rangle$ of the Heisenberg chain: $\hat{H}_H = \sum_{n=1}^{N} \mathbf{S}_n \cdot \mathbf{S}_{n+1}$. The target space we provided as input to the EHC method was the same as for the XX chain discussed in the main text, i.e., it was spanned by all possible two-site spin interactions of the form $\{S_n^x S_m^x, S_n^y S_m^y, S_n^z S_m^z\}$, where S^x, S^y, S^z are spin-1/2 operators and $n, m = 1, \ldots, N$. Applying the EHC method to an $N = 12$ length chain, we found an eigenstate space of $|\psi_H\rangle$ of dimension $3N + 3 = 39$. In this space we found $3N = 36$ operators related to conserved quantities, discussed in a later section. The three remaining Hamiltonians in this space are

$$\hat{H}_H^{(a)} = \sum_{n=1}^{N} f^a(n) \mathbf{S}_n \cdot \mathbf{S}_{n+1}, \tag{A.9}$$

where $f^a(n) = 1, \cos(2\pi n/N), \sin(2\pi n/N)$ for $a = 0, 1, 2$, respectively. The state $|\psi_H\rangle$ is a zero energy eigenstate of the sinusoidally modulated Hamiltonians $\hat{H}_H^{(1)}, \hat{H}_H^{(2)}$. Using DMRG, we studied the following Hamiltonians

$$\hat{H}_H + \alpha \hat{H}_H^{(1)} + \beta \hat{H}_H^{(2)}, \tag{A.10}$$

and empirically found that the $|\psi_H\rangle$ state is a ground state in the region $\alpha^2 + \beta^2 \leq 1$. We also verified numerically for small finite sizes that $\hat{H}_H, \hat{H}_H^{(1)}, \hat{H}_H^{(2)}$ all do not commute with one another.

A.3.3 Majumdar-Ghosh model (singlet dimer) ground states

In this section, we discuss our DEHC results for the two degenerate singlet dimer state ground states $|\psi_{SD}^{\pm}\rangle$ of the Majumdar-Ghosh model. We used the same $d_T = 3N(N-1)/2 = 198$ dimensional target space as for the XX chain and Heisenberg chain ground state phase expansion results. Applying the EHC method to a chain of length $N = 12$, we found a large eigenstate space containing 108 "block" operators of the form

$$\hat{H}_{MG}^{(\rho,i,\nu)} = \sum_{j=1}^{2\nu-1} \sum_{k=j+1}^{2\nu} S_{i+j}^{\rho} S_{i+k}^{\rho} \tag{A.11}$$

for all sites i, where $\rho = x, y, z$ and $\nu = 1, \ldots, N/4$. Ref. [197] showed that the singlet dimer states $|\psi_{SD}^{\pm}\rangle$ are ground states of the isotropic versions of these block operators, i.e., $\sum_\rho \hat{H}_{MG}^{(\rho,i,\nu)}$, and that the isotropic block operators do not commute with the Majumdar-Ghosh model $\hat{H}_{MG}$.

This large eigenstate space is consistent with the fact that $\hat{H}_{MG} = \frac{1}{2}\sum_{i=1}^{N}\sum_{\rho=x,y,z} \hat{H}_{MG}^{(\rho,i,1)}$ is frustration-free. Due to the frustration-free nature of the Majumdar-Ghosh model, the target states $|\psi_{SD}^{\pm}\rangle$ are also the degenerate ground states of a large family of Hamiltonians constructed from these local operators. The eigenstate space of models discussed in the state collision example in the main text is a specific example of Hamiltonians which can be constructed from these "block operators."

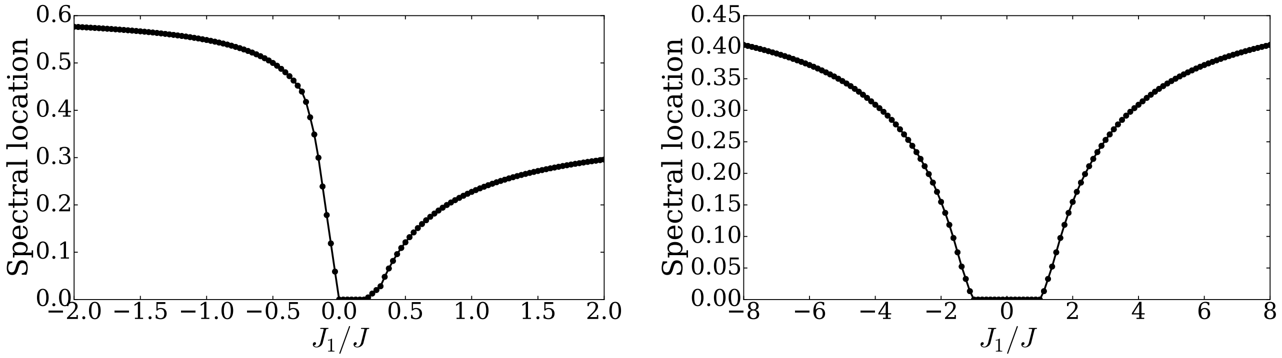

(a) (b)

Figure A.1: The spectral location of two target states for Hamiltonians found with EHC, calculated with ED for size $N = 12$ systems. The spectral location is defined as $(E_T - E_0)/(E_f - E_0)$, where E_T is the target state energy, E_0 is the ground state energy, and E_f is the largest energy eigenvalue of the Hamiltonian. Zero means that the target state is a ground state and one means that it is an anti-ground state. (a) The location of the UFI state $|\psi_{UFI}\rangle$ in the spectrum of the Hamiltonian $J\hat{H}_I + J_1(\hat{H}^{(1)}_{UFI} + \hat{H}^{(2)}_{UFI})$ with $J > 0$. (b) The location of the Heisenberg chain ground state $|\psi_H\rangle$ in the spectrum of the Hamiltonian $J\hat{H}_H + J_1\hat{H}^{(1)}_H$ with $J > 0$.

A.4 Energetics and degeneracy of target states in EHC

While the EHC method is able to find Hamiltonians with the target state $|\psi_T\rangle$ as an eigenstate, it is not able to guarantee that the target state is a ground state of these Hamiltonians. In fact, as we discuss in the main text, $|\psi_T\rangle$ only remains in the ground state manifold of the eigenstate space Hamiltonians for certain ranges of parameters and is otherwise an excited state. One scenario for an eigenstate is that it is low in the spectrum. In such situations, the physics of this eigenstate is potentially important at finite temperature or when excitations are probed experimentally. Alternatively, low-lying eigenstates may suggest a nearby level crossing with the ground state (implying the existence of a nearby phase) or indicate one sector of a topologically degenerate system.

Another scenario is that the eigenstate might be high in the spectrum. In the case of non-degenerate area (or log) law eigenstates, this would be a violation of the eigenstate thermalization hypothesis (ETH). Alternatively the eigenstate might be area-law but degenerate with other eigenstates, which does not directly violate ETH since there might be a purification of the degenerate space in which the degenerate states are volume-law. Eigenstate degeneracy is independently interesting, since generically we expect that level repulsion would prevent such degeneracy, and could indicate additional local integrals of motion.

Fig. A.1 shows two examples of the spectral locations of target states for Hamiltonians constructed in the Hamiltonian discovery of the UFI model and in the phase expansion of the Heisenberg model. We find that while in some parameter regimes it is a ground state, in others it is an eigenstate high in the spectrum.

For $|\psi_{UFI}\rangle$, we find that, in the parameters considered in Fig. A.1(a), the eigenstate is linearly degenerate allowing for its location high in the spectrum. Interestingly, for $|\psi_H\rangle$, shown in Fig. A.1(b), we find that the state is the unique eigenstate in spite of its location in the spectrum, suggesting a violation of ETH.

We also consider the degeneracy of other operators in the eigenstate space. For $\hat{H}^{(2)}_{UFI}$ on an $N = 12$ site ladder, the uniform frustrated Ising state $|\psi_{UFI}\rangle$ is a zero energy eigenstate in a degenerate subspace consisting of 124 degenerate eigenstates; for the Hamiltonian $\hat{H}^{(1)}_H$ on a $N = 12$ site chain, the $|\psi_H\rangle$ state is a zero energy eigenstate in a degenerate subspace of 260 eigenstates. However, it is important to note that such eigenstate degeneracy can be dramatically modified by adding other Hamiltonians in the eigenstate space. For example, the random Hamiltonian $\hat{H}_I - 0.03\hat{H}^{(1)}_{UFI} + 1.31\hat{H}^{(2)}_{UFI}$ on $N = 12$ sites has $|\psi_{UFI}\rangle$ as one of 8 degenerate excited states; in a more extreme example, the Hamiltonian $\hat{H}_H + \alpha\hat{H}^{(1)}_H$ for most α has the state $|\psi_H\rangle$ as a unique eigenstate.

A.5 Constructed Hamiltonians and conserved quantities

In our phase expansion results for the XX and Heisenberg chains of length $N = 12$, we encountered non-local operators in our eigenstate space that are related to conserved quantities.

For example, the XX chain Hamiltonian $\hat{H}_{XX} = \sum_{n=1}^{N}(S^x_n S^x_{n+1} + S^y_n S^y_{n+1})$ commutes with the total S^z operator, $S^z_{tot} \equiv \sum_{n=1}^{N} S^z_n$. Since the target space we considered for the phase expansion of the XX chain contains only two-site interactions, $S^\rho_n S^\rho_m$, the total S^z operator itself is not in the target space. However, from our results, we found that the eigenstate space contained N operators related to S^z_{tot} of the following form

$$\hat{H}^{(n_0)}_z = \sum_{n\neq n_0} S^z_{n_0} S^z_n = S^z_{n_0}(S^z_{tot} - S^z_{n_0}) = S^z_{n_0} S^z_{tot} - 1/4 \tag{A.12}$$

where $n_0 = 1, \ldots, N$. These operators connect a single site n_0 with all other sites on the chain through an Ising spin-spin interaction. Since $S^z_{tot}|\psi_{XX}\rangle = 0$ for even length spin chains, $|\psi_{XX}\rangle$ is an eigenstate of all $\hat{H}^{(n_0)}_z$ operators with eigenvalue $-1/4$ when N is even. Despite the fact that $[\hat{H}_{XX}, S^z_{tot}] = 0$, the related $\hat{H}^{(n_0)}_z$ operators do not commute with $\hat{H}_{XX}$, which we checked numerically for small finite-size chains. Interestingly, the operator $(S^z_{tot})^2$, which does commute with $\hat{H}_{XX}$, can be constructed as a linear combination of the $\hat{H}^{(n_0)}_z$ operators.

For the Heisenberg chain, we found a similar situation for even N chains. Namely, there are $3N$ operators of the form $\hat{H}^{(n_0)}_\rho \equiv \sum_{n\neq n_0} S^\rho_{n_0} S^\rho_n$ for $\rho = x, y, z$ in the eigenstate space of $|\psi_H\rangle$. The Heisenberg chain ground state $|\psi_H\rangle$ is also an eigenstate of $\hat{H}^{(n_0)}_\rho$ with eigenvalue $-1/4$. We also numerically determined that the $\hat{H}_\rho^{(n_0)}$ operators do not commute with $\hat{H}_H$ for small finite-size chains.

A.6 Boundary condition and finite-size effects with constructed Hamiltonians

For our phase expansion calculations of the XX chain and Heisenberg chain, we found different parent Hamiltonians when the boundary conditions used to define the target state $|\psi_T\rangle$ were open instead of periodic. For example, we used the EHC method to construct parent Hamiltonians for $|\psi_{oH}\rangle$, the ground state of the open Heisenberg chain. For this target state and the same target space as considered in the periodic case, we found only two operators in the eigenstate space

$$\hat{H}_{oH}^{(c)} = \sum_{n=1}^{N-1} h^c(n)\mathbf{S}_n \cdot \mathbf{S}_{n+1}, \tag{A.13}$$

where $h^c(n) = 1, \sin(\pi(n - N/2)/(N+1))$ for $c = 0, 1$. Likewise, we used the EHC method to construct parent Hamiltonians for $|\psi_{oXX}\rangle$, the ground state of the open XX chain, and found the reduced eigenstate space of operators

$$\hat{H}_{oXX}^{(d,\epsilon)} = \sum_{n=1}^{N-1} \epsilon^n r^d(n) \left(S_n^x S_{n+1}^x + \epsilon S_n^y S_{n+1}^y\right) \tag{A.14}$$

where $\epsilon = \pm 1$, and $r^d(n) = 1, \sin(\pi(n-N/2)/(N+1))$ for $d = 0, 1$. In both cases, two full-period sinusoidally modulated Hamiltonians were replaced by a single half-period sinusoidally modulated Hamiltonian centered at the bond between sites $N/2$ and $N/2+1$.

Finally, when applying the EHC method to the periodic XX chain ground state $|\psi_{XX}\rangle$, we found four operators in our eigenstate space of the form

$$\hat{H}_{XX}^{(k)} = \sum_{n=1}^{N} u^k(n) \left(S_n^x S_{n+1}^x + S_n^y S_{n+1}^y\right) + \sum_{n=1}^{N} \sum_{r=1}^{N-1} v^k(n,r) S_n^z S_{n+r}^z \tag{A.15}$$

where $k = 0, 1, 2, 3$ and

$$\begin{aligned}
u^0(n) &= \sin\left(\frac{4\pi}{N}n + \frac{3\pi}{N}\right) & v^0(n,r) &= +2\sin(\pi/N)\sin\left(\frac{4\pi}{N}(n-1) + \frac{2\pi}{N}r\right) \\
u^1(n) &= \cos\left(\frac{4\pi}{N}n + \frac{3\pi}{N}\right) & v^1(n,r) &= +2\sin(\pi/N)\cos\left(\frac{4\pi}{N}(n-1) + \frac{2\pi}{N}r\right) \\
u^2(n) &= \sin\left(\frac{6\pi}{N}n + \frac{9\pi}{N}\right) & v^2(n,r) &= +\cos\left(\frac{\pi}{N}r\right)\cos\left(\frac{6\pi}{N}(n-1) + \frac{3\pi}{N}r\right) \\
u^3(n) &= \cos\left(\frac{6\pi}{N}n + \frac{9\pi}{N}\right) & v^3(n,r) &= -\cos\left(\frac{\pi}{N}r\right)\sin\left(\frac{6\pi}{N}(n-1) + \frac{3\pi}{N}r\right)
\end{aligned}$$

We believe that these operators, which contain sinusoidally modulated nearest neighbor XX interactions as well as sinusoidally modulated long-range Ising interactions, are related to finite-size effects on the $N = 12$ chain.

Appendix B

From symmetries to Hamiltonians

B.1 Derivation of commutant matrix

In this section, we derive Eq. (4.7), which expresses the commutator norm between Hamiltonian $\hat{H}$ and integral of motion $\hat{\mathcal{O}}$ in terms of the commutant matrix.

Consider a space of Hermitian operators spanned by a d-dimensional basis of Hermitian operators $\hat{\mathcal{S}}_a$ for $a = 1, \ldots, d$. The commutator of two basis vectors in this space satisfies $[\hat{\mathcal{S}}_a, \hat{\mathcal{S}}_b] = -[\hat{\mathcal{S}}_b, \hat{\mathcal{S}}_a] = -[\hat{\mathcal{S}}_a, \hat{\mathcal{S}}_b]^\dagger$ and is therefore anti-Hermitian. An anti-Hermitian operator can be represented as an imaginary number times a Hermitian operator. So if this space of operators is large enough, then the operator $[\hat{\mathcal{S}}_a, \hat{\mathcal{S}}_b]$ can be represented as $[\hat{\mathcal{S}}_a, \hat{\mathcal{S}}_b] = \sum_{c=1}^{d} f_{ab}^{c} \hat{\mathcal{S}}_c$, where the expansion coefficients f_{ab}^{c} are purely imaginary. Note that if this equation holds for all a, b in the space of operators we are considering, then the space is a Lie algebra with the commutator as the Lie bracket and f_{ab}^{c} as the (basis-dependent) structure constants of the Lie algebra.

Consider two operators $\hat{H}$ and $\hat{\mathcal{O}}$ expressed in our basis so that $\hat{H} = \sum_{a=1}^{d} J_a \hat{\mathcal{S}}_a$ and $\hat{\mathcal{O}} = \sum_{b=1}^{d} g_b \hat{\mathcal{S}}_b$ with real J_a, g_b. Their commutator is

$$
\begin{aligned}
[\hat{H}, \hat{\mathcal{O}}] &= \sum_{a,b} J_a g_b [\hat{\mathcal{S}}_a, \hat{\mathcal{S}}_b] = \sum_{a,b,c} J_a g_b f_{ab}^{c} \hat{\mathcal{S}}_c \\
&= \sum_{a,c} J_a \left(\sum_{b} g_b f_{ab}^{c} \right) \hat{\mathcal{S}}_c = \sum_{a,c} \left(L_{\hat{\mathcal{O}}}\right)_{ca} J_a \hat{\mathcal{S}}_c
\end{aligned}
$$

where $(L_{\hat{\mathcal{O}}})_{ca} \equiv \sum_b g_b f_{ab}^c$. The norm of the commutator is then

$$
\begin{aligned}
\left\|[\hat{H}, \hat{\mathcal{O}}]\right\|^2 &= \left\|\sum_{a,c} J_a (L_{\hat{\mathcal{O}}})_{ca} \hat{\mathcal{S}}_c\right\|^2 \\
&= \frac{1}{\operatorname{tr}\left(\hat{I}\right)} \operatorname{tr}\left(\left(\sum_{a,c} J_a (L_{\hat{\mathcal{O}}})_{ca} \hat{\mathcal{S}}_c\right)^\dagger \left(\sum_{a',c'} J_{a'} (L_{\hat{\mathcal{O}}})_{c'a'} \hat{\mathcal{S}}_{c'}\right)\right) \\
&= \sum_{a,a'} J_a \left(\sum_{c,c'} (L_{\hat{\mathcal{O}}})^*_{ca} \frac{\operatorname{tr}\left(\hat{\mathcal{S}}_c^\dagger \hat{\mathcal{S}}_{c'}\right)}{\operatorname{tr}\left(\hat{I}\right)} (L_{\hat{\mathcal{O}}})_{c'a'}\right) J_{a'} \\
&= \sum_{a,a'} J_a \left(\sum_{c,c'} (L_{\hat{\mathcal{O}}})^*_{ca} O_{cc'} (L_{\hat{\mathcal{O}}})_{c'a'}\right) J_{a'} \\
&= J^T {L_{\hat{\mathcal{O}}}}^\dagger O L_{\hat{\mathcal{O}}} J \\
&\equiv J^T C_{\hat{\mathcal{O}}} J
\end{aligned}
$$

where $C_{\hat{\mathcal{O}}} \equiv {L_{\hat{\mathcal{O}}}}^\dagger O L_{\hat{\mathcal{O}}}$ is the commutant matrix. The matrix $O_{cc'} = \operatorname{tr}\left(\hat{\mathcal{S}}_c^\dagger \hat{\mathcal{S}}_{c'}\right)/\operatorname{tr}\left(\hat{I}\right) = \langle \hat{\mathcal{S}}_c, \hat{\mathcal{S}}_{c'} \rangle$ is an overlap (or Gram) matrix, which is Hermitian and positive semi-definite, and is calculated by taking inner products between all operator strings. Since we require that the $\hat{\mathcal{S}}_a$ form a basis, they are linearly independent, making the overlap matrix O non-singular and therefore positive definite. Since O is Hermitian and positive definite, ${L_{\hat{\mathcal{O}}}}^\dagger O L_{\hat{\mathcal{O}}}$ is Hermitian and positive semi-definite. For orthonormal bases, $O_{cc'} = \delta_{cc'}$ and the commutant matrix simplifies to $C_{\hat{\mathcal{O}}} = {L_{\hat{\mathcal{O}}}}^\dagger L_{\hat{\mathcal{O}}}$.

B.2 Properties of Pauli string basis

In this section, we describe some properties of the Pauli string basis, a complete basis for the space of Hermitian operators that can act on n qubits, and discuss how to compute the structure constants f_{ab}^c for this basis.

The Pauli string operators, which are tensor products of the identity matrix and Pauli matrices, are defined in Eq. (4.2). These operators are Hermitian and unitary. These properties imply that the operators square to identity and have eigenvalues ±1. Moreover, except for the identity operator $\hat{I}$, the operators in this basis are traceless, implying that they have an equal number of $+1$ and -1 eigenvalues. Therefore, the Pauli strings $\hat{\mathcal{S}}_a$ are highly degenerate, with two 2^{n-1}-dimensional degenerate subspaces.

The Pauli string basis is orthonormal with respect to the Frobenius inner product $\langle \hat{A}, \hat{B} \rangle \equiv \operatorname{tr}\left(\hat{A}^\dagger \hat{B}\right)/\operatorname{tr}\left(\hat{I}\right)$.

To see this, consider two Pauli strings

$$\begin{aligned}\hat{\mathcal{S}}_a &= \hat{\sigma}_1^{s_1} \otimes \cdots \otimes \hat{\sigma}_n^{s_n} \\ \hat{\mathcal{S}}_b &= \hat{\sigma}_1^{t_1} \otimes \cdots \otimes \hat{\sigma}_n^{t_n}.\end{aligned} \tag{B.1}$$

The product of two $\hat{\sigma}_i^{s_i}$ operators on the same site i obey the following relations

$$\hat{\sigma}_i^s \hat{\sigma}_i^t = \begin{cases} \delta_{st}\hat{I} + i\epsilon_{stu}\hat{\sigma}_i^u & s,t \in \{1,2,3\} \\ \hat{\sigma}_i^t & s = 0 \\ \hat{\sigma}_i^s & t = 0 \end{cases} \tag{B.2}$$

where ϵ_{stu} is the fully antisymmetric tensor. When multiplying two Pauli strings, we multiply operators site by site in the tensor product and apply Eq. (B.2):

$$\begin{aligned}\hat{\mathcal{S}}_a\hat{\mathcal{S}}_b &= (\hat{\sigma}_1^{s_1}\hat{\sigma}_1^{t_1}) \otimes \cdots \otimes (\hat{\sigma}_n^{s_n}\hat{\sigma}_n^{t_n}) \\ &= \delta_{s_1t_1}\cdots\delta_{s_nt_n}\hat{I} + \cdots .\end{aligned}$$

The term with the identity operator, which is non-zero only if $(s_1, \ldots, s_n) = (t_1, \ldots, t_n)$, i.e., only if $\hat{\mathcal{S}}_a = \hat{\mathcal{S}}_b$, is the only operator with non-zero trace in the expansion of the product. Therefore $\langle \hat{\mathcal{S}}_a, \hat{\mathcal{S}}_b \rangle = \mathrm{tr}\left(\hat{\mathcal{S}}_a\hat{\mathcal{S}}_b\right)/\mathrm{tr}\left(\hat{I}\right) = \delta_{ab}$ and the basis is orthonormal.

Next, we describe in more detail how to compute the product, and thereby the structure constants, of Pauli strings. The commutator of the two strings in Eq. (B.1) is

$$\begin{aligned}[\hat{\mathcal{S}}_a, \hat{\mathcal{S}}_b] &= \hat{\mathcal{S}}_a\hat{\mathcal{S}}_b - \hat{\mathcal{S}}_b\hat{\mathcal{S}}_a \\ &= (\hat{\sigma}_1^{s_1}\hat{\sigma}_1^{t_1}) \otimes \cdots \otimes (\hat{\sigma}_n^{s_n}\hat{\sigma}_n^{t_n}) \\ &\quad - (\hat{\sigma}_1^{t_1}\hat{\sigma}_1^{s_1}) \otimes \cdots \otimes (\hat{\sigma}_n^{t_n}\hat{\sigma}_n^{s_n}) \\ &\equiv f_{ab}^c\hat{\mathcal{S}}_c.\end{aligned}$$

To compute the structure constants f_{ab}^c in the final line for a particular (a, b)-pair in our basis, we need to apply Eq. (B.2). To precisely illustrate this calculation, we need to introduce some notation. We say that two Pauli strings "agree" on p sites $i_1, \ldots, i_p$ when the operators on those sites match: $s_{i_1} = t_{i_1}, \ldots, s_{i_p} = t_{i_p}$. They "trivially disagree" on q sites $j_1, \ldots, j_q$ when the operators on those sites do not match, but one of the two operators on the site is identity: $s_{j_1} \neq t_{j_1}, \ldots, s_{j_q} \neq t_{j_q}$ and $s_{j_m} = 0$ or $t_{j_m} = 0$ for all $m = 1, \ldots, q$.

Finally, the two strings "non-trivially disagree" on $r = n - p - q$ sites $k_1, \ldots, k_r$ when the operators do not match and are both non-identity operators: $s_{k_1} \neq t_{k_1}, \ldots, s_{k_r} \neq t_{k_r}$ and $s_{k_1}, t_{k_1}, \ldots, s_{k_r}, t_{k_r} \in \{1, 2, 3\}$. According to Eq. (B.2), the sites that agree become identity operators, while the sites that disagree, both trivially and non-trivially, become Pauli matrices. We then see that

$$\begin{aligned}
[\hat{\mathcal{S}}_a, \hat{\mathcal{S}}_b] &= \hat{\mathcal{S}}_a \hat{\mathcal{S}}_b - \text{H.c.} \\
&= \prod_{m=1}^{q} (\delta_{s_{j_m},0} \hat{\sigma}_{j_m}^{t_{j_m}} + \delta_{t_{j_m},0} \hat{\sigma}_{j_m}^{s_{j_m}}) \prod_{l=1}^{r} \left(i \epsilon_{s_{k_l} t_{k_l} u_{k_l}} \hat{\sigma}_{k_l}^{u_{k_l}} \right) \\
&\quad - \text{H.c.}
\end{aligned} \tag{B.3}$$

From this result, we see that if r is even, then the two terms are purely real and cancel, leading to $[\hat{\mathcal{S}}_a, \hat{\mathcal{S}}_b] = 0$ and $f_{ab}^c = 0$ for all c. If r is odd, then the two terms are purely imaginary and add, resulting in a single c for which $f_{ab}^c \neq 0$. Therefore, the structure constant associated with $\hat{\mathcal{S}}_a$ and $\hat{\mathcal{S}}_b$ is

$$f_{ab}^c = \begin{cases} 2 i^r \prod_{l=1}^{r} \epsilon_{s_{k_l} t_{k_l} u_{k_l}} & r \text{ is odd} \\ 0 & r \text{ is even} \end{cases} \tag{B.4}$$

and $\hat{\mathcal{S}}_c = \prod_{m=1}^{q} (\delta_{s_{j_m},0} \hat{\sigma}_{j_m}^{t_{j_m}} + \delta_{t_{j_m},0} \hat{\sigma}_{j_m}^{s_{j_m}}) \prod_{l=1}^{r} \hat{\sigma}_{k_l}^{u_{k_l}}$ when r is odd.

The structure constants in Eq. (B.4) can be computed efficiently, in time $O(q + r)$, for each pair of operator strings $\hat{\mathcal{S}}_a$ and $\hat{\mathcal{S}}_b$. Therefore, for a d-dimensional basis of k-local Pauli strings, all of the structure constants for the basis can be computed in time $O(kd^2)$.

B.3 Properties of fermion string basis

In this section, we describe some properties of the fermion string basis, a complete basis for the space of Hermitian operators that can act on n fermions. A similarly defined basis was considered in Ref. [246].

Fermion strings, expressed in terms of the standard fermionic creation and anhillation operators $\hat{c}_i^\dagger$ and $\hat{c}_i$, are defined in Eq. (4.3). Unlike the Pauli strings, fermion strings are neither unitary, traceless, nor orthonormal according to the Frobenius inner product.

As shown in Eq. (4.3), we classify the fermion string operators into three types.

The first type is of the form $\hat{\mathcal{S}}_a^{(1)} = \hat{c}_{i_1}^\dagger \cdots \hat{c}_{i_m}^\dagger \hat{c}_{i_m} \cdots \hat{c}_{i_1} = \hat{n}_{i_1} \cdots \hat{n}_{i_m}$ and can be interpreted as a product of number operators $\hat{n}_i \equiv \hat{c}_i^\dagger \hat{c}_i$. There are $\sum_{m=0}^{n} \binom{n}{m} = 2^n$ ways to choose the $i_1, \ldots, i_m$ labels and so there are 2^n linearly independent $\hat{\mathcal{S}}_a^{(1)}$ operators including the identity operator $\hat{I}$. These operators are idempotent, so that $(\hat{\mathcal{S}}_a^{(1)})^2 = \hat{\mathcal{S}}_a^{(1)}$, which means that they only have eigenvalues 0 or 1. Consider the Fock space (occupation number) basis states that span the fermionic Hilbert space: $|\{n\}\rangle \equiv |n_1, \dots, n_n\rangle \equiv ((1-n_1) + n_1\hat{c}_1^\dagger) \cdots ((1-n_1) + n_n\hat{c}_n^\dagger)|0\rangle$ where $n_i \in \{0,1\}$ and $\hat{I} = \sum_{\{n\}} |\{n\}\rangle \langle\{n\}|$. The $\hat{\mathcal{S}}_a^{(1)}$ operators are diagonal in this basis and possess non-zero trace.

The second type of operator we define is of the form $\hat{\mathcal{S}}_a^{(2)} = \hat{c}_{i_1}^\dagger \cdots \hat{c}_{i_m}^\dagger \hat{c}_{j_l} \cdots \hat{c}_{j_1} + \text{H.c.}$, where the indices are lexicographically ordered so that $(j_1, \dots, j_l) < (i_1, \dots, i_m)$. There are $\sum_{a=1}^{2^n} \sum_{b=1}^{a-1} 1 = 2^{n-1}(2^n - 1)$ ways to choose the labels in these operators and so there are this many linearly independent $\hat{\mathcal{S}}_a^{(2)}$ operators. By working in the Fock space basis, we can see that these operators are traceless. Note that the third type of operator, $\hat{\mathcal{S}}_a^{(3)} = i\hat{c}_{i_1}^\dagger \cdots \hat{c}_{i_m}^\dagger \hat{c}_{j_l} \cdots \hat{c}_{j_1} + \text{H.c.}$, has the same properties as the $\hat{\mathcal{S}}_a^{(2)}$ operators.

Altogether, from our counting, we see that the $\{\hat{\mathcal{S}}_a^{(1)}, \hat{\mathcal{S}}_a^{(2)}, \hat{\mathcal{S}}_a^{(3)}\}$ fermion string basis consists of $2^n + 2 \times 2^{n-1}(2^n - 1) = 4^n$ linearly independent Hermitian operators and therefore spans the entire space of Hermitian operators.

Finally, we note that the product of two fermion strings, $\hat{\mathcal{S}}_a \hat{\mathcal{S}}_b$, and therefore the commutator, is non-trivial to calculate. Rather than working out the commutator and structure constants in the fermion string basis, we compute the structure constants in the Majorana string basis, which spans the same space of operators. We can then convert to and from the fermion string basis as needed by applying an invertible basis transformation, as discussed in the next section.

B.4 Properties of Majorana string basis

In this section, we describe some properties of the Majorana string basis – another complete basis for the space of Hermitian operators that can act on n fermions. We also discuss how to compute the structure constants f_{ab}^c for this basis and how to convert from the Majorana string basis to the fermion string basis. The Majorana string basis, while more difficult to interpret physically than the fermion string basis, is more amenable to the computation of structure constants, making it useful for our methods.

Majorana strings, which are products of the identity operator $\hat{I}$, Majorana fermion operators $\hat{a}_i, \hat{b}_i$, and the fermion parity operator $\hat{d}_i = -i\hat{a}_i\hat{b}_i$, are defined in Eq. (4.4). Like Pauli strings, Majorana strings are Hermitian, unitary, and – excluding the identity operator – traceless. In fact, Majorana strings and Pauli strings can be directly related to one another via the Jordan-Wigner transformation

$$\hat{a}_i = \left(\prod_{j=1}^{i-1} \hat{\sigma}_j^z\right) \hat{\sigma}_i^x, \qquad \hat{b}_i = \left(\prod_{j=1}^{i-1} \hat{\sigma}_j^z\right) \hat{\sigma}_i^y, \qquad \hat{d}_i = \hat{\sigma}_i^z,$$
$$\hat{\sigma}_i^x = \left(\prod_{j=1}^{i-1} \hat{d}_j\right) \hat{a}_i, \qquad \hat{\sigma}_i^y = \left(\prod_{j=1}^{i-1} \hat{d}_j\right) \hat{b}_i, \qquad \hat{\sigma}_i^z = \hat{d}_i,$$

and so the properties of Majorana strings can be thought of as being inherited from the Pauli strings.

To understand the properties of the Majorana string basis, it is important to understand the algebraic properties of the $\hat{a}_i, \hat{b}_i, \hat{d}_i$ operators. Operators with different labels $i \neq j$, satisfy the following commutation and anti-commutation relations:

$$\begin{gathered}[\hat{a}_i, \hat{d}_j] = [\hat{b}_i, \hat{d}_j] = [\hat{d}_i, \hat{d}_j] = 0 \\ \{\hat{a}_i, \hat{a}_j\} = \{\hat{b}_i, \hat{b}_j\} = \{\hat{a}_i, \hat{b}_j\} = 0,\end{gathered} \tag{B.5}$$

which one can derive from the canonical fermionic anti-commutation relations $\{\hat{c}_i, \hat{c}_j^\dagger\} = \delta_{ij}$ and $\{\hat{c}_i, \hat{c}_j\} = 0$. One can also show that operators with identical labels $i = j$ obey the relations:

$$\hat{a}_i\hat{b}_i = i\hat{d}_i \quad \hat{a}_i\hat{d}_i = -i\hat{b}_i \quad \hat{b}_i\hat{d}_i = i\hat{a}_i. \tag{B.6}$$

Using the $(\hat{\tau}_i^0, \hat{\tau}_i^1, \hat{\tau}_i^2, \hat{\tau}_i^3) = (\hat{I}, \hat{a}_i, \hat{b}_i, \hat{d}_i)$ notation, the relations from Eq. (B.6) can be rewritten as

$$\hat{\tau}_i^s \hat{\tau}_i^t = \begin{cases} \delta_{st}\hat{I} + i\epsilon_{stu}\hat{\tau}_i^u & s, t \in \{1,2,3\} \\ \hat{\tau}_i^t & s = 0 \\ \hat{\tau}_i^s & t = 0 \end{cases} \tag{B.7}$$

which are identical to the same-label algebraic relations, Eq. (B.2), of the Pauli string basis.

Next, we clarify the imaginary prefactor in Eq. (4.4). Note that, unlike the Pauli string basis in Eq. (4.2), the Majorana string basis in Eq. (4.4) involves products, not tensor products, of operators. This is because the ordering of the operators are important in our calculations due to the anti-commutation relations of the $\hat{a}_i, \hat{b}_i$ operators shown in Eq. (B.5). We now illustrate the effect of the operator ordering with an example. Suppose that, of the n sites of a Majorana string $\hat{\mathcal{S}}_a$, m_{AB} of the sites have $\hat{a}_i$ or $\hat{b}_i$ operators on them so that $m_{AB} = \sum_{i=1}^n (\delta_{t_i,1} + \delta_{t_i,2})$. For example, the Majorana string $\hat{\mathcal{S}}_a = i^{\sigma_a}\hat{a}_2\hat{a}_3\hat{b}_4\hat{a}_5$ has $m_{AB} = 4$. For this $\hat{\mathcal{S}}_a$ to be Hermitian, we require that $\hat{\mathcal{S}}_a^\dagger = (-i)^{\sigma_a}\hat{a}_5\hat{b}_4\hat{a}_3\hat{a}_2 = \hat{\mathcal{S}}_a$ upon the reordering of the anti-commuting $\hat{a}_i, \hat{b}_i$

operators. In general, reversing the order of these operators can be done with $\binom{m_{AB}}{2} = m_{AB}(m_{AB}-1)/2$ swaps, which multiplies the operator by a sign $(-1)^{m_{AB}(m_{AB}-1)/2}$. Therefore, we use the convention that $\sigma_a = m_{AB}(m_{AB}-1)/2 \bmod 2$ to make $\hat{\mathcal{S}}_a$ Hermitian. Note, from Eq. (B.5), that the identity operator and parity operators $\hat{d}_i$ commute with operators on different sites, so they do not contribute signs like the $\hat{a}_i$ and $\hat{b}_i$ operators do.

Now, we discuss how to compute a product of Majorana strings, which will demonstrate the orthonormality of the Majorana string basis. Consider a pair of length n Majorana strings

$$\begin{aligned}\hat{\mathcal{S}}_a &= i^{\sigma_a}\hat{\tau}_1^{s_1}\cdots\hat{\tau}_n^{s_n}\\ \hat{\mathcal{S}}_b &= i^{\sigma_b}\hat{\tau}_1^{t_1}\cdots\hat{\tau}_n^{t_n}\end{aligned}$$

where the $\sigma_a, \sigma_b \in \{0,1\}$ and $\hat{\tau}_i^{t_i}$ are as defined above and $s_i, t_i \in \{0,1,2,3\}$. The product of these two operators is

$$\begin{aligned}\hat{\mathcal{S}}_a\hat{\mathcal{S}}_b &= (i^{\sigma_a}\hat{\tau}_1^{s_1}\cdots\hat{\tau}_n^{s_n})(i^{\sigma_b}\hat{\tau}_1^{t_1}\cdots\hat{\tau}_n^{t_n})\\ &= i^{\sigma_a+\sigma_b}s_{ab}(\hat{\tau}_1^{s_1}\hat{\tau}_1^{t_1})\cdots(\hat{\tau}_n^{s_n}\hat{\tau}_n^{t_n}) \qquad \text{(B.8)}\end{aligned}$$

where $s_{ab} = \pm 1$ is a sign picked up from reordering the $\hat{a}_i$ and $\hat{b}_i$ operators. (In practice, we compute the sign s_{ab} by sorting the $\hat{a}_i$ and $\hat{b}_i$ operators in the $\hat{\mathcal{S}}_a\hat{\mathcal{S}}_b$ string with a stable sorting algorithm and counting the number of swaps performed. An odd number of swaps leads to a minus sign.) Since $\hat{a}_i, \hat{b}_i, \hat{d}_i$, and strings of these operators are traceless, we see that the only possible term with non-zero trace in the final line is the identity operator, which occurs when $\hat{\mathcal{S}}_a = \hat{\mathcal{S}}_b$. Therefore, just like the Pauli string basis, the Majorana string basis is orthonormal, satisfying $\langle\hat{\mathcal{S}}_a, \hat{\mathcal{S}}_b\rangle = \mathrm{tr}\left(\hat{\mathcal{S}}_a\hat{\mathcal{S}}_b\right)/\mathrm{tr}\left(\hat{I}\right) = \delta_{ab}$.

Next, we discuss how to compute the structure constants. From Eq. (B.8), we see that the commutator of two Majorana strings is

$$\begin{aligned}[\hat{\mathcal{S}}_a, \hat{\mathcal{S}}_b] &= \hat{\mathcal{S}}_a\hat{\mathcal{S}}_b - \hat{\mathcal{S}}_b\hat{\mathcal{S}}_a\\ &= i^{\sigma_a+\sigma_b}s_{ab}(\hat{\tau}_1^{s_1}\hat{\tau}_1^{t_1})\cdots(\hat{\tau}_n^{s_n}\hat{\tau}_n^{t_n})\\ &\quad - i^{\sigma_a+\sigma_b}s_{ba}(\hat{\tau}_1^{t_1}\hat{\tau}_1^{s_1})\cdots(\hat{\tau}_n^{t_n}\hat{\tau}_n^{s_n})\\ &\equiv f_{ab}^{c}\hat{\mathcal{S}}_c. \qquad \text{(B.9)}\end{aligned}$$

After the reordering of the Majorana operators, the calculation of f_{ab}^{c} and $\hat{\mathcal{S}}_c$ parallels the one for the Pauli string basis. To compute the structure constants f_{ab}^c in the final line of Eq. (B.9) for a particular (a,b)-pair in our basis, we need to apply Eq. (B.7). To describe this calculation, we use the same notation as we used for the Pauli strings. We say that two Majoranas strings "agree" on p sites $i_1, \ldots, i_p$ when the operators on those sites match: $s_{i_1} = t_{i_1}, \ldots, s_{i_p} = t_{i_p}$. They "trivially disagree" on q sites $j_1, \ldots, j_q$ when the operators on those sites do not match, but one of the two operators on the site is identity: $s_{j_1} \neq t_{j_1}, \ldots, s_{j_q} \neq t_{j_q}$ and $s_{j_m} = 0$ or $t_{j_m} = 0$ for all $m = 1, \ldots, q$. Finally, the two strings "non-trivially disagree" on $r = n - p - q$ sites $k_1, \ldots, k_r$ when the operators do not match and are both non-identity operators: $s_{k_1} \neq t_{k_1}, \ldots, s_{k_r} \neq t_{k_r}$ and $s_{k_1}, t_{k_1}, \ldots, s_{k_r}, t_{k_r} \in \{1,2,3\}$. According to Eq. (B.7), the sites that agree become identity operators, while the sites that disagree, both trivially and non-trivially, become $\hat{a}_i, \hat{b}_i$ or $\hat{d}_i$ operators. We then see that

$$\begin{aligned}
&[\hat{\mathcal{S}}_a, \hat{\mathcal{S}}_b] = \hat{\mathcal{S}}_a \hat{\mathcal{S}}_b - \hat{\mathcal{S}}_b \hat{\mathcal{S}}_a \\
&= i^{\sigma_a + \sigma_b} s_{ab} \\
&\quad \times \left[\!\!\left[\prod_{m=1}^{q} (\delta_{s_{j_m},0} \hat{\tau}_{j_m}^{t_{j_m}} + \delta_{t_{j_m},0} \hat{\tau}_{j_m}^{s_{j_m}}) \prod_{l=1}^{r} \left(i \epsilon_{s_{k_l} t_{k_l} u_{k_l}} \hat{\tau}_{k_l}^{u_{k_l}} \right) \right]\!\!\right] \\
&\quad - i^{\sigma_a + \sigma_b} s_{ba} \\
&\quad \times \left[\!\!\left[\prod_{m=1}^{q} (\delta_{s_{j_m},0} \hat{\tau}_{j_m}^{t_{j_m}} + \delta_{t_{j_m},0} \hat{\tau}_{j_m}^{s_{j_m}}) \prod_{l=1}^{r} \left(i \epsilon_{t_{k_l} s_{k_l} u_{k_l}} \hat{\tau}_{k_l}^{u_{k_l}} \right) \right]\!\!\right] \\
&= i^{\sigma_a + \sigma_b + r} (s_{ab} - (-1)^r s_{ba}) \\
&\quad \times \left[\!\!\left[\prod_{m=1}^{q} (\delta_{s_{j_m},0} \hat{\tau}_{j_m}^{t_{j_m}} + \delta_{t_{j_m},0} \hat{\tau}_{j_m}^{s_{j_m}}) \prod_{l=1}^{r} \left(\epsilon_{s_{k_l} t_{k_l} u_{k_l}} \hat{\tau}_{k_l}^{u_{k_l}} \right) \right]\!\!\right] \qquad \text{(B.10)}
\end{aligned}$$

where the notation $[\![\cdot]\!]$ indicates that the bracketed $\hat{\tau}_i^{t_i}$ operators are ordered by their labels i.

From Eq. (B.10), we see that if $s_{ab} = (-1)^r s_{ba}$, then the two terms cancel, leading to $[\hat{\mathcal{S}}_a, \hat{\mathcal{S}}_b] = 0$ and $f_{ab}^c = 0$ for all c. If $s_{ab} = -(-1)^r s_{ba}$, then the two terms add, resulting in a single $\hat{\mathcal{S}}_c \neq 0$. Therefore, in this second case, the structure constant associated with $\hat{\mathcal{S}}_a$ and $\hat{\mathcal{S}}_b$ is

$$f_{ab}^c = 2 i^{\sigma_a + \sigma_b - \sigma_c + r} s_{ab} \prod_{l=1}^{r} \epsilon_{s_{k_l} t_{k_l} u_{k_l}}$$

which corresponds to

$$\hat{\mathcal{S}}_c = i^{\sigma_c} \left[\!\!\left[\prod_{m=1}^{q} (\delta_{s_{j_m},0} \hat{\tau}_{j_m}^{t_{j_m}} + \delta_{t_{j_m},0} \hat{\tau}_{j_m}^{s_{j_m}}) \prod_{l=1}^{r} \hat{\tau}_{k_l}^{u_{k_l}} \right]\!\!\right].$$

Finally, we discuss the conversion of Majorana strings to linear combinations of fermion strings. This conversion is done by applying the definitions $\hat{a}_i = \hat{c}_i + \hat{c}_i^\dagger$, $\hat{b}_i = -i\hat{c}_i + i\hat{c}_i^\dagger$, and $\hat{d}_i = \hat{I} - 2\hat{c}_i^\dagger \hat{c}_i$. Inserting these relations into Eq. (4.4) and expanding, we see that we obtain 2^k terms made of products of $\hat{c}_i$ and $\hat{c}_i^\dagger$, where k is the number of non-identity terms in the Majorana string. These terms can cancel and can be combined to form non-diagonal fermion strings, which involve Hermitian conjugates. To correctly convert these terms to the fermion strings of Eq. (4.3), we need to normal order our expanded operators and reorder them so that they follow our label ordering convention. We implement this process algorithmically to build up a basis transformation matrix B_{ab}, which is invertible but not unitary, since the fermion string operators are not orthonormal. The construction of the B matrix takes time $O(d \min(2^k, d))$.

B.5 Representations in the operator string basis

Here we discuss how to compute the representations D_g of a symmetry transformation $g \in G$ in the operator string basis for a few common discrete symmetries.

For fermionic systems, spatial unitary symmetry transformations can be represented by their action on the fermionic creation and anhillation operators $\hat{c}_i^\dagger$ and $\hat{c}_i$ [299]

$$\hat{c}_i \to \hat{c}'_i \equiv g \cdot \hat{c}_i \equiv \hat{\mathcal{U}}_g \hat{c}_i \hat{\mathcal{U}}_g^{-1} = \sum_j U_{ji} \hat{c}_j \tag{B.11}$$

where i, j label lattice site degrees of freedom and U_{ji} is a unitary matrix. For example, for reflection and rotation symmetries, the matrix U_{ji} is a permutation matrix that specifies how lattice site labels are permuted under the transformation. Eq. (B.11) and its generalizations provide us with a rule for how to transform fermionic operator strings $\hat{\mathcal{S}}_a$. For Majorana fermions, Eq. (B.11) can be re-expressed as

$$\hat{\mathcal{U}}_g \hat{a}_i \hat{\mathcal{U}}_g^{-1} = \sum_j U_{ji} \hat{a}_j \qquad \hat{\mathcal{U}}_g \hat{b}_i \hat{\mathcal{U}}_g^{-1} = \sum_j U_{ji} \hat{b}_j. \tag{B.12}$$

Now we can see that, for a Majorana string operator made of many Majorana fermion operators, these rules specify how the string transforms. For example, the string $i\hat{a}_i\hat{b}_j$ transforms as

$$\begin{aligned}
\hat{\mathcal{U}}_g i\hat{a}_i\hat{b}_j\hat{\mathcal{U}}_g^{-1} &= i\hat{\mathcal{U}}_g\hat{a}_i\hat{\mathcal{U}}_g^{-1}\hat{\mathcal{U}}_g\hat{b}_j\hat{\mathcal{U}}_g^{-1} \\
&= \sum_{kl} U_{ki}U_{lj} i\hat{a}_k\hat{b}_l \\
&\equiv \sum_{(kl),(ij)} U'_{(kl),(ij)} i\hat{a}_k\hat{b}_l.
\end{aligned}$$

For a space group symmetry, this is particularly simple and the $U_{ki}, U_{lj}, U'_{(kl),(ij)}$ matrices are all permutation matrices. For non-spatial symmetry transformations, such as charge-conjugation or time-reversal symmetry, the transformations also involve changes in sign in addition to permutations (see Tab. B.1).

For Pauli strings, spatial symmetry transformations work the same way as for Majorana strings: they simply permute the labels of the Pauli matrices. The time-reversal symmetry transformation, on the other hand, involves an additional sign for every Pauli matrix, $\hat{\mathcal{T}}\hat{\sigma}_i^\alpha\hat{\mathcal{T}}^{-1} = -\hat{\sigma}_i^\alpha$.

Symmetry $\hat{\mathcal{U}}$	$\hat{\mathcal{U}}\hat{a}_j\hat{\mathcal{U}}^{-1}$	$\hat{\mathcal{U}}\hat{b}_j\hat{\mathcal{U}}^{-1}$	$\hat{\mathcal{U}}\hat{d}_j\hat{\mathcal{U}}^{-1}$	$\hat{\mathcal{U}}i\hat{\mathcal{U}}^{-1}$
$\hat{\mathcal{T}}$	$\hat{a}_j$	$-\hat{b}_j$	$\hat{d}_j$	$-i$
$\hat{\mathcal{C}}$	$\hat{a}_j$	$-\hat{b}_j$	$-\hat{d}_j$	i

Table B.1: The effect of (spinless) time-reversal $\hat{\mathcal{T}}$ and charge-conjugation $\hat{\mathcal{C}}$ symmetries on Majorana fermion operators $\hat{a}_j, \hat{b}_j$, the fermion parity operator $\hat{d}_j = -i\hat{a}_j\hat{b}_j$, and the imaginary number i.

B.6 QOSY library

The Quantum Operators from Symmetry (QOSY) library is a `Python` package [47] designed for finding operators that obey a desired list of symmetries. QOSY has convenient syntax for performing such calculations with operator strings. It supports the algebraic manipulation of operators that are sums of Pauli strings, Fermion strings, or Majorana strings. Using QOSY, one can, for example, take products, commutators, or anticommutators of such operators and convert operators into different operator string bases. The core functions of QOSY are numerical implementations of the methods discussed in Section 4.2: methods for finding Hamiltonians that commute (or anti-commute) with desired operators and methods for finding Hamiltonians that are invariant (or anti-invariant) under desired discrete symmetry transformations. Altogether, QOSY provides a convenient, simple set of tools for designing operators with desired symmetry properties.

The public repository for QOSY also contains a "tutorials" folder that includes most of the code used to generate the results in this work. Other code or data used in this work is available upon request.

B.7 Derivation of Hamiltonians that commute with zero modes

Here we derive a large family of Hamiltonians that commute with desired zero modes. First, we look for two-site Hamiltonians that commute with a single zero mode. Then, we look for two-site Hamiltonians that commute with a pair of zero modes. Finally, we discuss how these two-site Hamiltonians can be used to construct many-body Hamiltonians with desired zero modes.

Suppose that we wish to find Hamiltonians that commute with a single zero mode of the form $\hat{\gamma} = \sum_j (\alpha_j \hat{a}_j + \beta_j \hat{b}_j)$. On the two sites i and j, this zero mode has support $\hat{\gamma}_{ij} = \alpha_i \hat{a}_i + \beta_i \hat{b}_i + \alpha_j \hat{a}_j + \beta_j \hat{b}_j$. To find two-site fermion-parity-conserving Hamiltonians, we construct the commutant matrix $C_{\hat{\gamma}_{ij}}$ in the 7-dimensional basis spanned by the Majorana strings

$$\hat{\mathcal{S}}_1, \dots, \hat{\mathcal{S}}_7 = \hat{d}_i,\, \hat{d}_j,\, i\hat{a}_i\hat{a}_j,\, i\hat{a}_i\hat{b}_j,\, i\hat{b}_i\hat{a}_j,\, i\hat{b}_i\hat{b}_j,\, \hat{d}_i\hat{d}_j. \tag{B.13}$$

In this basis, the 7×7 commutant matrix is

$$C_{\hat{\gamma}_{ij}} = 4 \begin{pmatrix} \alpha_i^2 + \beta_i^2 & 0 & -\alpha_j\beta_i & -\beta_i\beta_j & \alpha_i\alpha_j & \alpha_i\beta_j & 0 \\ \cdot & \alpha_j^2 + \beta_j^2 & \alpha_i\beta_j & -\alpha_i\alpha_j & \beta_i\beta_j & -\alpha_j\beta_i & 0 \\ \cdot & \cdot & \alpha_i^2 + \alpha_j^2 & \alpha_j\beta_j & \alpha_i\beta_i & 0 & 0 \\ \cdot & \cdot & \cdot & \alpha_i^2 + \beta_j^2 & 0 & \alpha_i\beta_i & 0 \\ \cdot & \cdot & \cdot & \cdot & \alpha_j^2 + \beta_i^2 & \alpha_j\beta_j & 0 \\ \cdot & \cdot & \cdot & \cdot & \cdot & \beta_i^2 + \beta_j^2 & 0 \\ \cdot & \cdot & \cdot & \cdot & \cdot & \cdot & \alpha_i^2 + \beta_i^2 + \alpha_j^2 + \beta_j^2 \end{pmatrix}$$

where the lower triangle of this matrix is specified by the upper triangle since it is symmetric. We find that this matrix has three null vectors and four degenerate eigenvectors with positive eigenvalue $4(\alpha_i^2 + \beta_i^2 + \alpha_j^2 + \beta_j^2) > 0$.

For $\alpha_i, \beta_i, \alpha_j, \beta_j \neq 0$, the three null vectors correspond to the following three operators that commute with $\hat{\gamma}_{ij}$

$$\begin{aligned} -\beta_i\beta_j i\hat{a}_i\hat{a}_j + \alpha_i\alpha_j i\hat{b}_i\hat{b}_j - \alpha_j\beta_j\hat{d}_i + \alpha_i\beta_i\hat{d}_j \\ \beta_i i\hat{a}_i\hat{a}_j - \alpha_i i\hat{b}_i\hat{a}_j + \alpha_j\hat{d}_i \\ \alpha_j i\hat{a}_i\hat{b}_j - \beta_j i\hat{a}_i\hat{a}_j + \alpha_i\hat{d}_j \end{aligned}$$

where $i\hat{a}_i\hat{a}_j = i\hat{c}_i^\dagger\hat{c}_j + i\hat{c}_i^\dagger\hat{c}_j^\dagger + \text{H.c.}, i\hat{a}_i\hat{b}_j = \hat{c}_i^\dagger\hat{c}_j - \hat{c}_i^\dagger\hat{c}_j^\dagger + \text{H.c.}, i\hat{b}_i\hat{a}_j = -\hat{c}_i^\dagger\hat{c}_j - \hat{c}_i^\dagger\hat{c}_j^\dagger + \text{H.c.}$, and $i\hat{b}_i\hat{b}_j = i\hat{c}_i^\dagger\hat{c}_j - i\hat{c}_i^\dagger\hat{c}_j^\dagger + \text{H.c.}$. In summary, when we looked for two-site Hamiltonians that commute with *one* zero mode, we found three such Hamiltonians.

Now suppose that we wish to find Hamiltonians with *two* particular zero modes, $\hat{\gamma}^{(1)} = \sum_j (\alpha_j^{(1)}\hat{a}_j + \beta_j^{(1)}\hat{b}_j)$ and $\hat{\gamma}^{(2)} = \sum_j (\alpha_j^{(2)}\hat{a}_j + \beta_j^{(2)}\hat{b}_j)$, with support $\hat{\gamma}_{ij}^{(1)}$ and $\hat{\gamma}_{ij}^{(2)}$ on sites i, j. To find the two-site Hamiltonians that commute with both of these zero modes, we examined the null space of the sum of their commutant matrices $C_{\hat{\gamma}_{ij}^{(1)}} + C_{\hat{\gamma}_{ij}^{(2)}}$ in the same 7-dimensional basis as before. We found a one-dimensional null space of this matrix, which corresponds to a unique two-site Hamiltonian that commutes with *both* of the desired zero modes. This unique Hamiltonian, converted into complex fermions, is

$$\begin{aligned}\hat{h}_{ij} = \Big[&(\tilde{t}_{ij}^R + i\tilde{t}_{ij}^I)\hat{c}_i^\dagger \hat{c}_j + (\tilde{\Delta}_{ij}^R + i\tilde{\Delta}_{ij}^I)\hat{c}_i^\dagger \hat{c}_j^\dagger + \text{H.c.}\Big] \\ &+ \tilde{\mu}_i^{(ij)}\hat{n}_i + \tilde{\mu}_j^{(ij)}\hat{n}_j \end{aligned} \tag{B.14}$$

where

$$\begin{aligned}\tilde{t}_{ij}^R &\equiv -\alpha_i^{(1)}\beta_j^{(2)} + \beta_i^{(1)}\alpha_j^{(2)} - \alpha_j^{(1)}\beta_i^{(2)} + \beta_j^{(1)}\alpha_i^{(2)}, \\ \tilde{t}_{ij}^I &\equiv -\alpha_i^{(1)}\alpha_j^{(2)} - \beta_i^{(1)}\beta_j^{(2)} + \alpha_j^{(1)}\alpha_i^{(2)} + \beta_j^{(1)}\beta_i^{(2)}, \\ \tilde{\Delta}_{ij}^R &\equiv -\alpha_i^{(1)}\beta_j^{(2)} - \beta_i^{(1)}\alpha_j^{(2)} + \alpha_j^{(1)}\beta_i^{(2)} + \beta_j^{(1)}\alpha_i^{(2)}, \\ \tilde{\Delta}_{ij}^I &\equiv +\alpha_i^{(1)}\alpha_j^{(2)} - \beta_i^{(1)}\beta_j^{(2)} - \alpha_j^{(1)}\alpha_i^{(2)} + \beta_j^{(1)}\beta_i^{(2)}, \\ \tilde{\mu}_i^{(ij)} &\equiv 2(\alpha_j^{(1)}\beta_j^{(2)} - \beta_j^{(1)}\alpha_j^{(2)}), \\ \tilde{\mu}_j^{(ij)} &\equiv 2(\alpha_i^{(1)}\beta_i^{(2)} - \beta_i^{(1)}\alpha_i^{(2)}). \end{aligned} \tag{B.15}$$

Note that if we consider the zero mode coefficients as vectors $\gamma^{(1)} \equiv (\alpha_i^{(1)}, \beta_i^{(1)}, \alpha_j^{(1)}, \beta_j^{(1)})^T$ and $\gamma^{(2)} \equiv (\alpha_i^{(2)}, \beta_i^{(2)}, \alpha_j^{(2)}, \beta_j^{(2)})^T$, then each of the parameters of the Hamiltonian are indefinite quadratic forms, e.g., $\tilde{t}_{ij}^R = {\gamma^{(1)}}^T A \gamma^{(2)}$ for a particular antisymmetric matrix A.

Next, we checked if the operator $\hat{h}_{ij}$ commuted with zero modes other than $\hat{\gamma}^{(1)}$ and $\hat{\gamma}^{(2)}$. We performed this check by computing the commutant matrix $C_{\hat{h}_{ij}}$ in the four-dimensional basis spanned by the Majorana fermions $\hat{a}_i, \hat{b}_i, \hat{a}_j, \hat{b}_j$. For the bond operator specified by Eqs. (B.14) and (B.15), the commutant matrix has a null space that is exactly two-dimensional and spanned precisely by the $\hat{\gamma}_{ij}^{(1)}$ and $\hat{\gamma}_{ij}^{(2)}$ zero modes. The two remaining eigenstates of the 4×4 $C_{\hat{h}_{ij}}$ matrix are degenerate with eigenvalue $4\Delta\varepsilon_{ij}$, where

$$\begin{aligned}\Delta\varepsilon_{ij} = &({\alpha_i^{(1)}}^2 + {\beta_i^{(1)}}^2 + {\alpha_j^{(1)}}^2 + {\beta_j^{(1)}}^2) \\ &\quad \times ({\alpha_i^{(2)}}^2 + {\beta_i^{(2)}}^2 + {\alpha_j^{(2)}}^2 + {\beta_j^{(2)}}^2) \\ &- (\alpha_i^{(1)}\alpha_i^{(2)} + \beta_i^{(1)}\beta_i^{(2)} + \alpha_j^{(1)}\alpha_j^{(2)} + \beta_j^{(1)}\beta_j^{(2)})^2 \\ = &||\hat{\gamma}_{ij}^{(1)}||^2 ||\hat{\gamma}_{ij}^{(2)}||^2 - |\langle \hat{\gamma}_{ij}^{(1)}, \hat{\gamma}_{ij}^{(2)} \rangle|^2 \end{aligned} \tag{B.16}$$

This eigenvalue gap is non-negative ($\Delta\varepsilon_{ij} \geq 0$) by the Cauchy-Schwarz inequality and is positive as long as $\hat{\gamma}_{ij}^{(1)} \not\propto \hat{\gamma}_{ij}^{(2)}$. It is largest when the two zero modes are orthogonal on sites i and j.

Finally, we discuss how the $\hat{h}_{ij}$ bond operator can be used as a building block to construct Hamiltonians that commute with desired zero modes. Since $\hat{h}_{ij}$ is even in fermionic operators, $[\hat{h}_{ij}, \hat{a}_k] = [\hat{h}_{ij}, \hat{b}_k] = 0$ for $k \neq i, j$. The above derivation showed that $[\hat{h}_{ij}, \hat{\gamma}^{(1)}_{ij}] = [\hat{h}_{ij}, \hat{\gamma}^{(2)}_{ij}] = 0$. Together, these two facts imply that $[\hat{h}_{ij}, \hat{\gamma}^{(1)}] = [\hat{h}_{ij}, \hat{\gamma}^{(2)}] = 0$ for the entire zero modes $\hat{\gamma}^{(1)}$ and $\hat{\gamma}^{(2)}$.

Let us examine what happens when we attempt to construct an N-site Hamiltonian made of only the bond operators

$$\hat{H}_{ZM} = \sum_{ij} J_{ij} \hat{h}_{ij}. \tag{B.17}$$

In this procedure, imagine that we have beforehand decided on a desired pair of zero modes, $\hat{\gamma}^{(1)}, \hat{\gamma}^{(2)}$, so that we have specified the $\alpha^{(1)}_k, \beta^{(1)}_k, \alpha^{(2)}_k, \beta^{(2)}_k$ parameters for all $k = 1, \ldots, N$. This in turn specifies all of the $\hat{h}_{ij}$ operators. To avoid the case where $\Delta\varepsilon_{ij} = 0$, we also require that $\hat{\gamma}^{(1)}_{ij} \not\propto \hat{\gamma}^{(2)}_{ij}$ for the (i, j) pairs that we consider below.

Suppose that we start building our Hamiltonian from the zero operator, so that $J_{ij} = 0$ for all i, j. In this case, there are $2N$ zero modes that (trivially) commute with $\hat{H}_{ZM} = 0$: $\hat{a}_k, \hat{b}_k$ for $k = 1, \ldots, N$. Note that each site has two zero modes and each bond has four. Next, suppose that we turn on a bond $J_{lm} \neq 0$ for a particular pair of sites l, m. On sites l, m, the bond operator gaps out two of the four zero modes, so that only *two* zero modes $\hat{\gamma}^{(1)}_{lm}, \hat{\gamma}^{(2)}_{lm}$ on sites l, m commute with the Hamiltonian. After laying down the first bond, there are $2N - 2$ zero modes. Moreover, the zero modes on sites l, m are now constrained to locally match $\hat{\gamma}^{(1)}$ and $\hat{\gamma}^{(2)}$. Now, consider iterating the procedure and laying down one bond at a time. If we connect the bonds together, e.g., so that $J_{lm}, J_{mn}, J_{np} \neq 0$, then each bond we lay down eliminates two zero modes from the system and acts as a constraint that forces the zero modes on those sites to match our desired zero modes. If we think of the non-zero J_{ij} as being the edges of a graph, then we can see that we are building a connected component into the graph and that the only zero modes that commute with the Hamiltonian on that connected component are constrained to match $\hat{\gamma}^{(1)}$ and $\hat{\gamma}^{(2)}$. In general, if we build the $\hat{H}_{ZM}$ Hamiltonian to have N_C connected components, then there will be $2N_C$ zero modes, each of which are "pieces" of the $\hat{\gamma}^{(1)}$ and $\hat{\gamma}^{(2)}$ zero modes. If $N_C = 1$, i.e., the graph is connected, then the only two zero modes are exactly the entire $\hat{\gamma}^{(1)}$ and $\hat{\gamma}^{(2)}$ operators.

Finally, we mention that it is straightforward to perform similar calculations as those discussed above to construct Hamiltonians that commute with more than two zero modes. This would involve constructing generalized bond operators that commute with more than two desired zero modes, which would extend over more than two sites, using larger commutant matrices.

B.8 Level-spacing statistics of perturbed spin Hamiltonians

The Hamiltonians discussed in Sec. 4.4 have many integrals of motion. Using the eigenstates of these integrals of motion, we block diagonalized the Hamiltonians according to their quantum number sectors and analyzed the level-spacing statistics in particular sectors. Many of these Hamiltonians have significant eigenstate degeneracy in these sectors, which makes analysis of the level-spacing statistics unreliable or inconclusive. We observed that particular perturbations of these Hamiltonians possess the same integrals of motions as the unperturbed Hamiltonians, though at the cost of breaking spatial symmetries. These perturbed Hamiltonians, however, have almost no degenerate eigenstates, which allows us to gather more reliable level-spacing statistics. Below, we describe how we computed the level-spacing statistics of these perturbed Hamiltonians while accounting for as many integrals of motion as possible.

On the square lattice, we analyzed the perturbed Hamiltonian of Eq. (4.43). Like the unperturbed model, the perturbed model commutes with straight-line Z Wilson loops and products of two straight-line X loops, which are listed in Eq. (4.40).

We diagonalized these Hamiltonians in a basis of states that are eigenstates of the known integrals of motion. Here we describe how we found these eigenstates. The $+1$ eigenstates of the $\hat{Z}_{\mathcal{L}}$ integrals of motion, for example, are simply product state spin configurations $|S\rangle$ that satisfy $\hat{Z}_{\mathcal{L}}|S\rangle = +|S\rangle$, i.e., spin configurations that have an even number of down spins on the sites of loop $\mathcal{L}$. The $+1$ eigenstates $|S'\rangle$ of the $\hat{X}_{\mathcal{L}}\hat{X}_{\mathcal{L}'}$ operators can be constructed from spin configurations $|S\rangle$ in the following way: $|S'\rangle = \frac{1}{\sqrt{2}}(\hat{I} + \hat{X}_{\mathcal{L}}\hat{X}_{\mathcal{L}'})|S\rangle$. Using these two facts, we are able to construct all $+1$ eigenstates of the $\hat{Z}_{\mathcal{L}}$ and $\hat{X}_{\mathcal{L}}\hat{X}_{\mathcal{L}'}$ integrals of motion (with slight modification, we can build -1 eigenstates as well). In addition to the Z and X loop integrals of motion, there is also a global integral of motion $\hat{B}$, slightly modified from the operator in Eq. (4.42), which is a sum of the terms of Hamiltonian Eq. (4.43) that lie on B-sublattice squares. We determine the eigenstates of $\hat{B}$ by perturbing the Hamiltonian by $\hat{B}$. In particular, instead of diagonalizing $\hat{H}_{\text{square}} + \epsilon\delta\hat{H}$, we diagonalize $\hat{H}_{\text{square}} + \epsilon\delta\hat{H} + \lambda\hat{B}$ for a large constant λ. The $\hat{B}$-perturbation separates out the eigenstates of $\hat{B}$ so that they are far away from one another in energy. This allows us to numerically identify eigenstates with the same eigenvalue of $\hat{B}$.

We also attempted to account for integrals of motion that we were not able to identify directly. Such unknown integrals of motion, if left unaccounted for, would give rise to Poisson level-spacing statistics. This would occur when neighboring energy levels E_n, E_{n+1} are in different quantum number sectors of these integrals of motion. Note that here we are considering a family of perturbed Hamiltonians, $\hat{H}_0 + \epsilon\delta\hat{H}$, where $[\hat{H}_0, \delta\hat{H}] \neq 0$. If there is a hidden integral of motion $\hat{\mathcal{O}}$ that commutes with $\hat{H}_0 + \epsilon\delta\hat{H}$ for all ϵ, then $[\hat{H}_0, \hat{\mathcal{O}}] = [\delta\hat{H}, \hat{\mathcal{O}}] = 0$. This means that one can block diagonalize $\delta\hat{H}$ according to the eigenstates of $\hat{\mathcal{O}}$

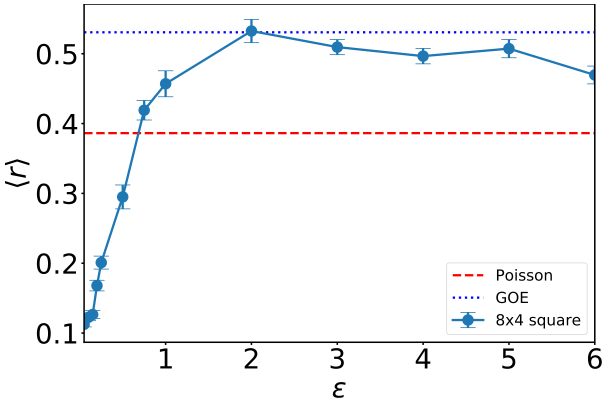

Figure B.1: The average level-spacing ratios versus disorder strength ϵ for the Hamiltonian Eq. (4.43) on an 32-site square lattice (8x4 square) averaged over 10 random Hamiltonians. The energy levels considered were obtained in particular quantum number sectors, as described in the main text.

and that eigenstates $|\psi_1\rangle, |\psi_2\rangle$ of $\hat{\mathcal{O}}$ with different eigenvalues satisfy $\langle\psi_2|\delta\hat{H}|\psi_1\rangle = 0$. Moreover, energy eigenstates $|\psi_j\rangle$ of $\hat{H}_0 + \epsilon\delta\hat{H}$ that are non-degenerate are also eigenstates of $\hat{\mathcal{O}}$. Using these observations, we computed the perturbation overlaps $\delta H_{ij} = \langle\psi_i|\delta\hat{H}|\psi_j\rangle$ in the basis of $\{|\psi_j\rangle\}$ obtained with ED. We then reordered the states so as to block diagonalize the δH_{ij} matrix. When block diagonalizing δH_{ij}, we considered entries of the matrix smaller than 10^{-6} to be zero. The eigenstates within the same block were considered as a "sector" of the hidden integrals of motion. We performed our level-spacing ratio calculations using the energies in these sectors, which are also contained within the known integral of motion quantum number sectors mentioned above.

Accounting for both known and unknown integrals of motion as described above, we computed the level-spacing ratios of 4096 eigenvalues in the $+1$ sectors of the Z loops and X product loops for the Hamiltonians of Eq. (4.43) on an 8×4 square lattice. We did this for 10 random realizations of the perturbed Hamiltonians for ϵ from 0.05 to 2. After accounting for the global integral of motion, the energy eigenstates typically separated into sectors of 64 states. After accounting for the hidden integrals of motion, these 64 states separated further into three sectors containing 28 states, 35 states, and 1 state. We computed the level-spacing ratios between states of neighboring energies in the 28 and 35-dimensional sectors and averaged the results over all such sectors and over random realizations of the Hamiltonians. The resulting average level-spacing ratios for ϵ from 0 to 6 are depicted in Fig. B.1.

On the kagome lattice, we analyzed the perturbed Hamiltonians of Eqs. (4.52) and (4.53). Both of these Hamiltonians commute with Z Wilson loops and products of two X loops. However, the Hamiltonian of Eq. (4.52) also commutes with the local hexagon integrals of motion $\hat{Z}_{\hexagon}$, while Eq. (4.53) is a generic Hamiltonian that does not.

Using the same techniques described above to account for known and unknown integrals of motion, we performed ED on the Hamiltonians of Eq. (4.52)-(4.53) for $3 \times 2 \times 3 = 18$ site and $3 \times 3 \times 3 = 27$ site kagome lattices. For the Eq. (4.52) Hamiltonians on the 18-site lattice, we performed ED in a 256-dimensional basis corresponding to the $+1$ quantum number sector of each of the Wilson loops and hexagon local integrals of motion. We were not able to identify any "hidden" quantum number sectors in this 256-dimensional space and found that all energies in this sector were unique. For the Eq. (4.52) Hamiltonians on the 27-site lattice, we performed ED in a 8192-dimensional basis. In this case, we did find "hidden" integral of motion sectors that were 2048-dimensional and contained no degeneracies. For the Eq. (4.53) Hamiltonians on the 18-site lattice, we performed ED in a 1024-dimensional basis. In this case, the global integral of motion (a modified version of operator $\hat{D}$ from Eq. (4.51) that only contains the hexagon interactions of the Hamiltonian) split the space into three sectors, which are 256, 256, and 512-dimensional. Interestingly, while the first two sectors have no degeneracies, the third sector is doubly-degenerate in each of its energy eigenstates. In this case, we ignored the degeneracy when computing the level-spacing statistics. We did not find any hidden integral of motion sectors for these Hamiltonians. For the Hamiltonians of Eq. (4.52)-(4.53) at a particular disorder strength ϵ, we averaged the level-spacing ratios $\langle r \rangle$ of the sectors over many random realizations of the random variables $h_{\triangle}$ (100 realizations for the 18-site kagome lattice and 10 realizations for the 27-site lattice). The average level-spacing ratios as a function of ϵ are shown in Fig. 4.9.

Appendix C

Numerical evidence for many-body localization in two and three dimensions

C.1 Hard-core Bose-Hubbard model as a spin-1/2 model

If the bosons in the Bose-Hubbard model of Eq. (5.2) are hard-core bosons, then they can be represented with Pauli matrices. In particular, the creation and annihilation operators can be represented as $a_i^\dagger = \sigma_i^+ = (\sigma_i^x + i\sigma_i^y)/2$ and $a_i = \sigma_i^- = (\sigma_i^x - i\sigma_i^y)/2$ and the number operator as $n_i = a_i^\dagger a_i = (I + \sigma_i^z)/2 = n_i^2$. Substituting these expressions into Eq. (5.2), we obtain the spin-1/2 Hamiltonian

$$H = -\frac{J}{2}\sum_{\langle ij\rangle}\left(\sigma_i^x\sigma_j^x + \sigma_i^y\sigma_j^y\right) + \frac{1}{2}\sum_i \delta_i\sigma_i^z \tag{C.1}$$

plus a term proportional to the identity operator, which we ignore because it commutes with all operators. This is a two-dimensional XX model with random magnetic fields. We use Eq. (C.1) in our hard-core Bose-Hubbard calculations.

C.2 Algorithmic details

Here we describe the details of the gradient descent calculation performed to optimize the objective function in Eq. (5.6). As described in Ref. [44], for an operator $O = \sum_a c_a\mathcal{O}_a$, the norm of the commutator with a Hamiltonian $H = \sum_a J_a\mathcal{O}_a$ can be expressed as the quadratic form

$$Z_C \equiv \|[H, O]\|^2 = \sum_{ab} c_a (C_H)_{ab} c_b \tag{C.2}$$

where $(C_H)_{ab} = \mathrm{tr}\left([H, \mathcal{O}_a]^\dagger [H, \mathcal{O}_b]\right)/\mathrm{tr}\,(I)$ is the commutant matrix, which is Hermitian and positive semi-definite. Finding the (normalized) operator O that minimizes this quantity amounts to finding the smallest eigenvalue eigenvector of C_H. Since the Pauli strings $\mathcal{O}_a$ are orthonormal with respect to the Frobenius inner product, the commutant matrix can be written as $C_H = L_H^\dagger L_H$, where $(L_H)_{ca} = \sum_b J_b f_{ba}^c$ is the Liouvillian matrix and f_{ab}^c are structure constants that describe how Pauli strings commute ($[\mathcal{O}_a, \mathcal{O}_b] = \sum_c f_{ab}^c\mathcal{O}_c$). For

Pauli strings, the tensor f_{ab}^{c} and matrix L_H are sparse and efficient to compute numerically [44].

The "binarity" $\|O^2 - I\|^2$ of the operator O can be written as

$$\begin{aligned} Z_B \equiv \|O^2 - I\|^2 &= \|\frac{1}{2}\{O,O\} - I\|^2 \\ &= \|\frac{1}{2}\sum_{ab} c_a c_b \{\mathcal{O}_a, \mathcal{O}_b\} - I\|^2 \\ &= \|\sum_{c}\left(\frac{1}{2}\sum_{ab} c_a c_b \bar{f}_{ab}^{c} - \delta_{c,0}\right)\mathcal{O}_c\|^2 \\ &= 1 - \sum_{ab} c_a c_b \bar{f}_{ab}^{0} + \frac{1}{4}\sum_{aba'b'c} c_a c_b c_{a'} c_{b'} \bar{f}_{ab}^{c} \bar{f}_{a'b'}^{c}, \end{aligned} \tag{C.3}$$

where $\bar{f}_{ab}^{c}$ are real constants that describe how Pauli strings anti-commute ($\{\mathcal{O}_a, \mathcal{O}_b\} = \sum_c \bar{f}_{ab}^{c} \mathcal{O}_c$) and the $c = 0$ index corresponds to the identity operator so that $\mathcal{O}_0 = I$. Note that Z_B is *quartic* in the $\{c_a\}$ parameters, making it difficult to minimize in general.

To minimize the non-linear objective $\alpha Z_C + \beta Z_B$, we perform gradient descent using Newton's method, which requires calculation of gradients and Hessians. To avoid the numerical cost and stability issues of using finite-difference derivatives, we use exact expressions for these quantities. The gradient and Hessian of the commutator norm can be expressed as

$$\partial_a Z_C \equiv \frac{\partial Z_C}{\partial c_a} = \sum_b \left(C_H + C_H^{\dagger}\right)_{ab} c_b \tag{C.4}$$

and

$$\partial_a \partial_b Z_C = \left(C_H + C_H^{\dagger}\right)_{ab}. \tag{C.5}$$

The gradient and Hessian of the binarity can be expressed as

$$\partial_a Z_B = \sum_{bc} c_b (\bar{L}_O)_{bc} (\bar{L}_O)_{ca} - 2(\bar{L}_O)_{a,0} \tag{C.6}$$

and

$$\partial_a \partial_b Z_B = \sum_c \left[2(\bar{L}_O)_{ca}(\bar{L}_O)_{cb} + \sum_d (\bar{L}_O)_{cd} c_d \bar{f}_{ab}^{c}\right] - 2 f_{ab}^{0}, \tag{C.7}$$

where $(\bar{L}_O)_{ca} \equiv \sum_b c_b \bar{f}_{ba}^{c}$ is itself a function of the $\{c_a\}$ parameters. We checked Eqs. (C.4)–(C.7) numerically against finite-difference derivatives and Hessians and found that they agreed.

Our open-source Python code for performing this optimization is available online [251]. To compute commutators and anti-commutators between Pauli strings, we used the quantum operators from symmetry (QOSY) python package [47, 44]. The gradient descent was performed using Newton's method with conjugate-gradient iteration as implemented in the `scipy.optimize.minimize` function in the scipy library [300], with the desired relative error required for convergence set to `xtol`$= 10^{-6}$. We used python version 3.5.5, scipy version 1.0.0, and numpy version 1.14.2.

During the calculations, we stored the commutators and anti-commutators between Pauli strings, i.e., the constants f_{ab}^{c} and $\bar{f}_{ab}^{c}$, into python dictionaries (hash tables). In our calculations, memory was a main bottleneck, which prevented us from working with larger basis sizes $|B|$. To gather reliable statistics, we performed many independent optimizations on different random realizations of the Hamiltonians in Eqs. (1) and (2) by running the optimization in parallel over many processes and nodes of the Blue Waters supercomputer at the National Center for Supercomputing Applications at the University of Illinois at Urbana-Champaign. A typical slow single disorder realization for a low-disorder, three-dimensional calculation (for all 11 basis expansions) takes approximately 1 core-hour and about 7 gigabytes of memory on a Blue Waters XE node. Running the full suite of realizations/models in this work takes approximately 10,000 node-hours on Blue Waters.

C.3 Future extensions

In future work, it would be useful to consider alternative more memory-efficient numerical minimization procedures that would allow us to go to larger basis sizes and/or optimize more disordered realizations in parallel. It would also be interesting to develop other basis initializations or basis expansion procedures that are more efficient or lead to better minimization of the objective Eq. (5.6). One could also explore whether basis reduction techniques for pruning the basis of Pauli strings could improve performance and memory usage. It would also be interesting to use this method to find many mutually commuting binary integrals of motion at once, which can be done by modifying the objective in Eq. (5.6) to include multiple τ_i^z operators, but we generally expect this to be computationally expensive.

Another interesting extension would be to modify the second term in objective function in Eq. (5.6) from a binarity to a *unitarity*, i.e., $\|U^\dagger U - I\|^2$. This would allow the algorithm to find unitaries that commute with the given Hamiltonian.

C.4 Statistical properties of the approximate integrals of motion

C.4.1 Quantities considered

In this work, we analyzed a variety of quantities to understand the properties of the approximate ℓ-bits that our algorithm produced as output. In summary, given an approximate ℓ-bit, we consider its commutator norm, binarity, normalization, overlap with a single-site τ_i^z operator, range (r), locality (k), correlation length (ξ), and the IPR.

The commutator norm $\|[H, \tau_i^z]\|^2$ and binarity $\|(\tau_i^z)^2 - I\|^2$ make up the objective function in Eq. (5.6) that we minimize with our algorithm. Note that the minimization of Eq. (5.6) is performed without any constraint on the normalization of τ_i^z; a perfectly binary operator is normalized, and so minimizing the binarity takes care of keeping operators nearly normalized. Therefore, it is interesting to consider $\|\tau_i^z\|$ as a metric for the performance of the algorithm. A strong deviation from $\|\tau_i^z\| \approx 1$ potentially indicates a failure of our algorithm. Note that for consistency the commutator norms, binarities, and other quantities depicted in all of the figures in the main text and the supplemental material use *normalized* τ_i^z operators.

An important quantity that we discuss in the main text is the overlap of the τ_i^z operator with σ_i^z. As shown in Fig. 5.3 in the main text, the probability distribution of $|\langle \tau_i^z, \sigma_i^z \rangle|^2$ changes significantly as one decreases disorder strength. In particular, the distribution rapidly changes near the ergodic-MBL transition for the 1D Heisenberg model and behaves similarly for the other models considered.

Another quantity related to the spatial localization of a τ_i^z operator is the "range"

$$r = \frac{1}{\sum_b |c_b|^2} \left(\sum_a |c_a|^2 \max_{\mathbf{r}, \mathbf{r}' \in R_a} \|\mathbf{r} - \mathbf{r}'\| \right), \tag{C.8}$$

where R_a is the set of lattice coordinates that Pauli string $\mathcal{O}_a$ acts on. The range is a weighted average over the spatial extents of the operator's Pauli strings and is similar to other definitions for the range of an ℓ-bit used in studies of 1D MBL systems [106, 234]. A similar quantity that we consider is the "locality" k of a τ_i^z operator, which is defined as

$$k = \frac{\sum_a |c_a|^2 k_a}{\sum_b |c_b|^2}, \tag{C.9}$$

where $k_a = |R_a|$ is the number of sites a Pauli string $\mathcal{O}_a$ acts on (i.e., $\mathcal{O}_a$ is k_a-local), regardless of their position in the lattice. The locality measures the average contribution of non-local Pauli strings to the operator.

In Eq. (5.5) in the main text, we introduced the weights $w_{\mathbf{r}}$ of a τ_i^z operator, which can be interpreted as the spatial probability distribution of τ_i^z over the lattice positions $\mathbf{r}$. We fit the weights $w_{\mathbf{r}}$ of each τ_i^z operator to an exponential decay with a correlation length ξ. In addition, we also use the weights $w_{\mathbf{r}}$ to define the operator inverse participation ratio

$$IPR = \frac{1}{\sum_{\mathbf{r}} w_{\mathbf{r}}^2}, \tag{C.10}$$

a quantity analogous to inverse participation ratios considered in other MBL studies [301, 105, 210]. For a τ_i^z operator localized on site i, $w_{\mathbf{r}} \approx \delta_{\mathbf{r},\mathbf{r}_i}$ and so $IPR \approx 1$. For a τ_i^z operator delocalized evenly over N sites, $w_{\mathbf{r}}$ is approximately $1/N$ on those sites so that $IPR \approx 1/(N \cdot 1/N^2) = N$.

C.4.2 Distributions

Figs. C.1–C.3 show interpolated histograms of $|\langle \tau_i^z, \sigma_i^z \rangle|^2$, r, and ξ versus disorder strength for the four models studied and for different iterations of the algorithm. The histograms are normalized so that at a fixed disorder strength the maximum of the histogram is one.

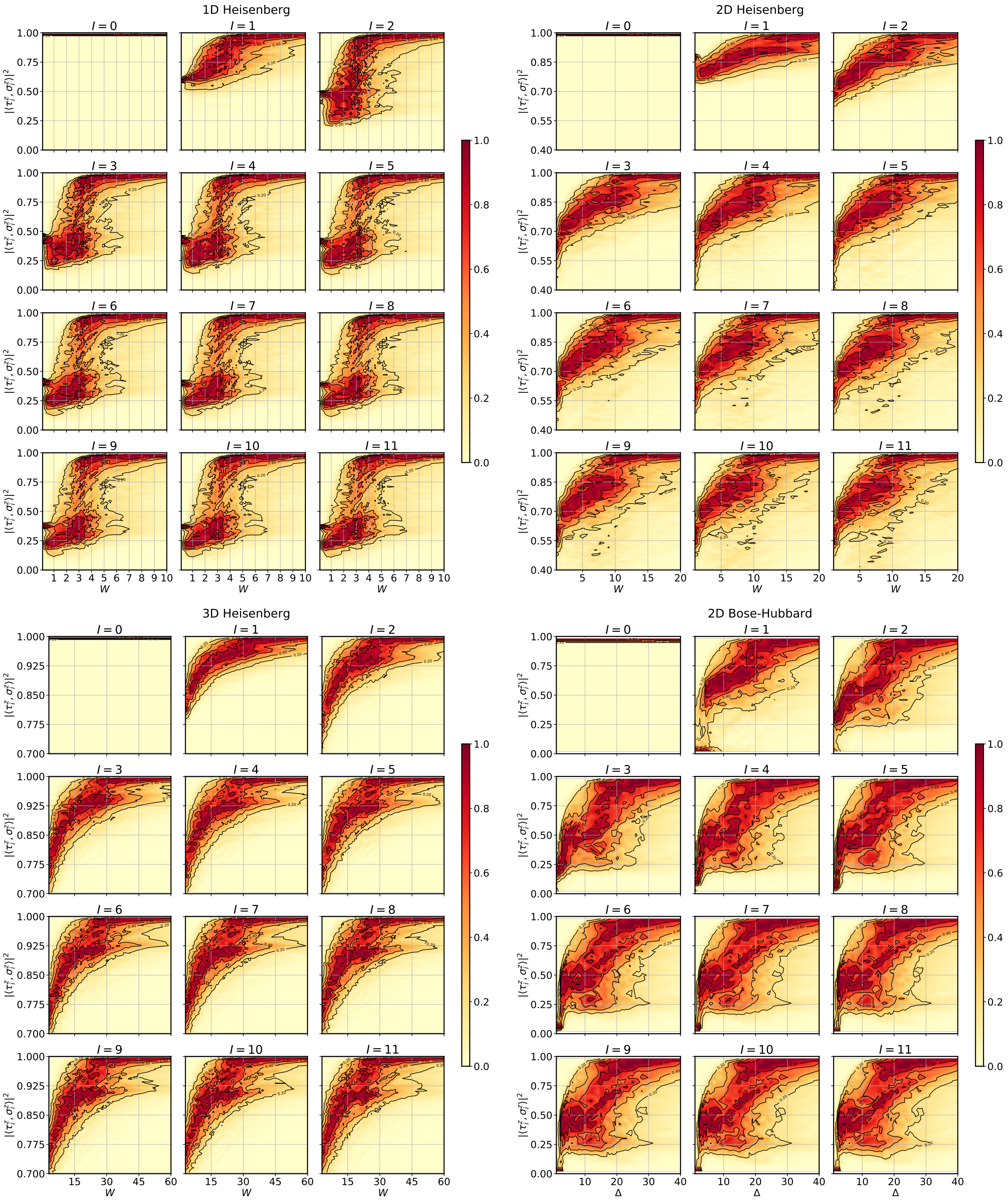

Figure C.1: Interpolated histograms of $|\langle\tau_i^z, \sigma_i^z\rangle|^2$ overlaps at different disorder strengths for the four models studied at different iterations I of the basis expansion.

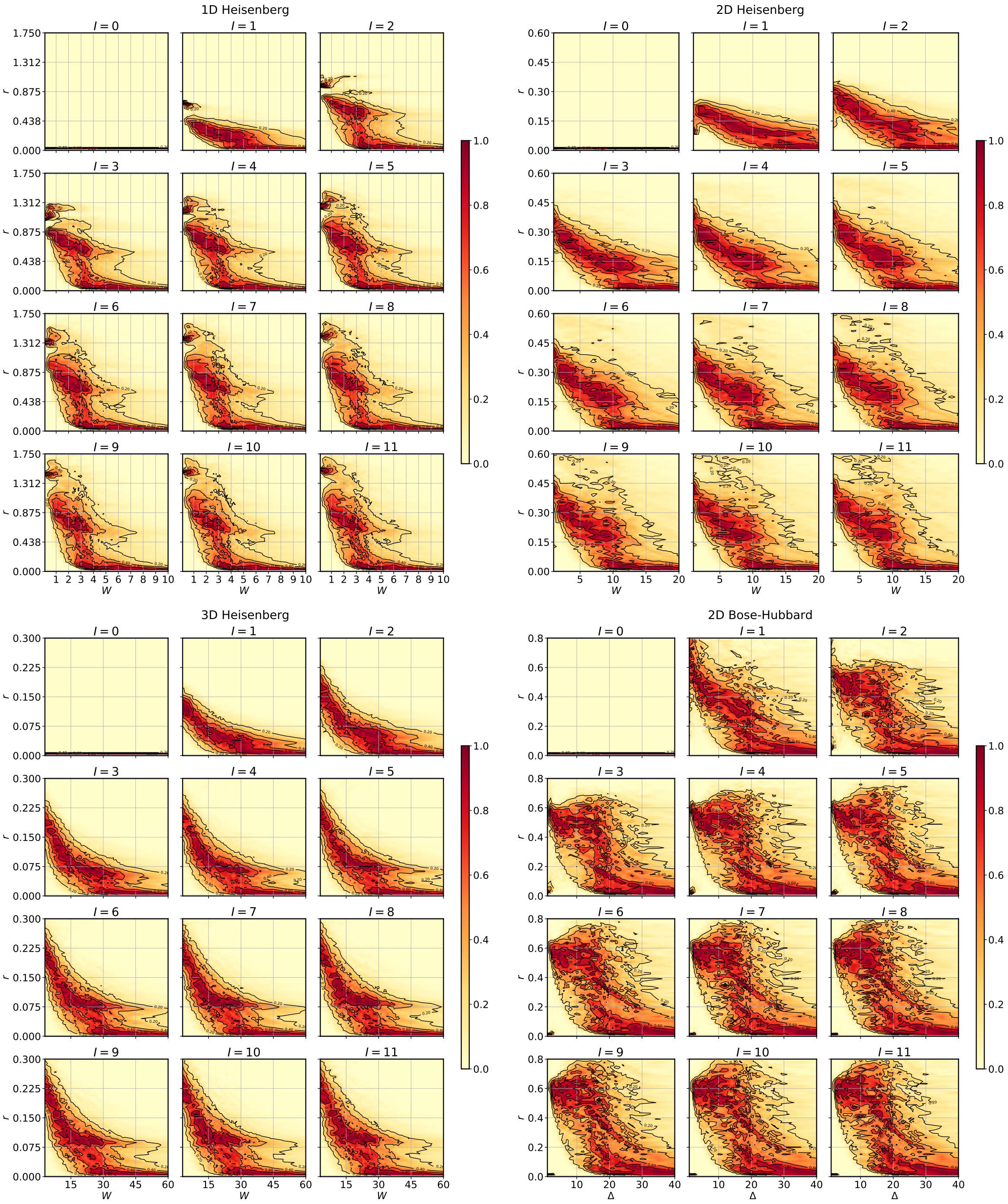

Figure C.2: Interpolated histograms of the range r at different disorder strengths for the four models studied at different iterations I of the basis expansion.

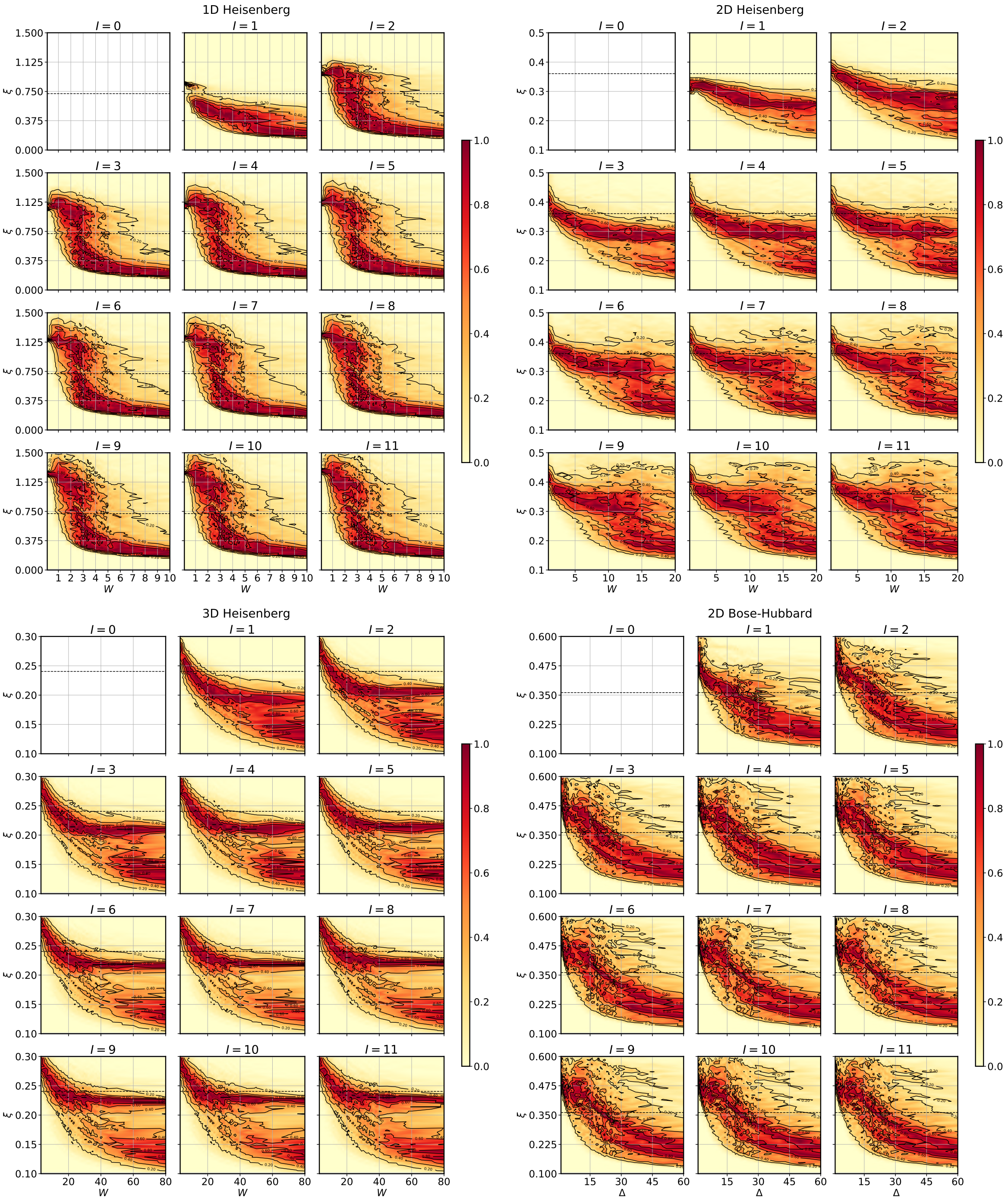

Figure C.3: Interpolated histograms of the correlation length ξ at different disorder strengths for the four models studied at different iterations I of the basis expansion. For reference, $1/\ln(4^d)$, where d is the spatial dimension, is marked with a horizontal dashed line.

C.4.3 Averages, medians, and fluctuations

Figs. C.4–C.11 show the averages, standard deviations, medians, and median absolute deviations (MAD, defined as the median distance from the median: $Med[|x - Med[x]|]$) of the previously discussed quantities versus disorder strength for the optimized τ_i^z operators that our algorithm produces. The medians and MADs are included for comparison since they are more robust to outliers than averages and standard deviations. Different colored lines represent calculations done in different basis sizes, i.e., at different steps in our expansion procedure. For visual guidance, we mark the approximate locations of local maxima in the plots with blue stars, which were obtained by fitting third-order polynomials to data in the windows marked by dashed blue lines. The locations of these maxima versus basis size are shown in Fig. C.12.

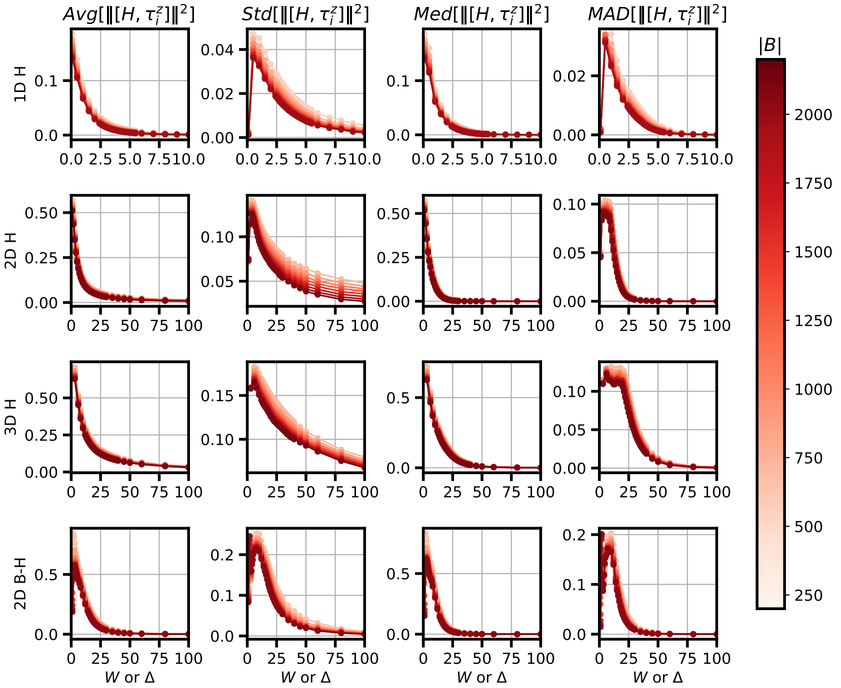

Figure C.4: Statistics of commutator norms for different models and basis sizes.

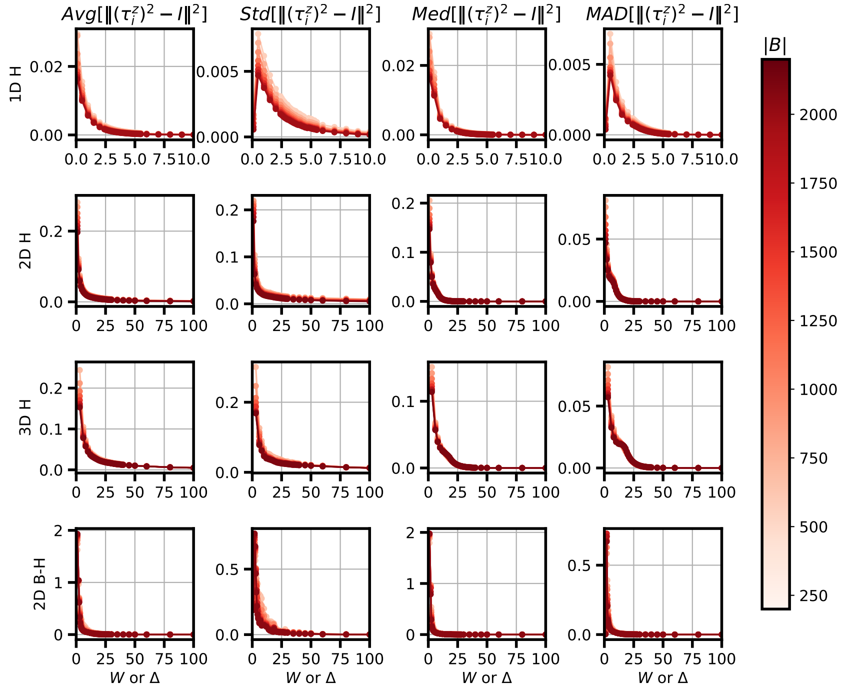

Figure C.5: Statistics of binarities for different models and basis sizes.

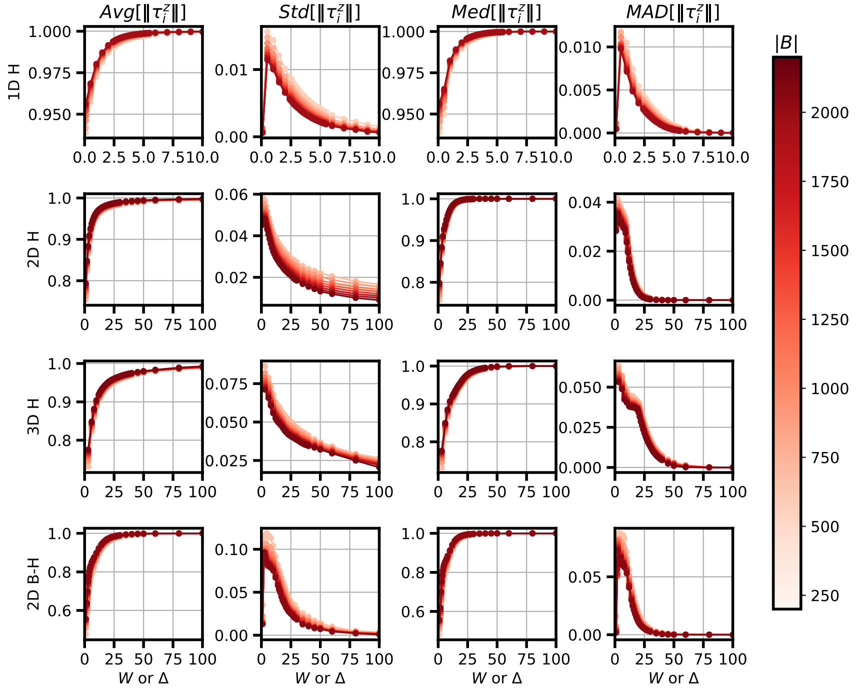

Figure C.6: Statistics of operator norms for different models and basis sizes.

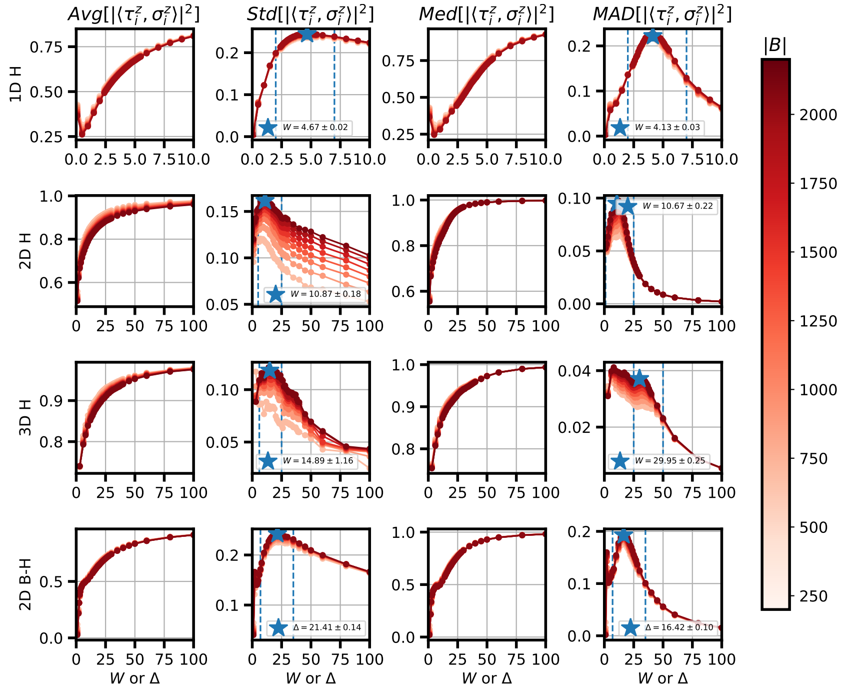

Figure C.7: Statistics of $|\langle\tau_i^z,\sigma_i^z\rangle|^2$ for different models and basis sizes.

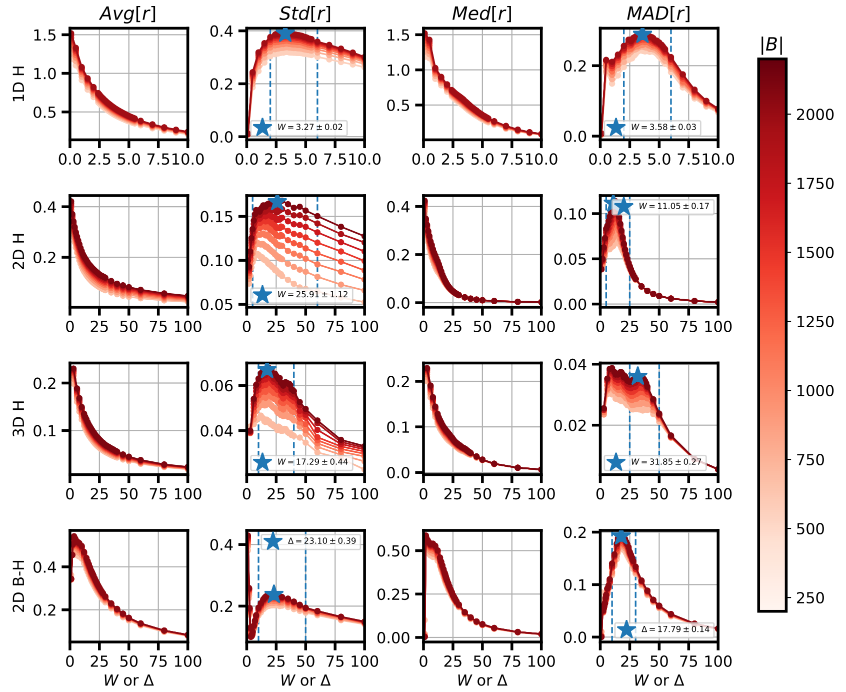

Figure C.8: Statistics of ranges for different models and basis sizes.

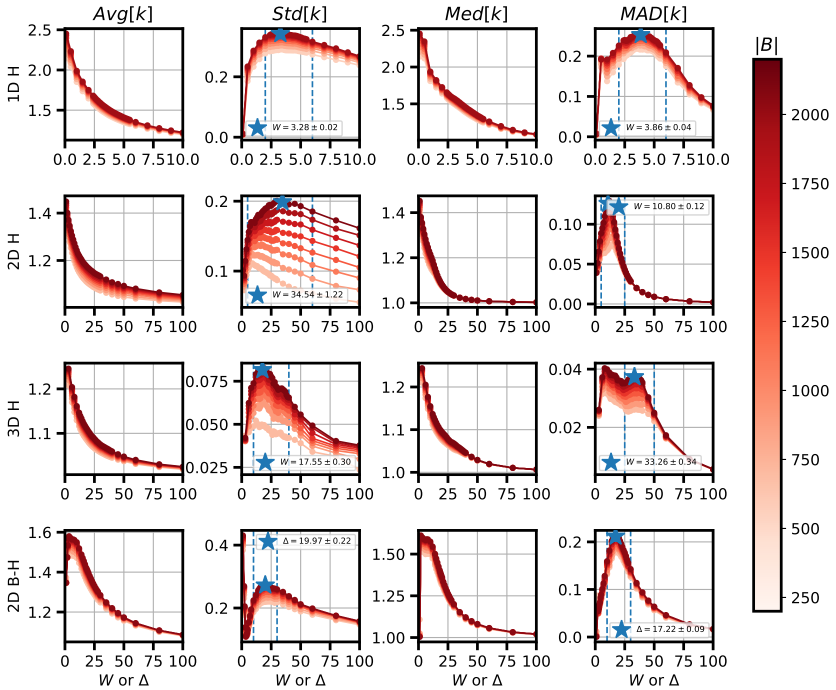

Figure C.9: Statistics of localities for different models and basis sizes.

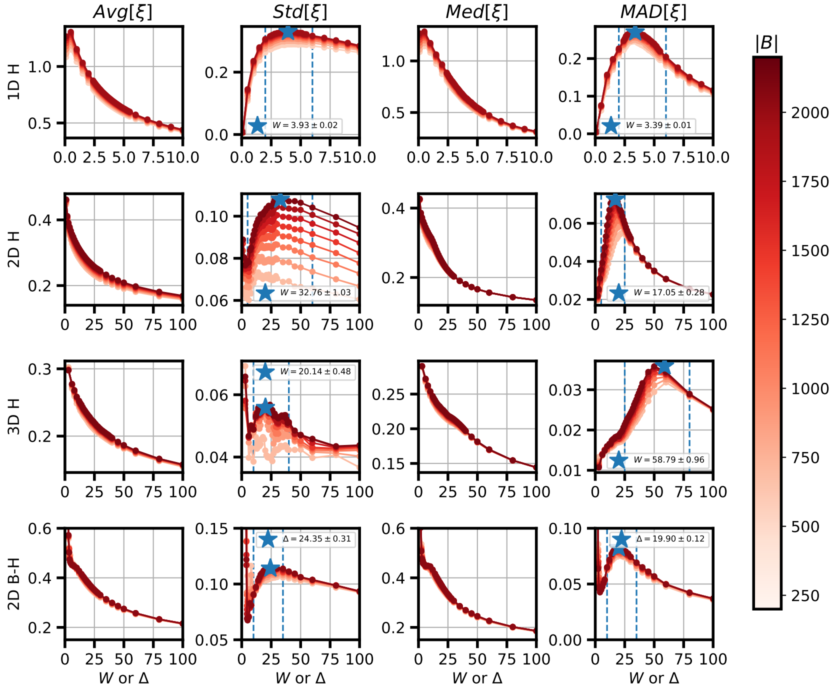

Figure C.10: Statistics of correlation lengths for different models and basis sizes.

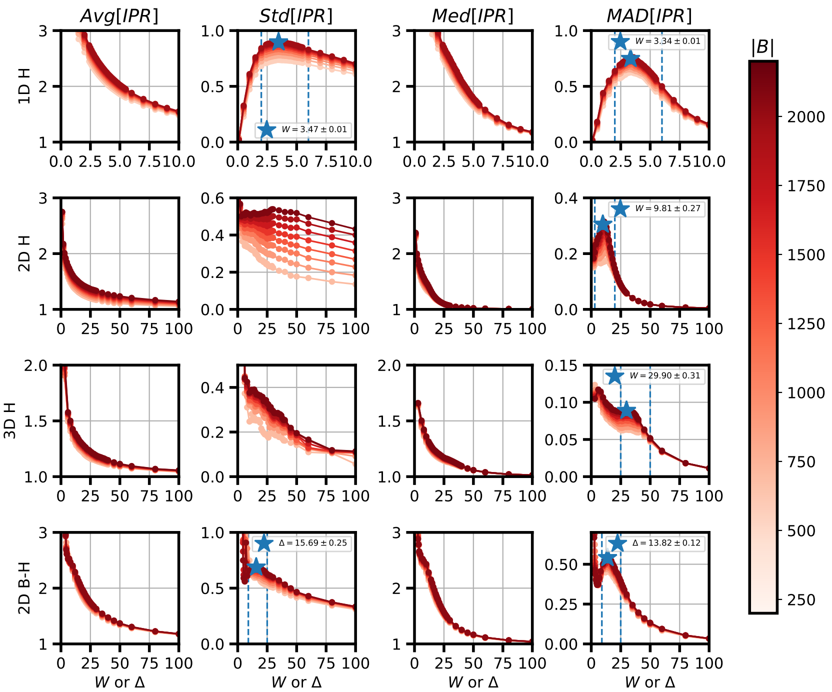

Figure C.11: Statistics of operator inverse participation ratios for different models and basis sizes.

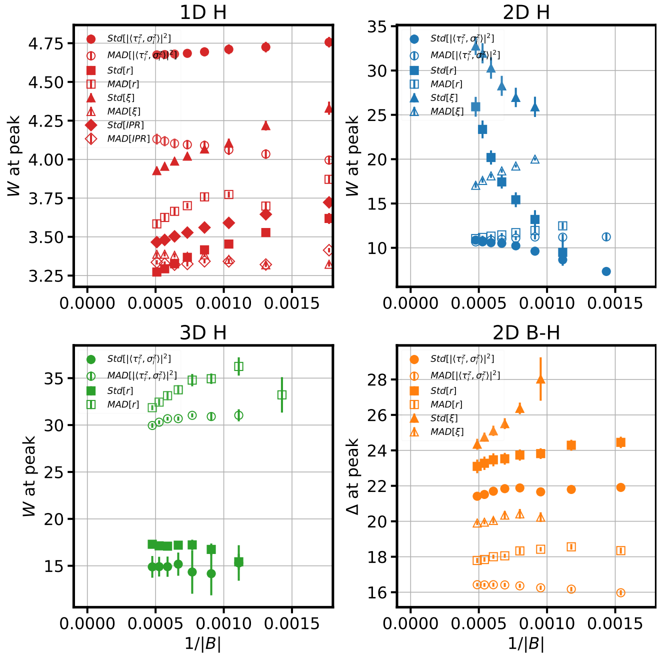

Figure C.12: The disorder strengths at which the standard deviations or MADs of various quantities are maximized versus $1/|B|$ for the four models studied.

C.4.4 Correlations between quantities

Note that many of the quantities discussed above are strongly correlated with one another. The correlations between the commutator norm, binarity, $|\langle \tau_i^z, \sigma_i^z \rangle|^2$ overlaps, ranges, and localitites can be seen in the scatterplots shown in Figs. C.13 and C.14. The range r and locality k in particular are highly correlated so that $r \approx k - 1$ to high accuracy.

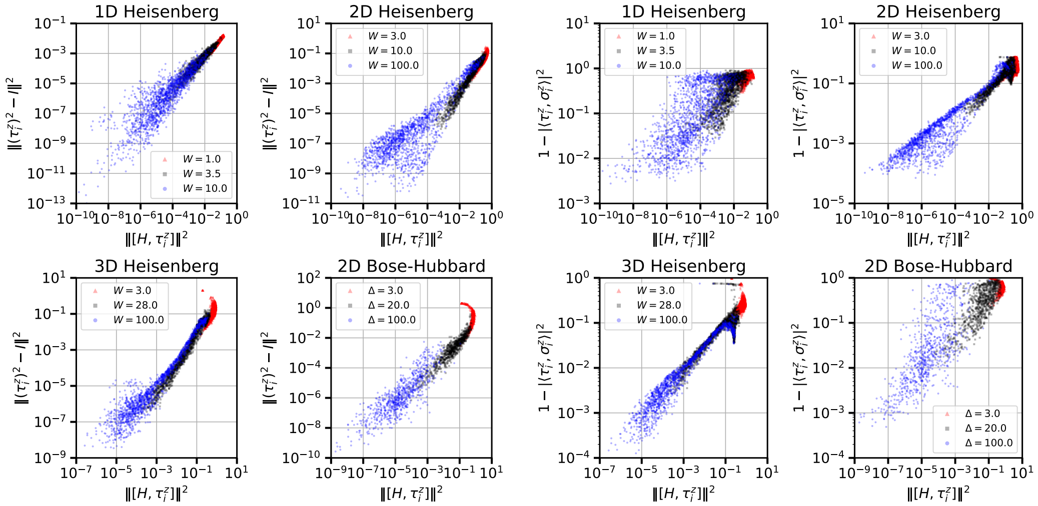

Figure C.13: Scatterplots of binarity versus commutator norm (left) and $1 - |\langle \tau_i^z, \sigma_i^z \rangle|^2$ versus commutator norm (right) for τ_i^z obtained with our algorithm for the four models studied.

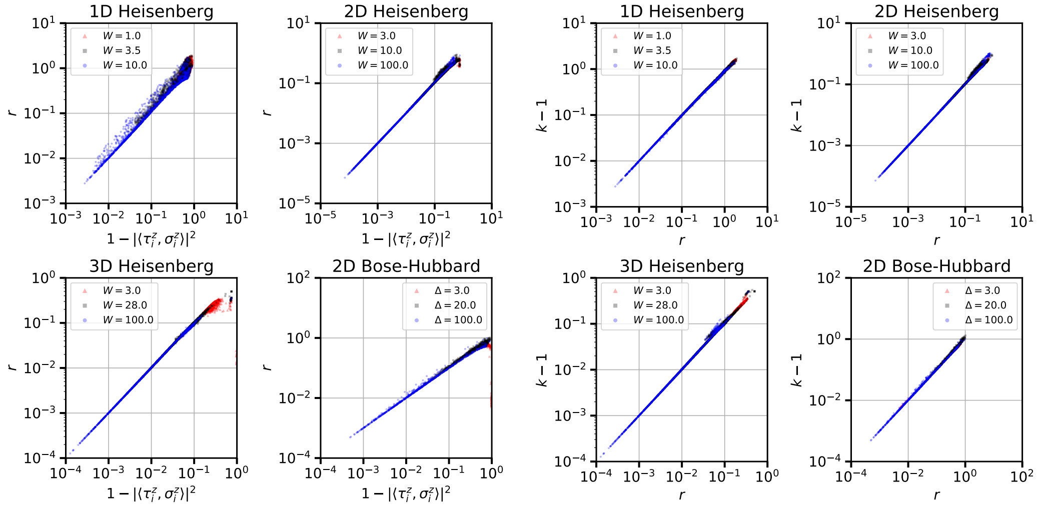

Figure C.14: Scatterplots of range r versus $1 - |\langle \tau_i^z, \sigma_i^z \rangle|^2$ (left) and $k - 1$ versus r (right) for τ_i^z obtained with our algorithm for the four models studied.

C.5 Analysis of correlation lengths

In past MBL studies, many correlation or localization lengths, defined in various ways, have been examined. Here we compare the correlation lengths of our τ_i^z operators obtained with our method against other ℓ-bit lengthscales obtained in past studies of the 1D Heisenberg model [302, 96, 109, 211, 113] and the 2D hard-core Bose-Hubbard model [98]. We include this comparison for reference, but stress that these quantities are measured in different ways and might not be directly comparable. Fig. C.3 shows the distributions of our correlation lengths for the different models studied. Fig. C.15 (and Fig. 5.4 from the main text) shows how our average correlation lengths compare with previous studies.

Rademaker 2017 [302] obtained approximate ℓ-bits obtained using a displacement transformation technique. Their data shown in Fig. C.15 (taken from Fig. 10 of Ref. [302]) was obtained by fitting an exponential decay to a quantity similar to the weight $w_{\mathbf{r}}$ of their approximate ℓ-bits generated by a sixth-order displacement transformation on a length $L = 20$ chain. Kulshreshta 2018 [109] obtained ℓ-bits using a hybrid ED-tensor network approach that involves matching eigenstates. Their average correlation lengths (taken from Fig. 3 of Ref. [109]) were obtained by fitting to the weights of their ℓ-bits for a length $L = 14$ chain. Thomson 2018 [96] found approximate ℓ-bits using a continuous unitary flow procedure, in which they restricted their Hamiltonian and ℓ-bit ansatze to be composed of 1 and 2-local fermionic operators. Their average correlation lengths (taken from Fig. 1(c) of Ref. [96]) were obtained by fitting an exponential decay to coupling constants of their approximately diagonalized MBL Hamiltonian for a $L = 100$ chain. Pancotti 2018 [211] obtained approximate integrals of motion (that are often not binary ℓ-bits) using the slow-operator method [45], exact diagonalization, and tensor networks. Their correlation lengths (taken from the inset of Fig. 2(b) of Ref. [211]) were also obtained by fitting to the weights of their operators. Villalonga 2018 [234] obtained approximate ℓ-bits from one-particle orbitals using matrix product states. Their correlation lengths (taken from Fig. 4 of Ref. [234]) were obtained by fitting to a quantity similar to the weight of their operators for a length $L = 32$ chain. Varma 2019 [112] obtained approximate ℓ-bits using a Wegner-Wilson flow. The shown correlation lengths (taken from Fig. 1 of Ref. [112]) are obtained from fitting an exponential to a transverse correlation function $|\langle n|\sigma_i^x \tau_j^x|n\rangle|$. Peng 2019 [113] obtained ℓ-bits using a "quicksort-like" algorithm involving ED for constructing binary ℓ-bits that have high overlap with σ_i^z. Their correlation lengths (taken from Fig. 4(c) of Ref. [113]) were obtained by fitting to the overlaps $\langle \tau_i^z, \sigma_j^z\rangle \sim \exp(-|i-j|/\xi)$ for a chain of length $L = 12$.

Interestingly, there is significant disagreement in the correlation lengths shown in Fig. C.15. Some studies predict that $\xi \approx 1/\ln(2)$ at the transition, though Ref. [112] suggests that $\xi \approx 1/\ln(4)$ at the transition. Some of the data in the figure agree better with $1/\ln(2)$, though our data appear more consistent with

$1/\ln(4)$. This discrepancy can potentially be attributed to whether the ℓ-bits considered are "edge" or "bulk" spins, which has to do with whether the chain has periodic or open boundary conditions. In all of the studies mentioned above, Refs. [302, 109, 96, 211, 234, 112, 113], the authors considered chains with open boundary conditions (this is implied, but not explicitly stated in Ref. [96]) while we considered the bulk of arbitrarily large chains. Moreover, except for Ref. [211], all of the mentioned studies found every ℓ-bit (including edge ℓ-bits) in the system for each disordered realization, while we only found a single ℓ-bit at a time. This suggests that a significant fraction of previously considered ℓ-bits might be "edge" spins, while our ℓ-bits are "bulk" spins. Other potential explanations for the disagreements in the correlation length data include: the existence of multiple length-scales in MBL systems, finite-size effects, finite basis-size effects, differences in methodology, differences in correlation length definitions, algorithmic biases, and the non-uniqueness of ℓ-bits.

For the 2D hard-core Bose-Hubbard model, we compared our average correlation lengths with the average correlation lengths obtained by Wahl 2019 [98] (see Fig. 5.4 in main text). In their work, they used a shallow 2D tensor network to represent a short quantum circuit U that could be used to construct binary ℓ-bits of the form $\tau_i^z = U^\dagger \sigma_i^z U$. Their correlation lengths (taken from Fig. 6 of Ref. [98]) were obtained by fitting an exponential decay to a disordered-averaged eigenstate-averaged density-density correlation function. Our correlation lengths agree with Wahl 2019 at large disorder ($\Delta \geq 150$), though are larger at smaller disorder (Fig. 5.4 in the main text). Also, as shown in Fig. 5.2(b), the average commutator norms of our approximate ℓ-bits are orders of magnitude lower than their average commutator norms (scaled appropriately). This suggests that our method is able to construct more accurate ℓ-bits with longer-range correlations than the shallow tensor network method used in Ref. [98].

Fig. C.15(b) shows the average correlation lengths that we measure over many decades of disorder strength. For all of the models studied, we find that the inverse correlation lengths scale logarithmically with disorder strength in the large disorder strength limit.

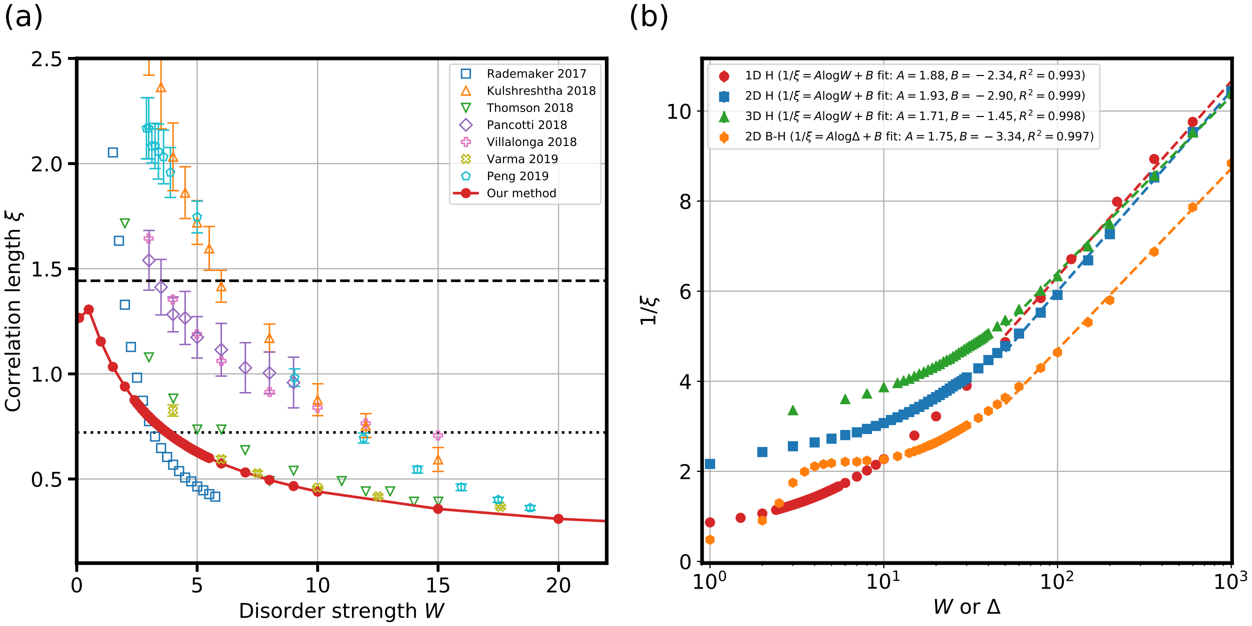

Figure C.15: (a) The average correlation lengths obtained with our method compared against values from past studies (described in text) for the 1D Heisenberg model. The dotted (dashed) horizontal line corresponds to a value of $1/\ln(4)$ ($1/\ln(2)$). (b) The inverse correlation lengths versus disorder strengths on a log-scale for the four models studied with fits to their large disorder strength (≥ 50) behavior.

C.6 Behavior of 2D hard-core Bose-Hubbard model at low disorder

Here we comment on the properties of the τ_i^z operators that we find at very low disorder strength $\lesssim 5$ for the 2D hard-core Bose-Hubbard model (see Fig. C.16). At very low disorder, we find that many of the τ_i^z operators are essentially linear combinations of only single-site Pauli matrices so that $\tau_i^z \approx \sum_j c_j \sigma_j^z$ with $|c_j|^2$ peaked at site i and spread over many sites (with occasional two-site Pauli strings contributing strongly). This causes τ_i^z to have a large IPR and ξ but small $|\langle \tau_i^z, \sigma_i^z \rangle|^2$, r, and k. Because of the small basis size, our algorithm is unable to reduce the binarity $\|(\tau_i^z)^2 - I\|^2$ of the τ_i^z operator, as one can see in Fig C.16. However, the algorithm is able to improve the commutator norm $\|[H, \tau_i^z]\|^2$ by constructing a delocalized operator of the form $\tau_i^z \approx \sum_j c_j \sigma_j^z$. This particular delocalized operator commutes well with the Hamiltonian because it has high overlap with the total magnetization operator, $S_{tot}^z = \sum_{j=1}^N \sigma_j^z$, which is an exact integral of motion of the Hamiltonian. Note that for all four of the Hamiltonians considered S_{tot}^z is an integral of motion and this tendency for producing τ_i^z that have high overlap with S_{tot}^z at very low disorder exists. Yet, as we find empirically, this tendency is particularly strong in the Bose-Hubbard model. This might be due to the physics of the particular model or perhaps the nature of the disorder, which is generated from Gaussian instead of uniform sampling. Interestingly, the transition into this behavior is observed at low disorder, near $\Delta \approx 5$, close to the transition value of $\Delta_c^{exp} \approx 5.5(4)$ obtained by the experiment in Ref. [118] (with non-hard-core bosons and interaction strength $U' = 24.4$).

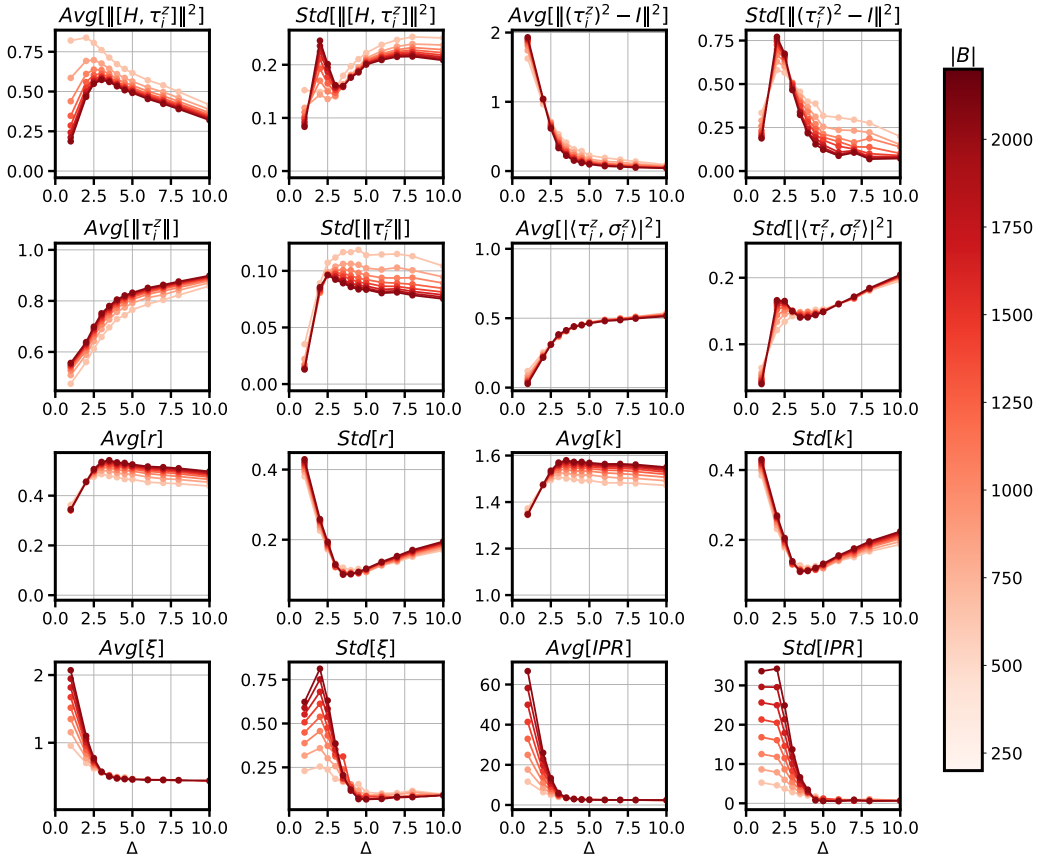

Figure C.16: A zoomed-in look at the averages and standard deviations of various quantities for the 2D hard-core Bose-Hubbard model at low disorder strength Δ where the algorithm fails to find binary operators.

We also note here that, for the Bose-Hubbard model, about half of the Pauli strings in the basis produced during our basis expansion heuristic had amplitudes c_a in the $\tau_i^z = \sum_a c_a \mathcal{O}_a$ operators that were zero to machine precision. This was not the case for the other Hamiltonians and we believe might be due to the symmetries of the model. While this affects the effective basis sizes for the Bose-Hubbard model, it does not change any of our results or conclusions.

C.7 Analysis of cumulative distribution functions

A key feature of the distributions of $|\langle\tau_i^z,\sigma_i^z\rangle|^2$ in the MBL phase is the presence of the sharp peak at $|\langle\tau_i^z,\sigma_i^z\rangle|^2\approx 1$ (see Fig. C.1), indicating a large probability of observing highly localized ℓ-bits in the system. Here we analyze the cumulative distribution function (CDF) of $|\langle\tau_i^z,\sigma_i^z\rangle|^2$ for values of $|\langle\tau_i^z,\sigma_i^z\rangle|^2\approx 1$. In particular, we fit the CDF of $x = 1-|\langle\tau_i^z,\sigma_i^z\rangle|^2$ to a function of the form $CDF(x) = Ax^\gamma$ for small x and identified the exponent γ for different disorder strengths (see Fig. C.17). The idea is that, since the probability density function (PDF) is the derivative of the CDF, if $\gamma = 1$ as $x\to 0^+$ then $PDF(x\to 0^+)\propto \lim_{x\to 0^+} x^{\gamma-1}$ is constant and there is a finite probability of observing a highly localized ℓ-bit. For all of the models considered, at high disorder $\gamma\approx 1$. At disorder strengths near the transition regions (see Fig. 5.3 in the main text), γ begins to diverge, potentially suggesting a transition. Note that we observe the same behavior for $x = r$.

However, we would like to emphasize that the results in Fig. C.17, while suggestive, are not entirely trustworthy. As can be seen by the fits used to obtain the values of γ, shown in Fig. C.18, the CDF is not obviously captured by a power-law form and has a noticeable change at very low $1-|\langle\tau_i^z,\sigma_i^z\rangle|^2$, which we do not fully understand. When we perform our fitting, we first sort the N data points $x_1,\ldots,x_N$ (e.g., the $1-|\langle\tau_i^z,\sigma_i^z\rangle|^2$ values of the τ_i^z operators) in increasing order so that $x_1\leq x_2\leq\cdots\leq x_N$. Then, we define $CDF(x_n) = n/N$ as a discretized representation of the CDF. Finally, we perform linear fits on the data points $(\log_{10}(x_n),\log_{10}(CDF(x_n)))$ and determine the slope γ. We perform these fits using only points with x_n in the range $c_0\leq CDF(x_n)\leq c_1$. For the 1D, 2D, and 3D Heisenberg models, we set $c_0 = 0.05$ and $c_1 = 0.4$. For the 2D hard-core Bose-Hubbard model, we set $c_0 = 0.03$ and $c_1 = 0.35$. Setting (c_0, c_1) to different values changes this fit, making our results somewhat arbitrary. Also, in Fig. C.17, we omit γ values obtained from bad linear fits with $R^2 < 0.95$, which occur for small values of Δ for the 2D Bose-Hubbard model. Note that the CDFs and fits for $x = r$ look similar. While these results are not completely reliable or systematic, we include them here for completeness.

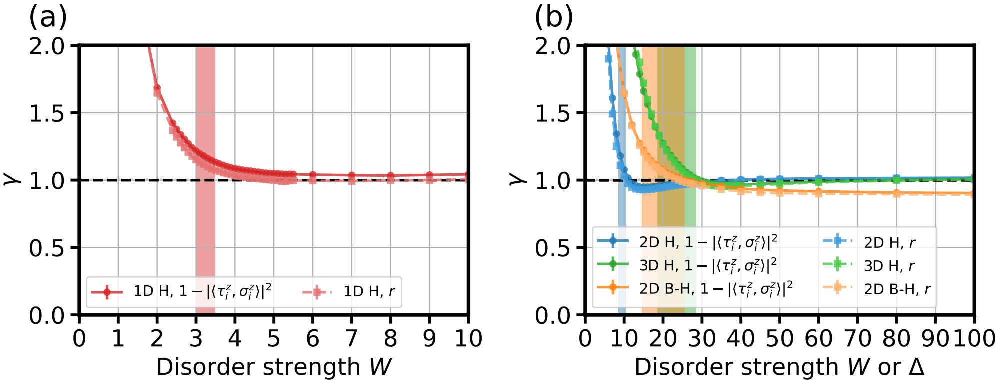

Figure C.17: The exponent γ of the cumulative distribution function $CDF(x) \propto x^{\gamma}$ (obtained from fitting) versus disorder strength for $x = 1 - |\langle\tau_i^z, \sigma_i^z\rangle|^2$ and $x = r$. (a) The exponents for the 1D Heisenberg model. (b) The exponents for the 2D and 3D Heisenberg models and the 2D Bose-Hubbard model. The approximate transition regions for the four models (see Fig. 5.3 in main text) are shaded for reference.

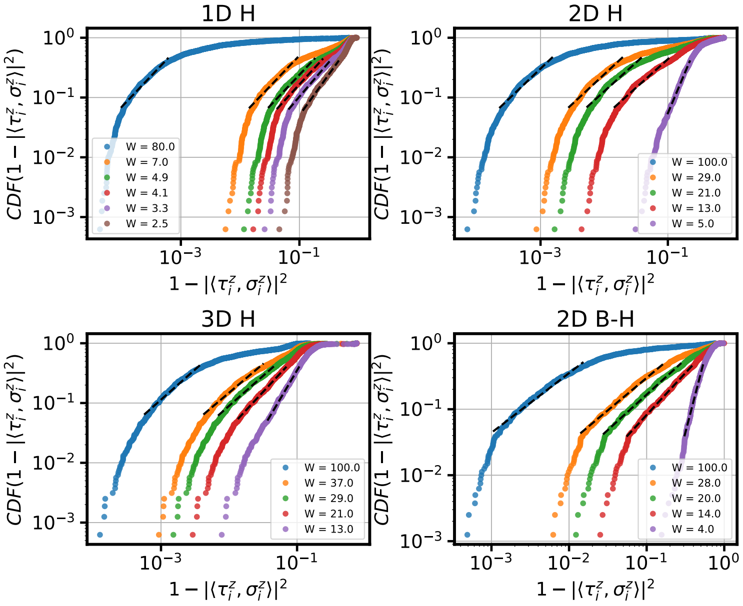

Figure C.18: Cumulative distribution functions (CDFs) of $1 - |\langle\tau_i^z, \sigma_i^z\rangle|^2$ on a log-log scale superimposed with linear fits for different disorder strengths and different models.

C.8 Drift of ℓ-bits

At low disorder, it is possible for our algorithm to find τ_i^z operators that are not located at the original site i used to initialize the basis $B = \{\sigma_i^z\}$. However, as shown in Fig. C.19, this algorithmic "drift" of ℓ-bits away from their initial site is not significant for most disorder strengths considered. In particular, it only becomes significant in certain models and only for disorder strengths significantly below where we observe signatures of MBL transitions.

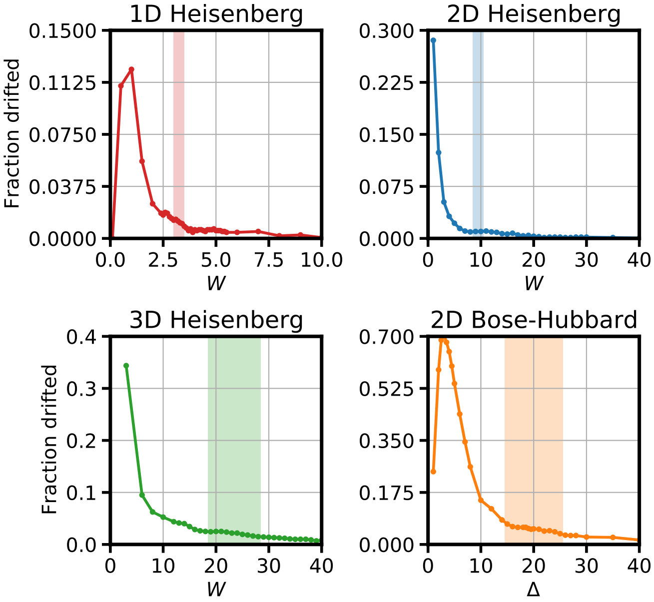

Figure C.19: The fraction of τ_i^z operators that drift away from their original site versus disorder strength for the four models studied. A τ_i^z operator has drifted away if its weight $w_{\mathbf{r}}$ is not maximal at the position where it was initialized. For reference, we shade the approximate transition regions (see Fig. 5.3 in the main text).

C.9 Basis expansion heuristic behavior

As described in the main text, the algorithm that we use to construct the approximate ℓ-bit operators works by systematically expanding the basis of Pauli strings used to represent the ℓ-bit. We know that our procedure is reasonable because the objective function (commutator norm plus binarity) systematically decreases after each expansion iteration. That said, it is interesting to see whether our procedure is able to identify more important Pauli strings at earlier iterations. Indeed, we see this behavior in Fig. C.20, which shows that the Pauli strings added in later iterations typically contribute less to the final optimized

τ_i^z operators than the Pauli strings added in the earlier iterations.

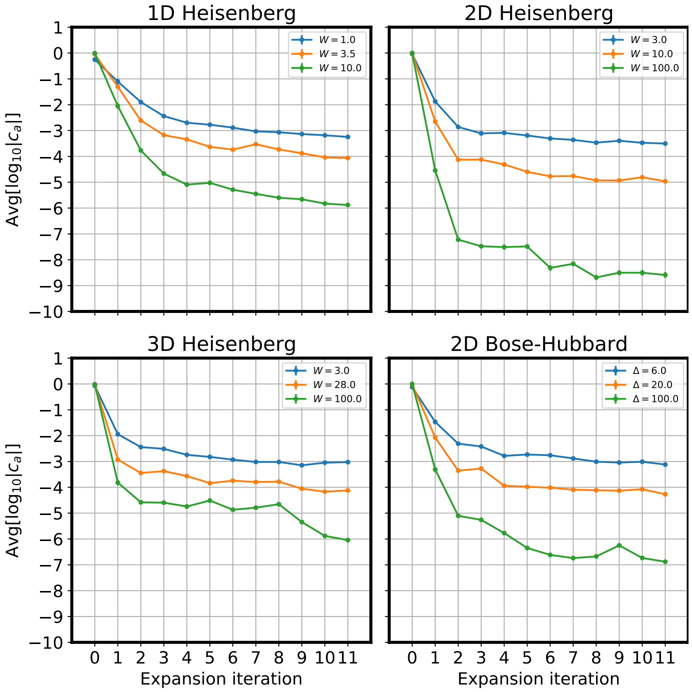

Figure C.20: Log-averages of the amplitudes c_a of the Pauli strings $\mathcal{O}_a$ that were added at each expansion iteration of the algorithm. The amplitudes shown here were from the optimized $\tau_i^z = \sum_a c_a \mathcal{O}_a$ operator produced after the final (11th) expansion iteration. We show examples of single τ_i^z operators for each of the four models studied at low, high, and intermediate disorder strengths. The errorbars (standard errors of $\log_{10}|c_a|$) are smaller than the markers.

C.10 Estimation of transition regions

In this section we describe the method used to estimate the delocalization transition regions quoted in the main text for the various models studied. As discussed in the main text, we observe signatures of bimodality in the distribution of the overlap of ℓ-bits with single-site σ_i^z operators, $|\langle \tau_i^z, \sigma_i^z \rangle|^2$ (see Fig. 3 of the main text). This can be seen as the coexistence of highly localized and substantially delocalized ℓ-bits: at disorder strengths higher than the transition values the overlap is close to 1, while below the transition the overlap is substantially smaller than 1; at the transition region, both behaviors coexist. Note that other hints of bimodal behavior at the transition are also found in the literature [236, 85, 234].

In order to estimate the transition regions in a systematic way, we perform an analysis on the data presented in Fig. 3 of the main text, which shows the histograms of the overlap $|\langle \tau_i^z, \sigma_i^z \rangle|^2$ at fixed disorder strength W (Δ in the case of the 2D Bose-Hubbard), normalized so that their maximum is 1, and interpolated over a window of values of W (resp. Δ). Let us denote this by $f(W, |\langle\tau_i^z, \sigma_i^z\rangle|^2)$. A straightforward way to approximately identify the region of bimodality of f is to establish a threshold t_{overlap} and plot the regions where $f > t_{\text{overlap}}$; we anticipate unimodal behavior (at fixed W) above and below the transition, and bimodal behavior around the transition. In Fig.C.21 we show the result of applying a threshold $t_{\text{overlap}} = 0.75$, and estimate transition regions by bounding the regions of bimodality; as for Fig. 5.3 of the main text, this figure is generated with data from the last iteration of the basis expansion, *i.e.* $I = 11$. Fig. C.22 shows how the thresholded regions change at each iteration of the basis expansion.

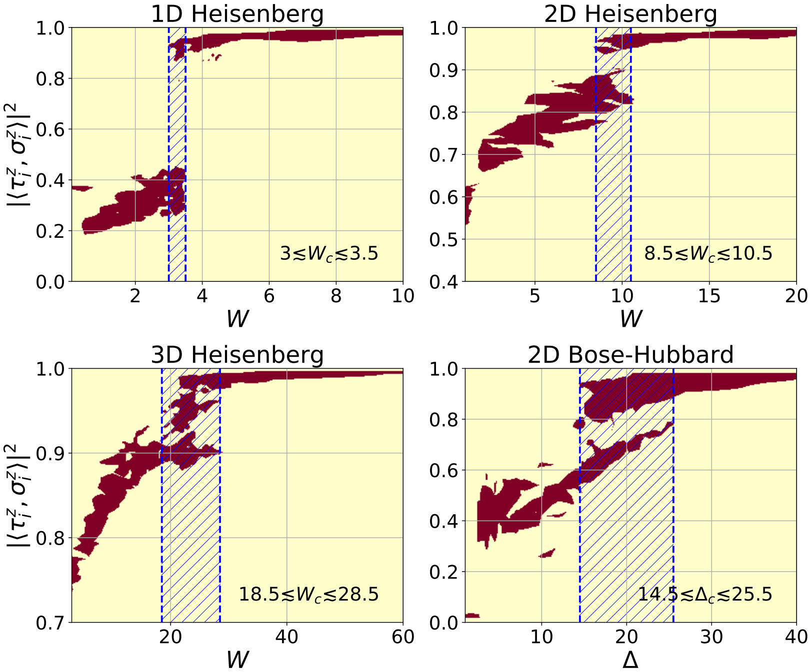

Figure C.21: Estimation of the transition regions of the four models studied. A threshold $t_{\text{overlap}} = 0.75$ is applied to the data presented in Fig. 5.3 of the main text, which results in the clear identification of a bimodal region around the transition. The transition regions are shaded in the plot, and their approximate lower and upper bounds are written in the lower right corner of each panel.

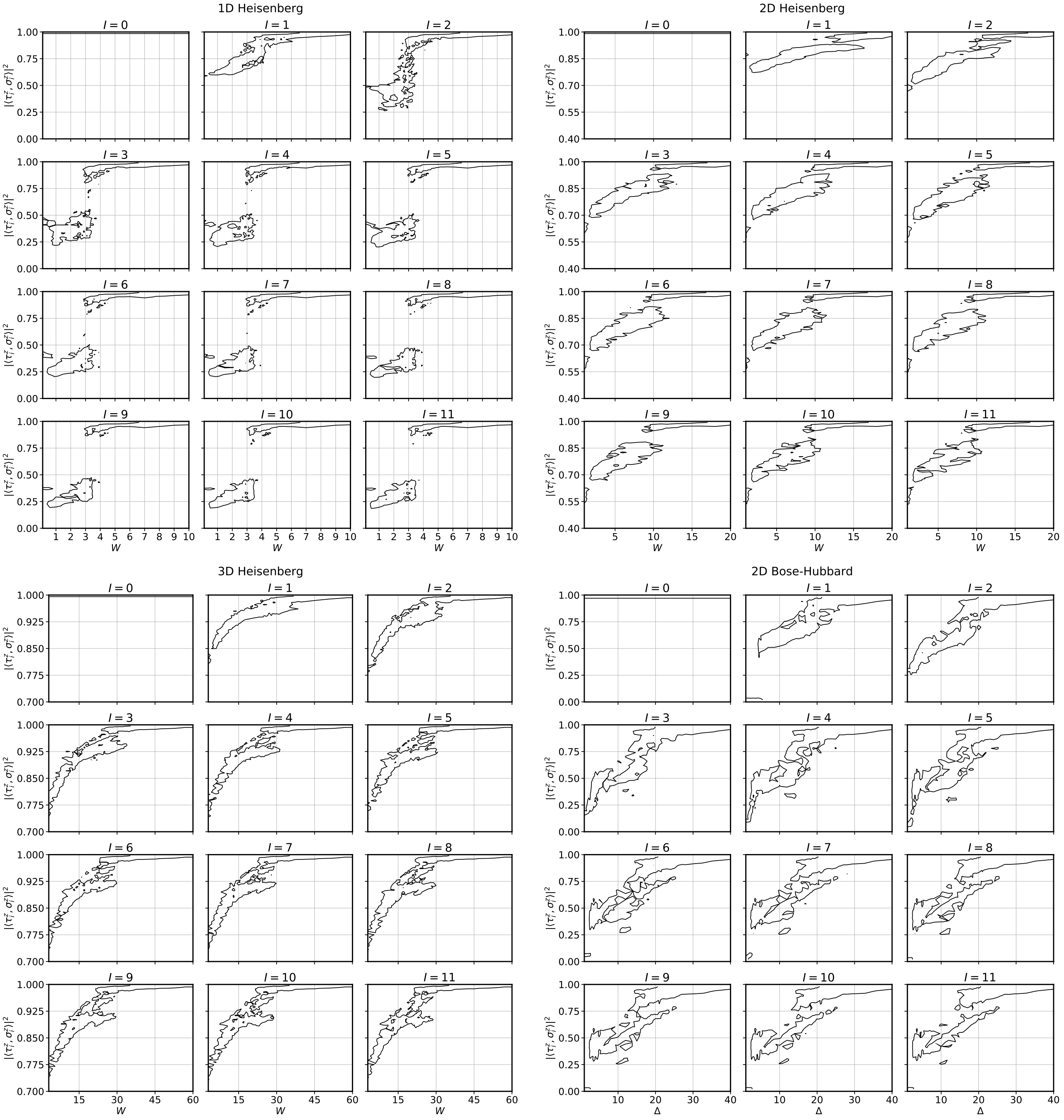

Figure C.22: Outlines of the regions with $f(W,|\langle\tau_i^z,\sigma_i^z\rangle|^2) > t_{\text{overlap}} = 0.75$ for iterations $I = 0,\ldots,11$ of the basis expansion heuristic. Lines represent contour lines at $f(W,|\langle\tau_i^z,\sigma_i^z\rangle|^2) = 0.75$

C.11 Scaling of the commutator norm and the binarity with basis size

In this section we study the scaling of the commutator norm and binarity with the basis size $|B|$. In Fig. C.23 we show the values of the log-averaged commutator norm $\|[H,\tau_i^z]\|^2$ as a function of $|B|$ for a subset of disorder strengths (which includes the transition region) for the four models studied. At large values of $|B|$, the behavior is consistent with a power law of the form $\|[H,\tau_i^z]\|^2 = C_{\rm comm}B^{-\alpha_{\rm comm}}$.

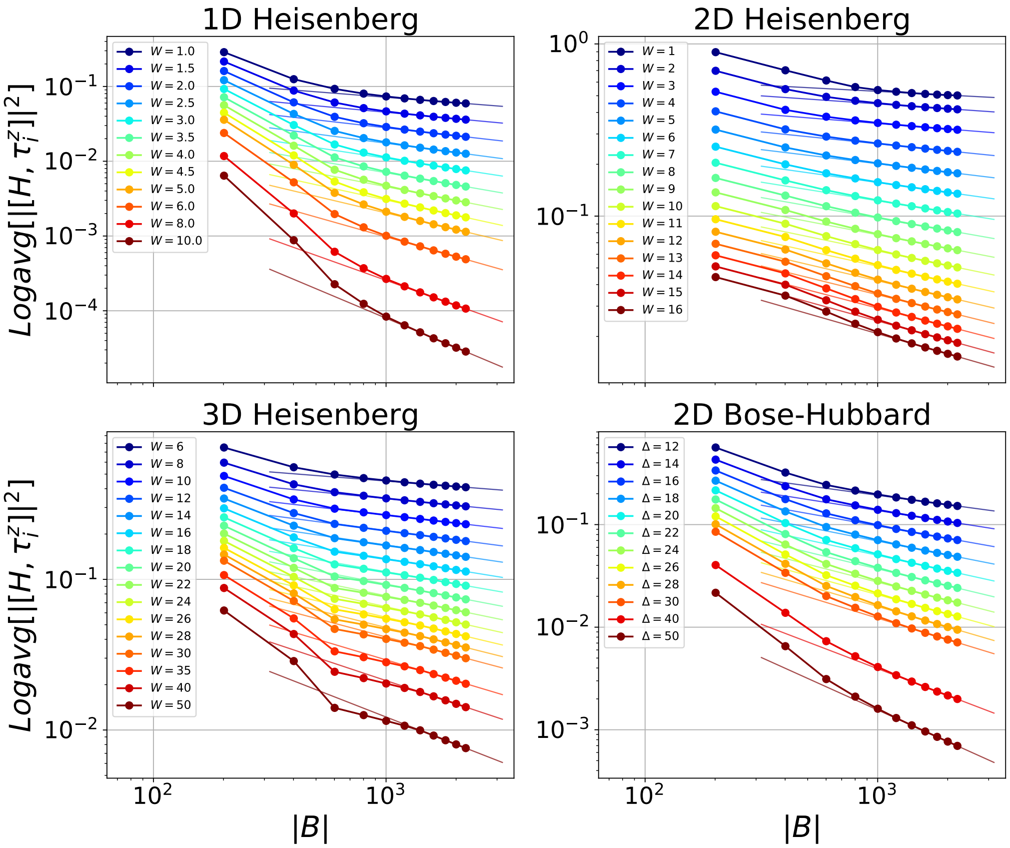

Figure C.23: Log-log plot of the log-averaged commutator norm as a function of basis size $|B|$ for a set of disorder strengths. At large $|B|$, the scaling resembles a power law, as shown by the quality of the fit to a straight line.

Similar to the case of the commutator norm, we show in Fig. C.24 the values of the log-averaged binarity $\|(\tau_i^z)^2 - I\|^2$ for a subset of disorder strengths for the four models studied. Again, at large values of $|B|$, the behavior is consistent with a power law of the form $\|(\tau_i^z)^2 - I\|^2 = C_{\rm bin}B^{-\alpha_{\rm bin}}$. Now, however, the scaling is less clean than the scaling of the commutator norm. Note that the binarity is exactly zero (*i.e.*, optimal) before any basis expansion (not shown), *i.e.*, when $I = 0$, since we have $\tau_i^z = \sigma_i^z$. For that reason, it is natural for the binarity to increase over the first few iterations and eventually decrease monotonically as it is optimizaed over larger basis sizes. This behavior can be observed with the 2D and 3D Heisenberg models.

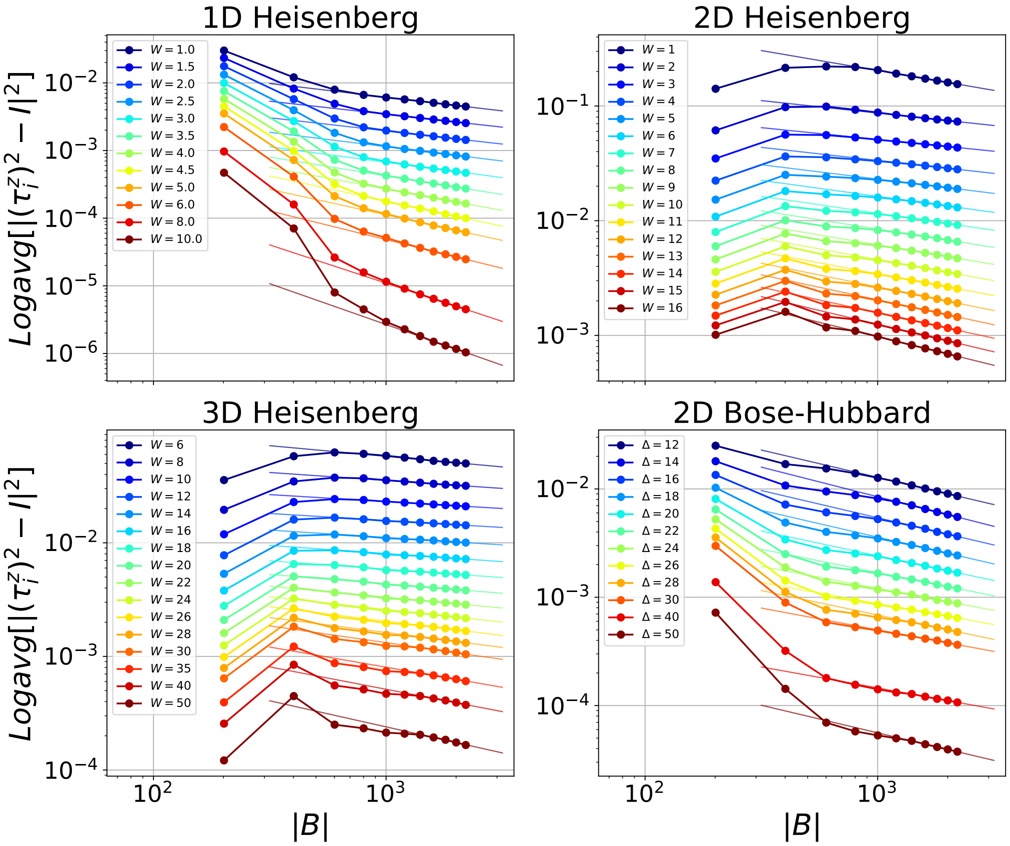

Figure C.24: Log-log plot of the log-averaged binarity as a function of basis size $|B|$ for a set of disorder strengths. At large $|B|$, the scaling resembles a power law, as shown by the quality of the fit to a straight line.

In Fig. C.25 we show the values of the exponents α_{comm} and α_{bin} as a function of the disorder strength. α_{comm} smoothly increases with disorder strength. Interestingly, there is no sign of a transition in α_{comm}. The α_{bin} exponent follows a similar trend, although its behavior is much noisier and more difficult to describe with the current data. Interestingly, both α_{comm} and α_{bin} are of a comparable magnitude and, in the case of the 1D disordered Heisenberg model, track each other closely around the transition region.

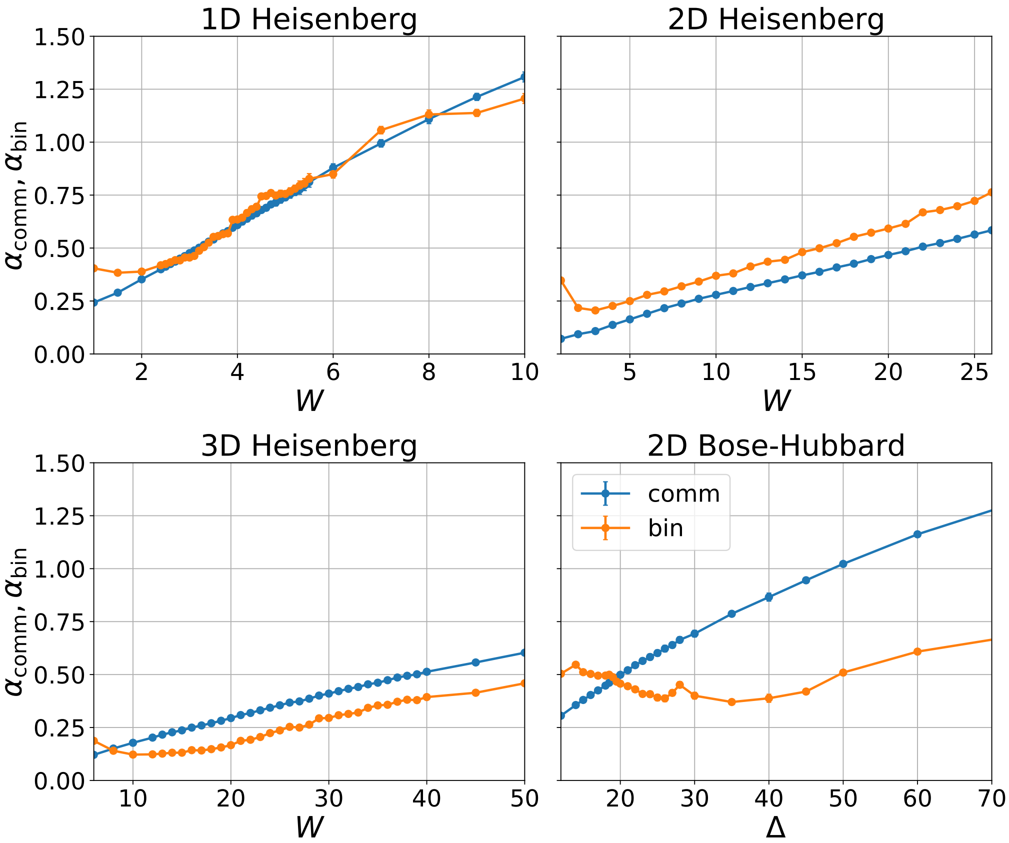

Figure C.25: Exponents of the power law scaling of the commutator norm and the binarity with basis size $|B|$, α_{comm} and α_{bin}.

At very high disorder strength ($W = 1000$ or $\Delta = 1000$), the last iteration of the algorithm reaches a log-averaged commutator norm of about 10^{-22} for the 1D Heisenberg model, 10^{-10} for the 2D Heisenberg model, 10^{-7} for the 3D Heisenberg model, and 10^{-10} for the 2D Bose-Hubbard model. Similarly, the binarity reaches log-averaged values of about 10^{-24}, 10^{-10}, 10^{-8}, and 10^{-12}, respectively.

Appendix D

Motif magnetism and quantum-many body scars

D.1 Time-evolution of spiral colored states

Consider time-evolving the initial product state $|C\rangle$ in Eq. (6.8) by the Hamiltonian $\hat{H}$ in Eq. (6.7):

$$|C(t)\rangle = e^{-it\hat{H}}|C\rangle$$

By construction, $|C\rangle$ is an eigenstate of each motif Hamiltonian $\hat{H}_p[Q_p]$ with energy E_p. Also, $[\hat{H}_p, \sum_j \hat{\sigma}^z_j] = 0$. Together, these imply that

$$\begin{aligned} |C(t)\rangle &= e^{ith\sum_j \hat{\sigma}^z_j} e^{-it\sum_p J_p \hat{H}_p}|C\rangle \\ &= e^{-it\sum_p J_p E_p} e^{ith\sum_j \hat{\sigma}^z_j}|C\rangle \\ &= e^{-it\sum_p J_p E_p} \bigotimes_j e^{ith\hat{\sigma}^z_j}|\gamma_j\rangle_j. \end{aligned}$$

This indicates that, up to a global phase, the time evolution applied to this state causes each spin to precess around the z-axis at the same rate.

Consider a particular spin j in $|C\rangle$ initially in state $|\gamma_j\rangle = |+\rangle = (1,1)^T/\sqrt{2}$. After time t, this spin's state will be

$$e^{ith\hat{\sigma}^z}|+\rangle = \begin{pmatrix} e^{ith} & 0 \\ 0 & e^{-ith} \end{pmatrix} \frac{1}{\sqrt{2}} \begin{pmatrix} 1 \\ 1 \end{pmatrix} = \frac{e^{ith}}{\sqrt{2}} \begin{pmatrix} 1 \\ e^{-2ith} \end{pmatrix},$$

which is $\propto |+\rangle$ when $t = T = \pi/h$.

Appendix E

Complications in the eigenstate-to-Hamiltonian construction

In this thesis, we have shown that the eigenstate-to-Hamiltonian (EHC) algorithm can be used to find interesting new physics. However, in general the output of the EHC algorithm can be difficult to interpret for a variety of reasons. Here we describe why this is the case.

Recall that in EHC, we look for Hamiltonians with a desired eigenstate $|\psi\rangle$ by computing the quantum covariance matrix (QCM). The eigenvectors of the quantum covariance matrix correspond to Hamiltonians and the eigenvalues correspond to the variance of the Hamiltonian with respect to state $|\psi\rangle$.

When using EHC, it is important to keep in mind these considerations:

1. *EHC can fail to find any exact solutions.* A generic $|\psi\rangle$ is not an exact eigenstate of any local Hamiltonian, so EHC will not generally find exact Hamiltonians with zero variance.

2. *EHC can find many solutions.* The QCM can have many low-lying eigenvalues, corresponding to many Hamiltonians with low variance. Any linear combination of these Hamiltonians will have $|\psi\rangle$ as nearly an eigenstate.

3. *EHC does not find parent Hamiltonians.* The state $|\psi\rangle$ can be anywhere in the spectrum of the Hamiltonians found with EHC. While this is not necessarily an issue, it can make it difficult to analyze the results if one is specifically interested in finding parent Hamiltonians with $|\psi\rangle$ as a ground state.

4. *EHC's non-exact solutions can be hard to analyze without additional information.* Non-zero eigenvalues σ^2 of the QCM are difficult to interpret. This is because the variance σ^2 of a Hamiltonian $\hat{H} = \sum_a J_a \hat{h}_a$ can be significantly modified by changing the normalization of the Hamiltonian coupling constants J_a or the basis operators $\hat{h}_a$. Moreover, without knowledge of the spectra of the Hamiltonians found in EHC (which is expensive to compute), it is unclear how many eigenstates are within σ energy of $|\psi\rangle$ for these Hamiltonians, which could affect how one interprets how "close" $|\psi\rangle$ is to an eigenstate.

5. *EHC solutions can be "non-unique."* The operators produced by EHC do not necessarily uniquely correspond to the input state $|\psi\rangle$. In general, the operators can have highly degenerate spectra. For

instance, if $|\psi\rangle$ exhibits a local symmetry, then EHC will find as the output the corresponding local symmetry operators, which can have highly degenerate spectra and many other states in the same quantum number sector as $|\psi\rangle$. Similarly, EHC can find projected operators of the form $\hat{H}_l' = \hat{P}\hat{H}_l\hat{P}$ where $\hat{P}$ is a projector onto a space orthogonal to $|\psi\rangle$ so that $\hat{P}|\psi\rangle = 0$. Since $\hat{P}$ can be orthogonal to a large part of the Hilbert space, the $\hat{H}_l'$ operators will have many degenerate zero-energy states that include $|\psi\rangle$ among them.

To deal with these issues, it is useful to combine EHC with additional information, either through pre- or post-processing. This can be done by restricting the space of Hamiltonians one provides as input to EHC or by analyzing the properties of the Hamiltonians produced as output using other methods. It will be interesting future work to come up with systematic procedures for dealing with these issues.

Appendix F

Ground state manifolds

F.1 Ground state manifolds are convex

As discussed in Chapter 3, the set of Hamiltonians that have a particular state $|\psi_0\rangle$ as an eigenstate forms a vector space. Suppose that this d-dimensional vector space is spanned by operators $\hat{H}_l$ so that the Hamiltonians in this space are of the form

$$\hat{H} = \sum_{l=1}^{d} J_l \hat{H}_l. \tag{F.1}$$

The state $|\psi_0\rangle$ can be anywhere in the spectrum of $\hat{H}$. Suppose that we restrict ourselves to the $\hat{H}$ in this space with $|\psi_0\rangle$ as a ground state, which we call the *ground state manifold.* What can we say about the properties of this set? It turns out that the ground state manifold is convex.

To see this, consider a set of states $|\psi_n\rangle$ not equal to $|\psi_0\rangle$. By the variational principle, discussed in Section 2.2.3, we know that Hamiltonians in the ground state manifold must satisfy

$$\langle\psi_0|\hat{H}|\psi_0\rangle \leq \langle\psi_n|\hat{H}|\psi_n\rangle \quad \forall n. \tag{F.2}$$

This can be rewritten as

$$\begin{aligned}\sum_{l=1}^{d} J_l \left(\langle\psi_n|\hat{H}_l|\psi_n\rangle - \langle\psi_0|\hat{H}_l|\psi_0\rangle\right) \geq 0 \\ \sum_{l=1}^{d} J_l E_l^{(n)} \geq 0 \\ \mathbf{J}\cdot\mathbf{E}^{(n)} \geq 0 \quad \forall n\end{aligned} \tag{F.3}$$

where $E_l^{(n)} = \langle\psi_n|\hat{H}_l|\psi_n\rangle - \langle\psi_0|\hat{H}_l|\psi_0\rangle$ is a vector of energy differences between states $|\psi_n\rangle$ and $|\psi_0\rangle$ for Hamiltonians $\hat{H}_l$. For each state $|\psi_n\rangle$, Eq. (F.3) specifies a half-space in d dimensions where ground state manifold Hamiltonians can exist. Half-spaces are convex sets. To exactly determine the ground state manifold, one could take the intersection of all possible half-spaces defined by Eq. (F.3) for all possible states $|\psi_n\rangle$. Since the intersection of convex sets is convex, this means that the ground state manifold is a convex set.

F.2 Methods

Using the eigenstate-to-Hamiltonian construction (EHC) combined with methods for computing ground states, such as ED, DMRG, or VMC, we can find Hamiltonians that have a given $|\psi_0\rangle$ as a ground state, i.e., parent Hamiltonians for $|\psi_0\rangle$. Here we describe two algorithms for doing so, one which approximates the entire ground state manifold using a convex hull and another which searches for a single parent Hamiltonian. The first algorithm is computationally expensive, so should only be used when the Hamiltonian space is low dimensional. Both algorithms use ground state algorithms as a subroutine, so are limited in their efficiency by those algorithms.

The first step in both methods is to perform EHC to find the space of Hamiltonians in Eq. (F.1) with $|\psi_0\rangle$ as an eigenstate.

F.2.1 Approximating the ground state manifold

Eq. (F.3) can be used to approximate a ground state manifold numerically. The main idea is to iteratively propose new states $|\psi_n\rangle$ and use those states to find better and better approximations to the convex set. The intersection of a finite number of half-spaces defines a convex hull, which can be numerically determined using the quickhull algorithm [303]. The general procedure that we propose is to use N states as follows:

1. Initialize $G = [-1,1]^d$ and $n = 1$. Pick an initial $\mathbf{J} \in G$, which defines a Hamiltonian $\hat{H} = \mathbf{J} \cdot \mathbf{H} = \sum_l J_l \hat{H}_l$.
2. **(State proposal)** Propose a new $|\psi_n\rangle$ using Hamiltonian $\hat{H}$.
3. **(Convex hull update)** Compute the half-space condition in Eq. (F.3) using $|\psi_n\rangle$. Update the convex hull G using the new condition by using the Quickhull algorithm [303].
4. **(Hamiltonian proposal)** Propose a new $\hat{H} = \mathbf{J} \cdot \mathbf{H}$ by using a new $\mathbf{J} \in G$.
5. Set $n \leftarrow n+1$. If $n \leq N$, go to 2.

As output, the procedure would produce a convex hull G that approximates the true ground state manifold. Here we describe a few ways to implement the state and Hamiltonian proposal steps. It would be interesting future work to explore improvements to these methods or alternative approaches.

For the state proposal step, we could use the ground state or a low-lying eigenstate of $\hat{H}$, which could be computed exactly using ED, or a low-energy state, which could be computed approximately using VMC, DMRG, or other methods. The idea for choosing this state is that it should be competitive in energy with $|\psi_0\rangle$ in some part of G that has not been well explored. Consider a point on the boundary of the ground state manifold. At this point, an energy crossing between $|\psi_0\rangle$ and another state $|\psi'\rangle$ must occur. Using $|\psi'\rangle$ to generate a half-space condition would be informative, since that half-space would exactly intersect the true ground state manifold. We expect that for nearby Hamiltonians $|\psi'\rangle$ is low in energy since it eventually becomes the ground state.

For the Hamiltonian proposal step, a natural Hamiltonian to propose is the one that is "deepest" in the current approximation to the ground state manifold G. This can be done by finding the Chebyshev center of G, the point the farthest from the edges of the convex hull [304]. Finding the Chebyshev center can be done efficiently by solving the linear programming (LP) [17] problem:

$$\begin{aligned} \max_{J_l, r} \quad & r \\ \text{s.t.} \quad & E\mathbf{J} + r\|\mathbf{E}^{(n)}\| \leq 0 \quad \forall n \\ & -1 \leq J_l \leq +1 \quad \forall l \end{aligned} \tag{F.4}$$

where E is a $N \times d$ matrix whose rows are $\mathbf{E}^{(n)}$. The solution of this LP problem is the Chebyshev center $\mathbf{J}$ of G that is distance r from the closest edge of the convex hull.

Note that a potential difficulty in this procedure is the computational complexity of storing the convex hull G for high dimensional Hamiltonian spaces. As G is updated, an efficient representation of it needs to be stored, which involves computing the vertices or faces of the d-dimensional convex polytope that it defines, which takes time exponential in d [303].

For low dimensions d, this procedure could prove useful for mapping out phase diagrams. For example, arbitrary two-dimensional projections of the ground state manifold could be visualized by adding an additional half-space intersection through the relevant plane and using the Quickhull algorithm to identify the vertices of the convex hull on that plane.

F.2.2 Finding a parent Hamiltonian

Suppose that instead of finding an approximation to the entire ground state manifold, we are interested in finding a single parent Hamiltonian with $|\psi_0\rangle$ as a ground state. Then we can use essentially the same procedure but with a modified convex hull update step:

3'. **(Convex hull update)** Compute the half-space condition in Eq. (F.3) using $|\psi_n\rangle$. Store $\mathbf{E}^{(n)}$, but do not compute a representation for G.

In this modified step we do not invoke the Quickhull algorithm, which involves an exponentially costly computation of the vertices or faces of the convex polytope. Instead, we simply store the half-space intersection information for later use in the Hamiltonian proposal LP problem stated in Eq. (F.4). Since solving an LP problem can be done in polynomial time, this procedure is more efficient than the ground state manifold estimation algorithm described above. The algorithm terminates as soon as one has found a Hamiltonian whose ground state is $|\psi_0\rangle$. Again, this procedure still relies on ground state algorithms as subroutines, so would still be potentially costly to implement on systems with many degrees of freedom or in dimensions greater than one.

Finally, we note that one does not actually need to start the parent Hamiltonian algorithm or the ground state manifold algorithm using a space of Hamiltonians found using EHC. In these algorithms, this initialization is mostly a convenience to ensure that $|\psi_0\rangle$ is already an eigenstate and that one has a (likely) low-dimensional space of operators to work with. Instead, one could use an arbitrary space of Hamiltonians and still apply the same procedure. This could be useful, for instance, when one is interested in finding approximate parent Hamiltonians, with the state $|\psi_0\rangle$ as close as possible to the true ground state, or when EHC is unable to find any Hamiltonians with $|\psi_0\rangle$ as an exact eigenstate.

References

[1] J. Hubbard, J. Proc. R. Soc. A **276**, 238 (1963).

[2] N. F. Mott, Proc. Phys. Soc. A **62**, 416 (1949).

[3] J. G. Bednorz and K. A. Müller, Z. Phys. B **64**, 189 (1986).

[4] P. A. Lee, N. Nagaosa, and X.-G. Wen, Rev. Mod. Phys. **78**, 17 (2006).

[5] Nature Phys. **9**, 523 (2013).

[6] Y. LeCun, Y. Bengio, and G. Hinton, Nature **521**, 436 (2015).

[7] A. Krizhevsky, I. Sutskever, and G. E. Hinton, in *Adv. Neural Inf. Process. Syst. 25*, edited by F. Pereira, C. J. C. Burges, L. Bottou, and K. Q. Weinberger (Curran Associates, Inc., 2012) p. 1097.

[8] D. Silver *et al.*, Nature **529**, 484 (2016).

[9] H. C. Nguyen, R. Zecchina, and J. Berg, Adv. Phys. **66**, 197 (2017).

[10] T. Broderick, M. Dudik, G. Tkacik, R. E. Schapire, and W. Bialek, "Faster solutions of the inverse pairwise ising problem," (2007), arXiv:0712.2437 [q-bio.QM] .

[11] J. Pearl, in *Probabilistic Reasoning in Intelligent Systems*, edited by J. Pearl (Morgan Kaufmann, San Francisco (CA), 1988) pp. 1–28.

[12] J. Yedidia, W. Freeman, and Y. Weiss, Information Theory, IEEE Transactions on **51**, 2282 (2005).

[13] R. Gallager, IRE Transactions on Information Theory **8**, 21 (1962).

[14] D. J. C. MacKay, *Information theory, inference, and learning algorithms* (Cambridge University Press, 2003).

[15] R. A. DiStasio, Jr., É. Marcotte, R. Car, F. H. Stillinger, and S. Torquato, Phys. Rev. B **88**, 134104 (2013).

[16] É. Marcotte, R. A. DiStasio, Jr., F. H. Stillinger, and S. Torquato, Phys. Rev. B **88**, 184432 (2013).

[17] G. B. Dantzig, *Linear Programming and Extensions* (RAND Corporation, Santa Monica, CA, 1963).

[18] S. Kirkpatrick, C. D. Gelatt, and M. P. Vecchi, Science **220**, 671 (1983).

[19] E. Chertkov, R. A. DiStasio, G. Zhang, R. Car, and S. Torquato, Phys. Rev. B **93**, 064201 (2016).

[20] S. Torquato, Soft Matter **5**, 1157 (2009).

[21] M. C. Rechtsman, F. H. Stillinger, and S. Torquato, Phys. Rev. Lett. **101**, 085501 (2008).

[22] M. Fannes, B. Nachtergaele, and R. F. Werner, Commun. Math. Phys. **144**, 443 (1992).

[23] B. Nachtergaele, Commun. Math. Phys. **175**, 565 (1996).

[24] D. Perez-Garcia, F. Verstraete, M. M. Wolf, and J. I. Cirac, Quantum Info Comput. **7**, 401 (2007).

[25] F. Verstraete and J. I. Cirac, (2004), arXiv:cond-mat/0407066 [cond-mat.str-el] .

[26] D. Perez-Garcia, F. Verstraete, M. M. Wolf, and J. I. Cirac, Quantum Info Comput. **8**, 650 (2008).

[27] N. Schuch, D. Pérez-García, and I. Cirac, Phys. Rev. B **84**, 165139 (2011).

[28] X. Chen, Z.-C. Gu, and X.-G. Wen, Phys. Rev. B **83**, 035107 (2011).

[29] A. Seidel, Phys. Rev. B **80**, 165131 (2009).

[30] N. Schuch, D. Poilblanc, J. I. Cirac, and D. Pérez-García, Phys. Rev. B **86**, 115108 (2012).

[31] Z. Zhou, J. Wildeboer, and A. Seidel, Phys. Rev. B **89**, 035123 (2014).

[32] C. Granade, C. Ferrie, N. Wiebe, and D. G. Cory, New J. Phys. **14**, 103013 (2012).

[33] I. M. Georgescu, S. Ashhab, and F. Nori, Rev. Mod. Phys. **86**, 153 (2014).

[34] N. Wiebe, C. Granade, C. Ferrie, and D. G. Cory, Phys. Rev. Lett. **112**, 190501 (2014).

[35] N. Wiebe, C. Granade, C. Ferrie, and D. Cory, Phys. Rev. A **89**, 042314 (2014).

[36] N. Wiebe, C. Granade, and D. G. Cory, New Journal of Physics **17**, 022005 (2015).

[37] E. Bairey, I. Arad, and N. H. Lindner, Phys. Rev. Lett. **122**, 020504 (2019).

[38] A. Valenti, E. van Nieuwenburg, S. Huber, and E. Greplova, Phys. Rev. Research **1**, 033092 (2019).

[39] T. J. Evans, R. Harper, and S. T. Flammia, "Scalable bayesian hamiltonian learning," (2019), arXiv:1912.07636 [quant-ph] .

[40] Z. Li, L. Zou, and T. H. Hsieh, Phys. Rev. Lett. **124** (2020).

[41] E. Chertkov and B. K. Clark, Phys. Rev. X **8**, 031029 (2018).

[42] X.-L. Qi and D. Ranard, Quantum **3**, 159 (2019).

[43] M. Greiter, V. Schnells, and R. Thomale, Phys. Rev. B **98**, 081113(R) (2018).

[44] E. Chertkov, B. Villalonga, and B. K. Clark, Phys. Rev. Research **2**, 023348 (2020).

[45] H. Kim, M. C. Bañuls, J. I. Cirac, M. B. Hastings, and D. A. Huse, Phys. Rev. E **92**, 012128 (2015).

[46] T. E. O'Brien, D. A. Abanin, G. Vidal, and Z. Papić, Phys. Rev. B **94**, 144208 (2016).

[47] E. Chertkov, "Qosy: Quantum Operators from Symmetry," `https://github.com/ClarkResearchGroup/qosy`.

[48] E. Bairey, C. Guo, D. Poletti, N. H. Lindner, and I. Arad, New J. Phys. **22**, 032001 (2020).

[49] M. Dupont and N. Laflorencie, Phys. Rev. B **99**, 020202 (2019).

[50] M. Dupont, N. Macé, and N. Laflorencie, Phys. Rev. B **100**, 134201 (2019).

[51] N. Swain, H.-K. Tang, B. Khor, F. Assaad, S. Adam, and P. Sengupta, "Numerical evidence for a many-body localization transition in two dimensions," (2021), APS March Meeting.

[52] K. Zhang, S. Lederer, K. Choo, T. Neupert, G. Carleo, and E.-A. Kim, "Hamiltonian reconstruction as metric for variational studies," (2021), arXiv:2102.00019 [cond-mat.str-el] .

[53] A. Haim, R. Kueng, and G. Refael, "Variational-correlations approach to quantum many-body problems," (2020), arXiv:2001.06510 [cond-mat.str-el] .

[54] L. Balents, Nature **464**, 199 (2010).

[55] L. Savary and L. Balents, Rep. Prog. Phys. **80**, 016502 (2017).

[56] C. Broholm, R. J. Cava, S. A. Kivelson, D. G. Nocera, M. R. Norman, and T. Senthil, Science **367** (2020).

[57] X.-G. Wen, Phys. Rev. B **65**, 165113 (2002).

[58] X. Chen, Z.-C. Gu, and X.-G. Wen, Phys. Rev. B **82**, 155138 (2010).

[59] C. Nayak, S. H. Simon, A. Stern, M. Freedman, and S. Das Sarma, Rev. Mod. Phys. **80**, 1083 (2008).

[60] A. Y. Kitaev, Ann. Phys. (N. Y.) **303**, 2 (2003).

[61] C. Castelnovo, M. Troyer, and S. Trebst, "Topological order and quantum criticality," in *Understanding Quantum Phase Transitions* (CRC Press / Taylor and Francis, 2010) p. 167.

[62] Y. Zhang, T. Grover, A. Turner, M. Oshikawa, and A. Vishwanath, Phys. Rev. B **85**, 235151 (2012).

[63] M. Norman, Reviews of Modern Physics **88** (2016).

[64] J. Wen, S.-L. Yu, S. Li, W. Yu, and J.-X. Li, npj Quantum Materials **4** (2019).

[65] A. Kitaev, Annals of Physics **321**, 2–111 (2006).

[66] T.-H. Han, J. S. Helton, S. Chu, D. G. Nocera, J. A. Rodriguez-Rivera, C. Broholm, and Y. S. Lee, Nature **492**, 406–410 (2012).

[67] J. Preskill, Quantum **2**, 79 (2018).

[68] K. J. Satzinger *et al.*, "Realizing topologically ordered states on a quantum processor," (2021), arXiv:2104.01180 [quant-ph] .

[69] M. S. and Y. A., Rep. Prog. Phys. **80**, 076501 (2017).

[70] S. D. Sarma, M. Freedman, and C. Nayak, npj Quantum Inf. **1** (2015).

[71] N. E. Bonesteel, L. Hormozi, G. Zikos, and S. H. Simon, Physical Review Letters **95** (2005).

[72] L. Hormozi, G. Zikos, N. E. Bonesteel, and S. H. Simon, Phys. Rev. B **75**, 165310 (2007).

[73] A. Y. Kitaev, Ann. Phys. **303**, 2 (2003).

[74] R. M. Lutchyn, E. P. A. M. Bakkers, L. P. Kouwenhoven, P. Krogstrup, C. M. Marcus, and Y. Oreg, Nat. Rev. Mater. **3**, 52 (2018).

[75] V. Mourik, K. Zuo, S. M. Frolov, S. R. Plissard, E. P. A. M. Bakkers, and L. P. Kouwenhoven, Science **336**, 1003–1007 (2012).

[76] J. P. T. Stenger, N. T. Bronn, D. J. Egger, and D. Pekker, "Simulating the dynamics of braiding of Majorana zero modes using an IBM quantum computer," (2021), arXiv:2012.11660 [quant-ph] .

[77] D. A. Abanin, E. Altman, I. Bloch, and M. Serbyn, Rev. Mod. Phys. **91**, 021001 (2019).

[78] P. W. Anderson, Phys. Rev. **109**, 1492 (1958).

[79] R. Nandkishore and D. A. Huse, Annu. Rev. Condens. Matter Phys. **6**, 15 (2015).

[80] D. M. Basko, I. L. Aleiner, and B. L. Altshuler, Ann. Phys. (N. Y.) **321**, 1126 (2006).

[81] V. Oganesyan and D. A. Huse, Phys. Rev. B **75**, 155111 (2007).

[82] A. Pal and D. A. Huse, Phys. Rev. B **82**, 174411 (2010).

[83] D. J. Luitz, N. Laflorencie, and F. Alet, Phys. Rev. B **91**, 081103(R) (2015).

[84] M. Serbyn and J. E. Moore, Phys. Rev. B **93**, 041424(R) (2016).

[85] X. Yu, D. J. Luitz, and B. K. Clark, Phys. Rev. B **94**, 184202 (2016).

[86] M. Žnidarič, T. Prosen, and P. Prelovšek, Phys. Rev. B **77**, 064426 (2008).

[87] J. H. Bardarson, F. Pollmann, and J. E. Moore, Phys. Rev. Lett. **109**, 017202 (2012).

[88] A. D. Luca and A. Scardicchio, EPL **101**, 37003 (2013).

[89] F. Pollmann, V. Khemani, J. I. Cirac, and S. L. Sondhi, Phys. Rev. B **94**, 041116(R) (2016).

[90] X. Yu, D. Pekker, and B. K. Clark, Phys. Rev. Lett. **118**, 017201 (2017).

[91] V. Khemani, F. Pollmann, and S. L. Sondhi, Phys. Rev. Lett. **116**, 247204 (2016).

[92] D. Pekker and B. K. Clark, Phys. Rev. B **95**, 035116 (2017).

[93] T. B. Wahl, A. Pal, and S. H. Simon, Phys. Rev. X **7**, 021018 (2017).

[94] Y. B. Lev and D. R. Reichman, EPL **113**, 46001 (2016).

[95] S. Inglis and L. Pollet, Phys. Rev. Lett. **117**, 120402 (2016).

[96] S. J. Thomson and M. Schiró, Phys. Rev. B **97**, 060201(R) (2018).

[97] D. M. Kennes, (2018), arXiv:1811.04126 .

[98] T. B. Wahl, A. Pal, and S. H. Simon, Nat. Phys. **15**, 164 (2019).

[99] A. Geißler and G. Pupillo, Phys. Rev. Research **2**, 042037 (2020).

[100] G. De Tomasi, F. Pollmann, and M. Heyl, Phys. Rev. B **99**, 241114(R) (2019).

[101] H. Théveniaut, Z. Lan, G. Meyer, and F. Alet, Phys. Rev. Research **2** (2020).

[102] A. Kshetrimayum, M. Goihl, and J. Eisert, Phys. Rev. B **102** (2020).

[103] F. Pietracaprina and F. Alet, SciPost Phys. **10**, 44 (2021).

[104] E. V. H. Doggen, I. V. Gornyi, A. D. Mirlin, and D. G. Polyakov, Phys. Rev. Lett. **125**, 155701 (2020).

[105] M. Serbyn, Z. Papić, and D. A. Abanin, Phys. Rev. Lett. **111**, 127201(R) (2013).

[106] D. A. Huse, R. Nandkishore, and V. Oganesyan, Phys. Rev. B **90**, 174202 (2014).

[107] D. Pekker, B. K. Clark, V. Oganesyan, and G. Refael, Phys. Rev. Lett. **119**, 075701 (2017).

[108] D. Pekker, B. K. Clark, V. Oganesyan, and G. Refael, Phys. Rev. Lett. **119**, 075701 (2017).

[109] A. K. Kulshreshtha, A. Pal, T. B. Wahl, and S. H. Simon, Phys. Rev. B **98**, 184201 (2018).

[110] M. Goihl, M. Gluza, C. Krumnow, and J. Eisert, Phys. Rev. B **97**, 134202 (2018).

[111] X. Yu, D. Pekker, and B. K. Clark, (2019), arXiv:1909.11097 .

[112] V. K. Varma, A. Raj, S. Gopalakrishnan, V. Oganesyan, and D. Pekker, Phys. Rev. B **100**, 115136 (2019).

[113] P. Peng, Z. Li, H. Yan, K. X. Wei, and P. Cappellaro, Phys. Rev. B **100**, 214203 (2019).

[114] S. P. Kelly, R. Nandkishore, and J. Marino, Nucl. Phys. B **951**, 114886 (2020).

[115] S. S. Kondov, W. R. McGehee, W. Xu, and B. DeMarco, Phys. Rev. Lett. **114**, 083002 (2015).

[116] M. Schreiber, S. S. Hodgman, P. Bordia, H. P. Lüschen, M. H. Fischer, R. Vosk, E. Altman, U. Schneider, and I. Bloch, Science **349**, 842 (2015).

[117] J. Smith, A. Lee, P. Richerme, B. Neyenhuis, P. W. Hess, P. Hauke, M. Heyl, D. A. Huse, and C. Monroe, Nat. Phys. **12**, 907–911 (2016).

[118] J.-Y. Choi, S. Hild, J. Zeiher, P. Schauß, A. Rubio-Abadal, T. Yefsah, V. Khemani, D. A. Huse, I. Bloch, and C. Gross, Science **352**, 1547 (2016).

[119] P. Bordia, H. Lüschen, S. Scherg, S. Gopalakrishnan, M. Knap, U. Schneider, and I. Bloch, Phys. Rev. X **7**, 041047 (2017).

[120] P. Roushan *et al.*, Science **358**, 1175–1179 (2017).

[121] K. Xu, J.-J. Chen, Y. Zeng, Y.-R. Zhang, C. Song, W. Liu, Q. Guo, P. Zhang, D. Xu, H. Deng, and et al., Phys. Rev. Lett. **120** (2018).

[122] B. Chiaro *et al.*, "Direct measurement of non-local interactions in the many-body localized phase," (2020), arXiv:1910.06024 [cond-mat.dis-nn] .

[123] Q. Guo, C. Cheng, Z.-H. Sun, Z. Song, H. Li, Z. Wang, W. Ren, H. Dong, D. Zheng, Y.-R. Zhang, and et al., Nat. Phys. **17**, 234–239 (2020).

[124] A. Smith, M. S. Kim, F. Pollmann, and J. Knolle, npj Quantum Information **5** (2019).

[125] A. W. Sandvik, AIP Conference Proceedings **1297**, 135 (2010).

[126] M. Stone and P. Goldbart, *Mathematics for Physics: A Guided Tour for Graduate Students* (Cambridge University Press, 2009).

[127] D. Kochkov, *On numerical methods in quantum spin systems*, Ph.D. thesis, University of Illinois at Urbana-Champaign (2019).

[128] F. Becca and S. Sorella, "Correlated models and wave functions," in *Quantum Monte Carlo Approaches for Correlated Systems* (Cambridge University Press, 2017) pp. 101–164.

[129] N. Metropolis, A. W. Rosenbluth, M. N. Rosenbluth, A. H. Teller, and E. Teller, The Journal of Chemical Physics **21**, 1087 (1953).

[130] W. K. Hastings, Biometrika **57**, 97 (1970).

[131] G. Carleo and M. Troyer, Science **355**, 602 (2017).

[132] T. Li, F. Becca, W. Hu, and S. Sorella, Phys. Rev. B **86**, 075111 (2012).

[133] U. Schollwöck, Ann. Phys. (N. Y.) **326**, 96–192 (2011).

[134] R. Orús, Ann. Phys. **349**, 117 (2014).

[135] J. C. Bridgeman and C. T. Chubb, J. Phys. A **50**, 223001 (2017).

[136] J. Biamonte and V. Bergholm, "Tensor networks in a nutshell," (2017), arXiv:1708.00006 [quant-ph] .

[137] R. Orús, Nature Reviews Physics **1**, 538–550 (2019).

[138] I. Cirac, D. Perez-Garcia, N. Schuch, and F. Verstraete, "Matrix product states and projected entangled pair states: Concepts, symmetries, and theorems," (2020), arXiv:2011.12127 [quant-ph] .

[139] M. B. Hastings, J. Stat. Mech.: Theory Exp **2007**, P08024–P08024 (2007).

[140] S. R. White, Phys. Rev. Lett. **69**, 2863 (1992).

[141] M. Fishman, S. R. White, and E. M. Stoudenmire, "The ITensor software library for tensor network calculations," (2020), arXiv:2007.14822 .

[142] T. B. Wahl, "Tensor network states for the description of quantum many-body systems," (2015), arXiv:1509.05984 [cond-mat.str-el] .

[143] `https://tensornetwork.org/`, accessed: 2021-04-16.

[144] Y.-Y. Shi, L.-M. Duan, and G. Vidal, Phys. Rev. A **74**, 022320 (2006).

[145] G. Vidal, Phys. Rev. Lett. **101** (2008).

[146] N. Nakatani and G. K.-L. Chan, J. Chem. Phys **138**, 134113 (2013).

[147] P. W. Anderson, Mater. Res. Bull. **8**, 153 (1973).

[148] P. W. Anderson, Science **235**, 1196 (1987).

[149] C. Gros, D. Poilblanc, T. M. Rice, and F. C. Zhang, Physica C Supercond **153**, 543 (1988).

[150] A. Paramekanti, M. Randeria, and N. Trivedi, Phys. Rev. Lett. **87**, 217002 (2001).

[151] R. B. Laughlin, Phys. Rev. Lett. **50**, 1395 (1983).

[152] S. A. Trugman and S. Kivelson, Phys. Rev. B **31**, 5280 (1985).

[153] Z. Wang, Y. Xu, H. Pu, and K. R. A. Hazzard, Phys. Rev. B **96**, 115110 (2017).

[154] E. Kapit and E. Mueller, Phys. Rev. Lett. **105**, 215303 (2010).

[155] D. Gottesman, *Stabilizer codes and quantum error correction*, Ph.D. thesis, California Institute of Technology (1997).

[156] R. Raussendorf, D. E. Browne, and H. J. Briegel, Phys. Rev. A **68**, 022312 (2003).

[157] M. Hein, J. Eisert, and H. J. Briegel, Phys. Rev. A **69**, 062311 (2004).

[158] D. F. Schroeter, E. Kapit, R. Thomale, and M. Greiter, Phys. Rev. Lett. **99**, 097202 (2007).

[159] R. Thomale, E. Kapit, D. F. Schroeter, and M. Greiter, Phys. Rev. B **80**, 104406 (2009).

[160] M. Greiter, D. F. Schroeter, and R. Thomale, Phys. Rev. B **89**, 165125 (2014).

[161] F. D. M. Haldane, Phys. Rev. Lett. **51**, 605 (1983).

[162] H. L. Stormer, D. C. Tsui, and A. C. Gossard, Rev. Mod. Phys. **71**, S298 (1999).

[163] M. C. Rechtsman, F. H. Stillinger, and S. Torquato, Phys. Rev. Lett. **95**, 228301 (2005).

[164] M. Rechtsman, F. Stillinger, and S. Torquato, Phys. Rev. E **73**, 011406 (2006).

[165] H. Cohn and A. Kumar, Proc. Nat. Acad. Sci. USA **160**, 9570 (2009).

[166] É. Marcotte, F. H. Stillinger, and S. Torquato, Soft Matter **7**, 2332 (2011).

[167] M. C. Rechtsman, F. H. Stillinger, and S. Torquato, Phys. Rev. E **75**, 031403 (2007).

[168] C. L. Müller and I. F. Sbalzarini, Evol. Comput. **20**, 543 (2012).

[169] A. F. Hannon, Y. Ding, W. Bai, C. A. Ross, and A. Alexander-Katz, Nano Lett. **14**, 318 (2014).

[170] G. Zhang, F. H. Stillinger, and S. Torquato, Phys. Rev. E **88**, 042309 (2013).

[171] A. Jain, J. R. Errington, and T. M. Truskett, Phys. Rev. X **4**, 031049 (2014).

[172] A. Jain, J. A. Bollinger, and T. M. Truskett, AiChE Journal **60**, 2732 (2014).

[173] M. C. Rechtsman, F. H. Stillinger, and S. Torquato, J. Phys. Chem. A **111**, 12816 (2007).

[174] A. Ramezanpour, Phys. Rev. A **93**, 062125 (2016).

[175] H. J. Changlani, H. Zheng, and L. K. Wagner, J. Chem. Phys. **143**, 102814 (2015).

[176] H. Zheng, H. J. Changlani, K. T. Williams, B. Busemeyer, and L. K. Wagner, Front. Phys. **6** (2018).

[177] A. Franceschetti and A. Zunger, Nature **402**, 60 (1999).

[178] G. L. W. Hart, V. Blum, M. J. Walorski, and A. Zunger, Nat. Mater. **4**, 391 (2005).

[179] V. Blum, G. L. W. Hart, M. J. Walorski, and A. Zunger, Phys. Rev. B **72**, 165113 (2005).

[180] W. L. McMillan, Phys. Rev. **138**, A442 (1965).

[181] F. Wang and A. Vishwanath, Phys. Rev. B **74**, 174423 (2006).

[182] Y.-M. Lu, Y. Ran, and P. A. Lee, Phys. Rev. B **83**, 224413 (2011).

[183] Y. Iqbal, F. Becca, and D. Poilblanc, Phys. Rev. B **84**, 020407 (2011).

[184] C. Gros, Ann. Phys. **189**, 53 (1989).

[185] J. McGreevy, B. Swingle, and K.-A. Tran, Phys. Rev. B **85**, 125105 (2012).

[186] C. K. Majumdar and D. K. Ghosh, J. Math. Phys. **10**, 1388 (1969).

[187] C. K. Majumdar, J. Phys. C **3**, 911 (1970).

[188] H. J. Changlani, D. Kochkov, K. Kumar, B. K. Clark, and E. Fradkin, Phys. Rev. Lett. **120** (2018).

[189] J. R. Garrison and T. Grover, ArXiv e-prints (2015), arXiv:1503.00729 [cond-mat.str-el] .

[190] B. Villalonga, X. Yu, D. J. Luitz, and B. K. Clark, Phys. Rev. B **97** (2018).

[191] B. Swingle and I. H. Kim, Phys. Rev. Lett. **113**, 260501 (2014).

[192] Q. Qu, J. Sun, and J. Wright, ArXiv e-prints (2014), arXiv:1412.4659 [cs.IT] .

[193] F. Becca and S. Sorella, *Quantum Monte Carlo Approaches for Correlated Systems* (Cambridge University Press, 2017).

[194] D. S. Rokhsar and S. A. Kivelson, Phys. Rev. Lett. **61**, 2376 (1988).

[195] R. Moessner and S. L. Sondhi, Phys. Rev. Lett. **86**, 1881 (2001).

[196] G. Misguich, D. Serban, and V. Pasquier, Phys. Rev. Lett. **89**, 137202 (2002).

[197] B. Kumar, Phys. Rev. B **66**, 024406 (2002).

[198] L. C. Venuti and M. Roncaglia, Phys. Rev. A **81**, 060101 (2010).

[199] L. D. Landau and E. M. Lifschitz, *Statistical Physics - Course of Theoretical Physics Vol 5* (Pergamon, London, 2003).

[200] D. Varjas, T. Ö. Rosdahl, and A. R. Akhmerov, New J. Phys. **20**, 093026 (2018).

[201] E. Majorana, Il Nuovo Cimento (1924-1942) **14**, 171 (1937).

[202] A. Y. Kitaev, Phys. Usp. **44**, 131 (2001).

[203] C. W. J. Beenakker, Annu. Rev. Condens. Matter Phys. **4**, 113 (2013).

[204] S. B. Bravyi and A. Y. Kitaev, (1998), arXiv:9811052 [quant-ph] .

[205] E. Dennis, A. Y. Kitaev, A. Landahl, and J. Preskill, J. Math. Phys. **43**, 4452 (2002).

[206] M. A. Levin and X.-G. Wen, Phys. Rev. B **71**, 045110 (2005).

[207] S. S. Bullock and G. K. Brennen, J. Phys. A **40**, 3481 (2007).

[208] S. Yan, D. A. Huse, and S. R. White, Science **332**, 1173 (2011).

[209] J. Carrasquilla, Z. Hao, and R. G. Melko, Nat. Commun. **6**, 7421 (2015).

[210] C.-J. Lin and O. I. Motrunich, Phys. Rev. B **96**, 214301 (2017).

[211] N. Pancotti, M. Knap, D. A. Huse, J. I. Cirac, and M. C. Bañuls, Phys. Rev. B **97**, 094206 (2018).

[212] G. Kells, N. Moran, and D. Meidan, Phys. Rev. B **97**, 085425 (2018).

[213] M. Zwolak and G. Vidal, Phys. Rev. Lett. **93**, 207205 (2004).

[214] P. Fendley, J. Stat. Mech. Theory Exp. **2012**, P11020 (2012).

[215] J. Alicea and P. Fendley, Annu. Rev. Condens. Matter Phys. **7**, 119 (2016).

[216] P. Fendley, J. Phys. A **49**, 30LT01 (2016).

[217] H. Katsura, D. Schuricht, and M. Takahashi, Phys. Rev. B **92**, 115137 (2015).

[218] S. Jevtic and R. Barnett, New J. Phys. **19**, 103034 (2017).

[219] F. Hassler and D. Schuricht, New J. Phys. **14**, 125018 (2012).

[220] M. Yankowitz, S. Chen, H. Polshyn, Y. Zhang, K. Watanabe, T. Taniguchi, D. Graf, A. F. Young, and C. R. Dean, Science **363**, 1059 (2019).

[221] C. W. Hicks, D. O. Brodsky, E. A. Yelland, A. S. Gibbs, J. A. N. Bruin, M. E. Barber, S. D. Edkins, K. Nishimura, S. Yonezawa, Y. Maeno, and A. P. Mackenzie, Science **344**, 283 (2014).

[222] M. D. Bachmann *et al.*, Science **366**, 221 (2019).

[223] W. A. Benalcazar, B. A. Bernevig, and T. L. Hughes, Science **357**, 61 (2017).

[224] F. Schindler, A. M. Cook, M. G. Vergniory, Z. Wang, S. S. P. Parkin, B. A. Bernevig, and T. Neupert, Sci. Adv. **4** (2018).

[225] S. Ryu, A. P. Schnyder, A. Furusaki, and A. W. W. Ludwig, New J. Phys. **12**, 065010 (2010).

[226] C. Wu and S.-C. Zhang, Phys. Rev. B **71**, 155115 (2005).

[227] D. Zheng, G.-M. Zhang, and C. Wu, Phys. Rev. B **84**, 205121 (2011).

[228] Z.-X. Li, Y.-F. Jiang, and H. Yao, Phys. Rev. Lett. **117**, 267002 (2016).

[229] E. Chertkov, B. Villalonga, and B. K. Clark, Phys. Rev. Lett. **126**, 180602 (2021).

[230] L. Fleishman and P. W. Anderson, Phys. Rev. B **21**, 2366 (1980).

[231] I. V. Gornyi, A. D. Mirlin, and D. G. Polyakov, Phys. Rev. Lett. **95**, 206603 (2005).

[232] D. A. Abanin and Z. Papić, Ann. Phys. (Berl.) **529**, 1700169 (2017).

[233] J. Z. Imbrie, V. Ros, and A. Scardicchio, Ann. Phys. (Berl.) **529**, 1600278 (2017).

[234] B. Villalonga, X. Yu, D. J. Luitz, and B. K. Clark, Phys. Rev. B **97**, 104406 (2018).

[235] B. Bauer and C. Nayak, J. Stat. Mech. **2013**, P09005 (2013).

[236] J. A. Kjäll, J. H. Bardarson, and F. Pollmann, Phys. Rev. Lett. **113**, 107204 (2014).

[237] D. J. Luitz, Phys. Rev. B **93**, 134201 (2016).

[238] S. P. Lim and D. N. Sheng, Phys. Rev. B **94**, 045111 (2016).

[239] R. K. Panda, A. Scardicchio, M. Schulz, S. R. Taylor, and M. Žnidarič, EPL **128**, 67003 (2020).

[240] W. De Roeck and F. Huveneers, Phys. Rev. B **95**, 155129 (2017).

[241] W. De Roeck and J. Z. Imbrie, Philos. Trans. R. Soc. A **375**, 20160422 (2017).

[242] A. Chandran, A. Pal, C. R. Laumann, and A. Scardicchio, Phys. Rev. B **94**, 144203 (2016).

[243] K. Agarwal, E. Altman, E. Demler, S. Gopalakrishnan, D. A. Huse, and M. Knap, Ann. Phys. (Berl.) **529**, 1600326 (2017).

[244] S. Gopalakrishnan and D. A. Huse, Phys. Rev. B **99**, 134305 (2019).

[245] A. Chandran, I. H. Kim, G. Vidal, and D. A. Abanin, Phys. Rev. B **91**, 085425 (2015).

[246] M. Mierzejewski, M. Kozarzewski, and P. Prelovšek, Phys. Rev. B **97**, 064204 (2018).

[247] C. F. Bender and E. R. Davidson, Phys. Rev. **183**, 23 (1969).

[248] J. L. Whitten and M. Hackmeyer, J. Chem. Phys. **51**, 5584 (1969).

[249] A. A. Holmes, N. A. Tubman, and C. J. Umrigar, J. Chem. Theory Comput. **12**, 3674 (2016).

[250] N. M. Tubman, J. Lee, T. Y. Takeshita, M. Head-Gordon, and K. B. Whaley, J. Chem. Phys. **145**, 044112 (2016).

[251] E. Chertkov, "BIOMS: Binary Integrals of Motion," `https://github.com/ClarkResearchGroup/bioms` (2020).

[252] D. Pekker, G. Refael, E. Altman, E. Demler, and V. Oganesyan, Phys. Rev. X **4**, 011052 (2014).

[253] E. Chertkov and B. K. Clark, "Motif magnetism and quantum many-body scars," (2021), arXiv:2105.04567 [cond-mat.str-el] .

[254] J. M. Deutsch, Phys. Rev. A **43**, 2046 (1991).

[255] M. Srednicki, Phys. Rev. E **50**, 888 (1994).

[256] M. Rigol, V. Dunjko, and M. Olshanii, Nature **452**, 854–858 (2008).

[257] L. D'Alessio, Y. Kafri, A. Polkovnikov, and M. Rigol, Adv. Phys. **65**, 239 (2016).

[258] J. M. Deutsch, Rep. Prog. Phys **81**, 082001 (2018).

[259] D. M. Basko, I. L. Aleiner, and B. L. Altshuler, Ann. Phys. (N. Y.) **321**, 1126 (2006).

[260] H. Bernien *et al.*, Nature **551**, 579 (2017).

[261] N. Shiraishi and T. Mori, Phys. Rev. Lett. **119**, 030601 (2017).

[262] C. J. Turner, A. A. Michailidis, D. A. Abanin, M. Serbyn, and Z. Papić, Nature Physics **14**, 745 (2018).

[263] C. J. Turner, A. A. Michailidis, D. A. Abanin, M. Serbyn, and Z. Papić, Phys. Rev. B **98**, 155134 (2018).

[264] S. Moudgalya, S. Rachel, B. A. Bernevig, and N. Regnault, Phys. Rev. B **98**, 235155 (2018).

[265] S. Moudgalya, N. Regnault, and B. A. Bernevig, Phys. Rev. B **98**, 235156 (2018).

[266] W. W. Ho, S. Choi, H. Pichler, and M. D. Lukin, Phys. Rev. Lett. **122**, 040603 (2019).

[267] C.-J. Lin and O. I. Motrunich, Phys. Rev. Lett. **122**, 173401 (2019).

[268] V. Khemani, C. R. Laumann, and A. Chandran, Phys. Rev. B **99**, 161101 (2019).

[269] S. Choi, C. J. Turner, H. Pichler, W. W. Ho, A. A. Michailidis, Z. Papić, M. Serbyn, M. D. Lukin, and D. A. Abanin, Phys. Rev. Lett. **122**, 220603 (2019).

[270] K. Bull, I. Martin, and Z. Papić, Phys. Rev. Lett. **123**, 030601 (2019).

[271] M. Schecter and T. Iadecola, Phys. Rev. Lett. **123**, 147201 (2019).

[272] S. Ok, K. Choo, C. Mudry, C. Castelnovo, C. Chamon, and T. Neupert, Phys. Rev. Research **1**, 033144 (2019).

[273] T. Iadecola, M. Schecter, and S. Xu, Phys. Rev. B **100**, 184312 (2019).

[274] T. Iadecola and M. Schecter, Phys. Rev. B **101**, 024306 (2020).

[275] P. Sala, T. Rakovszky, R. Verresen, M. Knap, and F. Pollmann, Phys. Rev. X **10**, 011047 (2020).

[276] V. Khemani, M. Hermele, and R. Nandkishore, Phys. Rev. B **101** (2020).

[277] C.-J. Lin, A. Chandran, and O. I. Motrunich, Phys. Rev. Research **2**, 033044 (2020).

[278] K. Lee, R. Melendrez, A. Pal, and H. J. Changlani, Phys. Rev. B **101**, 241111 (2020).

[279] S. Moudgalya, E. O'Brien, B. A. Bernevig, P. Fendley, and N. Regnault, Phys. Rev. B **102**, 085120 (2020).

[280] A. A. Michailidis, C. J. Turner, Z. Papić, D. A. Abanin, and M. Serbyn, Phys. Rev. Research **2**, 022065 (2020).

[281] X. Yu, D. Luo, and B. K. Clark, Phys. Rev. B **98**, 115106 (2018).

[282] S. Moudgalya, N. Regnault, and B. A. Bernevig, Phys. Rev. B **102**, 085140 (2020).

[283] C.-J. Lin, V. Calvera, and T. H. Hsieh, Phys. Rev. B **101**, 220304 (2020).

[284] P. A. McClarty, M. Haque, A. Sen, and J. Richter, Phys. Rev. B **102**, 224303 (2020).

[285] J. Wildeboer, A. Seidel, N. S. Srivatsa, A. E. B. Nielsen, and O. Erten, "Topological quantum many-body scars in quantum dimer models on the kagome lattice," (2020), arXiv:2009.00022 [cond-mat.str-el] .

[286] I. Mondragon-Shem, M. G. Vavilov, and I. Martin, "The fate of quantum many-body scars in the presence of disorder," (2020), arXiv:2010.10535 [cond-mat.quant-gas] .

[287] H. J. Changlani, S. Pujari, C.-M. Chung, and B. K. Clark, Phys. Rev. B **99**, 104433 (2019).

[288] S. Pal, P. Sharma, H. J. Changlani, and S. Pujari, Phys. Rev. B **103**, 144414 (2021).

[289] C. D. Batista, Phys. Rev. B **80**, 180406 (2009).

[290] C. Batista and R. Somma, Phys. Rev. Lett. **109**, 227203 (2012).

[291] K. Essafi, O. Benton, and L. D. C. Jaubert, Nature Comm. **7**, 10297 (2016).

[292] J. H. Conway, *The symmetries of things* (A.K. Peters, Wellesley, Mass, 2008).

[293] D. Shechtman, I. Blech, D. Gratias, and J. W. Cahn, Phys. Rev. Lett. **53**, 1951 (1984).

[294] D. Levine and P. J. Steinhardt, Phys. Rev. Lett. **53**, 2477 (1984).

[295] R. Penrose, Bull. Inst. Math. Appl. **10**, 266 (1974).

[296] G. Vidal, Phys. Rev. Lett. **91**, 147902 (2003).

[297] D. N. Page, Phy. Rev. Lett. **71**, 1291–1294 (1993).

[298] L. Coopmans, D. Luo, G. Kells, B. K. Clark, and J. Carrasquilla, "Protocol Discovery for the Quantum Control of Majoranas by Differentiable Programming and Natural Evolution Strategies," (2021), arXiv:2008.09128 [cond-mat.str-el] .

[299] C.-K. Chiu, J. C. Y. Teo, A. P. Schnyder, and S. Ryu, Rev. Mod. Phys. **88**, 035005 (2016).

[300] P. Virtanen *et al.*, Nature Methods **17**, 261 (2020).

[301] E. Canovi, D. Rossini, R. Fazio, G. E. Santoro, and A. Silva, Phys. Rev. B **83**, 094431 (2011).

[302] L. Rademaker, M. Ortuño, and A. M. Somoza, Ann. Phys. (Berl.) **529**, 1600322 (2017).

[303] C. B. Barber, D. P. Dobkin, and H. Huhdanpaa, ACM Transactions on Mathematical Software (TOMS) **22**, 469 (1996).

[304] S. Boyd and L. Vandenberghe, *Convex Optimization* (Cambridge University Press, 2004).